Keigwin, L.D., Rio, D., Acton, G.D., et al., 1998
Proceedings of the Ocean Drilling Program, Initial Reports, Vol. 172

4. INTERMEDIATE DEPTH BLAKE OUTER RIDGE, SITES 1056, 1057, 1058, AND 1059[1]

Shipboard Scientific Party[2]

HOLE 1056A

Position: 32°29.100′N, 76°19.803′W (Blake Outer Ridge)

Start hole: 2209 hr, 23 February 1997

End hole: 0340 hr, 24 February 1997

Time on hole: 5.52 hr (0.23 days)

Seafloor (drill-pipe measurement from rig floor, mbrf): 2178.0

Distance between rig floor and sea level (m): 11.3

Water depth (drill-pipe measurement from sea level, m): 2166.7

Total depth (from rig floor, mbrf): 2187.5

Penetration (m): 9.5

Coring totals:

Type: APC; Number: 1; Cored: 9.50 m; Recovered: 9.98 m (105.05%)

Oldest formation cored: late Pleistocene clay with nannofossils

HOLE 1056B

Position: 32°29.102′N, 76°19.799′W (Blake Outer Ridge)

Start hole: 0340 hr, 24 February 1997

End hole: 1625 hr, 24 February 1997

Time on hole: 12.75 hr (0.53 days)

Seafloor (drill-pipe measurement from rig floor, mbrf): 2177.9

Distance between rig floor and sea level m): 11.3

Water depth (drill-pipe measurement from sea level, m): 2166.6

Total depth (from rig floor, mbrf): 2333.5

Penetration (m): 155.6

Coring totals:

Type: APC; Number: 17; Cored: 155.60 m; Recovered: 171.81 m (110.42%)

Oldest formation cored: early Pleistocene clay and nannofossil clayey mixed sediment

HOLE 1056C

Position: 32°29.111′N, 76°19.811′W (Blake Outer Ridge)

Start hole: 1625 hr, 24 February 1997

End hole: 0500 hr, 25 February 1997

Time on hole: 12.58 hr (0.52 days)

Seafloor (drill-pipe measurement from rig floor, mbrf): 2178.2

Distance between rig floor and sea level (m): 11.3

Water depth (drill-pipe measurement from sea level, m): 2166.9

Total depth (from rig floor, mbrf): 2333.0

Penetration (m): 154.8

Coring totals:

Type: APC; Number: 17; Cored: 154.80 m; Recovered: 166.25 m (107.40%)

Oldest formation cored: early Pleistocene clay and clay with silt

HOLE 1056D

Position: 32°29.122′N, 76°19.825′W (Blake Outer Ridge)

Start hole: 0500 hr, 25 February 1997

End hole: 1945 hr, 25 February 1997

Time on hole: 14.75 hr (0.61 days)

Seafloor (drill-pipe measurement from rig floor, mbrf): 2177.7

Distance between rig floor and sea level (m): 11.3

Water depth (drill-pipe measurement from sea level, m): 2166.4

Total depth (from rig floor, mbrf): 2299.5

Penetration (m): 121.8

Coring totals:

Type: APC; Number: 13; Cored: 121.80 m; Recovered: 132.46 m (108.75%)

Oldest formation cored: early Pleistocene clay with nannofossils and foraminifers

HOLE 1057A

Position: 32°1.751′N, 76°4.753′W (Blake Outer Ridge)

Start hole: 2246 hr, 25 February 1997

End hole: 1458 hr, 26 February 1997

Time on hole: 16.20 hr (0.68 days)

Seafloor (drill-pipe measurement from rig floor, mbrf): 2595.0

Distance between rig floor and sea level (m): 11.3

Water depth (drill-pipe measurement from sea level, m): 2583.7

Total depth (from rig floor, mbrf): 2726.0

Penetration (m): 131.0

Coring totals:

Type: APC; Number: 14; Cored: 131.00 m; Recovered: 141.67 m (108.15%)

Oldest formation cored: early Pleistocene clay with silt and nannofossils

---

[1] Keigwin, L.D., Rio, D., Acton, G.D., et al., 1998. *Proc. ODP, Init. Repts.,* 172: College Station, TX (Ocean Drilling Program).

[2] Shipboard Scientific Party is given in the list preceding the Table of Contents.

Prior Chapter Contents Next Chapter

HOLE 1057B

Position: 32°1.732′N, 76°4.754′W (Blake Outer Ridge)

Start hole: 1458 hr, 26 February 1997

End hole: 0355 hr, 27 February 1997

Time on hole: 12.95 hr (0.54 days)

Seafloor (drill-pipe measurement from rig floor, mbrf): 2595.8

Distance between rig floor and sea level (m): 11.3

Water depth (drill-pipe measurement from sea level, m): 2584.5

Total depth (from rig floor, mbrf): 2732.5

Penetration (m): 136.7

Coring totals:
Type: APC; Number: 15; Cored: 136.70 m; Recovered: 145.08 m (106.13%)

Oldest formation cored: early Pleistocene clay with silt and nannofossils

HOLE 1057C

Position: 32°1.714′N, 76°4.755′W (Blake Outer Ridge)

Start hole: 0355 hr, 27 February 1997

End hole: 1515 hr, 27 February 1997

Time on hole: 11.33 hr (0.47 days)

Seafloor (drill-pipe measurement from rig floor, mbrf): 2594.5

Distance between rig floor and sea level (m): 11.3

Water depth (drill-pipe measurement from sea level, m): 2583.2

Total depth (from rig floor, mbrf): 2668.0

Penetration (m): 73.5

Coring totals:
Type: APC; Number: 8; Cored: 73.50 m; Recovered: 77.46 m (105.39%)

Oldest formation cored: middle Pleistocene clay with silt and nannofossils

HOLE 1058A

Position: 31°41.415′N, 75°25.805′W (Blake Outer Ridge)

Start hole: 2109 hr, 27 February 1997

End hole: 1659 hr, 28 February 1997

Time on hole: 19.83 hr (0.83 days)

Seafloor (drill-pipe measurement from rig floor, mbrf): 2996.0

Distance between rig floor and sea level (m): 11.5

Water depth (drill-pipe measurement from sea level, m): 2984.5

Total depth (from rig floor, mbrf): 3148.0

Penetration (m): 152.0

Coring totals:
Type: APC; Number: 16; Cored: 152.0 m; Recovered: 164.56 m (108.26%)

Oldest formation cored: early Pleistocene clay with silt

HOLE 1058B

Position: 31°41.402′N, 75°25.804′W (Blake Outer Ridge)

Start hole: 1659 hr, 28 February 1997

End hole: 0655 hr, 1 March 1997

Time on hole: 13.93 hr (0.58 days)

Seafloor (drill-pipe measurement from rig floor, mbrf): 2995.5

Distance between rig floor and sea level (m): 11.5

Water depth (drill-pipe measurement from sea level, m): 2984.0

Total depth (from rig floor, mbrf): 3153.5

Penetration (m): 158.0

Coring totals:
Type: APC; Number: 17; Cored: 158.0 m; Recovered: 166.00 m (105.06%)

Oldest formation cored: early Pleistocene clay with silt

HOLE 1058C

Position: 31°41.386′N, 75°25.801′W (Blake Outer Ridge)

Start hole: 0655 hr, 1 March 1997

End hole: 0515 hr, 2 March 1997

Time on hole: 22.33 hr (0.93 days)

Seafloor (drill-pipe measurement from rig floor, mbrf): 2996.0

Distance between rig floor and sea level (m): 12.0

Water depth (drill-pipe measurement from sea level, m): 2984.0

Total depth (from rig floor, mbrf): 3160.0

Penetration (m): 164.0

Coring totals:
Type: APC; Number: 18; Cored: 164.0 m; Recovered: 173.81 m (105.98%)

Oldest formation cored: early Pleistocene clay with silt

HOLE 1059A

Position: 31°40.461′N, 75°25.127′W (Blake Outer Ridge)

Start hole: 2307 hr, 3 March 1997

End hole: 1445 hr, 4 March 1997

Time on hole: 15.63 hr (0.65 days)

Seafloor (drill-pipe measurement from rig floor, mbrf): 2996.7

Distance between rig floor and sea level (m): 11.3

Water depth (drill-pipe measurement from sea level, m): 2985.4

Total depth (from rig floor, mbrf): 3095.5

Penetration (m): 98.8

Coring totals:
Type: APC; Number: 11; Cored: 98.8 m; Recovered: 105.49 m (106.77%)

Oldest formation cored: middle Pleistocene clay with silt and nannofossils

HOLE 1059B

Position: 31°40.453′N, 75°25.112′W (Blake Outer Ridge)

Start hole: 1445 hr, 4 March 1997

End hole: 0010 hr, 5 March 1997

Time on hole: 9.42 hr (0.39 days)

Seafloor (drill-pipe measurement from rig floor, mbrf): 2996.8

Distance between rig floor and sea level (m): 11.6

Water depth (drill-pipe measurement from sea level, m): 2985.2

Total depth (from rig floor, mbrf): 3089.0

Penetration (m): 92.2

Coring totals:
Type: APC; Number: 10; Cored: 92.2 m; Recovered: 95.91 m (104.02%)

Oldest formation cored: middle Pleistocene clay with silt and nannofossils

HOLE 1059C

Position: 31°40.442′N, 75°25.098′W (Blake Outer Ridge)

Start hole: 0010 hr, 5 March 1997

End hole: 1424 hr, 5 March 1997

Time on hole: 14.23 hr (0.59 days)

Seafloor (drill-pipe measurement from rig floor, mbrf): 2996.0

Distance between rig floor and sea level (m): 11.3

Water depth (drill-pipe measurement from sea level, m): 2984.7

Total depth (from rig floor, mbrf): 3091.0

Penetration (m): 95.0

Coring totals:
Type: APC; Number: 10; Cored: 95.0 m; Recovered: 100.54 m (105.83%)

Oldest formation cored: middle Pleistocene clay with silt and nannofossils

Principal results: The sedimentary succession recovered from the four holes at Site 1056 consists of a well-dated, ~155-m-thick interval of early Pleistocene to Holocene alternating clay and nannofossil ooze with variable amounts of foraminifers and diatoms. Compared to shallower Sites 1054 and 1055, Site 1056 shows much less evidence of downslope transport and current activity. The reworking of both planktonic foraminifers and calcareous nannofossils is surprisingly low. Stratigraphic correlation based on multisensor track (MST) records from all holes suggests that we have recovered a complete stratigraphic sequence.

Two lithologic units were recognized. Unit I (0–95 mbsf; Holocene to middle Pleistocene) is characterized by alternating clay-dominated and carbonate-rich nannofossil sediments. The unit is defined largely on the basis of relatively high carbonate content (as much as 67%) and higher amplitude oscillations in color reflectance than the underlying unit. Distinct layers of red lutite, from 1 to 1.6 m thick, occur at 15, 64, and 90 mbsf in Hole 1056B. Unit II (95−155 mbsf; middle Pleistocene to early Pleistocene), is defined by predominant, clayey lithologies with decreased carbonate content and color variability with respect to the overlying unit. Unit II has been subdivided into two subunits. Subunit IIA is a 5-m-thick convoluted clayey interval. Subunit IIB is made up of fairly homogeneous, greenish to gray clayey lithologies (clay, silty clay, clayey silt, nannofossil clay, and, more rarely, nannofossil-clay mixed sediments). Nannofossil ooze layers, present in the overlying unit, are missing. Numerous thin silt layers occur at various levels, suggesting winnowing by deep-water flow and/or deposition by turbidity currents. A 60-cm-thick biogenic sandy layer with a sharp lower contact occurs at 133 mbsf in Hole 1056B.

The succession contains abundant and well-preserved calcareous nannofossils and common to few planktonic and benthic foraminifers with good to moderate preservation. Diatoms are few to common and often fragmented. Seven calcareous nannofossil and planktonic foraminifer datum levels give sedimentation rates of 81−82 m/m.y. for the past 0.5 m.y. and 105−110 m/m.y. in the underlying interval. The oldest sediments recovered date to the early Pleistocene (between 1.25 and 1.58 Ma).

Magnetic susceptibility and magnetic intensity records show cyclic variations that can be correlated with marine oxygen isotope stages for at least the past ~600 k.y. Magnetic polarity assessment is difficult because of the effects of overprint, reduction diagenesis, and core disturbance caused by gas expansion. The onset of the Brunhes Chron (0 to 0.78 Ma) is possibly located at 92 mbsf in Hole 1056D, with the Jaramillo Subchron (0.99−1.07 Ma) between 99 and 112 mbsf.

Calcium carbonate contents fluctuate between 11 and 67 wt%, gradually decreasing with increasing sediment depth. Total organic carbon (TOC) contents vary between 0.1 and 1.14 wt%, increasing downhole. C/N values of samples that contain more than 0.5 wt% TOC average 5.5, and are indicative of predominantly marine organic material. Results of Rock-Eval pyrolysis analyses indicate that organic matter is thermally immature with respect to petroleum generation.

Pore-water profiles from Site 1056 are typical of sediments in which sulfate reduction and methanogenesis occur. The sulfate reduction zone extends to only 16 mbsf, and carbonate precipitation probably occurs below that level. Chloride shows a trend of increasing concentration with depth. Anomalous excursions toward lower chloride values at discrete depths suggest the presence of gas hydrate, which could comprise as much as 5.5% of the sediment volume. The C_1/C_2 values and the absence of major contributions of higher molecular-weight hydrocarbons suggest that the source for methane is most likely in situ bacterial methanogenesis resulting from decomposition of organic matter in the sediments.

Site 1056 provides an expanded succession ideally suited for high-resolution paleoceanographic studies on the climatic variability of the past 1.5 m.y. on both the Milankovitch and the millennial time scales. The alternations of nannofossil ooze and clay intervals are interpreted as a switching of the climate system from interglacial to glacial times, respectively. The pattern of alternating lithologies in Unit I is likely to be a function of both changes in surface-water productivity patterns and varying quality and quantity of terrigenous sediment input. On longer time scales, the transition from the 41-k.y. climatic variability to the 100-k.y. variability is obvious in the Site 1056 record, correlating with the transition from lithologic Unit II to Unit I.

The three holes at Site 1057 contain a well-dated 136-m-thick interval of early Pleistocene to Holocene alternating nannofossil ooze and clay with variable amounts of foraminifers and diatoms. Compared to Site 1056, Site 1057 contains more silt layers in intervals inferred to be glacial epochs, and those intervals appear to be thicker. In contrast, the shallower site seems to have thicker interglacial episodes. Stratigraphic correlation based on MST records from all holes suggests that we have recovered a complete stratigraphic sequence.

Two lithologic units were recognized. The upper Unit I (0−80 mbsf; Holocene to middle Pleistocene) is characterized by alternating clay-dominated and carbonate-rich nannofossil sediments. The unit is defined largely on the basis of relatively high carbonate content (as much as 64 wt%) and higher amplitude oscillations in color reflectance than the underlying units. This unit correlates with Unit I at Site 1056. At Site 1057, however, the darker clay intervals are considerably thicker than the light nannofossil-rich layers, which is the opposite of what was observed at Site 1056, despite the short distance between the two sites. Unit II (78−138 mbsf; middle Pleistocene to early Pleistocene) has been subdivided into two subunits: Subunit IIA (80−89 mbsf in Hole 1057A and 78−85 mbsf in Hole 1057B) is contorted and deformed nannofossil clay and clay with nannofossils, without any lithologic contrast with the overlying and underlying units. Subunit IIB (85−90 to 137 mbsf) contains fairly homogeneous greenish to medium dark gray clayey lithologies (clay, nannofossil clay, clay with silt and nannofossils, and, more rarely, nannofossil-clay mixed sediments). The lack of nannofossil ooze layers, the lower carbonate content, and the low variability in the color reflectance are the features that distinguish Subunit IIB from Unit I. Silt layers occur at various levels, suggesting winnowing by deep-water flow and/or deposition by turbidity currents.

Site 1057 contains abundant and well-preserved calcareous nannofossils and common to few planktonic and benthic foraminifers with good to moderate preservation. Diatoms are few and often fragmented. Sedimentation rates were 70 m/m.y. in the past 0.5 m.y., and 125 m/m.y. between 0.5 and 1.25 Ma. Oldest sediments are early Pleistocene (between 0.96 and 1.25 Ma).

The magnetic polarity assessment is difficult because of the effects of overprint, reduction diagenesis, and core disturbance caused by gas expansion. The onset of the Brunhes Chron (0–0.78 Ma) is tentatively located at 78 mbsf in Hole 1057A, with the Jaramillo Subchron (0.99–1.07 Ma) occurring between 107 and 122 mbsf. These initial magnetic polarity data agree very well with biochronological results based on calcareous plankton. As at Sites 1055 and 1056, magnetic susceptibilities and magnetic intensities show cyclic variations that correlate with marine oxygen isotope stages for at least the past 600 k.y.

Calcium carbonate contents fluctuate between 11 and 64 wt%, gradually decreasing with increasing sediment depth. TOC contents vary between 0.1 and 1.14 wt%, increasing downhole. C/N values of samples containing more than 0.5 wt% TOC average 9.0 wt%, and are indicative of predominantly marine organic material. Results of Rock-Eval analysis indicate that organic matter is thermally immature with respect to petroleum generation.

As at Site 1056, pore-water profiles from Site 1057 are typical of sediments in which sulfate reduction and methanogenesis occur. The top of the sulfate reduction zone is close to the seafloor. The onset of the methanogenic zone occurs at 15–20 mbsf, coincident with the level of zero pore-water sulfate. The distributions of dissolved Ca and Mg suggest active Mg-enriched carbonate precipitation near the sulfate/methane interface and within the methanogenic zone. Chlorinity shows a trend toward lower values below 83 mbsf and suggests the underlying occurrence of gas hydrate, which could occupy a maximum of 4.2% of the sediment volume. C_1/C_2 values and the absence of major contributions of higher molecular-weight hydrocarbons suggest that the source for methane is most likely in situ bacterial methanogenesis resulting from decomposition of organic matter in the sediments.

Site 1057 provides an expanded succession ideally suited for high-resolution paleoceanographic studies on the climatic variability of the past 1.0 m.y. on both Milankovitch and millennial time scales. On longer time scales, the transition from the 41-k.y. to the 100-k.y. climatic variability is obvious in the Site 1057 record, correlating with the transition from lithologic Unit II to Unit I. The alternation of nannofossil ooze and clay intervals in Unit I are interpreted as the switching of the climate system from interglacial to glacial times, respectively. The pattern of alternating lithologies is likely to be a function of both changes in surface-water productivity patterns and varying quality and quantity of terrigenous sediment input. No clear evidence is available at this stage for the former process, although the latter process is supported by the changes in sedimentation rates and sediment type between Sites 1056 and 1057. The smaller scale differences between sites during the same climatic interval (i.e., carbonate-rich interglacials or clay-dominated glacials) can be explained by shifts of the Western Boundary Underwater Current (WBUC) between different depths in response to climate forcing. For instance, the fluctuating position and/or intensity of upper North Atlantic Deep Water (NADW) can be envisaged as a likely cause for the differences in sedimentation rates in glacial and interglacial times between Sites 1056 and 1057.

Sites 1058 and 1059 consist predominantly of rapidly accumulated nannofossil ooze, clay with nannofossils, and clays with minor amount of silts. The main component of lithologic variability occurs on decimeter-to-meter scales throughout the section in the form of cyclic changes in color that are mainly related to relative changes in the proportions of biogenic carbonate, detrital clay, and silt. Stratigraphic correlation based on MST records from all holes suggests that we have recovered a complete stratigraphic sequence at both sites.

Two lithologic units can be recognized at the location of Sites 1058 and 1059. Unit I (0–112 mbsf at Site 1058 and 0 to the total depth of 98 mbsf at Site 1059; Holocene to late and middle Pleistocene at Sites 1058 and 1059, respectively), is characterized by cyclically alternating light gray nannofossil ooze and dark greenish gray clay containing reddish brown layers. The latter are more common in the upper part of the unit. The unit is defined largely on the basis of its relatively high carbonate content (as much as 53 wt%) and higher amplitude oscillations in color reflectance than the underlying unit. Bioturbation, pyrite, and pyrite nodules are common in the olive gray nannofossil clay. Silt-sized biogenic layers are present at the top of light-colored nannofossil ooze intervals and have sharp upper contacts at Site 1058. Unit II (recovered only at Site 1058, between 112 mbsf and the total depth of 164 mbsf; early Pleistocene) is predominantly clay, clay with silt, and clay with nannofossils. It is characterized by a lower and less variable carbonate content (9–26 wt%). The red lutite layers are missing, and pyrite nodules occur throughout the unit.

These sites contain abundant to common calcareous nannofossils, which are generally well preserved. Reworking of mainly Cretaceous and Paleogene forms is present in the expanded section of Site 1059. Planktonic foraminifers are common to few with good to moderate preservation. Benthic foraminifers are rare to few and generally moderately well preserved. Diatoms are relatively common and well preserved in the middle part of the succession.

Age control is provided by integrated calcareous plankton biostratigraphy and magnetostratigraphy. At Site 1058 the oldest sediments are 1.24–1.58 Ma. Sedimentation rates average 95 m/m.y. during the past 0.5 m.y. and 110 m/m.y. in the underlying interval. At Site 1059 the oldest sediments date to 0.5 Ma and sedimentation rates average 120–140 m/m.y. during the past 0.5 m.y. Magnetic susceptibility and magnetic intensity records show cyclic variations, which evidently correlate with marine oxygen isotope stages, at least for the past 0.6 m.y. If correct, this correlation indicates that at Site 1059, late Pleistocene sedimentation rates may have been as high as 280 m/m.y.

Magnetic polarity assessment is difficult because of the effects of overprint, reduction diagenesis, and core disturbance caused by gas expansion. The onset of the Brunhes Chron (0 to 0.78 Ma) is tentatively located between 89 and 99 mbsf in Hole 1058A, with the Jaramillo Subchron (0.99–1.07 Ma) between 112 and 121 mbsf. At Site 1059 only normal-polarity directions were observed for the entire interval cored, which correlates to the Brunhes Chron. An excellent agreement is observed between the pass-through measurements of the archive halves and the best fit directions obtained from progressive AF demagnetization of the discrete samples.

Calcium carbonate contents fluctuate between 6.6 and 53 wt% at Site 1058 and between 9 and 49 wt% at Site 1059. TOC contents vary between 0.1 and 1.14 wt% at Site 1058 and between 0.2 and 1.14 wt% at Site 1059. C/N values of samples containing more than 0.5 wt% TOC average 6.5 and 7.0 wt% at Sites 1058 and 1059, respectively, and are indicative of predominantly marine organic material. Results of Rock-Eval analysis indicate that organic matter is thermally immature with respect to petroleum generation.

Pore-water chemistry shows a very thin sulfate reduction zone at both Site 1058 (between 7 and 16 mbsf) and Site 1059 (~12 mbsf). Carbonate precipitation probably occurs near the sulfate-methane interface and within the methanogenesis zone. At Site 1058, chlorinity gives equivocal indications concerning the presence of gas hydrate. Anomalous excursions toward lower chloride values at 94 and 139 mbsf suggest the possible occurrence of gas hydrate, which could comprise 1.5% of the sediment volume. At Site 1059, chlorinity decreases slightly downcore, suggesting the presence of gas hydrate at depth. The cored interval does not show anomalous excursions toward fresher chloride values and should be free of gas hydrate. At both sites the C_1/C_2 values and the absence of a major contribution of higher molecular-weight hydrocarbons suggest that the source for methane is most likely in situ bacterial methanogenesis resulting from decomposition of organic matter in the sediments.

Sites 1058 and 1059 provide expanded sections ideally suited for high-resolution paleoceanographic studies on the climatic variability of the past 1.0 m.y. on both Milankovitch and millennial time scales. As at Sites 1056 and 1057, the transition from the 41-k.y. to the 100-k.y. climatic variability is obvious at Sites 1058 and 1059 and correlates with the transition from lithologic Unit II to Unit I. The alternations of nannofossil ooze and clay intervals are interpreted as a switch of the climate system from interglacial to glacial times, respectively. It is noteworthy that at Site 1058, the top of the carbonate beds is persistently sharp and overlain by coarser sediments, suggesting stronger currents at the end of interglacial periods. This contrasts with Site 1059, where the base of the carbonate unit seems characterized by an abrupt transition and the top is gradual, indicating stronger currents at the beginning of the interglacials.

BACKGROUND AND OBJECTIVES

Sites 1056–1059 are located at intermediate water depths (2177 to 2997 m) along the crest of the Blake-Bahama Outer Ridge (BBOR), at locations ideal for monitoring Pleistocene to late Pliocene changes in production and flow of NADW. All four sites were cored with the advanced piston corer (APC) at least three times to ensure complete recovery of the stratigraphic section, a prerequisite for high-resolution paleoenvironmental studies. Site 1056 lies within the core of Upper NADW, Sites 1058 and 1059 are in the core of Lower NADW, and Site 1057 straddles the boundary between those two water masses (see Fig. 4, "Introduction" chapter, this volume). It is expected that, during glacial and stadial climate episodes, paleo-proxy data from Sites 1058 and 1059 will show increased nutrient content (reduced flow of Lower NADW), whereas shallower sites will show nutrient depletion (increased flow of Upper NADW).

The Blake Outer Ridge first becomes noticeable as a bulge in the continental slope at Site 1056; therefore, that site and those at greater depths should show progressively less influence of downslope sedimentary processes and greater influence of current-controlled sedimentation. Sites 1058 and 1059 provide a test location for the effects of current control. The two sites are only about one kilometer apart, but seismic surveys indicate enhanced sediment accumulation in the upper part of Site 1059 relative to Site 1058. Because they underlie the same surface waters, any sedimentological and mass accumulation rate differences between them must be ascribed to the local effects of Deep Western Boundary Current (DWBC) flow.

All four sites also lie in an area known for extensive presence of marine gas hydrate (Paull, Matsumoto, Wallace, et al., 1996). Seismic data show an approximately 1000-m-thick sediment sequence and a bottom-simulating reflector (BSR), which is produced at the base of the gas hydrate stability zone.

The objectives of drilling at these sites were to (1) determine the history of circulation change in the western North Atlantic; (2) provide high-resolution sections for paleomagnetic study; (3) provide sections for studying geochemical processes related to gas hydrate formation and dissociation; and (4) monitor the extent of gas hydrate along the BBOR.

OPERATIONS

At 1300 hr (local time) on 23 February 1997, 1 hr and 45 min after leaving Site 1055, the *JOIDES Resolution* slowed to deploy the seismic gear for a survey over Sites 1056 and 1057. A north-to-south survey line was collected over Site 1056 at 6 kt followed by a west-to-east crossing line (see "Site Geophysics" section, this chapter). The survey gear was left in as the ship followed a southeast course toward Site 1057 at 8 kt. The *JOIDES Resolution* again slowed to 6 kt as it crossed over Site 1057, first on a northwest-to-southeast course and then again on an east-to-west crossing line. The total survey length was 85 km. The multichannel streamer failed again during this survey, but was later fixed by changing the polarity of its pin configuration.

Site 1056

After returning to Site 1056, coring operations began at 2209 hr on 23 February and ended at 1945 hr on 25 February. Because the water depth was ~400 m deeper at Site 1056 than at the previous site, additional joints of pipe were used, which included the reconditioned drill pipe loaded in Charleston. This reconditioned pipe was first measured and "rabbited" (a process in which a small piece of bar or tubing of known diameter is passed through the drill pipe to ensure that it is free of obstructions or diameter restrictions).

At 0340 hr on 24 February, the initial attempt at a mudline core in Hole 1056A was obtained, but the core barrel was full and the seafloor depth could not be determined accurately. Hole 1056B was then started 7 m northeast of Hole 1056A and 6 m shallower. A mudline core was retrieved, and the seafloor depth at this hole was estimated at 2177.9 mbrf, which was 5.5 m shallower than the depth estimated by the precision depth recorder (PDR).

The ship was offset after Holes 1056B and 1056C, with Hole 1056C located 25 m northwest of Hole 1056B and Hole 1056D located 30 m northwest of Hole 1056C. The total core recovered at the site was 480.5 m with 108.8% recovery (Table 1). The large recovery percentage probably results from gas expansion. By 1945 hr on 25 February, the drilling equipment was secured and the vessel was under way, heading southeasterly to the next site.

Site 1057

Coring operations at Site 1057 began at 2246 hr on 25 February after a 31-nmi transit from Site 1056. All holes were APC cored with recovery ranging from 100% to 115% (Table 1). Starting with the third core in each hole, all cores downhole were oriented with the Tensor tool.

During operations on Hole 1057B, a chartered tuna boat, *The Winds of Fortune*, came alongside at 1345 hr on 26 February and disembarked two crew members, who joined us for the remainder of the cruise.

The seafloor depth was established at 2595.0 m at Hole 1057A, which was 6 m deeper than the PDR measurement. Hole 1057B is ~35 m south of Hole 1057A, and Hole 1057C is another ~33 m south of Hole 1057B. Relative to the drill string position for Hole 1057A, the drill string was raised 3 m higher for Hole 1057B and then lowered 2 m for Hole 1057C. By 1515 hr on 27 February, the vessel was under way.

Site 1058

The 30-nmi transit to Site 1058 was traveled at an average speed of 12 kt. At 1745 hr, the vessel slowed as the seismic gear was deployed about 8 nmi before Site 1058. The survey proceeded over both sites along a southeasterly course. The vessel came about and performed a northeast-to-southwest crossing over Site 1059 and then a southwest-to-northeast crossing over Site 1058. During the 24-km-long survey, data were collected simultaneously with a single-channel and a six-channel streamer. Accurate survey and drilling positions were obtained owing to the availability of the differential global positioning system (GPS). At 2045 hr on 27 February, the seismic equipment was retrieved and the vessel returned to Site 1058 for drilling operations.

Coring operations at Site 1058 began at 2109 hr on 27 February. All holes were APC cored, with recovery ranging from 98% to 114% (Table 1). Starting with the third core in each hole, all cores downhole were oriented with the Tensor tool.

The seafloor depth was established at 2996.0 mbrf in Hole 1058A, which was 4 m shallower than the PDR measurement. Hole 1058B is 24 m south of Hole 1058A, and Hole 1058C is another 30 m south and 5 m west of Hole 1058B. The starting drill-string position was vertically offset 3 m shallower for Hole 1058B than Hole 1058A and then another 3 m shallower for Hole 1058C.

On the evening of 28 February, we received sad news of a death in the family of an ODP crew member. After assessing all options, including queries to the local military installations in North and South Carolina, looking into the availability and suitability of local trans-

Table 1. Coring summary for Sites 1056, 1057, 1058, and 1059.

Core	Date (1997)	Time (UTC)	Interval (mbsf)	Length cored (m)	Length recovered (m)	Recovery (%)
172-1056A-						
1H	Feb. 24	0350	0-9.50	9.50	9.98	105.1
Coring totals:				9.50	9.98	105.1
172-1056B-						
1H	24 Feb	0425	0.0-3.6	3.6	3.64	101.1
2H	24 Feb	0455	3.6-13.1	9.5	9.53	100.3
3H	24 Feb	0540	13.1-22.6	9.5	9.95	104.7
4H	24 Feb	0620	22.6-32.1	9.5	9.99	105.2
5H	24 Feb	0655	32.1-41.6	9.5	10.37	109.2
6H	24 Feb	0735	41.6-51.1	9.5	10.44	109.9
7H	24 Feb	0810	51.1-60.6	9.5	10.43	109.8
8H	24 Feb	0850	60.6-70.1	9.5	10.38	109.3
9H	24 Feb	0925	70.1-79.6	9.5	10.25	107.9
11H	24 Feb	1040	89.1-98.6	9.5	10.98	115.6
12H	24 Feb	1115	98.6-108.1	9.5	10.65	112.1
13H	24 Feb	1155	108.1-117.6	9.5	10.74	113.1
14H	24 Feb	1240	117.6-127.1	9.5	10.29	108.3
15H	24 Feb	1320	127.1-136.6	9.5	10.76	113.3
16H	24 Feb	1400	136.6-146.1	9.5	10.86	114.3
17H	24 Feb	1445	146.1-155.6	9.5	11.96	125.9
Coring totals:				155.6	171.81	110.4
172-1056C-						
1H	24 Feb	1715	0.0-5.3	5.3	5.31	100.2
2H	24 Feb	1750	5.3-14.8	9.5	9.93	104.5
3H	24 Feb	1830	14.8-24.3	9.5	10.02	105.5
4H	24 Feb	1910	24.3-33.8	9.5	9.97	104.9
5H	24 Feb	1950	33.8-43.3	9.5	10.08	106.1
6H	24 Feb	2030	43.3-52.8	9.5	10.10	106.3
7H	24 Feb	2115	52.8-62.3	9.5	10.27	108.1
8H	24 Feb	2155	62.3-71.8	9.5	10.37	109.2
9H	24 Feb	2235	71.8-81.3	9.5	10.55	111.1
10H	24 Feb	2320	81.3-90.8	9.5	10.24	107.8
11H	24 Feb	2355	90.8-100.3	9.5	10.28	108.2
12H	25 Feb	0040	100.3-109.8	9.5	10.12	106.5
13H	25 Feb	0115	109.8-119.3	9.5	9.94	104.6
14H	25 Feb	0200	119.3-126.3	7.0	8.38	119.7
15H	25 Feb	0240	126.3-135.8	9.5	10.20	107.4
16H	25 Feb	0315	135.8-145.3	9.5	10.26	108.0
17H	25 Feb	0350	145.3-154.8	9.5	10.23	107.7
Coring totals:				154.8	166.25	107.4
172-1056D-						
1H	25 Feb	0600	0.0-7.8	7.8	7.8	100.0
2H	25 Feb	0630	7.8-17.3	9.5	9.8	102.8
3H	25 Feb	0705	17.3-26.8	9.5	10.0	105.7
4H	25 Feb	0750	26.8-36.3	9.5	10.0	104.8
5H	25 Feb	0905	36.3-45.8	9.5	10.1	106.6
6H	25 Feb	0945	45.8-55.3	9.5	10.2	107.8
7H	25 Feb	1015	55.3-64.8	9.5	10.3	107.9
8H	25 Feb	1055	64.8-74.3	9.5	10.6	111.5
9H	25 Feb	1130	74.3-83.8	9.5	10.9	115.2
10H	25 Feb	1210	83.8-93.3	9.5	11.4	119.6
11H	25 Feb	1255	93.3-102.8	9.5	10.6	111.8
12H	25 Feb	1340	102.8-112.3	9.5	10.7	112.2
13H	25 Feb	1425	112.3-121.8	9.5	10.1	106.3
Coring totals:				121.8	132.46	108.8
172-1057A-						
1H	26 Feb	0445	0-7.5	7.5	7.5	100
2H	26 Feb	0535	7.5-17	9.5	9.82	103.4
3H	26 Feb	0620	17-26.5	9.5	10.01	105.4
4H	26 Feb	0700	26.5-36	9.5	10.13	106.6
5H	26 Feb	0735	36-45.5	9.5	10.21	107.5
6H	26 Feb	0815	45.5-55	9.5	10.15	106.8
7H	26 Feb	0855	55-64.5	9.5	10.26	108
8H	26 Feb	0935	64.5-74	9.5	10.23	107.7
9H	26 Feb	1015	74-83.5	9.5	10.19	107.3
10H	26 Feb	1055	83.5-93	9.5	10.33	108.7
11H	26 Feb	1135	93-102.5	9.5	10.89	114.6
12H	26 Feb	1220	102.5-112	9.5	10.94	115.2
13H	26 Feb	1300	112-121.5	9.5	10.71	112.7
14H	26 Feb	1350	121.5-131	9.5	10.3	108.4
Coring totals:				131	141.67	108.2
172-1057B-						
1H	26 Feb	1555	0.0-3.7	3.7	3.69	99.7
2H	26 Feb	1640	3.7-13.2	9.5	9.81	103.3
3H	26 Feb	1730	13.2-22.7	9.5	9.87	103.9
4H	26 Feb	1815	22.7-32.2	9.5	9.95	104.7
5H	26 Feb	1900	32.2-41.7	9.5	10.00	105.3
6H	26 Feb	1945	41.7-51.2	9.5	10.05	105.8
7H	26 Feb	2030	51.2-60.7	9.5	10.16	106.9
8H	26 Feb	2110	60.7-70.2	9.5	10.21	107.5
9H	26 Feb	2150	70.2-79.7	9.5	10.64	112.0
10H	26 Feb	2235	79.7-89.2	9.5	10.28	108.2
11H	26 Feb	2310	89.2-98.7	9.5	9.99	105.2
12H	26 Feb	2355	98.7-108.2	9.5	10.06	105.9
13H	27 Feb	0040	108.2-117.7	9.5	10.12	106.5
14H	27 Feb	0125	117.7-127.2	9.5	10.14	106.7
15H	27 Feb	0205	127.2-136.7	9.5	10.11	106.4
Coring totals:				136.7	145.08	106.1
172-1057C-						
1H	27 Feb	0410	0.0-7.0	7.0	7.08	101.1
2H	27 Feb	0445	7.0-16.5	9.5	9.77	102.8
3H	27 Feb	0530	16.5-26.0	9.5	9.91	104.3
4H	27 Feb	0610	26.0-35.5	9.5	9.85	103.7
5H	27 Feb	0650	35.5-45.0	9.5	10.19	107.3
6H	27 Feb	0730	45.0-54.5	9.5	10.26	108.0
7H	27 Feb	0810	54.5-64.0	9.5	10.15	106.8
8H	27 Feb	0850	64.0-73.5	9.5	10.25	107.9
Coring totals:				73.5	77.46	105.4
172-1058A-						
1H	28 Feb	0425	0.0-9.5	9.5	9.85	103.7
2H	28 Feb	0515	9.5-19.0	9.5	9.77	102.8
3H	28 Feb	0605	19.0-28.5	9.5	9.88	104.0
4H	28 Feb	0645	28.5-38.0	9.5	9.97	104.9
5H	28 Feb	0730	38.0-47.5	9.5	10.13	106.6
6H	28 Feb	0810	47.5-57.0	9.5	10.22	107.6
7H	28 Feb	0855	57.0-66.5	9.5	10.32	108.6
8H	28 Feb	0935	66.5-76.0	9.5	10.31	108.5
9H	28 Feb	1015	76.0-85.5	9.5	10.25	107.9
10H	28 Feb	1100	85.5-95.0	9.5	10.28	108.2
11H	28 Feb	1145	95.0-104.5	9.5	10.85	114.2
12H	28 Feb	1235	104.5-114.0	9.5	10.61	111.7
13H	28 Feb	1325	114.0-123.5	9.5	10.70	112.6
14H	28 Feb	1410	123.5-133.0	9.5	10.56	111.2
15H	28 Feb	1505	133.0-142.5	9.5	10.55	111.1
16H	28 Feb	1550	142.5-152.0	9.5	10.31	108.5
Coring totals:				152.0	164.56	108.3
172-1058B-						
1H	28 Feb	1755	0.0-6.0	6.0	6.04	100.7
2H	28 Feb	1835	6.0-15.5	9.5	9.85	103.7
3H	28 Feb	1925	15.5-25.0	9.5	10.01	105.4
4H	28 Feb	2010	25.0-34.5	9.5	9.97	104.9
5H	28 Feb	2055	34.5-44.0	9.5	10.14	106.7
6H	28 Feb	2145	44.0-53.5	9.5	10.17	107.1
7H	28 Feb	2225	53.5-63.0	9.5	10.15	106.8
8H	28 Feb	2310	63.0-72.5	9.5	10.04	105.7
9H	28 Feb	2355	72.5-82.0	9.5	10.05	105.8
10H	1 March	0040	82.0-91.5	9.5	10.15	106.8
11H	1 March	0120	91.5-101.0	9.5	10.18	107.2
12H	1 March	0205	101.0-110.5	9.5	9.84	103.6
13H	1 March	0245	110.5-120.0	9.5	10.11	106.4
14H	1 March	0330	120.0-129.5	9.5	10.01	105.4
15H	1 March	0415	129.5-139.0	9.5	9.51	100.1
16H	1 March	0500	139.0-148.5	9.5	10.06	105.9
17H	1 March	0550	148.5-158.0	9.5	9.72	102.3
Coring totals:				158.0	166.00	105.1
172-1058C-						
1H	1 March	0755	0.0-2.5	2.5	2.46	98.4
2H	1 March	0830	2.5-12.0	9.5	9.74	102.5
3H	1 March	0915	12.0-21.5	9.5	10.06	105.9
4H	1 March	1000	21.5-31.0	9.5	10.02	105.5
5H	1 March	1040	31.0-40.5	9.5	10.08	106.1
6H	1 March	1120	40.5-50.0	9.5	10.12	106.5
7H	1 March	1205	50.0-59.5	9.5	10.10	106.3
8H	1 March	1250	59.5-69.0	9.5	10.16	106.9
9H	1 March	1340	69.0-78.5	9.5	10.21	107.5
10H	1 March	1435	78.5-88.0	9.5	10.08	106.1
11H	1 March	1525	88.0-97.5	9.5	10.01	105.4
12H	1 March	1610	97.5-107.0	9.5	10.22	107.6
13H	1 March	1700	107.0-116.5	9.5	10.19	107.3
14H	1 March	1745	116.5-126.0	9.5	10.25	107.9
15H	1 March	1835	126.0-135.5	9.5	10.46	110.1
16H	1 March	1925	135.5-145.0	9.5	9.99	105.2
17H	1 March	2015	145.0-154.5	9.5	9.57	100.7
18H	1 March	2105	154.5-164.0	9.5	10.09	106.2
Coring totals:				164.0	173.81	106.0
172-1059A-						
1H	4 March	0630	0.0-3.8	3.8	3.85	101.3
2H	4 March	0710	3.8-13.3	9.5	9.83	103.5
3H	4 March	0755	13.3-22.8	9.5	10.02	105.5
4H	4 March	0840	22.8-32.3	9.5	10.26	108.0
5H	4 March	0920	32.3-41.8	9.5	10.37	109.2
6H	4 March	1000	41.8-51.3	9.5	10.24	107.8
7H	4 March	1045	51.3-60.8	9.5	10.22	107.6
8H	4 March	1130	60.8-70.3	9.5	10.23	107.7

Table 1 (continued).

Core	Date (1997)	Time (UTC)	Interval (mbsf)	Length cored (m)	Length recovered (m)	Recovery (%)
9H	4 March	1215	70.3-79.8	9.5	10.16	106.9
10H	4 March	1305	79.8-89.3	9.5	10.15	106.8
11H	4 March	1350	89.3-98.8	9.5	10.16	106.9
Coring totals:				98.8	105.49	106.8
172-1059B-						
1H	4 March	1550	0.0-6.7	6.7	6.73	100.4
2H	4 March	1630	6.7-16.2	9.5	9.69	102.0
3H	4 March	1720	16.2-25.7	9.5	9.89	104.1
4H	4 March	1810	25.7-35.2	9.5	9.99	105.2
5H	4 March	1855	35.2-44.7	9.5	10.24	107.8
6H	4 March	1945	44.7-54.2	9.5	10.23	107.7
7H	4 March	2030	54.2-63.7	9.5	10.23	107.7
8H	4 March	2120	63.7-73.2	9.5	10.09	106.2
9H	4 March	2205	73.2-82.7	9.5	10.19	107.3
10H	4 March	2255	82.7-92.2	9.5	8.63	90.8
Coring totals:				92.2	95.91	104.0
172-1059C-						
1H	5 March	0115	0.0-9.5	9.5	9.68	101.9
2H	5 March	0155	9.5-19.0	9.5	9.90	104.2
3H	5 March	0255	19.0-28.5	9.5	10.03	105.6
4H	5 March	0325	28.5-38.0	9.5	10.07	106.0
5H	5 March	0410	38.0-47.5	9.5	10.23	107.7
6H	5 March	0455	47.5-57.0	9.5	10.23	107.7
7H	5 March	0540	57.0-66.5	9.5	10.18	107.2
8H	5 March	0625	66.5-76.0	9.5	10.20	107.4
9H	5 March	0710	76.0-85.5	9.5	9.88	104.0
10H	5 March	0800	85.5-95.0	9.5	10.14	106.7
Coring totals:				95.0	100.54	105.8

Notes: UTC = Universal Time Coordinated. For each site, an expanded coring summary table for each hole that includes lengths and depths of sections and sampling comments is included on CD-ROM (back pocket, this volume).

port (air and boat), and exploring the possibility of using a vessel of opportunity, it was decided to interrupt operations to divert the vessel to Charleston for a humanitarian evacuation. At 0515 hr on 2 March, operations ceased at Site 1058 and we proceeded to Charleston.

At 0354 hr on 3 March, the vessel arrived at the Charleston pilot station where it met the tug *Robert B. Turecaro.* Bill Stevens disembarked the vessel at 0414 hr, and by 0418 hr the vessel was under way to Site 1059. At 2207 hr on 3 March, a beacon was deployed at Site 1059 and coring operations began. The total round-trip distance for this unscheduled transit was 447 nmi and consumed 41.2 hr.

Site 1059

Coring operations at Site 1059 began at 2307 hr on 3 March. All holes were APC cored, with recovery ranging from 91% to 109% (Table 1). Starting with the third core in each hole, all cores downhole were oriented with the Tensor tool.

The seafloor depth was established at 2996.7 mbrf in Hole 1059A. Hole 1059B is 28 m southwest of Hole 1059A, and Hole 1059C is another 30 m southwest of Hole 1059B. The starting drill-string position was vertically offset 3 m shallower for Hole 1059B than for Hole 1059A and then another 2 m shallower for Hole 1059C. By 1424 hr on 5 March, the vessel was under way to the next location.

LITHOSTRATIGRAPHY

Sites 1056 through 1059, ranging in water depth from 2200 to 3000 m, all have similar lithologies and all meet the primary objective of recovering appropriate sediment for a high-resolution paleoceanographic study. At each location, there is a range in composition of upper sediments from clay dominated to nannofossil rich, with occasional interbeddings of red lutites. At Sites 1056 through 1058 this variation distinguishes Unit I from the underlying Unit II, which is more homogeneous and dominated by clay and silt and lacks carbonate-rich intervals and red lutites. Site 1059 consists of only one unit because of its higher deposition rate and shallower penetration.

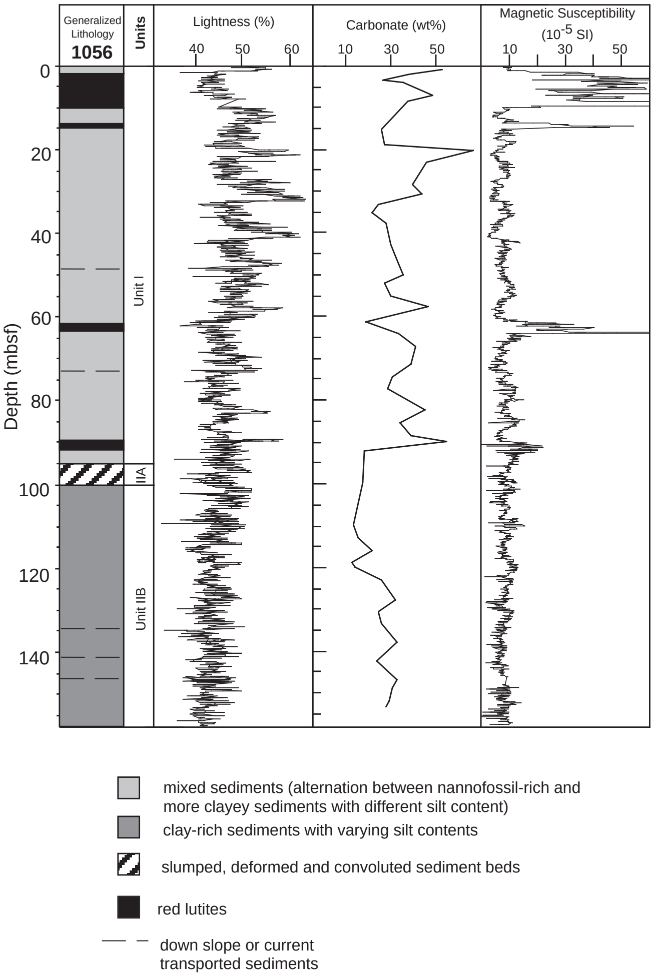

Figure 1. Generalized lithology, color reflectance, carbonate content, and magnetic susceptibility for Hole 1056B.

Description of the Lithostratigraphic Units

Site 1056

Four holes were drilled at Site 1056. The Holocene to early Pleistocene lithostratigraphy was based on Hole 1056B, where the maximum length of sediment was cored (155.6 mbsf). Although the sediments are affected by small depositional and erosional events in some intervals below 48 mbsf, these account for less than 5% of the section. The top of a deformed sediment interval is chosen as the boundary between Units I and II.

Unit I

Intervals: 172-1056A-1H-1, 0 cm, through 1H-CC, 18 cm (0–9.98 mbsf, base of hole); 172-1056B-1H-1, 0 cm, through 11H-5, 25 cm (0–95 mbsf); 172-1056C-1H-1, 0 cm, through 11H-4, 50 cm (0–95.8 mbsf); 172-1056D-1H-1, 0 cm, through 11H-4, 47 cm (0–97.1 mbsf)

Age: Holocene to middle Pleistocene

Unit I is defined by the presence of alternating beds of light greenish gray (5GY 8/1 or 5G 8/1) and greenish gray (5GY 6/1 or 5G 6/1) carbonate-rich units and reddish brown (10YR 5/3), oxidized sediments resulting in large downcore variations in color reflectance (data on CD-ROM, back pocket, this volume). The lower boundary of this unit is marked by an increase in clay content (Fig. 1). The uppermost 10 m of this unit consists predominantly of reddish brown or brownish gray (5YR 4/1) silty clay and clay beds, containing greenish gray clayey silt layers up to 1 cm thick. The reddish brown and brownish gray beds are up to 2 m thick, normally graded, and contain shell and pteropod fragments. Single thicker beds of greenish gray clay with nannofossils (up to 30 cm thick) and light greenish gray nannofossil clay (up to 1.10 m thick) are also observed in the uppermost 10 m.

The lower portion of Unit I is dominated by intercalated beds of light greenish gray clayey nannofossil ooze reaching up to 1.5 m thick, greenish gray to gray nannofossil clay, clayey nannofossil mixed sediment, clay with nannofossils, and clay. Greenish gray to gray (5GY 6/1 to 5Y 5/1) silty clay and clay with silt (up to 1 m thick), and silty pteropod debris beds (1–10 cm thick) are present in minor amounts. In general, the sediments of Unit I contain between 18 and 67 wt% carbonate (see “Organic Geochemistry” section, this chapter). The occurrence of reddish brown clays decreases downcore. Distinct layers of red lutite with a thickness between 1 and 1.6 m occur at around 15, 64, and 90 mbsf.

Coarser beds of silt and sand layers with biogenic components are relatively rare in the upper part of Unit I. At around 48 mbsf they become more common. A distinct, coarser bed (up to 24 cm thick) of dark olive green, sand-sized siliciclastic and biogenic components (e.g., foraminifer tests and pteropod fragments) interbedded with thinner silt and clay layers occurs at around 48 mbsf (Fig. 2). This bed is found in all holes at Site 1056 (intervals 172-1056B-6H-5, 54–79 cm; 172-1056C-6H-3, 46–70 cm; and 172-1056D-6H-2, 65–88 cm). The contact with the next lower bed is sharp and scoured, and marked by an abrupt color change downcore from dark greenish gray (10Y 4/1) to light greenish gray (5GY 6/1 or 7/1). The bed patterns suggest that this coarser interval was not formed during a single depositional event, because silt and sand beds are interlayered with adjacent clays. Also, they have partially bioturbated contacts with the clay layers. The upper coarser bed with mud clasts (interval 172-1056B-6H-5, 54–65 cm; Fig. 2) may have been deposited during a single event, most likely by turbidity currents. The lower part of the interval (65–79 cm) could have been formed by the same event and may represent sediments injected into underlying muds by turbidity currents, or they may represent earlier erosional/depositional events of a different origin. Other distinctly different silt/sand beds are also present. At around 94 mbsf, a 6-cm-thick bed shows an alternation of sand- and silt-sized layers (up to 1 cm thickness) with biogenic components and a scoured contact with the underlying layer (interval 172-1056D-10H-8, 32–38 cm; Fig. 3). The upper contact of this bed is gradational, although distinct, thin laminae can be traced laterally from coarser to finer sediments. Another distinctive feature is the cross-bedding (45°) of the upper part of the sand layer. A 0.5-cm-thick clay bed caps the unit, which is overlain by another, this time truncated, sand/silt bed. The generally uniform texture, thickness, and structure suggest that this bed was formed by current reworking, perhaps by contour currents.

Visual grain size estimations show that the sediments are predominantly clay sized. Silt-sized grains are common, while sand-sized grains are rare and linked to high energy deposits. Smear-slide analyses show that clay and calcite (mainly biogenic components) are the major components of Unit I. Minor components include quartz, detrital carbonate grains, pyrite, Fe-oxides (hematite and limonite), and glauconite. Iron oxides (<2%) are mainly associated with the red lutites (e.g., intervals 172-1056A-1H-2, 113 cm; and 172-1056B-1H-3, 15 cm). Glauconite is present locally in trace amounts. The biogenic calcareous constituents consist predominantly of nannofossils with minor amounts of foraminifers (0%–10%). Siliceous fossils are present as diatoms, sponge spicules, radiolarians, and very rare silicoflagellates. Locally, diatoms are common (>10%). Traces of ichnofossils like *Zoophycos* and *Chondrites* are abundant.

X-ray diffraction (XRD) data (Table 2) show that quartz, calcite, clay minerals, and mica (biotite, muscovite, and illite) are the major mineral components of Unit I. The quartz and calcite contents are marked by high-amplitude fluctuations. Minor components are feldspar, dolomite, aragonite, and pyrite. The dolomite content varies normally between 1% and 8%, but locally can increase up to 20%

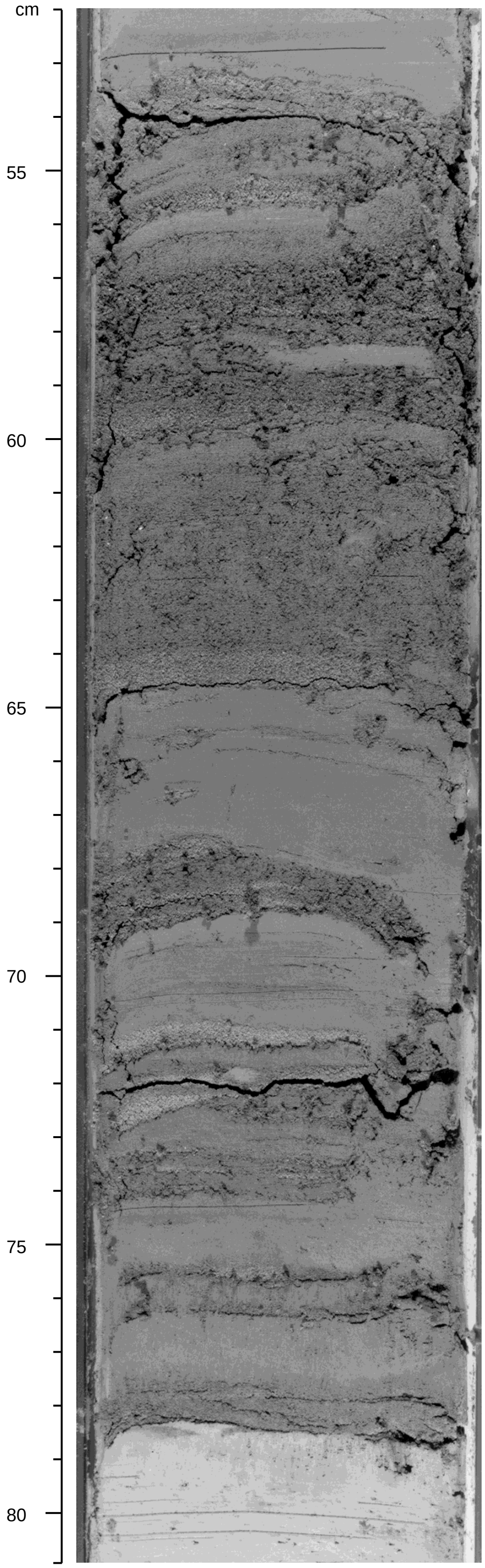

Figure 2. Photograph of interval 172-1056B-6H-5, 52–81 cm. The interval from 54 to 79 cm contains a sequence of coarser beds of sand-sized siliciclastic and biogenic components interbedded with silt and clay. The contact with the next lower bed (nannofossil-rich sediment) is sharp and scoured and marked by an abrupt color change from dark greenish gray (10Y 4/1) to light greenish gray (5GY 6/1 or 7/1).

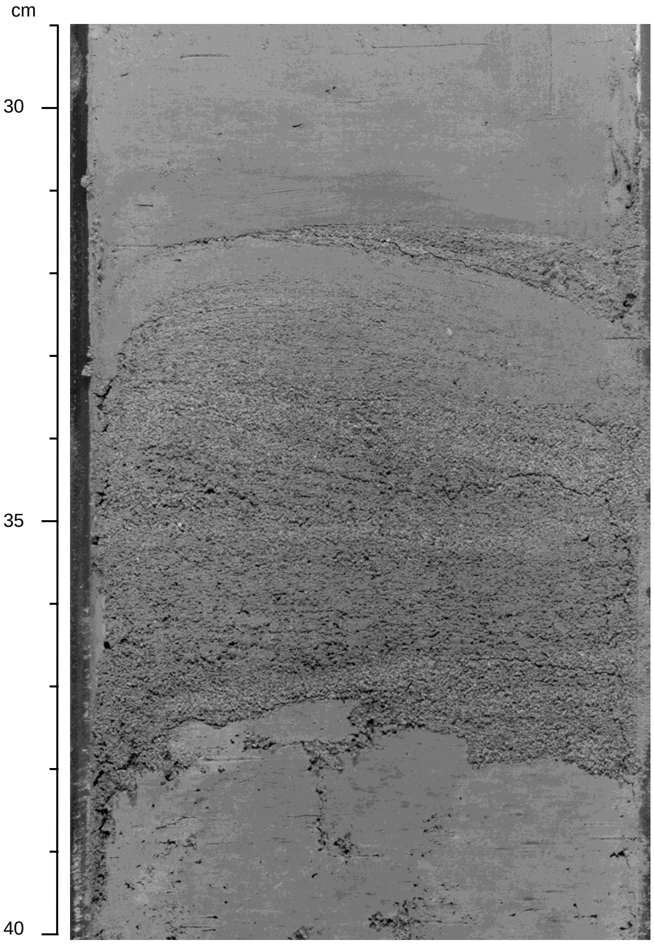

Figure 3. Photograph of interval 172-1056D-10H-8, 29–40 cm. The interval from 32 to 38 cm shows a mixed sand-silt-clay bed with biogenic components (e.g., foraminifers and scoured contact with the lower layer). Between 33.5 and 35 cm, cross-bedding with deepening to the right side of the photograph is observed.

(XRD Sample 172-1056B-9H-2, 110 cm). This increase may be the result of disseminated dolomite crystals in thin beds above a coarser sand/silt bed at around 73 mbsf (interval 172-1056B-9H-2, 120–145 cm). Pyrite is uncommon (<5 wt%). A visual core description shows that pyrite nodules appear first at around 47 mbsf. Below ~60 mbsf, the cores are moderately to heavily disturbed because of degassing.

Unit II

Intervals: 172-1056B 11H-5, 25 cm, through 17H (95–155.6 mbsf, base of hole); 172-1056C-11H-4, 50 cm, through 17H (95.8–154.8 mbsf, base of hole); 172-1056D 11H-4, 47 cm, through 13H (97.1–121.8 mbsf, base of hole)
Age: middle Pleistocene to early Pleistocene

In comparison to Unit I, the spectral reflectance of Unit II is reduced and the color changes between beds are more gradational (Fig. 1). Reddish brown clays are absent. Clay-sized sediments are dominant and silt- and sand-sized sediments are restricted to coarser intervals. XRD suggests that quartz, calcite, clay, and mica minerals are also the dominant mineral component in Unit II (Table 2). Minor components are feldspar, dolomite, aragonite, and pyrite.

Calcareous microfossils are generally rare, and foraminifers are abundant only in coarse-grained beds. Siliceous fossils are rare, but locally diatoms may reach 10%–20%, especially in the deeper portion of Unit II. In Unit II the core disturbances are significantly higher than in Unit I. Voids caused by degassing are abundant. Unit II is subdivided into two subunits because of the occurrence of a deformed sediment bed at the top of this unit.

Subunit IIA

Intervals: 172-1056B-11H-5, 25 cm, through 12H-2, 55 cm (95–99.5 mbsf); 172-1056C-11H-4, 50 cm, through 11H-6, 75 cm (95.8–98.9 mbsf); 172-1056D-11H-4, 47 cm, through 11H-6, 30 cm (97.1–100.5 mbsf)
Age: middle Pleistocene

Subunit IIA consists of a deformed and convoluted bed probably caused by multiple slumping events. The lithology of this thick (up to 5 m) deformed bed is brownish gray (5YR 4/1) silty nannofossil clay, greenish gray clay nannofossil mixed sediment, and nannofossil clay. At ~100 mbsf the base of the slump has a scoured contact with Subunit IIB.

Subunit IIB

Intervals: 172-1056B-12H-2, 55 cm, through 17H (99.5–155.6 mbsf, base of hole); 172-1056C-11H-6, 75 cm, through 17H (98.9–154.8 mbsf, base of hole); 172-1056D-11H-6, 30 cm, through 13 H (100.5–121.8 mbsf, base of hole)
Age: middle Pleistocene to early Pleistocene

Subunit IIB is dominated by olive gray (5Y 4/1) and dark greenish gray (5GY 4/1 or 5G 4/1) to greenish gray (5GY 6/1 or 5G 6/1) clay, silty clay, clay with silt, and clayey silt with individual beds up to 4.3 m thick. Also present in minor amounts are dark greenish gray to greenish gray clayey nannofossil mixed sediments and silty clay with nannofossils, foraminifers, and, in some intervals, diatoms. These layers can be up to 1.7 m thick. Total carbonate content varies between 13 and 33 wt% (see “Organic Geochemistry” section this chapter). A 60-cm-thick, poorly sorted, sand-sized bed occurs at 140 mbsf (interval 172-1056B-16H-6, 60–120 cm; Fig. 4), with a sharp contact to the lower layer and consisting predominantly of biogenic grains (mainly foraminifers and pteropod fragments in a clayey matrix). Numerous thin silt and sand beds (up to 3 cm thick) are more abundant in Unit II than in the upper part of Unit I.

Site 1057

At Site 1057 a good sedimentary succession was obtained in all three holes. Although the sediments are sometimes affected by small depositional and erosional events, the site is believed to contain very good, high-resolution sequences of Holocene to early Pleistocene sediments. The description and interpretation of the lithostratigraphy is based on Hole 1057A, which contains cyclic changes in the main lithologic components that characterize Unit I. Unit II, on the other hand, is constituted of generally homogeneous sediments, where lithologic changes are, on the whole, slight and gradual. The depth of 72.27 mbsf is chosen as the boundary between the two units, corresponding to the top of a ~10-m-long deformed sediment interval, which was also noted in Hole 1057B and at Site 1056.

Unit I

Intervals: 172-1057A-1H-1, 0 cm, through 9H-4, 140 cm (0–79.90 mbsf); 172-1057B-1H-1, 0 cm, through 9H-7, 145 cm (0–79.67 mbsf); 172-1057C-1H-1, 0 cm, through 8H-9, 41 cm (0–74.25 mbsf; base of hole)
Age: Holocene to middle Pleistocene

Unit I mainly consists of greenish gray, thick nannofossil clay or clay with nannofossil beds alternating with thinner nannofossil-dominated beds (Fig. 5). The nomenclature adopted accounts for the different mixtures of the above components and includes: (1) clay, clay with nannofossils (± silt), nannofossil clay (± silt), clay with silt, silty clay, and silt with clay for the clayey intervals and (2) nannofossil ooze and clayey nannofossil ooze for the nannofossiliferous intervals

Table 2. XRD data for Sites 1056, 1057, 1058, and 1059.

Core, section, interval (cm)	Quartz	K-spar	Plagioclase	Clay	Calcite	Dolomite	Aragonite	Pyrite	Mica group	Hematite	Unit
172-1056B-											
1H-3, 23	41.6	4.7	6.4	5.2	25.2	6	2.4	1.5	6.5	0.3	I
2H-3, 47	38.3	2.5	9.6	5.8	25.6	4.7	2.7	1.3	9.1	0.4	
3H-4, 14	31.1	5.8	8.5	4.3	36.1	1.5	6	1.8	4.3	0.5	
4H-4, 12	13.9	4	3.7	6	55.7	4.6	3.7	2.5	5.3	0.5	
5H-4, 15	31.1	6.8	24.7	2.7	18.5	8.4	1.5	1.9	4.1	0.3	
6H-1, 55	44.1	1.9	4	4.5	28.5	5.8	1.8	1.6	7.4	0.3	
7H-2, 73	37.8	7.7	17.1	4.3	18.8	5.6	1.8	2.4	4.4	0.2	
8H-2, 75	52.8	1.4	9.5	6.4	10.4	4.7	1.2	1.5	11.6	0.6	
9H-2, 110	20.3	3.7	5.2	3.7	33.5	18.3	2.4	2.7	9.6	0.6	
10H-6, 64	35.5	3.3	11.7	4.4	31.7	1.8	2.7	3.1	5.6	0.2	
11H-4, 44	36	9.9	13.2	4.4	20.1	4.5	1.4	2	8.4	0.1	
13H-5, 91	34.7	9.1	9.1	4	31	0.6	2.2	4.3	4.6	0.3	II
14H-3, 93	40.8	2.2	9.3	4.6	30.6	0	1.7	1.6	9	0.2	
15H-3, 98	24.7	2.1	13.7	5.6	32.7	5.2	1.2	2.3	12.4	0.1	
16H-2, 97	33.8	2.9	8.2	6	32.9	2.3	1.7	3.8	8.2	0.1	
17H-3, 20	38	3.4	4.5	5.1	33.3	3.6	3.2	2.9	5.7	0.3	
172-1057A-											
1H-1, 51	26.1	2.9	4.2	6.2	36.4	2	2.4	2.4	17.2	0.1	I
2H-1, 50	34.8	2.2	8.4	7	30	3.1	1.8	2	10.6	0	
3H-4, 84	31.6	1.4	6.3	6.8	32.9	7	1.6	2.1	10.3	0.1	
4H-1, 85	22.5	12.3	6.6	4.5	41.9	3.1	1.7	2.4	4.7	0.3	
5H-2, 33	42.2	0	11.1	5.7	19	6.7	1.4	2.4	11.2	0.3	
6H-1, 50	24.8	2.2	13.8	4.6	39.6	5.8	1.2	1.7	6.3	0	
8H-2, 80	36.3	3.7	22.9	2.8	16.1	6.3	1.5	3.1	7.1	0.1	
9H-3, 147	0.2	9.8	57.2	1.7	5.3	4.5	0.3	13.1	7.9	0	II
9H-4, 84	50.6	2.7	6.8	8.9	11.3	2.2	1.7	2.5	13.4	0	
10H-4, 84	51.9	0	6.8	5.6	14.3	9.3	1.3	1.6	8.8	0.3	
11H-4, 58	42.4	1.4	7.4	6.3	26.1	1.8	1.8	5.2	7.6	0	
13H-4, 75	27.9	2.9	17.9	6.5	23.6	2	1.1	4.4	13.6	0	
14H-7, 91	30.1	2.1	12.4	6.3	32.7	1.3	1.6	4.9	8.5	0	
172-1058A-											
1H-1, 118	46.7	0	11.1	6.6	14.8	7.3	1.3	2.4	9.3	0.5	I
2H-1, 32	34.3	2.7	13.4	5.5	19.8	10.2	1.5	3.1	9.4	0	
3H-2, 60	22.3	4.4	3.2	7	41	1	4.9	4.1	11.9	0.1	
4H-6, 82	47.6	6.2	16	5	10.1	3.7	1.2	3	7.2	0	
5H-4, 54	51.7	0	7.6	4.9	13.7	9.1	0.9	2.3	9	0.7	
6H-2, 46	32.2	4.8	6.6	5.1	37.6	3.7	1.4	3.9	4.3	0.3	
7H-4, 79	29.5	2.8	13.9	5.6	31	5.8	1.5	4.7	5.4	0	
8H-4, 61	42	7.4	9.8	5.3	19.8	2.9	1.4	4.6	6.7	0	
9H-5, 52	32.7	4.2	7.7	6.8	31.5	5.7	3.2	4	3.9	0.3	
10H-2, 55	27.2	2.6	17.7	7.8	25.5	5.3	1.5	4.8	7.6	0	
11H-1, 46	36.8	3.1	18.9	5	18.6	9	1.3	2.5	4.9	0	
12H-5, 48	43	2	8.6	6.9	24.8	0.9	1.2	5.2	7.4	0	II
13H-3, 51	32.4	3.2	17.4	7.3	21.8	3.2	1.5	5.1	8.2	0	
14H-5, 88	39.6	12.4	0	8.2	23.7	2.2	1.8	2.7	9.5	0	
15H-4, 38	37.1	2.1	9.5	6	32.7	1	2.1	3	6.4	0.1	
16H-6, 68	34.4	3.5	4.5	6.1	37.1	1.9	3.8	4	4.7	0.1	
172-1059A-											
1H-3, 32	47.0	2.0	8.9	5.4	12.4	8.4	1.0	1.9	12.6	0.3	I
2H-4, 96	45.5	2.2	10.5	6.0	14.1	9.5	1.0	2.4	8.8	0.0	
4H-3, 26	23.8	2.7	4.9	6.2	41.0	2.8	3.1	4.7	10.7	0.1	
5H-3, 27	45.6	0.0	8.6	7.5	17.3	6.7	0.7	2.1	10.5	0.9	
6H-4, 49	32.3	2.4	15.7	5.6	30.1	1.5	2.5	3.9	6.1	0.1	
7H-4, 80	45.2	2.6	11.0	5.9	15.4	8.5	1.1	2.8	7.6	0.0	
8H-4, 81	24.1	0.0	7.6	4.9	49.2	1.9	1.7	3.8	6.7	0.1	
9H-4, 62	36.1	0.0	10.6	3.9	32.5	3.4	1.5	4.9	7.0	0.0	
10H-4, 80	48.4	1.8	16.4	4.5	10.9	4.1	1.2	2.1	10.5	0.0	
11H-4, 78	34.8	2.5	19.2	5.7	23.8	5.5	1.8	1.2	5.4	0.0	

Notes: K-spar = potassium feldspar. All data shown are relative percentiles.

(see Section 3, this volume, for detailed information on sediment type variations). Smear-slide analysis mainly highlighted the changing abundances of the two main lithologic components throughout Unit I: clay and nannofossils. The abundance of the former almost always exceeded 40% and was commonly the dominant sediment component (>50%). The latter was often above 25% but rarely in excess of 50%. Smear-slide analysis has also shown variable amounts of diatoms and foraminifers, generally not exceeding 10% of the whole sediment composition. The measured calcium carbonate content varies from 10 to 64 wt% (see “Organic Geochemistry” section, this chapter) with the higher values characterizing the nannofossil ooze intervals.

The more thinly bedded (about 1 to 4 m) clay-bearing nannofossil oozes (hereafter called nannofossil ooze bed) are generally very light to light greenish gray (5GY 8/1 to 5GY 7/1), homogeneous in texture, and affected by variable levels of bioturbation. The thicker (generally between 7 and 10 m), clay-dominated intervals (hereafter called clay bed) range from various shades of greenish gray (5GY 6/1) to light brown, sometimes with a faint tinge of red, and contain numerous, thin, coarser intervals. The reddish color disappears at 25 mbsf, below which there are a few instances of fainter shades. The thin, coarser intervals generally occur as carbonate-rich, comparatively thin silty/sandy layers (up to 10 cm, but commonly 5 cm thick), often with sharp basal and gradational upper contacts (Fig. 6). These are regarded as the product of periods of increased deep-current intensity where the sediment is winnowed, creating a coarse lag deposit. However, there are fairly common exceptions to this pattern, where the contacts are either both sharp or both gradational. An obvious, scoured contact occurs at 44.68 mbsf; such contacts become more frequent below this depth.

The intensity of light reflectance seems to mirror very clearly the compositional changes characterizing the two lithologies in Unit I (Fig. 5; see data on CD-ROM, back pocket, this volume). Furthermore, because the reflectance record is a better detector of color changes than the human eye coupled with the use of Munsell charts, we employ it to interpret the more detailed structure of the sedimen-

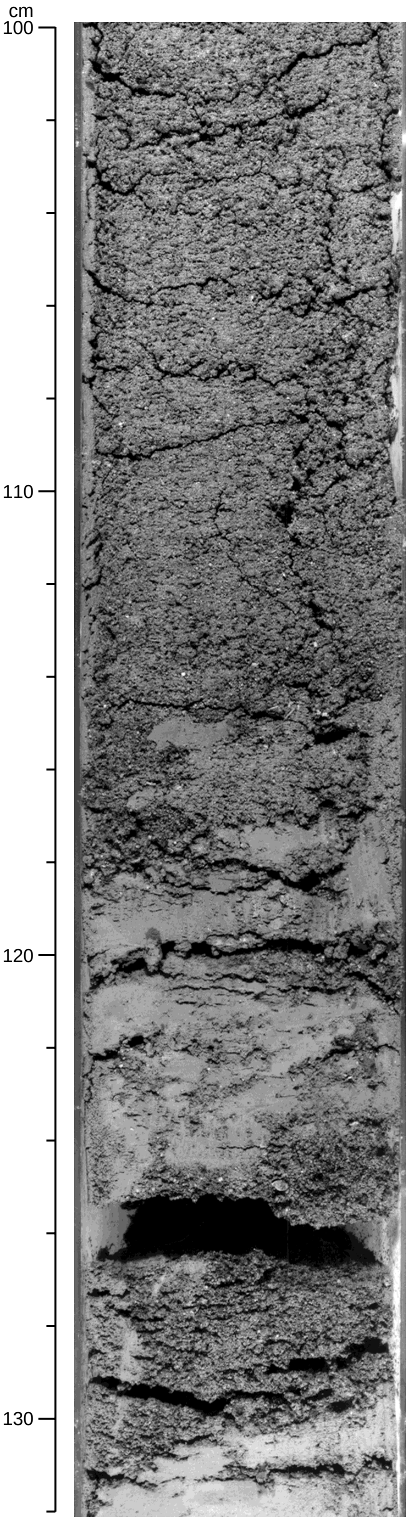

Figure 4. Photograph of interval 172-1056B-10H-6, 100−131 cm, showing the lower portion of a bed spanning the interval 60−120 cm. This bed consists predominantly of foraminifers and shell fragments, with the lower part consisting of a coarser biogenic sand bed with a scoured lower contact.

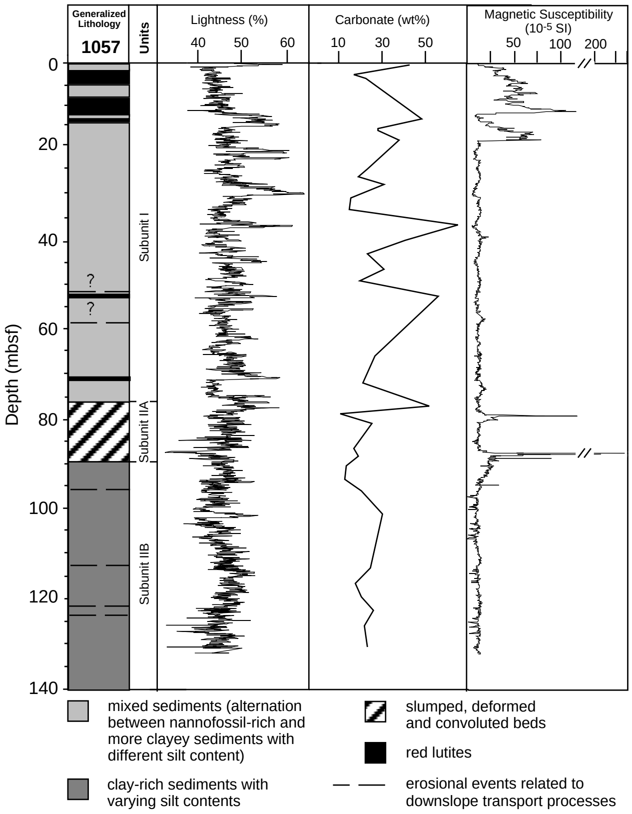

Figure 5. Generalized lithology, color reflectance, carbonate content, and magnetic susceptibility for Hole 1057A.

tary succession of Hole 1057A. Light reflectance data in Figure 5 show that in the top 50 mbsf, five cycles with similar repetitive patterns are identifiable, each consisting of a nannofossil ooze interval followed by a clay-dominated bed. For the top five complete nannofossil intervals (interval 172-1057A-2H through 5H, 10–45 mbsf) within each cycle, the passage from clay (low lightness values) to the base of the nannofossil ooze occurs over a short distance (30–70 cm). However, the transition from nannofossil ooze to the base of a clay bed occurs over a longer depth interval (70–200 cm). It can therefore be inferred that the physical processes responsible for the switches between lithotypes must be acting on short time scales and/or that they coincide with changes in sedimentation rates. The sharp contact at the bases of the nannofossil beds appears weakly bioturbated, and rapid lithologic change is evident. Although the transitions at the tops of the nannofossil layers may be equally sharp, they typically appear to be more gradual as the result of an increased sedimentation rate in the clay. Below Core 172-1057A-5H (45.50 mbsf), the nannofossil-dominated beds become very thin and the structure of the transitions is harder to see, with the exception of Core 172-1057A-8H (70 mbsf), where distinctive patterns can be recognized in the color reflectance data (Fig. 5).

The abundance of 1- or 2-point peaks, which imparts a very high-frequency variability to the reflectance record (10- to 20-cm scale) probably results from burrow mottling. However, many of the slightly lower frequency fluctuations do actually reflect primary, subtle lithologic changes. Furthermore, one of the distinctive features of this site is pervasive, diagenetic color-banding of the sediment, which consists of greenish (7.5G 5/2) 1- to 2-cm-thick horizons. These bands are interpreted as relic redox fronts, and their presence appears to bear a strong inverse relationship to the intensity of bioturbation. The most prominent features of this type occur in Cores 172-1057A-1H through 3H (0–27 mbsf).

Another notable diagenetic feature at this site is the post-depositional iron sulfide (pyrite) mineralization of burrow fills, which is

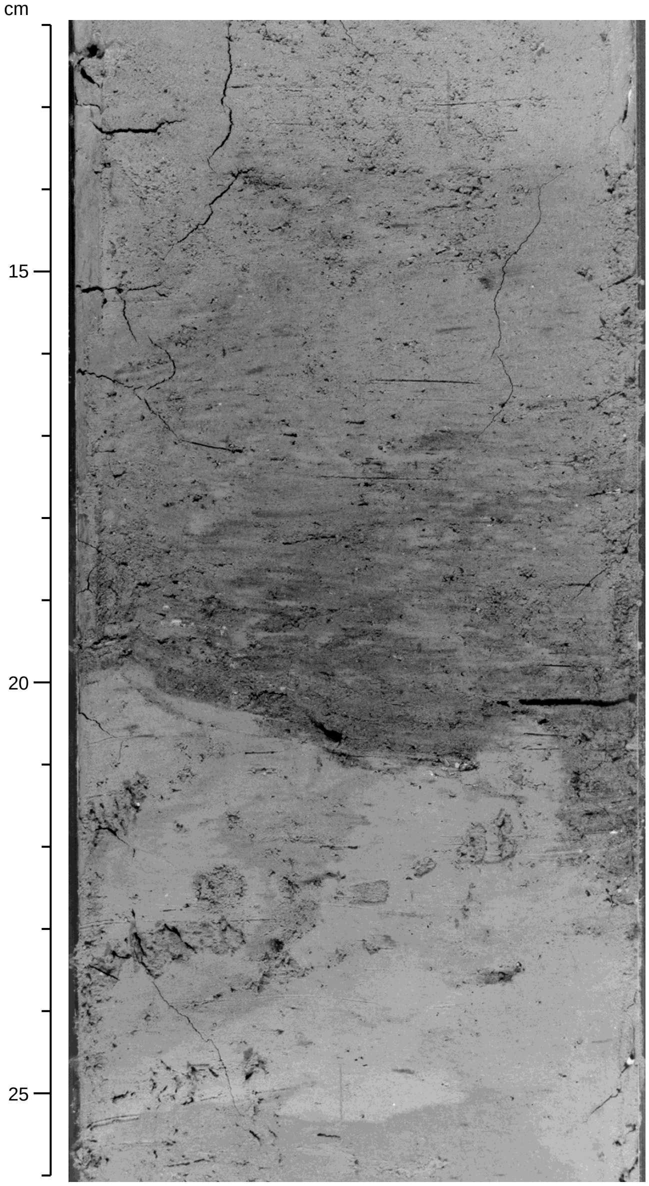

Figure 6. Photograph of interval 172-1057B-3H-5, 12–26 cm. An irregular sharp contact is present at the base of the dark unit (14–23 cm). The undulating pattern suggests some erosion might have occurred at the base of the layer.

common below 25 mbsf. Discrete XRD samples show that the main mineralogical components are quartz, calcite, and clay minerals including the mica group (Table 2). Other minerals are accessory, with the exception of plagioclase, which occasionally represents more than 10% of the sample. The nonsystematic and widely spaced XRD sampling makes detailed intercomparison between different intervals difficult. Nonetheless, it appears that the calcite values are generally inversely related to the abundance of terrigenous components, a conclusion that supports the smear-slide analysis. A pebble 2–3 cm in size is present at interval 172-1057A-9H-3, 147–149 cm (78.47–78.49 mbsf). XRD analysis showed that plagioclase (see Table 2) is the main component (57.2%), with lesser pyrite (13.1%), and pyroxene (augite). This analysis is consistent with a thin-section study, which showed the pebble to be of possible volcanic origin with euhedral crystals of albite and pyroxene in fine-grained groundmass. The presence of plagioclase precludes the possibility that the pebble is of diagenetic origin (although pyrite implies possible diagenetic origin), suggesting it must be allochthonous, possibly drifting to the site with plant material. This pebble could also be associated with a mass-transport deposit underlying Unit I (Subunit IIA, top at 79.90 mbsf).

Unit II

Subunit IIA

Intervals: 172-1057A-9H-4, 140 cm, through 10H-4, 143 cm (79.90–89.43 mbsf); 172-1057B-9H-7, 145 cm, through 10H-8, 31 cm (79.67–89.98 mbsf)
Age: early Pleistocene

This subunit consists of deformed and convoluted greenish gray nannofossil clay and clay with nannofossils, suggestive of one or more slumping events. This lithology is similar to the sediments above and below. The top of the subunit is defined by a dipping interval of coarse silt, whereas the base is more gradational and defined by the last appearance of dipping sedimentary structures. An interval of very intense, black iron sulfide staining occurs between 88.00 and 88.60 mbsf; it also contains a diagenetic nodule about 2 cm in diameter at interval 172-1057A-10H-3, 28–30 cm (Fig. 7). Some near-horizontal bedding is present in places (e.g., interval 172-1057A-10H-2, 50–85 cm), but it is not clear from the sedimentological evidence alone whether these beds represent an interval of normal deposition or part of the slump. However, paleomagnetic results suggest that it would be appropriate to regard the whole of Subunit IIA as a single depositional event (see “Paleomagnetism” section, this chapter). The upper and lower boundaries of the slump occur within two peaks characterized by the highest field intensity and whole-core magnetic susceptibility for Hole 1057A, distinguishing this subunit from the normal pattern of change in these variables. The peaks coincide with areas of intense diagenetic alteration of the sediments, which are believed to be associated with the virtually instantaneous deposition of large quantities of material. It must be noted that the shallower peak (78 mbsf) occurs about 1.5 m above the upper boundary of the slump, confirming that the sedimentologic evidence alone is not sufficient to define the extent of this event exactly.

Subunit IIB

Intervals: 172-1057A-10H-4, 143 cm, through 14H-8, 24 cm (89.43–131.80 mbsf; base of hole); 172-1057B-10H-8, 31 cm, through 15H-8, 23 cm (89.98–137.31 mbsf; base of hole)
Age: early Pleistocene

The common lithologies encountered in this homogeneous subunit are clay, nannofossil clay, clay with silt and nannofossils, and, more rarely, nannofossil clay mixed sediment. Sediment color only slightly departs from greenish gray (5GY 6/1) and medium dark greenish gray (5GY 5/1). The uniform character of the subunit is clearly seen from the light reflectance data (Fig. 5), which, beyond the background trend, are very stable if compared to the patterns present in Unit I. A notable exception is a clayey nannofossil ooze bed that lies between 100.14 and 101.14 mbsf. Replacement and mineralization of burrow fills by iron sulfides is common, and faint diagenetic color banding of the sediment is visible where bioturbation was low. Coarser, silty layers are present in various intervals, and again, as in Unit I, they mainly suggest winnowing by deep-water flow. Nonetheless, in some instances the rhythmic alternation of silt and clay laminae strongly suggests deposition by turbidity currents (Fig. 8; Pickering et al., 1989, chap. 9). These observations suggest that Unit II consists of sediments very similar to the clay beds of Unit I.

Site 1058

Three holes at Site 1058 contain the same sedimentary units as Sites 1056 and 1057, but the slump subunit is absent. Although the sediments are affected by small erosional and depositional events in some intervals, Site 1058 is believed to contain a complete succession of Holocene to early Pleistocene sediments. The following lithologic description and interpretation is based on Hole 1058A.

Unit I

Intervals: 172-1058A-1H-1, 0 cm, through 12H-3, 20 cm (0–106.6 mbsf); 172-1058B-1H-1, 0 cm, through 13H-2, 15 cm (0–112.15 mbsf); 172-1058C-1H-1, 0 cm, through 12H-5, 22 cm (0–102.83 mbsf)
Age: Holocene to middle Pleistocene

Unit I is defined by the high amplitude of fluctuation in calcium carbonate content ($CaCO_3$) and characterized by presence of reddish

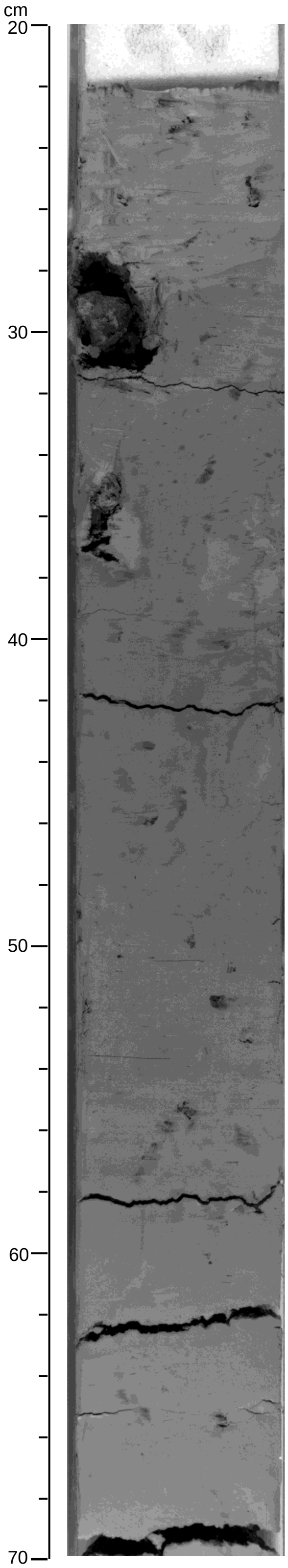

Figure 7. Photograph of interval 172-1057A-10H-3, 20–70 cm, showing the presence of a diagenetic nodule (2 cm in diameter) at 30 cm within the convoluted beds of the slumped interval. Immediately after splitting the core the whole of this interval was heavily stained with iron sulfides. However, by the time the core reached the photographic table, oxidation of metastable sulfides had occurred and the strong color had been lost (compare with whole-core photographs, where some of the color was still preserved).

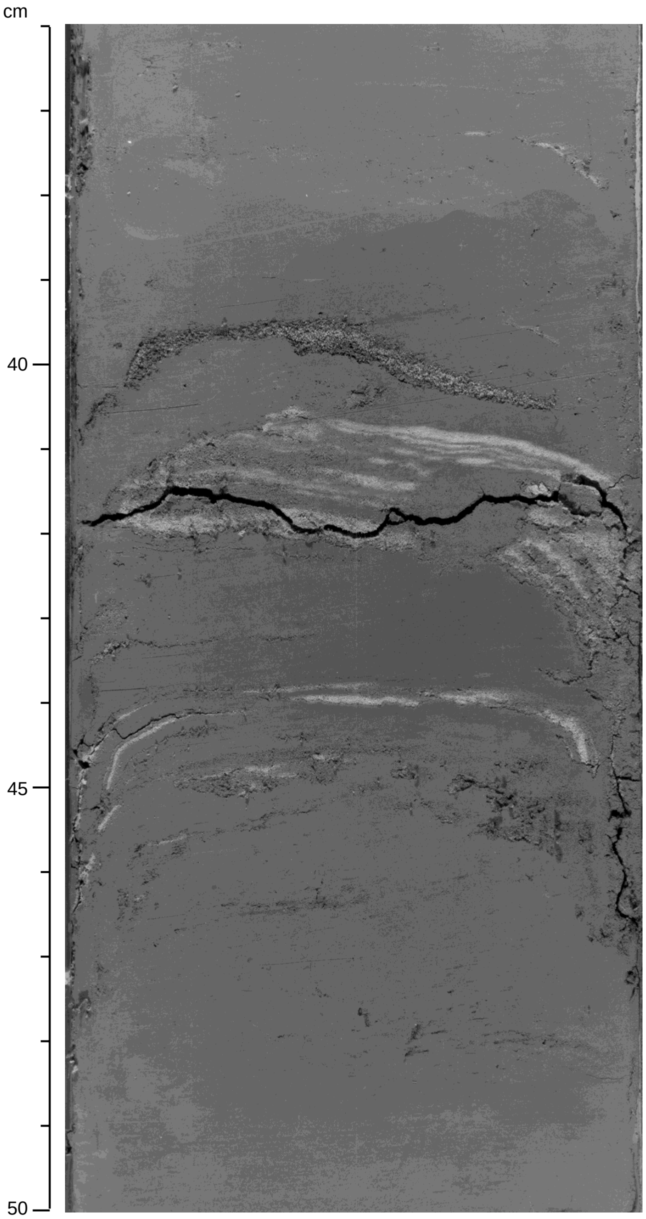

Figure 8. Photograph of interval 172-1057A-13H-7, 36–50 cm, showing three interbedded silt and clay laminae. These horizons are not always laterally continuous. This can be attributed to a slight coring disturbance and to the very fine nature of the features, which might have been partially obliterated upon scraping of the sediment for descriptive and photographic purposes. The interval between 41 and 42 cm has been affected by a large burrowing organism.

brown (around 3Y4/1), oxidized sediments, dark greenish gray clay (5GY4/1), and light greenish gray nannofossil oozes (5GY7/1). This sediment variability results in a relatively high variation of color reflectance (data on CD-ROM, back pocket, this volume). The uppermost 18 m of this unit consists predominantly of reddish brown (3Y4/1) clay with nannofossils. Thin (1-mm-thick) greenish layers with silt are interbedded at ~5-cm intervals in this reddish brown clay. The brownish clays (with nannofossils) occur at ~25 mbsf (4.5 m thick), 55 mbsf (0.5 m thick), and 100 mbsf (9 m thick), where fairly sharp peaks of magnetic susceptibility appear (Fig. 9).

The middle part of Unit I is dominated by bioturbated nannofossil clay with pyrite nodules. Color varies between light greenish gray, light olive gray, olive gray, greenish gray, and dark greenish gray, although lighter colors dominate. Minor lithologies are nannofossil ooze and nannofossil clay. Trace fossils such as *Planolites, Chondrites,* and *Zoophycos* are abundant, especially in the nannofossil clay and clay with nannofossils lithologies. Light greenish gray nannofossil ooze, greenish gray nannofossil clay, and dark greenish gray clay with nannofossils occur in order repeatedly at ~10-m intervals. Four major cycles are observed in each hole. Nannofossil ooze layers are 1 to 2 m thick. Each layer often has minor periodic color change superimposed on the major color change. The major color change from darker colored sediment, such as clay with nannofossils, to lighter colored sediment, such as nannofossil ooze, always occurs gradually upcore. Heavy to medium bioturbation is observed in the transition zones between darker and lighter lithologies. In contrast, the change from nannofossil ooze to clay with nannofossils is not always gradual. Light-colored nannofossil ooze (or nannofossil clay) is often truncated by sharp-based coarser (silt-sized) layers (Fig. 10; interval 172-1058B-5H-4, 114–128 cm, which is correlatable to the interval 172-1058A-5H-1, 88–93 cm). Frequent coarser layers (especially in Hole 1058B) contain biogenic components such as pteropod fragments and foraminifers. The upper and lower boundaries of the coarse layer are sometimes heavily bioturbated, and burrows filled with sand- or silt-sized foraminifers accompany these layers.

The lowermost 25 m of Unit I is dominated by clay with silt and nannofossils. The color varies from light greenish gray to light olive gray to greenish gray. Clay with silt is also interbedded, showing greenish gray, brownish gray, and light greenish gray color. Trace fossils such as *Planolites, Chondrites,* and *Zoophycos* are abundant, especially in clay with silt and nannofossils. Sharp-based silty clay layers are common in the lower part of Unit I, and some silt layers are correlatable among the three holes. For example, a zone that contains silt layers occurs in Sections 172-1058A-10H-5, 172-1058B-11H-6, and 172-1058C-11H-4, and these layers correlate to a peak of magnetic susceptibility. A 15-cm thick, sharp-based silty clay layer, which contains sand-sized foraminifers and shows a fining-upward sequence, is used to define the lower boundary of Unit I (e.g., inter-

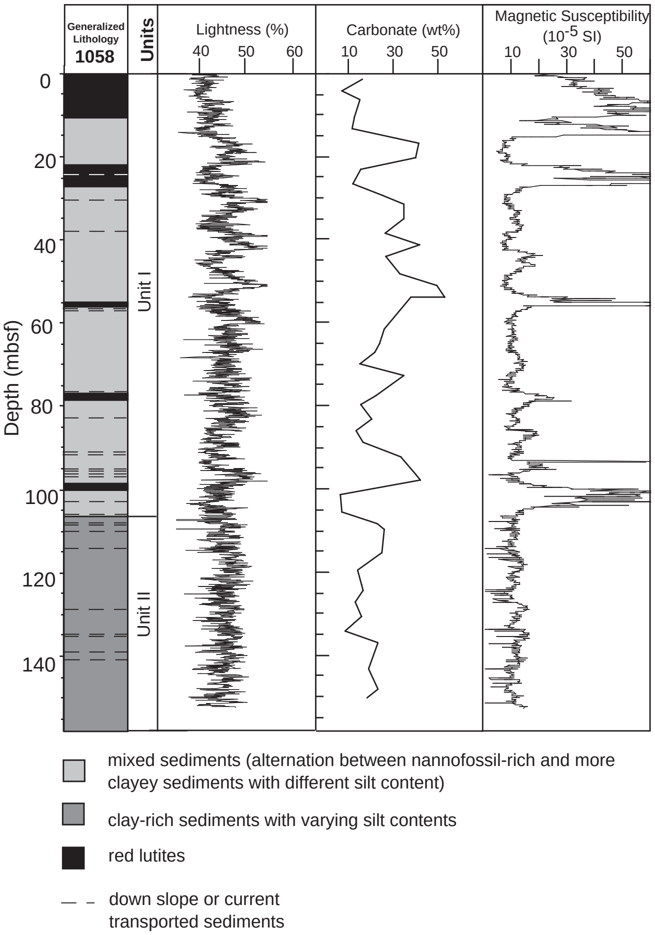

Figure 9. Generalized lithology, color reflectance, carbonate content, and magnetic susceptibility for Hole 1058A.

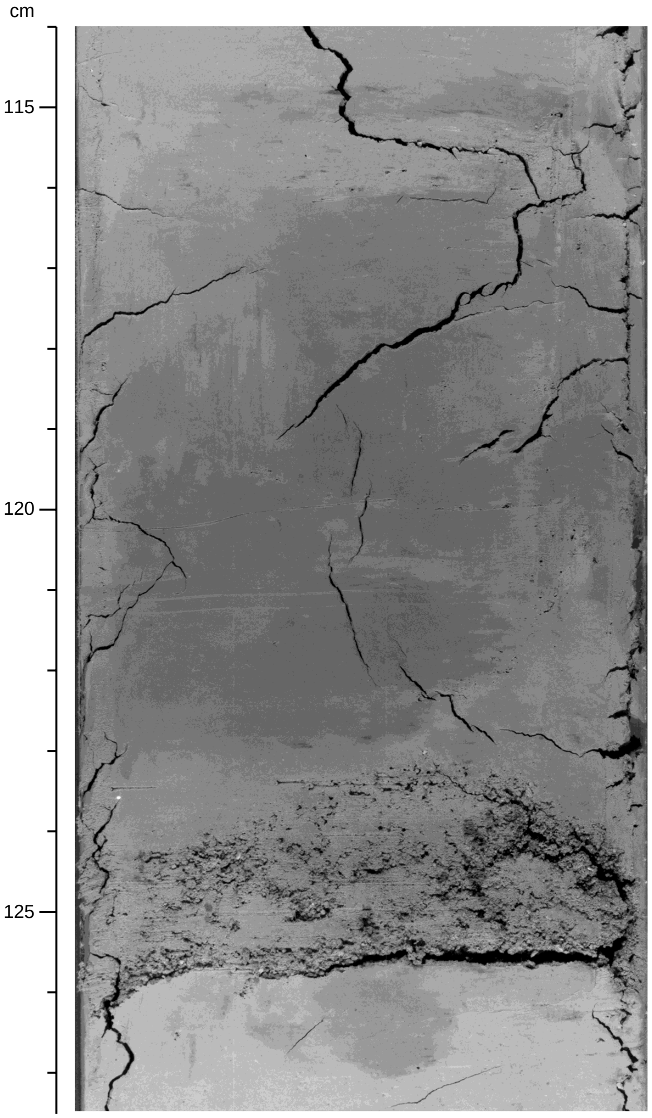

Figure 10. Photograph of a sharp-based silt layer, which truncates light greenish gray nannofossil ooze and is overlain by darker colored nannofossil clay (interval 172-1058B-5H-4, 114–127.5 cm). See details in text.

vals 172-1058A-12H-3, 20 cm; 172-1058B-13H-2, 15 cm; and 172-1058C-12H-5, 22 cm).

In general, the sediments of Unit I contain between 7 and 53 wt% calcium carbonate (see "Organic Geochemistry" section, this chapter). Visual grain size estimates show that the sediments are dominated by clay- and silt-sized grains. Sand-sized grains are rare and are almost all foraminifer and pteropod shell fragments. XRD analysis shows that quartz and calcite are the major mineral components through the core (Fig. 11). In Unit I, the amount of quartz and calcite seems to be anticorrelated and marked by high-amplitude fluctuations (although these data are likely aliased because of the low resolution of sampling and a regular sampling interval). Minor components are K-feldspar, plagioclase, clay, mica, dolomite, siderite, aragonite, and pyrite. Based on smear-slide analysis, pyrite reaches 10% in some layers, and pyrite nodules (1 cm in diameter) are common in olive gray nannofossil clays deeper than ~15 mbsf (see smear-slide summary). The presence of Fe-oxides (<2%) is mainly linked to the red lutites. Glauconite occurs locally in trace amounts. Biogenic carbonate consists predominantly of nannofossils and minor amounts of foraminifers (0%–10%). Siliceous fossils are present as diatoms, sponge spicules, radiolarians, and very rare silicoflagellates. Locally, diatoms are common (>10%) and are reported by paleontologists to be abundant in the core catchers of Cores 172-1058A-7H, 9H, and 11H.

Unit II

Intervals: 172-1058A-12H-3, 20 cm, through 16H-CC, 18 cm (106.6–152.81 mbsf; base of hole); 172-1058B-13H-2, 15 cm, through 17H-CC, 29 cm (112.15–158.22 mbsf; base of hole); 172-1058C-12H-5, 22 cm, through 18H-CC, 29 cm (102.83–164.59 mbsf; base of hole)
Age: middle to early Pleistocene

Sediments of Unit II are dominated by olive gray or dark greenish gray clay with silt, with minor amounts of greenish gray clay with silt and nannofossils. Carbonate content is lower and less variable than in Unit I (9–26 wt%; see "Organic Geochemistry" section, this chapter). Reflectivity decreases, but not so much as at other sites (e.g., Site 1056; Fig. 9). Pyrite nodules occur throughout Unit II, and they are especially common in olive gray layers. Trace fossils such as *Planolites*, *Chondrites*, and *Zoophycos* are also abundant throughout the unit. Visual estimates show that the sediments are dominated by clay- and silt-sized grains. Sand-sized grains, which are almost all foraminifers, are rare. XRD analysis shows that quartz and calcite are the major mineral components, although abundance variations are subdued compared to Unit I (Fig. 11). Minor components are K-feldspar, plagioclase, clay, mica, dolomite, siderite, aragonite, and pyrite. Glauconite is present locally in trace amounts. The biogenic calcareous constituents consist predominantly of nannofossils and minor amounts of foraminifers (0%–10%). Based on smear-side analysis (see smear-slide summary), diatoms reach 10% in cores deeper than Core 172-1058B-13H (110.5 mbsf). Diatoms were reported by paleontologists to be abundant in the core catchers of Cores 172-1058A-12H through 15H; other siliceous fossils include sponge spicules, radiolarians, and very rare silicoflagellates.

The upper 20 m of Unit II shows two major cycles of slight and gradual color change. Silt layers, common in the lowermost part of Unit I, are rare in the upper part of Unit II. Lighter colored intervals are clay with silt and nannofossils or clay with silt, and are moderately bioturbated. Darker intervals are clay with silt. In the lower part of Unit II (>130 mbsf), dark greenish to greenish gray clay with silt and the alternation of greenish gray clay and light greenish gray clay with biogenic components and silt show three cycles. The changing pattern from light to dark is similar to the middle part of Unit I. Lighter colored layers are often truncated and silty sand-sized, biogenic-component layers overlie them. A sand-sized, foraminifer-rich layer is correlatable among three holes, such as among intervals 172-1058A-15H-7, 50–70 cm, 172-1058B-17H-1, 0–15 cm, and 172-1058C-16-7, ~35–58 cm (thickness is uncertain because this interval is disturbed by degassing).

Site 1059

Site 1059 was cored ~1.5 km from Site 1058 at a location where seismic surveys suggested focusing of sediment by the DWBC (see "Site Geophysics," section, this chapter). The following description of the lithostratigraphy at Site 1059 is based on Hole 1059A.

Unit I

Intervals: 172-1059A-1H through 11H (0.0–98.8 mbsf; base of hole); 172-1059B-1H through 10H (0.0–92.2 mbsf; base of hole); 172-1059C-1H through 10H (0.0–95.0 mbsf; base of hole)
Age: Holocene to middle Pleistocene

The unit consists of alternating intervals of two generalized lithotypes (see Section 3, this volume, for a more detailed description) characterized primarily by nannofossil content and secondarily by color and texture (Fig. 12). The lithotypes are (1) light greenish gray (5GY 7–8/1) and greenish gray (5GY 6/1) nannofossil clay (<25% nannofossils) and nannofossil ooze, and (2) greenish gray (5GY 5/1) clay with nannofossils and silt and light brownish gray (5YR 6/1) to dark greenish gray (10Y 4–5/1–2) clay with silt. XRD analysis (Table 2) shows that quartz, calcite, and biotite are the major mineral components of Unit I. Quartz and calcite contents are marked by high-amplitude fluctuations that relate to similar carbonate fluctuations shown by the carbonate analysis. Carbonate content seems to

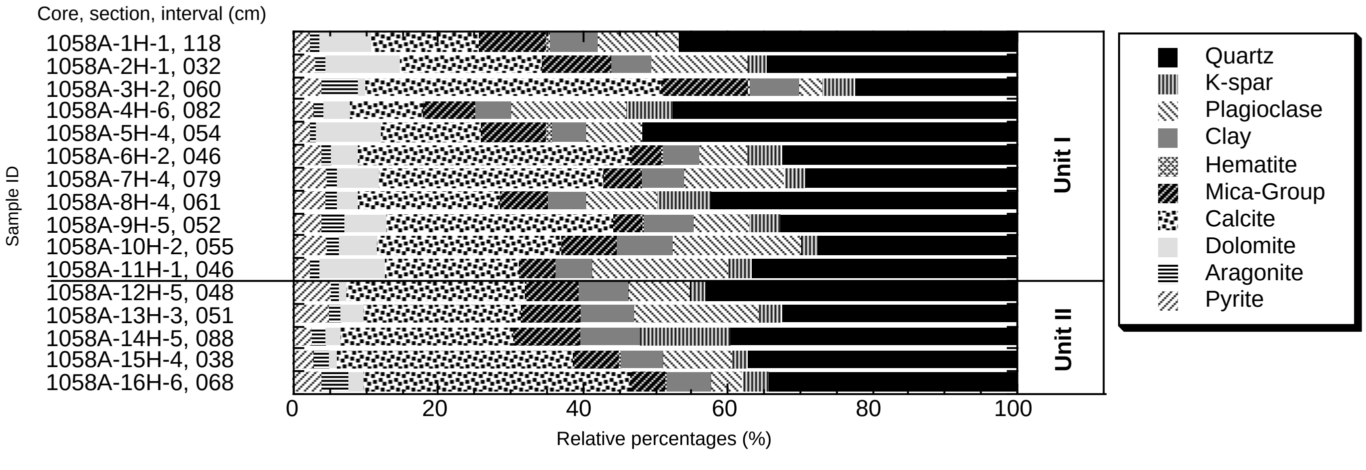

Figure 11. XRD results for Hole 1058A.

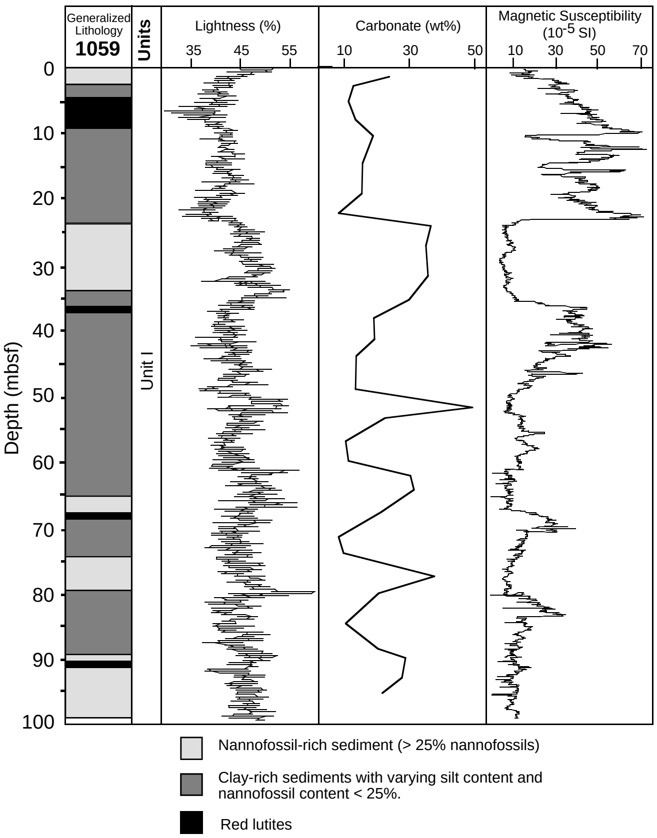

Figure 12. Generalized lithology, color reflectance, carbonate content, and magnetic susceptibility for Hole 1059A.

have a bimodal distribution with values fluctuating between 8 and 52 wt% (Fig. 12; see "Organic Geochemistry" section, this chapter). Variations in carbonate content are consistent with the considerable reflectivity (lightness) variations observed between the nannofossil-rich sediments and the clay with silt (data on CD-ROM, back pocket, this volume). Also, disseminated pyrite occurs in some of the clay with silt beds, leading to an amplified color contrast.

Thin beds (<5.0 cm) of more reddish (10R 4/2) and greenish (10GY 5/3) color are observed throughout the cores. Reddish intervals ("red lutites") are found at ~3–4, 36–40, 66–70, and 90–92 mbsf (Fig. 12). The intercalated greenish beds, normally 1–2 cm thick, are most likely relic redox boundaries.

Throughout Site 1059, cyclic dark (low carbonate) to light (high carbonate) color changes occur mostly on 5- to 10-m scales with gradational boundaries. In addition, color reflectance measurements reveal that rapid changes on a <1-m scale are superimposed on these large-scale variations. In general, the beds are massive and homogeneous, and internal structures of the individual beds are mostly caused by various bioturbation patterns (e.g., *Zoophycos* and *Chondrites*) and slight color banding caused by early diagenesis.

There is less evidence of natural sedimentary structures at Site 1059 compared to Sites 1056, 1057, and 1058. However, in the lower part of Holes 1059B and 1059C at 62.5 and 65.8 mbsf, respectively, silt laminae interbedded in clay are observed. Both beds are less than 10 cm thick and, in Hole 1059B, contacts are sharp below and gradual above, while in Hole 1059C both upper and lower contacts are abrupt (Fig. 13).

Interpretation

From the above summaries for Sites 1056–1059 notable similarities can be observed. These can be broadly described as follows:

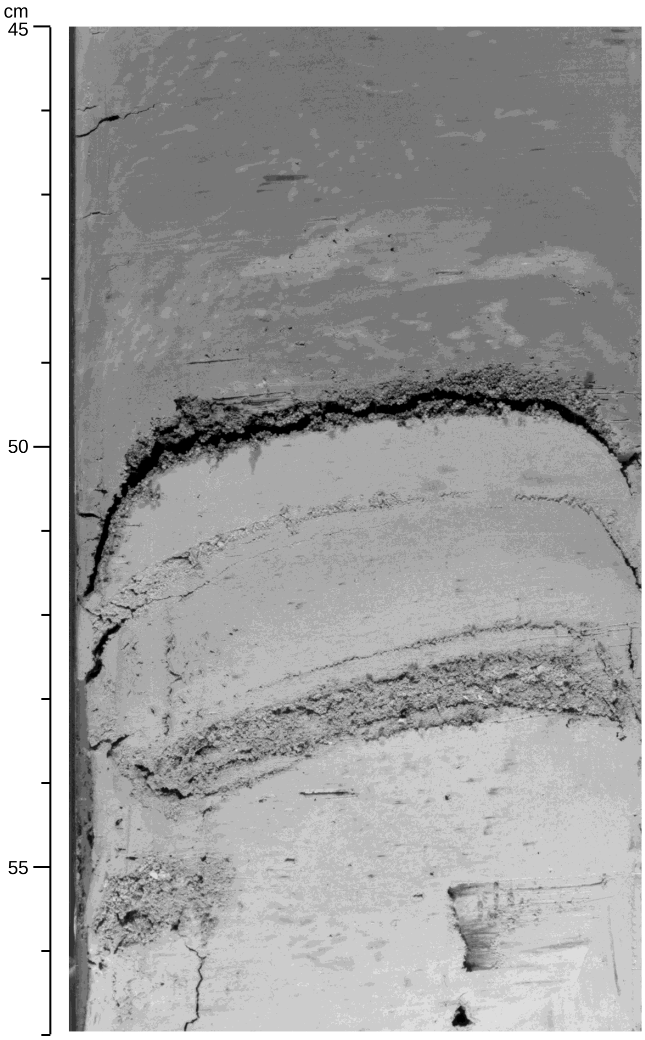

Figure 13. Photograph of interval 172-1059C-7H-6, 45–57 cm. Clay and silt interbedded with sharp lower and upper contacts, interpreted to be deposited by a contour current.

1. With the exception of Site 1059, all sites are characterized by two main lithologic units. Site 1059 contains only the upper unit, both because of its higher sedimentation rates and because of its shorter penetration. Unit I consists of alternating clay-dominated and nannofossil-rich sediments. Sediments in Unit II are, on the whole, more homogeneous and devoid of carbonate-rich intervals. Clay and clay with silt constitute most of the sediment in Unit II.
2. All sites contain intervals of reddish colored sediments, which commonly appear in the clay-dominated intervals of Unit I. These are most abundant in the upper half of the unit.
3. Two different types of coarser deposits are observed, reflecting formation under distinct flow regimes. Some beds are identified as contourites, having apparently been formed by currents reworking the sediment. Other beds are identified as turbidites or groups of turbidites, apparently having been deposited by one or more closely spaced turbidity currents. As shown by the figures in this chapter, some beds can readily be assigned to one or the other of these two groups. However, in many instances it was not possible to determine unequivocally the physical processes responsible for the deposition of the coarse layers, and final interpretations will follow shore-based investigations. It was also noted that these coarsening events

are rare in the nannofossiliferous intervals of Unit I, but common elsewhere in both units.

Some important trends and differences are also present across the four sites, which can be summarized as follows:

1. From the inorganic geochemistry data, it appears that both the nannofossil beds and clay beds at the shallower sites (Sites 1056 and 1057) contain more calcium carbonate than the corresponding intervals at the deeper sites (Sites 1058 and 1059). This difference can be ascribed to changes in sedimentation rates, which are higher at the deeper sites and might therefore be responsible for the dilution of the carbonate by terrigenous material. This explanation is preferred to carbonate dissolution because microscopic analysis of foraminifer tests shows good preservation, and all sites are presently above the lysocline, which today is located at around 4000 m (Balsam, 1983).
2. Interesting differences in sedimentation rates between clay and nannofossil layers and between sites are observed in Unit I. These are better seen in the color reflectance data for Sites 1056 (Fig. 1) and 1057 (Fig. 5), which are the easiest to compare because of the similar deposition rates. It is evident that the brighter intervals in Unit I at Site 1056 extend over a longer depth interval than at Site 1057, although the two sites are not far away from each other. The contrary is true for the darker intervals, which are considerably longer at Site 1057 than at Site 1056.
3. Overall, the amount of silt characterizing the background sediment from site to site and for both Units I and II seems to be decreasing with increasing depth, and the sediment appears to become finer grained. Similar patterns are also noted with regard to the size and frequency of turbidite events, which seem to be less common and of lower magnitude at the deeper sites. These observations could simply be related to an increasing distance from sources for downslope transport processes and to an increasing distance along the main deep-water current axis (Haskell and Johnson, 1993).
4. Sites 1056 and 1057 are characterized by intervals of mass-transport deposits at the top of Unit II, which are about 5 and 10 m thick, respectively.

Sites 1056–1059 are bathed by NADW flowing to the south, as a component of the WBUC. The alternations of nannofossil and clay intervals in the cores at the four sites are interpreted as a switching of the climate system from interglacial to glacial periods, respectively. This interpretation is mainly based on the work undertaken on the precruise site survey cores, during which a stable oxygen isotope stratigraphy and magnetic susceptibility were obtained at Site 1058 (Keigwin and Lund, unpubl. data). From these observations it appears that, although climate is the ultimate controlling factor through several interactions, deep-water flow, together with changes in the sediment sources, is the primary physical controlling factor that regulates input and distribution of terrigenous sediment quantities and types (Heezen et al., 1966; Johnson et al., 1988; Haskell and Johnson, 1993).

Given these observations it is possible to explain the structure of the various records at Sites 1056–1059 and the cause of the differences between sites. The general pattern of alternating lithologies, particularly clear in Unit I, is likely to be a function of both changes in surface-water productivity patterns and varying quality and quantity of terrigenous sediment input. However, no clear evidence is available at this stage for the former process. On the other hand, the latter process is supported by the intra- and intersite changes in sedimentation rates and sediment type listed above. The smaller scale differences between sites and within the same climatic interval (i.e., carbonate-rich interglacials or clay-dominated glacials) can be explained by shifts of the WBUC between different depths in response to climate forcing. For instance, the fluctuating position and/or intensity of upper NADW (Haskell et al., 1991) can be envisaged as a likely cause for the differences in sedimentation rates in glacial and interglacial times between Sites 1056 and 1057. At Site 1058, the top of the carbonate beds is persistently sharp and overlain by coarser sediments, suggesting stronger currents at the end of interglacial periods. This contrasts with Site 1057, where the base of the carbonate units seems characterized by an abrupt transition, whereas the top is gradual, indicating stronger currents at the beginning of the interglacials. Furthermore, the presence of typical contourite deposits suggests that flow position and strength vary with time. However, as shown from the summaries for each site, it has not always been possible to discriminate between coarse deposits originating from deep-water current reworking and turbidite events. For this reason, a more detailed interpretation must await further postcruise research.

The red lutites present at all sites in Unit I represent phases of reddish brown sediment flux during glacial times. These sediments are thought to have originated from the continental rise off Nova Scotia (Eastern Canada) and to have been transported by the WBUC to the BBOR sites (Heezen et al., 1966; Barranco et al., 1989; Keigwin and Jones, 1995). The various horizons of this lithology can be broadly correlated across sites. This is particularly true for the first glacial interval below the Holocene sediments. Below this depth various other reddish beds occur, but unambiguous correlation could not be achieved, with the possible exception of the last red layer above the boundary between Units I and II.

BIOSTRATIGRAPHY

Biostratigraphic and biochronologic controls at Sites 1056, 1057, 1058, and 1059 were provided by shipboard analyses of calcareous nannofossils and planktonic foraminifers. Nannofossils were examined in core-catcher samples from Holes 1056B, 1056C, 1057A, 1057B, 1058A, 1058B, 1059A, and 1059B, and the biohorizons were constrained using 0.3- to 1.5-m sample intervals in one hole for each site. Planktonic foraminifer analyses were confined to Holes 1056A, 1057A, 1058A, and 1059A, and foraminifer datums were constrained to within 1.5 m. Preservation of planktonic foraminifers was generally good, but decreased to moderate in some samples, apparently because of the oxidation of associated organic matter (see “Organic Geochemistry” section, this chapter). Abundance varied from common to few. Foraminifer numbers were reduced by both dissolution and dilution. Faunal assemblage changes in benthic foraminifers were also studied in Holes 1056B, 1056C, 1057A, 1057B, 1058A, 1058B, 1059A, and 1059B. Diatoms were examined along with nannofossils in core-catcher sediments.

The recovered stratigraphic sequences include the time interval from the Holocene to the Pleistocene. No significant hiatuses were identified. The positions of the biohorizons recognized are reported in Table 3 and Figures 14 through 17. Recovery at all four sites exceeded the actual depth drilled because methane gas expanded the sediment when it was brought to the surface.

Calcareous Nannofossils

Site 1056

Calcareous nannofossils recovered at Site 1056 represent a stratigraphic sequence from the Holocene (corresponding to the interval of *Emiliania huxleyi* dominance) to the lower Pleistocene (~1.6 Ma). Smear slides from core-catcher samples and from samples within cores in Hole 1056B were examined to better constrain the biohorizons (Table 3). The presence of abundant terrigenous input and clay minerals throughout the succession does not affect the nannofossil assemblages, which are mostly well preserved, diversified, and abundant. There is no evidence for severe sediment mixing, either through sedimentological or coring processes. We were not able to identify with certainty the beginning of the interval of *E. huxleyi* dominance (calibrated at 0.085 Ma), or its first occurrence (FO; calibrated at 0.26

Table 3. Calcareous microfossil datums in Hole 1056B, 1057A, 1058A, and 1059A.

		Age	Core, section, interval (cm)		Depth (mbsf)			Depth (mcd)
Event	ID	(Ma)	Top	Bottom	Top	Bottom	Mean	Mean
172-1056B-								
T *G. tumida flexuosa*	F1	0.068	2H-5, 70-72	2H-6, 70-72	10.30	11.80	11.05	11.35
Reent. *G. tumida flexuosa*	F2	0.401	5H-7, 80-82	5H-8, 70-72	40.58	42.00	41.29	44.09
T *P. lacunosa*	N1	0.46	6H-1, 114-115	6H-2, 39-40	42.74	43.49	43.11	49.06
B *G. tumida flexuosa*	F	?	7H-6, 70-72	7H-CC, 40-43	59.40	61.50	60.45	67.45
B *G. crassaformis hessi*	F3	0.75	9H-2, 70-72	9H-3, 70-72	72.30	73.80	73.05	81.49
Reent. m. *Gephyrocapsa* spp.	N2	1.00	11H-8, 39-40	12H-2, 59-60	99.34	99.55	99.44	114.51
T large *Gephyrocapsa* spp.	N3	1.24	14H-CC	15H-1, 39-40	127.10	127.49	127.30	147.14
T *G. obliquus*	F4	1.3	15H-3, 69-71	15H-4, 69-71	129.97	131.47	130.72	151.03
B large *Gephyrocapsa* spp.	N4	1.58	17H-4, 40-41	17H-5, 61-62	149.89	151.59	150.74	170.38
172-1057A-								
T *G. tumida flexuosa*	F1	0.068	2H-3, 70-72	2H-4, 70-72	11.20	12.70	11.95	11.98
Reent. *G. tumida flexuosa*	F2	0.401	5H-2, 70-72	5H-3, 70-72	38.20	39.70	38.95	41.76
T *P. lacunosa*	N1	0.46	5H-3, 39-40	5H-3, 70-71	39.39	39.70	39.45	42.26
B *G. crassaformis hessi*	F3	0.75	8H-3, 70-72	8H-4, 70-72	68.20	69.70	68.95	74.06
B *G. tumida flexuosa*		?	8H-4, 70-72	8H-5, 70-72	69.20	71.20	70.45	75.56
Reent. m. *Gephyrocapsa* spp.	N2	1.00	12H-3, 140-141	12H-4, 39-40	106.90	107.40	107.15	119.53
172-1058A-								
T *G. tumida flexuosa*	F1	0.068	2H-5, 70-72	2H-6, 70-72	16.20	17.70	16.95	19.40
Reent. *G. tumida flexuosa*	F2	0.401	6H-5, 71-73	6H-6, 70-72	54.20	55.70	54.95	60.45
T *P. lacunosa*	N1	0.46	6H-5, 70-71	6H-5, 115-116	54.20	54.65	54.43	59.93
B *G. tumida flexuosa*		?	9H-5, 70-72	9H-6, 70-72	82.60	84.10	83.35	91.02
B *G. crassaformis hessi*	F3	0.75	9H-5, 70-72	9H-6, 70-72	82.60	84.10	83.35	91.02
Reent. m. *Gephyrocapsa* spp.	N2	1.00	13H-1, 39-40	13H-2, 39-40	114.39	114.86	114.62	127.99
T large *Gephyrocapsa* spp.	N3	1.24	15H-6, 70-71	15H-6, 114-115	140.12	140.56	140.34	156.61
T *G. obliquus*	F4	1.3	15H-5, 70-72	15H-6, 70-72	138.62	140.12	139.37	155.64
172-1059A-								
T *G. tumida flexuosa*	F1	0.068	4H-3, 70-72	4H-3, 70-72	26.50	28.30	27.40	30.43
Reent. *G. tumida flexuosa*	F2	0.401	9H-CC, 23-26	10H-1, 70-72	80.43	80.50	80.47	96.41
T *P. lacunosa*	N1	0.46	10H-3, 40-41	10H-3, 65-66	83.20	83.65	83.43	100.45

Notes: Event abbreviations: T = top, B = base, Reent. = reentrance, m = medium sized. ID abbreviations: F = planktonic foraminifer datum, N = nannofossil datum. ID numbers correspond to those in Figures 54, 57, 60, and 63.

Ma), because these events can only be precisely identified with a scanning electron microscope. Nevertheless, qualitative analyses of samples from the upper 10 m of Hole 1056B indicate that these sediments could be placed within the acme interval of *E. huxleyi,* whereas the marker seems to disappear within Core 172-1056B-3H. The pattern of extinction of *Pseudoemiliania lacunosa* shows the typical trend, with a sharp decrease in abundance followed by the upward scattered presence of rare specimens. Of the Pleistocene gephyrocapsid events (see “Biostratigraphy” section, “Carolina Slope” chapter, this volume), we observed the reentrance of medium-sized forms between Cores 172-1056B-11H and 12H, and the disappearance of large forms between Cores 172-1056B-14H and 15H. The appearance of large *Gephyrocapsa* spp. specimens observed in the lowermost part of the succession (within Core 172-1056B-17H) allows this interval to be assigned to the lower Pleistocene (slightly older than 1.58 Ma). Although this event has not been accurately constrained (because of the small number of samples in the critical interval), it seems to occur rather abruptly, suggesting the presence of a minor hiatus in the lowermost part of Hole 1056B.

Site 1057

Calcareous nannofossils are common to abundant throughout the continuous sedimentary section recovered at Site 1057. The observed assemblages indicate ages that range from the Holocene to the middle Pleistocene (from Zone CN15 to Zone CN14). The biohorizons determined in Hole 1057A were constrained to within 0.4–0.8 m, and are presented in Table 3 and Figure 15. As already explained in the “Carolina Slope” chapter (this volume), the upper Pleistocene biohorizons at the bottom of the *E. huxleyi* acme and the FO of *E. huxleyi* cannot be accurately detected, because of the small size of the marker (1–2 µm). On the basis of the preliminary shipboard analyses, the upper 15 m of the section is placed in the interval of *E. huxleyi* dominance, whereas the FO of *E. huxleyi* probably occurs within Core 172-1057A-4H (between 1057A-3H-CC and 4H-CC). *P. lacunosa* becomes extinct within Core 172-1057A-5H. The gephyrocapsid population is abundant and well diversified, and dominates the nannofossil assemblage together with *P. lacunosa.* The absence of the medium-sized gephyrocapsids in the oldest sediments recovered at the base of the Site 1057 sedimentary section (from ~107 mbsf to the bottom of the hole) suggests an age between 0.96 and 1.24 Ma for this interval (see “Explanatory Notes” chapter, this volume).

Site 1058

Calcareous nannofossils recovered at Site 1058 represent a stratigraphic sequence from the Holocene (corresponding to the interval of *E. huxleyi* dominance) to the lower Pleistocene (~1.3 Ma). Preservation of the rich nannofossil assemblages is generally good, and no strong reworking has been observed. In the uppermost interval (0–10 mbsf) of Hole 1058A, the presence of relatively large numbers of *E. huxleyi* indicates an age of <0.085 Ma (within Zones CN15/NN21) for these sediments. *E. huxleyi* decreases in abundance through the interval corresponding to Cores 172-1058A-2H and 3H, and probably disappears within Core 172-1058A-4H. The last occurrence (LO) of *P. lacunosa* is distinct, as usual, and it occurs within Core 172-1058A-6H. The biostratigraphic interval characterized by the absence of medium-sized and large gephyrocapsids has been recognized between Cores 172-1058A-13H and 15H. From Core 172-1058A-15H to the bottom of the hole, the large specimens of gephyrocapsids are present. Together with the other representatives of the gephyrocapsid group, they dominate the assemblages. The presence of large *Gephyrocapsa* spp. indicates an age of ~1.3 Ma for the lowermost part of Site 1058.

Site 1059

The biostratigraphic constraints for this site were primarily provided by analyses of samples from Hole 1059A. The nannofossils are abundant to common, and generally well preserved. Terrigenous input and reworking affect the nannofossil assemblages throughout this sedimentary section. Cretaceous, Paleogene, and, in lesser amounts,

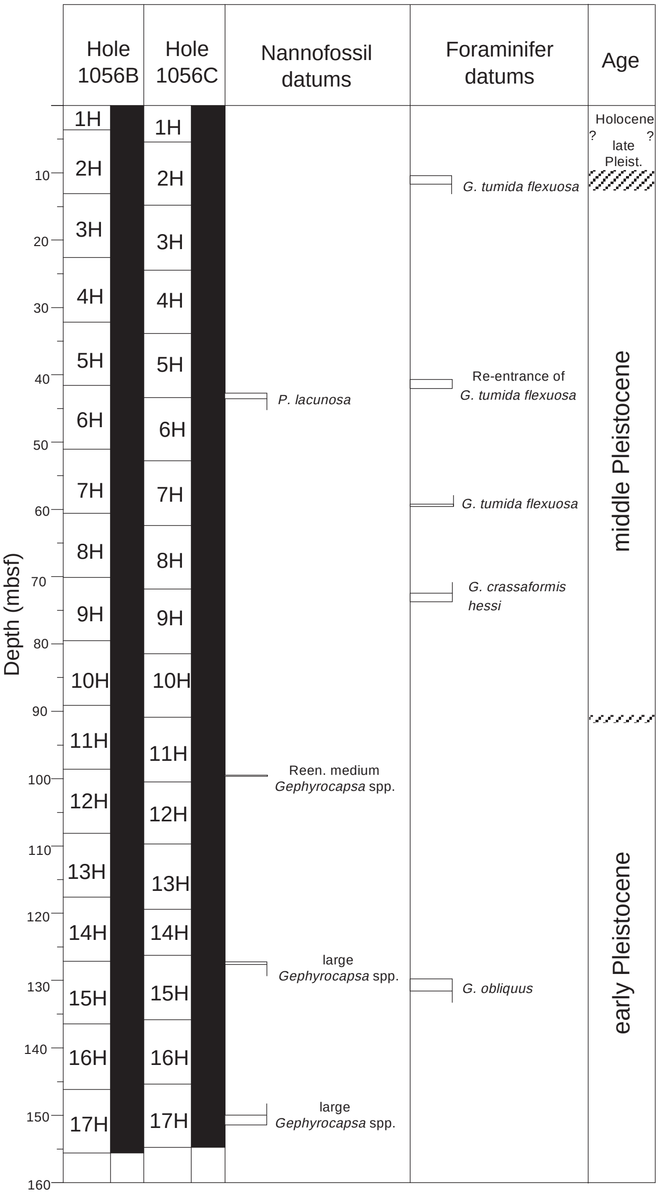

Figure 14. Core recovery and calcareous microfossil datum levels at Site 1056.

Neogene nannofossils have been observed in several intervals. Because of the aforementioned reasons, the base of the *E. huxleyi* acme and the base of *E. huxleyi* were only approximately recognized; the interval of *E. huxleyi* dominance extends through the bottom of Core 172-1059A-2H, whereas the FO of this species is probably within Core 172-1059A-6H. These preliminary biostratigraphic observations point out the great expansion of the Holocene to Pleistocene portion of the Site 1059 stratigraphic succession. The subsequent biohorizon (the LO of *P. lacunosa*) is within Core 172-1059A-10H. It is the oldest nannofossil event recognized at this site, which allows an age assignment of ~0.6 Ma for the bottom part of this stratigraphic section.

Planktonic Foraminifers

Site 1056

The LO and FO of *Globorotalia tumida flexuosa* (0.068 and 0.401 Ma) were the first two planktonic foraminifer datums to be delimited at all sites (Table 3). However, the FO of *G. tumida flexuosa* as defined by Berggren et al. (1995), seems not to be the real base of the range in the Blake-Bahamas area, but rather a reentrant event. During a search for the FO of *Truncorotalia crassaformis hessi* in Hole 1056B sediment, *G. tumida flexuosa* was discovered below its ostensible FO. Excursions of magnetic susceptibility values in the positive direction are interpreted as equivalent to glacial isotope stages (see “Physical Properties” section, this chapter). In Hole 1056B the LO of *G. tumida flexuosa* is associated with marine isotope stage (MIS) 5 and the reentrance (i.e., published FO) is associated with the transition from MIS 12 to MIS 11, but *G. tumida flexuosa* specimens were also found at a level (56.30–59.40 mbsf) associated with the transition from MIS 16 to MIS 15. Postcruise work will be necessary to date this FO and LO precisely before using it as a possible datum.

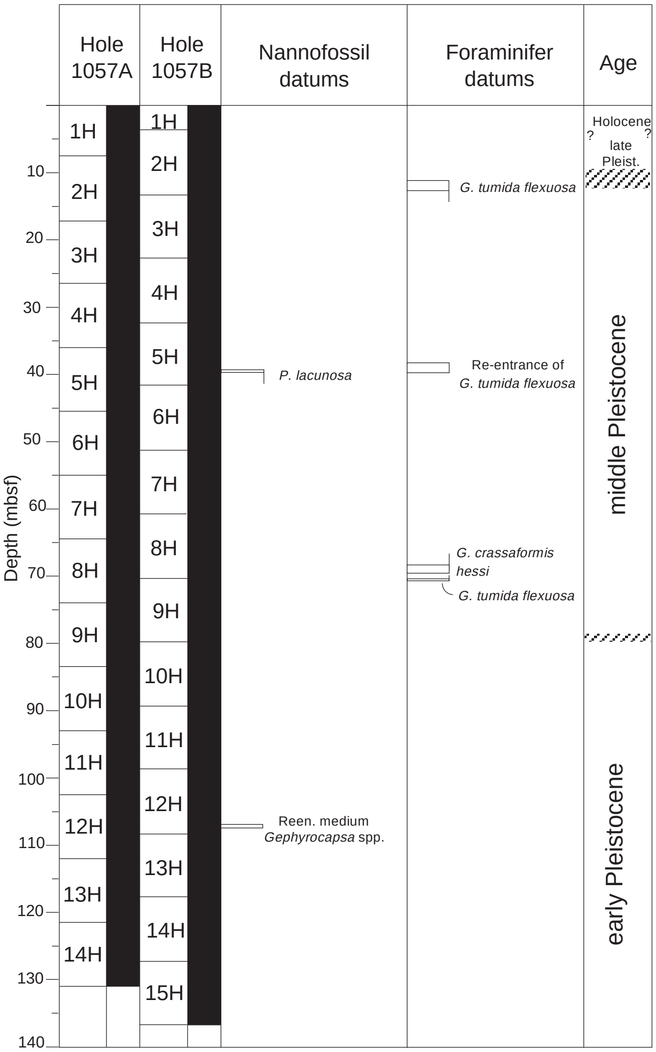

Figure 15. Core recovery and calcareous microfossil datum levels at Site 1057.

The FO of *T. crassaformis hessi* (0.75 Ma) was found in Hole 1056B sediment, although this species is not as easily recognizable as *G. tumida flexuosa. Truncorotalia crassaformis* with kummerform chambers are found nearly throughout its range, but the *T. crassaformis hessi* datum seems defined by a final chamber that is only slightly smaller than the penultimate chamber, so that the overall subquadrate shape of the periphery is preserved.

Determining the LO of *Globigerinoides obliquus* (1.3 Ma) is made difficult by the rarity of this taxon at the top of its range.

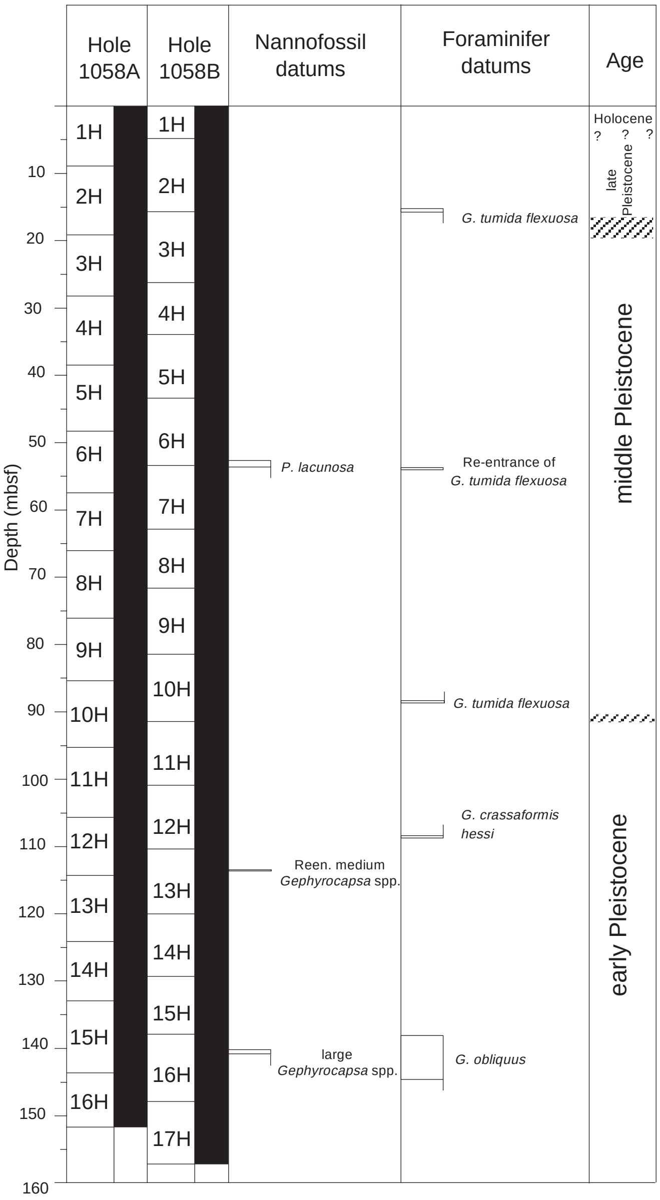

Figure 16. Core recovery and calcareous microfossil datum levels at Site 1058.

Site 1057

Comparison of foraminifer datum levels to the magnetic susceptibility record of Hole 1057A reveals that the LO and the reentrance of *G. tumida flexuosa* are, as in Hole 1056B, associated with the transitions from MIS 5 to MIS 4 and MIS 12 to MIS 11, respectively. However, the deeper occurrences of *G. tumida flexuosa* in Samples 172-1057A-8H-1, 70–72 cm, 8H-3, 70–72 cm, and 8H-4, 70–72 cm (65.20–69.70 mbsf) are associated with the transition from MIS 20 to MIS 19. This latter event nearly coincides with the FO of *T. crassaformis hessi* at 0.75 Ma in this hole. The FO of *T. crassaformis hessi* is associated with MIS 20 in both Holes 1056B and 1057A.

Site 1058

In Hole 1058A sediment the positions of *G. tumida flexuosa* and *T. crassaformis hessi* datums relative to the magnetic susceptibility record are similar to those from Hole 1057A, except that the reentrance of *G. tumida flexuosa* is found closer to the peak of MIS 12, rather than in the transition to MIS 11.

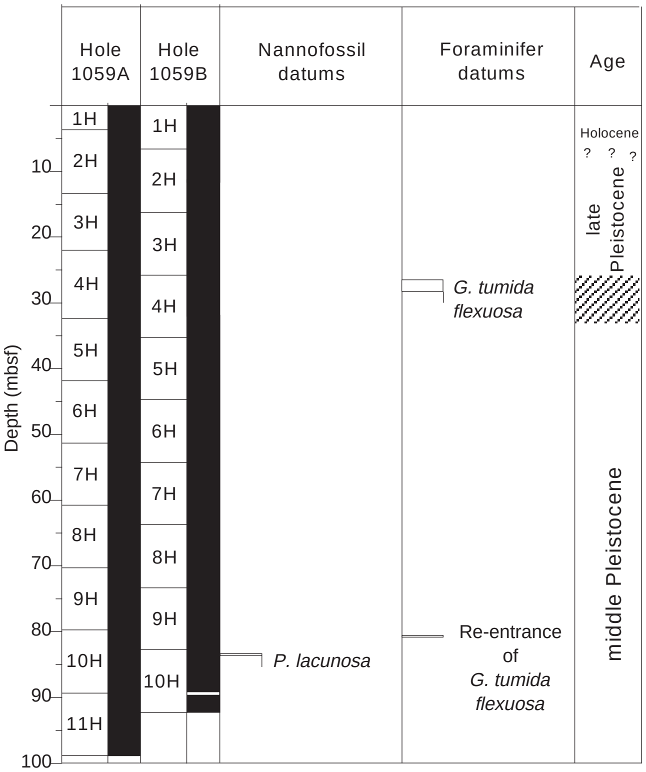

Figure 17. Core recovery and calcareous microfossil datum levels at Site 1059.

Site 1059

Only the LO and the reentrant datums of *G. tumida flexuosa* were delimited at this site. Many samples examined from Hole 1059A consisted of strongly sorted sediments. A disproportionate amount of the >63-µm fraction is made up of planktonic foraminifers between 63 and 250 µm; large planktonic foraminifers are rare. The LO level of *G. tumida flexuosa,* relative to the magnetic susceptibility record, is not as near to the top of MIS 5 as at previous sites, but rather is in the upper third, and the reentrance is at the bottom of MIS 11 rather than in the transition from MIS 12.

Benthic Foraminifers

Benthic foraminifers were studied mainly in core-catcher samples from Holes 1056B, 1056C, 1057A, 1057B, 1058A, 1058B, 1059A and 1059B. In addition, some samples from within cores were examined to better constrain the levels of major faunal changes.

Sites 1056 and 1057

At Sites 1056 and 1057 benthic foraminifers are generally well or moderately preserved, and few to common in abundance. A major faunal change, marked by a large increase in the numbers of infaunal species, is recognized between Samples 172-1056C-10H-CC and 172-1056B-11H-CC, and between Samples 172-1057A-10H-CC and 172-1057B-11H-CC. In Cores 172-1056B-1H through 1056C-10H, and 172-1057B-1H through 172-1057A-10H, the fauna is characterized by large fluctuations in the abundance of *Cibicidoides wuellerstorfi, Cassidulina carinata, Gyroidinoides* spp., *Melonis barleeanum, Bulimina marginata,* and *Bulimina costata.* The assemblages are characterized by flucuations in the abundance of infaunal (*B. marginata, M. barleeanum,* and *Globobulimina affinis*) vs. epifaunal taxa, with large numbers of epifaunal species during glacial intervals. In Cores 172-1056B-11H through 17H and 172-1057B-11H through 15H, the most common species are *Uvigerina peregrina* and *G. affinis,* with smaller numbers of *B. marginata, Bolivinita quadrilatera, and Stilostomella* spp. The dominance of shallow to deep infaunal taxa within this interval suggests increased amounts of organic carbon at the seafloor compared to what is found in the upper part of the hole. This may be the result of increased primary productivity and/or enhanced preservation of organic matter.

Site 1058

At Site 1058 benthic foraminifers are rare to few in abundance and generally moderately preserved. No major faunal fluctuations are observed within the recovered section, except for a large increase in the relative abundance of *Globobulimina* spp. in Cores 172-1058A-14H and 15H. The main components of the benthic fauna are *U. peregrina, M. barleeanum, B. marginata, Hoeglundina elegans, Oridorsalis umbonatus, C. wuellerstorfi,* and *Gyroidinoides* spp.

Site 1059

Benthic foraminifers are rare at this site, but are generally moderately to well preserved. The assemblages are dominated by small-sized specimens (between 63 and 125 µm), mainly of *Bolivina paula* and *Epistominella* spp., which suggests sorting during transport by bottom currents. Large specimens of *Globobulimina* spp., *C. wuellerstorfi,* and *O. umbonatus* are also present, but in very small numbers.

Diatoms

Diatoms were examined from Holes 1056B, 1056C, 1057A, 1057B, 1058A, 1058B, 1059A, and 1059B. Table 4 lists the preservation state and relative abundance of diatoms in each of the core-catcher samples of the first hole at each site.

Biostratigraphic markers were observed in small numbers at Sites 1056, 1057, 1058, and 1059 and, therefore, the biostratigraphic usefulness of diatoms is severely limited. The marker species, *Pseudoeunotia doliolus* and *Nitzschia reinholdii,* were relatively rare at the four sites considered in this chapter in comparison to other species present. All samples examined were younger than the FO of *P. doliolus,* at 1.8 Ma (Barron, 1985; Baldauf, 1987). The rarity of *N. reinholdii* makes it difficult to determine whether the ages of the samples are older than the LO of this species or their presence is a result of reworking. These data agree with both nannofossil and planktonic foraminifer datums.

The species present at Sites 1056, 1057, 1058, and 1059 were similar to those at Sites 1054 and 1055. As can be seen in Table 4, samples from Sites 1056 and 1057 had fewer diatoms, consisting of broken, fragmented assemblages. In contrast, sediments at Sites 1058 and 1059 were comparatively rich in diatoms. The entire middle portion of Hole 1058A had a diverse and well-preserved assemblage (with the exception of Sample 172-1058A-10H-CC). Samples from Hole 1059A had fewer and more scattered occurrences of similarly well-preserved diatoms. A few samples were dominated by *Paralia sulcata.* It is uncertain whether this dominance is a reflection of an actual environmental difference (such as increased nutrients), or transport from a source area different from that of the other samples. The samples examined from Holes 1058A and 1059A included species of coastal benthic diatoms (*Diploneis bombus, Raphoneis* spp., *Pinnularia* spp., *Pleurosigma* spp.) as well as some that are restricted to very low-salinity environments (*Navicula humerosa, Achnanthes brevipes,* and *Diploneis ovalis;* Hajós, 1973; Schrader, 1973; Baldauf, 1984; Barron, 1985; Hustedt and Jensen, 1985; Baldauf, 1987).

Table 4. Distribution of diatoms in Holes 1056B, 1057A, 1058A, and 1059A.

Core, section	Presence of diatoms
172-1056B-	
1H-CC	F - fragments
2H-CC	X - fragments
3H-CC	Barren
4H-CC	Barren
5H-CC	X - fragments
6H-CC	R - fragments
7H-CC	Barren
8H-CC	X - fragments
9H-CC	X - fragments
10H-CC	Barren
11H-CC	Barren
12H-CC	R - fragments
13H-CC	Barren
14H-CC	Barren
15H-CC	R - fragments
16H-CC	R - fragments
17H-CC	R - fragments
172-1057A-	
1H-CC	Barren
2H-CC	Barren
3H-CC	Barren
4H-CC	Barren
5H-CC	Barren
6H-CC	Barren
7H-CC	X - fragments
8H-CC	X - fragments
9H-CC	Barren
10H-CC	R - fragments/X - whole
11H-CC	R - fragments
12H-CC	X - fragments
13H-CC	X - fragments
14H-CC	F - fragments
172-1058A-	
1H-CC	C - fragments/F - whole
2H-CC	F - fragments/R - whole
3H-CC	R - fragments
4H-CC	R - fragments
5H-CC	F - fragments
6H-CC	R - fragments
7H-CC	A - fragments/C - whole
8H-CC	F - fragments/X - whole
9H-CC	A - fragments/C - whole
10H-CC	Barren
11H-CC	A - fragments & whole
12H-CC	A - fragments/C - whole
13H-CC	A - fragments & whole
14H-CC	A - fragments & whole
15H-CC	A - fragments/C - whole
16H-CC	C - fragments
172-1059A-	
1H-CC	F - fragments
2H-CC	A - fragments/F - whole
3H-CC	C - fragments/F - whole
4H-CC	C - fragments/X - whole
5H-CC	Barren
6H-CC	C - fragments/R - whole
7H-CC	C - fragments/F - whole
8H-CC	Barren
9H-CC	X - fragments
10H-CC	Barren
11H-CC	R - fragments

Note: Quantity abbreviations: X = scarce, R = rare, F = few, C = common, A = abundant.

PALEOMAGNETISM

The natural remanent magnetization (NRM) of the archive-half sections from all holes at Sites 1056, 1057, 1058, and 1059 (all APC cores) was measured at 5-cm intervals using the pass-through cryogenic magnetometer. After measuring the NRM, most sections were partially demagnetized at 20 mT with the aim of removing overprints to reveal the character of the geomagnetic field changes. More detailed alternating field (AF) demagnetization treatments up to 60 mT were conducted on a few sections to evaluate the demagnetization behavior of the sediments at higher fields. The data for all remanence measurements are given in Tables 5 through 17 on CD-ROM (back pocket, this volume).

The NRM inclinations are almost always strongly biased toward high positive inclinations (70° to 90°), which is inconsistent with the 49° to 52° inclinations expected for an axial dipole field at the latitude of these sites. The observed inclinations indicate that a magnetic overprint is present, as identified on many previous Deep Sea Drilling Project (DSDP) and Ocean Drilling Program (ODP) legs. This secondary overprint is characterized by steep inclinations and is probably acquired during drilling.

The intensity of magnetization after treatment at 20 mT at each of these sites covaries strongly with susceptibility. The intensities vary by up to three orders of magnitude, ranging from 5 $\times 10^{-5}$ to 5 $\times 10^{-2}$ A/m. At each of these sites we frequently observed large directional swings, spanning up to 30 cm, which occur with a strong increase in magnetization intensity. These are most likely the result of edge effects caused by magnetization contrasts and are not related to geomagnetic field behavior (Roberts et al., 1996). Most of these intervals have been deleted from the figures presented here.

Partial demagnetization in peak fields of 20 mT appears to remove most of the overprint for the upper 80 to 100 m of core at each hole as evidenced by directional data downcore (Figs. 18–21) and demagnetization behavior of discrete samples (Fig. 22). Below these depths, the intensities are very weak and the overprint sufficiently strong to make an assessment of magnetic polarity difficult from long-core measurements alone. Even so, we have been able to estimate the polarity stratigraphy at all four sites on the basis of combined discrete and long-core measurements (Table 18).

Orientation

The Tensor tool was used to orient the APC cores collected from these holes starting with the third core at each hole (Table 19 on CD-ROM, back pocket, this volume). The orientation data proved to be successful in aligning the declinations between cores in the majority of cases. Sharp offsets between some cores, however, suggest that either the Tensor tool did not function properly or that the core twisted or rotated as it entered the core barrel. In some cases disturbance resulting from gas expansion seriously affected the declination data. In general, however, the Tensor tool was successful at orienting the cores as indicated by the nearly random distribution of declinations prior to orientation and the tight grouping ~0° after applying the Tensor correction (Fig. 23). The Tensor-tool reorientation of declination was very useful in assessing polarity changes near the bases of Sites 1056, 1057, and 1058, where very steep, magnetic overprints were significant.

Discrete Sample Analysis

Oriented discrete samples (6-cm^3 plastic boxes) were collected from almost every core from Holes 1056A, 1057A, 1058A, and 1059A. These samples were generally subjected to stepwise AF demagnetization up to 60 mT in order to assess the magnetic coercivity of the sediments and estimate a demagnetization level suitable to remove the secondary magnetization. It is clear that a large (>60% of total NRM) magnetic overprint is present, which can be routinely removed by demagnetization at 20 mT (Fig. 22). Above 20 mT, the samples commonly decay toward the origin in a simple manner. With increasing depth, the effectiveness of the overprint removal decreases. This may be due to an increasingly coarser overall magnetic grain size, which is easier to remagnetize, or to downhole addition of new chemical magnetic phases with higher coercivity. Anhysteretic remanent magnetization (ARM), isothermal remanent magnetization (IRM) acquisition, and AF demagnetization curves on several of

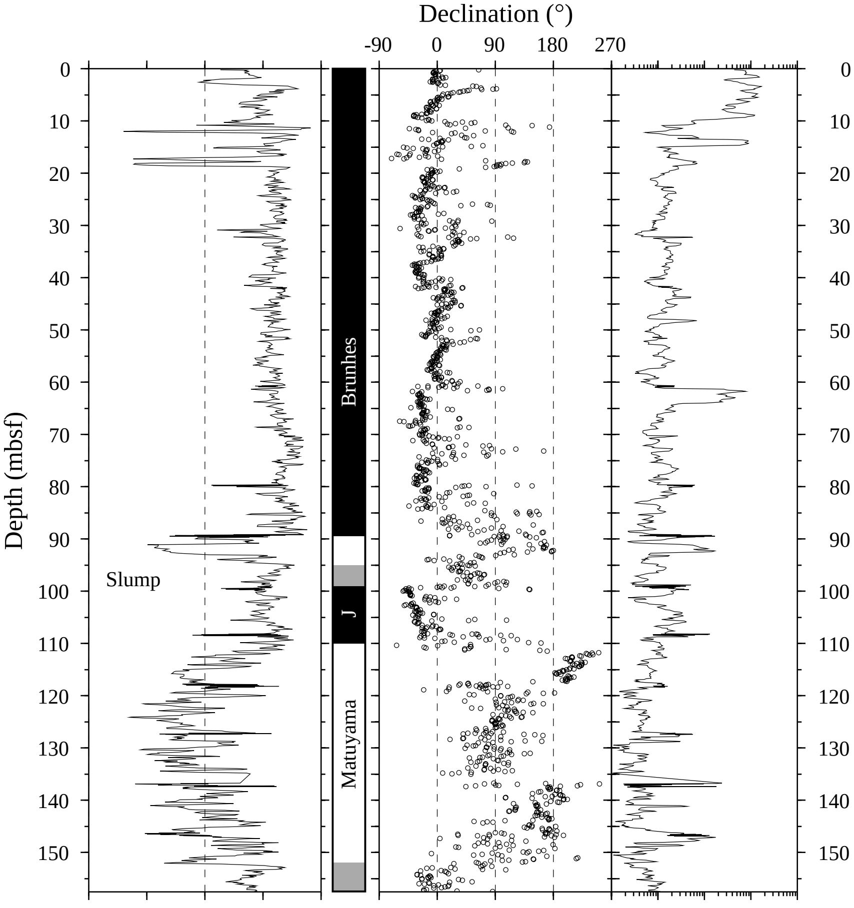

Figure 18. Downhole variation in the remanent magnetization direction and intensity after 20 mT demagnetization for Hole 1056B. Declinations were oriented with the Tensor tool data starting with the third core (13.10 mbsf). Above this, they were oriented by assuming that the mean declination for the core is 0°. J = Jaramillo.

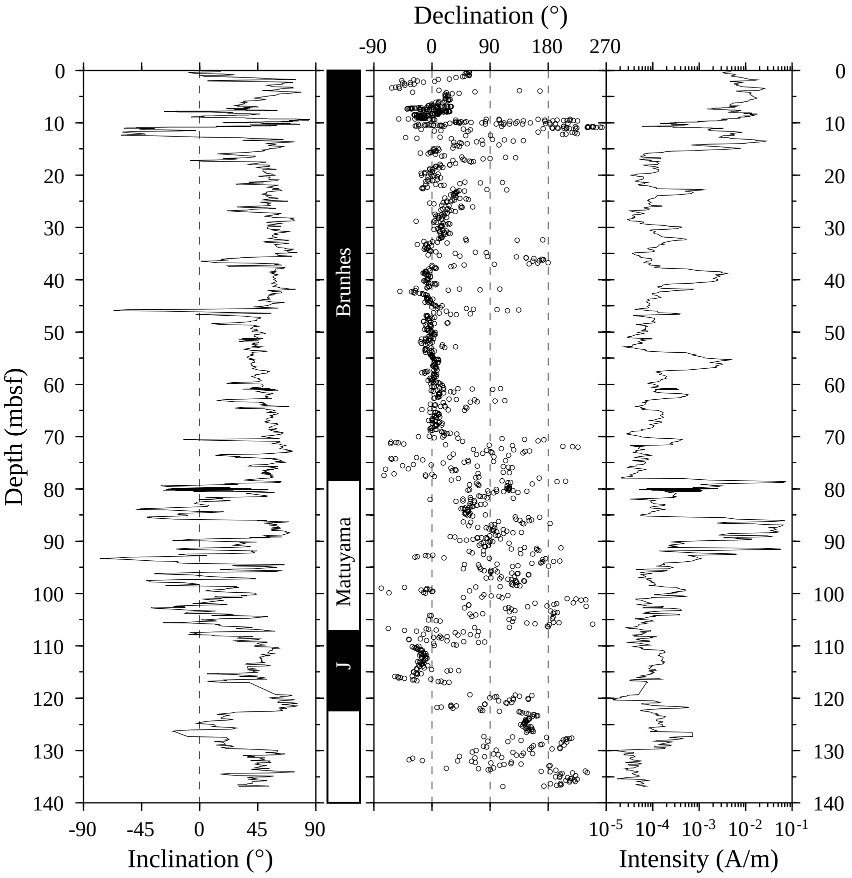

Figure 19. Downhole variation in the remanent magnetization direction and intensity after 20 mT demagnetization for Hole 1057B. Declinations were oriented with the Tensor tool data starting with the third core (13.20 mbsf). Above this, they were oriented by assuming that the mean declination for the core is 0°. J = Jaramillo.

these samples indicate that they can acquire a strong viscous remanent magnetization (VRM) very quickly. This may explain the difficulty in removing the steep downward component in several of these cores.

Excellent agreement is observed between the pass-through measurements of the archive halves and the best-fit directions obtained from progressive AF demagnetization of discrete samples at Site 1059 for most of the Brunhes Chron (Fig. 21). The intensities measured using discrete samples and pass-through measurements also agree. Some of the sharp peaks apparent in the split-core inclinations are not present in the discrete sample results, which we attribute to general drilling disturbance related to APC coring, sediment disturbance related to drilling holes in the liner for the cores to degas, or edge effects in the split-core measurements at section ends and at abrupt magnetization contrasts.

Magnetic Polarity Stratigraphy

Polarity assessment is difficult at these sites because of the effects of the overprint, reduction diagenesis, and core disturbance caused by gas expansion. For these reasons, composite polarity logs compiled from the multiple holes cored at each site proved useful in interpreting the polarity records. Polarity changes are often better defined by the record of oriented declinations (Tensor tool) rather than by the inclination records, most likely because of the large, steep downward overprint that affects these cores.

Site 1056

Normal-polarity directions are observed from the seafloor down to a depth of 89.5 mbsf in Hole 1056B and down to 92.0 mbsf in Hole 1056D (Fig. 18; Table 18). The average directions in the Brunhes Chron are declination = –12.3°, inclination = 50.8°, k = 16.0, α_{95} = 1.7°, N = 418, and R = 392.1. Reversed-polarity directions are observed across a short interval from 89.5 to 93 mbsf and from 92 to 94 mbsf in Holes 1056B and 1056D, respectively, but are not observed in Hole 1056C. This interval likely represents the uppermost part of the Matuyama Chron at this site. An interval of convoluted bedding that is probably a slump occurs immediately beneath the interval of reversed polarity. The slump was recovered to different degrees in the three holes (see “Stratigraphic Correlation” section, this chapter), which has complicated the polarity interpretation at this site. At 93–104 mbsf in Holes 1056B and 1056D, large directional changes occur, which we interpret as the top of the Jaramillo Subchron.

Site 1057

Normal-polarity directions (mean declination = –7.8°, inclination = 54.3°, k = 9.3, α_{95} = 2.2°, N = 426, and R = 380.4) are observed to a depth of 70 mbsf in Hole 1057B. The declinations become scattered in the interval from 70 to 78 mbsf, though the inclinations still average around 50°. From 78 to 85 mbsf, the inclinations become more scattered and move toward negative values, which is consistent with an incompletely removed overprint. We therefore place the base of the Brunhes at 78 mbsf (Fig. 19; Table 18). Between 85 and 90 mbsf, steep downward directions are observed that coincide with a dramatic increase in intensity and susceptibility, interpreted as an interval of lithologic and/or diagenetic change, which obscures the polarity record. These variations in lithology are apparently related to the slump identified in the interval. Normal-polarity declinations and inclinations are observed between 107 and 122.5 mbsf. This interval is interpreted as the Jaramillo Subchron.

Site 1058

The record from Hole 1058B exhibits normal-polarity inclinations that vary about a mean of 50° down to a depth of about 91 mbsf (Fig. 20; Table 18). The interval from 91 to 101 mbsf exhibits large

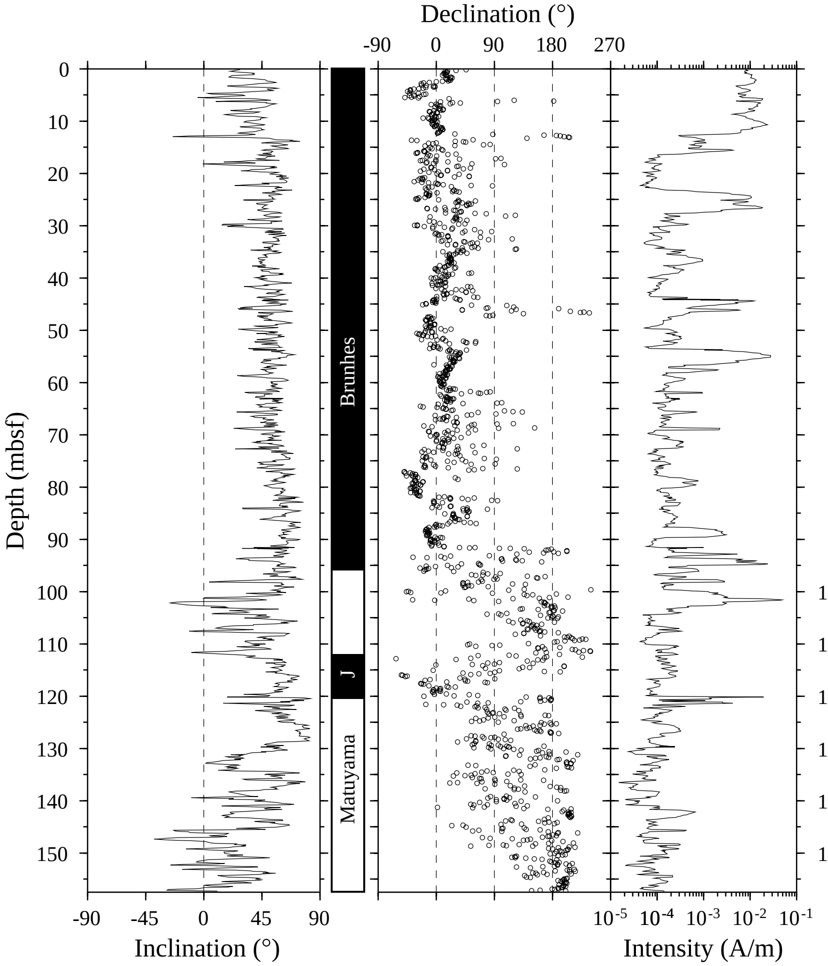

Figure 20. Downhole variation in the remanent magnetization direction and intensity after 20 mT demagnetization for Hole 1058B. Declinations were oriented with the Tensor tool data starting with the third core (15.50 mbsf). Above this, they were oriented by assuming that the mean declination for the core is 0°. J = Jaramillo.

variations in both inclinations and declinations in both pass-through as well as discrete sample measurements. In Hole 1058C, the declinations indicate normal polarity down to 95.5 mbsf, and are erratic from 95.5 to 98 mbsf. Based on both holes, we place the base of the Brunhes at 96 mbsf, although it could lie within ~5 m of this preferred location. From 101 to 112 mbsf in Hole 1058B, the declinations are roughly 180°, though the inclinations are erratic. We interpret this interval to be in the upper Matuyama Chron, with the interval of normal-polarity directions observed between 112 and 120.5 mbsf to be in the Jaramillo Subchron.

Site 1059

Normal-polarity directions were observed from the entire interval cored at Site 1059. The site mean direction is declination = 3.7°, inclination = 59.2°, k = 11.1, α_{95} = 0.96°, N = 1897, and R = 1726.316 (Fig. 21).

Magnetic Field Variability Between Reversals

As noted above, there were a number of large-amplitude swings in magnetic field direction, usually with intervals of reversed inclination, at all four sites. In virtually all cases, however, the "excursional" directions could not be replicated between different holes at each site and the anomalous directions are considered to be noise from viscous overprints or coring-induced sediment deformation.

At Site 1059, the sedimentation rates are considerably higher than at the other sites, averaging more than 200 m/m.y. in the Brunhes Chron. Given this high sedimentation rate, general trends in secular variation, which could be correlated among Holes 1059A, 1059B, and 1059C, were sought using magnetic susceptibility and NRM intensity as time lines for correlation. In none of the cases could apparent secular variation be reproduced among the holes, even in the uppermost 20 m.

At Site 1059 (and, to a lesser extent, the other sites), we noted a tendency for sediment intervals with stronger intensities to exhibit shallower inclinations than sediment intervals with lower intensities. This can be explained in a number of ways. For example, the sediments of weaker magnetization intensity may be affected to a greater extent by the effects of the steep downward overprint. There are likely significant variations in the composition of the paleomagnetic carrier between glacial intervals (high intensities and high susceptibilities) and interglacials (low intensities and low susceptibilities); moreover, the intensity record shows an exponential rather than linear relation to the susceptibility record. Mineralogical variations may also result in variations in the VRM acquisition or inclination flattening.

Directional Variation by Coring-Induced Sediment Deformation

Many of the APC cores at these sites were deformed near the core edges; the sediment is smeared downward along the core liner (the outer surface of the core). If the radial thickness of the smeared sediment is greater than 1 cm, the deformed sediment volume exceeds the undeformed core volume. Therefore the deformed volume may contribute a significant proportion of the remanent magnetization measured in half-core pass-through measurements.

To evaluate the influence of coring-induced deformation on the remanent magnetization, a model that predicts the directional change

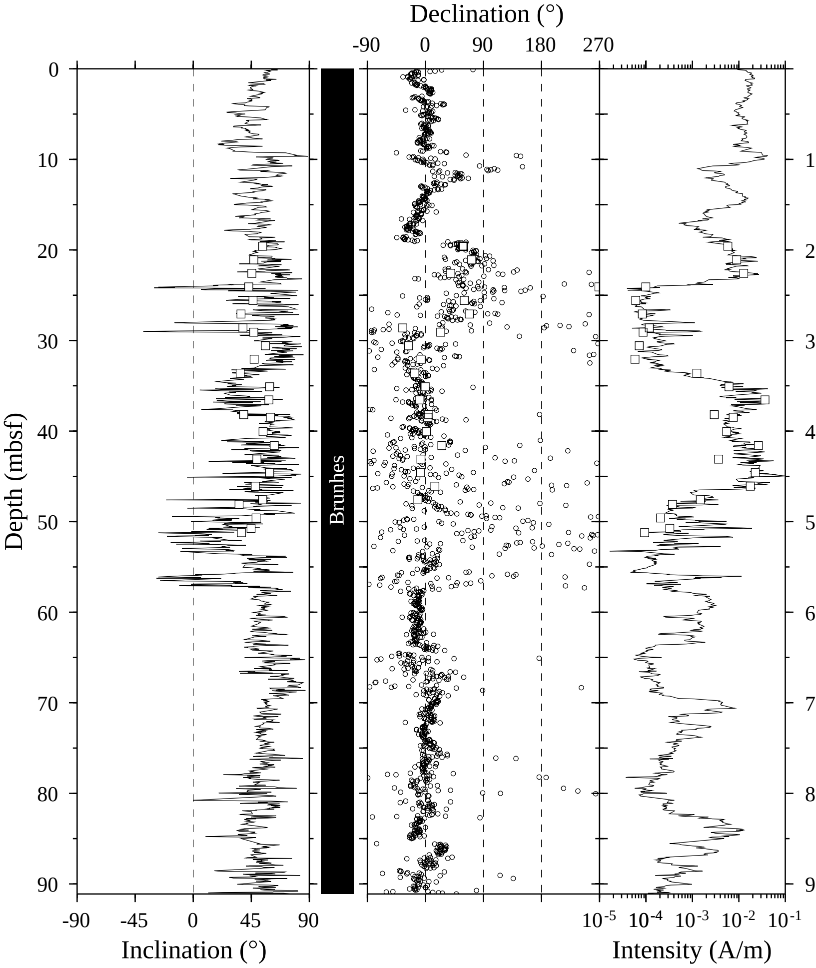

Figure 21. Downhole variation in the remanent magnetization direction and intensity after 20 mT demagnetization for Hole 1059C. The solid white squares are the results from progressive demagnetization of discrete samples taken from this hole. Declinations were oriented with the Tensor tool data, except for Cores 172-1059C-1H and 2H, where they were oriented by assuming that the mean declination for the core is 0°.

of the remanence in a core from deformation was proposed (M. Okada, unpubl. data). The model assumes simple shear of sediment caused by vertical movement of a core's liner. The amount of shear is estimated using a logarithmic function:

$$Z = -b\,[\log(R-r) + r],$$

where R = core radius, b = degree of deformation, and Z = the amount of shear at a point that is located a distance r from the center of the core. In most of the cores, the sediment deformation patterns seem to be reconstructed by this function when $b = 0.2$ (Fig. 24). The model divides the remanence at each point into three orthogonal components (vertical, radial, and perpendicular-to-the-radial directions) and assumes that the shearing movement causes physical rotation only for the radial components (Fig. 24). The amount of rotation increases with the extent of shear. As a result, magnetic components pointing toward the core liner tend to dip downward. For a normal-polarity direction from the Leg 172 sites, the resultant inclination becomes steeper and the total intensity increases. On the opposite side, the components tend to be rotated upward. For the same normal-polarity direction, the inclination becomes shallower and the total intensity decreases (Fig. 24). For components pointing at an angle to the liner on a horizontal plane, the degree of dip depends on the angle to the liner. Therefore, resultant inclination values of split-core measurements will vary depending on the angle between the NRM declination and the direction of the split-core face.

The model calculates the effects of deformation by integrating the rotated remanence vectors from the center of the core to the edge at 1° intervals around the circumference of a half core. When the original inclination is 50°, the integrated vector shows variable inclinations ranging from 45° to 59°, depending on the angle between the remanent declination and the split face of the core. For these calculations, this angle is estimated by assuming the remanent declination is zero (alternatively, the Tensor-tool orientation could be used). Thus, the declination of a half core can be used to determine the expected inclination errors caused by coring-induced deformation.

As an example, deflected inclinations resulting from sediment deformation, which were derived from Holes 1059A, 1059B, and 1059C, are shown in Figure 25. The geocentric axial dipole (GAD) inclination at Site 1059 of 49° was used as the expected inclination of the sediment prior to being cored. The direction in which the core was split was derived by fitting a linear trend to the declinations of each core. The results show that the calculated inclination anomalies caused by sediment core deformation are of the correct size and sense to explain most of the differences in measured inclination values among the cores at all three holes cored at this site. This result suggests that the core deformation model could be used to derive the original inclination values from long-core measurements.

Composite Depths and Stratigraphic Correlation

MST and color reflectance data collected on core from all holes at Sites 1055 through 1059 were smoothed over a 31-cm window and were used to correlate between individual holes at each site, to determine depth offsets in the composite section, and to create spliced records. MST and reflectance data on the composite depth scale (expressed as meters composite depth [mcd]) present features in adjacent holes aligned so that they occur at approximately the same depth. Working from the top of the sedimentary sequence, a constant was

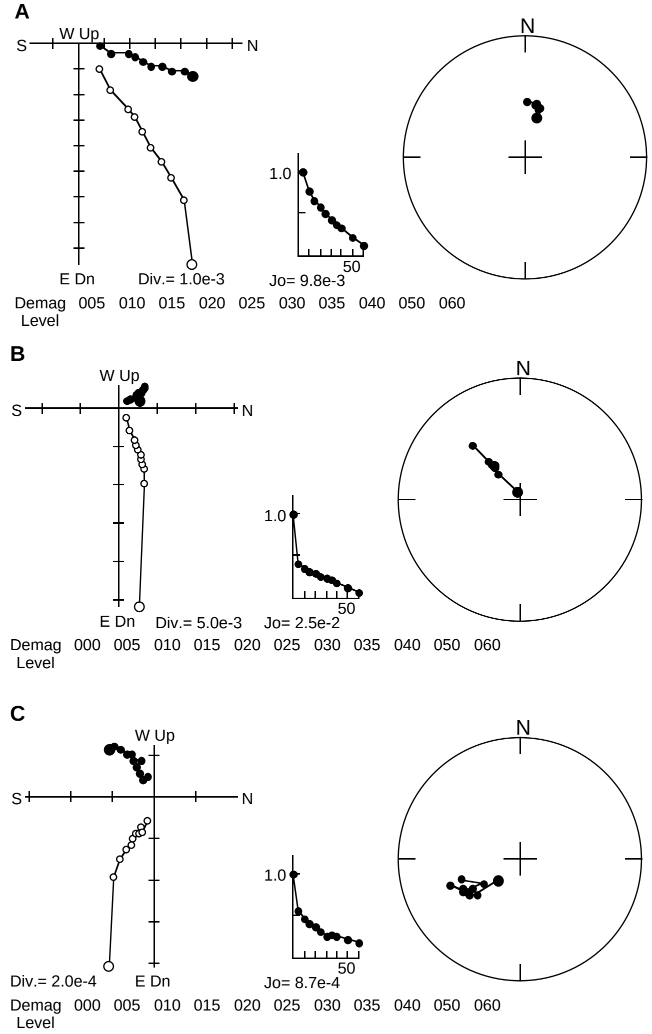

Figure 22. Examples of progressive AF demagnetization of discrete Samples (**A**) 172-1059C-3H-1, 61 cm, (**B**) 172-1059C-5H-1, 50 cm, and (**C**) 172-1059C-6H-3, 24 cm, using the pass-through degaussing coils and pass-through magnetometer. A steep downward component is removed by treatment of 5 to 20 mT.

Table 18. Magnetostratigraphy for Sites 1056, 1057, 1058, and 1059.

Hole	Reversal	Age (Ma)	Depth (mbsf)
1056B	Brunhes/Matuyama	0.78	89.5
	Jaramillo top	0.99	93-99
	Jaramillo base	1.07	108-112
1056D	Brunhes/Matuyama	0.78	92
	Jaramillo top	0.99	94-104
	Jaramillo base	1.07	110-115
1057A	Brunhes/Matuyama	0.78	78
	Jaramillo top	0.99	107-109
	Jaramillo base	1.07	122-125
1057B	Brunhes/Matuyama	0.78	78.5
	Jaramillo top	0.99	107
	Jaramillo base	1.07	122.5
1058B	Brunhes/Matuyama	0.78	96
	Jaramillo top	0.99	112
	Jaramillo base	1.07	120.5
1058C	Brunhes/Matuyama	0.78	95.5-98
1059A-C	All normal polarity		

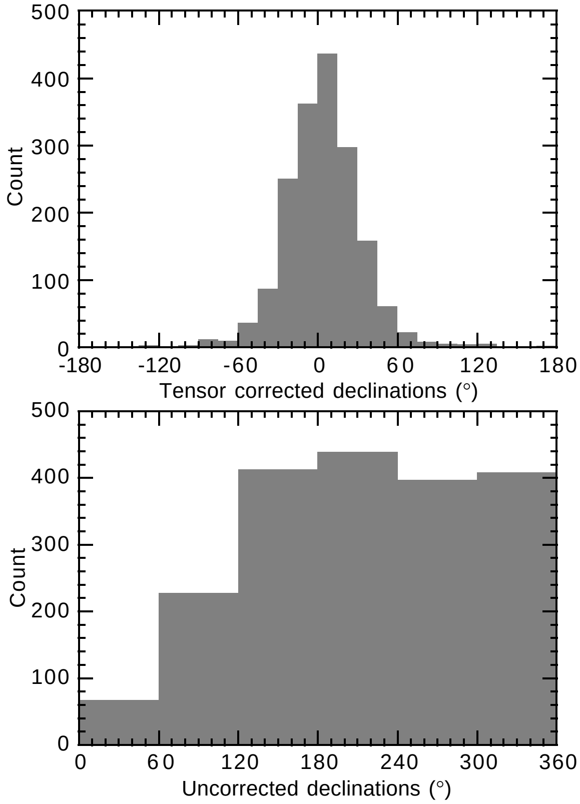

Figure 23. Comparison of uncorrected declinations and declinations corrected using the Tensor orientation tool measured after partial AF demagnetization at 20 mT.

added to the depth (mbsf) of each core in each hole to arrive at a composite depth for that core. A spliced record for each site was created by combining intervals of the individual composite depth sections to create an overall stratigraphic section. Intervals having significant disturbance, distortion, or potential gaps were avoided, if possible. This information, along with the offsets suggested for individual core sections, can be used as a sampling guide to recover a single sedimentary sequence and to identify variability in cored records between sites.

The depth offsets that comprise the composite depth section are given in Tables 20 and 21. Affine and splice tables appropriate for use in the Splicer computer program are on CD-ROM (back pocket, this volume). The integrity of the recovered sedimentary sequence could be documented for the entire length cored at Sites 1056 (175 mcd [155 mbsf]; especially shallower than about 125 mcd [114 mbsf]), 1057 (155 mcd [137 mbsf]), 1058 (180 mcd [164 mbsf]), and 1059 (117 mcd [99 mbsf]). At all sites there are intervals where precise correlations are difficult to make because of nearly uniform magnetic susceptibility and sediment color. However, after detailed correlations were re-established deeper in the core, minor variations in susceptibility and/or color within the previously questionable intervals could be correlated between holes.

Magnetic susceptibility and the color indices lightness (L*) and chromaticity (a* and b*) were the primary parameters used for correlation between holes. Gamma-ray attenuation porosity evaluator (GRAPE) density was also examined to provide additional support for composite construction, but it was often noisy because of core expansion. Natural gamma-ray measurements and *P*-wave velocity measurements were not systematically made on cores from all holes and were not used for correlation. The GRAPE records were used to identify voids (values less than 1.03 g/cm^3), and GRAPE data from these intervals were not used. No allowance was made, however, for core expansion resulting from large gas voids, decompression, or dis-

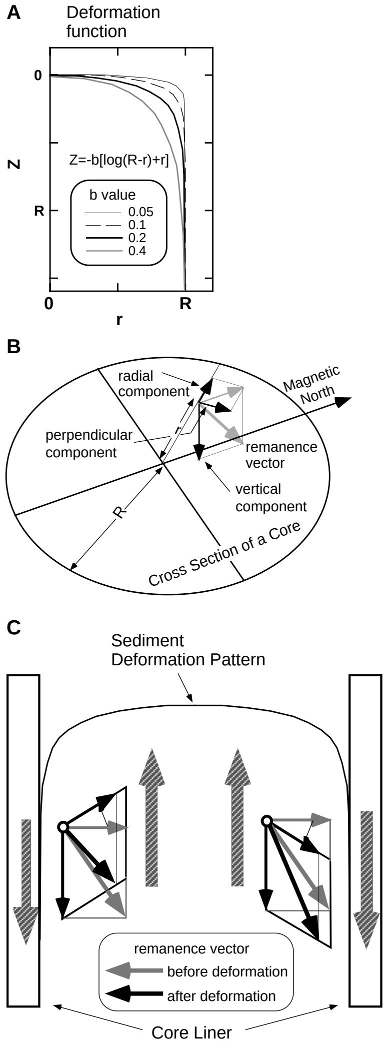

Figure 24. **A**. Deformation function that simulates sediment deformation patterns in a long core. **B**. Cross section of a core showing the remanence vector components. **C**. Schematic cross section of a split core illustrating the shear sense (large arrows with hatched pattern) sustained by the sediment in the core during APC coring and the rotation that the shear would induce for the radial component of the remanence vector.

tributed small gas voids. Within the Splicer computer program, cores can only be shifted as a whole, even where hiatuses are thought to exist within a core. More precise correlation between holes will necessarily be undertaken post-cruise, based on additional data.

The magnetic susceptibility, GRAPE, and color index (L*, a* and b*) records used to verify core overlap are shown on a composite depth scale in Figures 26 through 30 for Site 1056, 31 through 35 for Site 1057, 36 through 40 for Site 1058, and 41 through 45 for Site 1059. The data used for correlation for each hole (with composite depths) and the spliced data at each site are on CD-ROM (back pocket, this volume). Also shown on each figure is a spliced record created by combining selected intervals of the composite cores. Spliced magnetic susceptibility and color reflectance (L*, a*, b*) for Sites 1056 through 1059 are shown in Figures 46 through 49.

Site 1056

The magnetic susceptibility, lightness L*, and chromaticity parameters a* and b* appear well correlated among Holes 1056A, 1056B, 1056C, and 1056D. A complete record appears to have been recovered for the entire interval cored, although deeper than ~125 mcd (114 mbsf) the section was cored only twice and detailed correlations are difficult. As a result of core expansion, the composite depth scale is, on average, 15% larger than the drilled depths (mbsf), and it increases from ~5% larger in the upper 25 mcd to ~20% larger in 25 to 125 mcd (Fig. 50). Below 125 mcd, no additional offset is applied because of the difficulty in detailed correlation. GRAPE data were quite noisy at this site, but some of the larger features appear to correlate between sites, especially from ~40 to 80 mcd. The spliced records from this site utilize data primarily from Holes 1056B and 1056D. Hole 1056A correlates well with the other holes at this site, but is not plotted on the composite depth scale because it is only one core long.

Site 1057

The magnetic susceptibility, lightness L*, and chromaticity parameters a* and b* appear well correlated between holes, and a complete section is documented to the total depth cored (155 mcd [137 mbsf]). As a result of core expansion, the composite depth scale (mcd) is on average ~15% larger than drilled depths (mbsf) at this site, ranging from ~5% larger down to ~90 mbsf to >20% larger from 90 to 130 mbsf (Fig. 51). GRAPE bulk density is less well correlated between sites deeper in the cored interval, apparently because of cracks in the sediment, although some systematic changes, such as increases near 15 mcd and 55 mcd, appear correlated between cores. The spliced records from this site were created by combining portions of the composite records from Holes 1057B and 1057C in the upper part and Holes 1057A and 1057B in the lower part.

Site 1058

The magnetic susceptibility, lightness L*, and chromaticity parameters a* and b* appear well correlated between holes and demonstrate a complete section to the total depth cored (~180 mcd [~164 mbsf]). As a result of core expansion, the composite depth scale (mcd) is on average ~12% larger than drilled depths (mbsf) at this site, ranging from 5% larger at 40 mbsf to 10% larger from 40 to 90 mbsf, to ~20% larger from 90 to 150 mbsf (Fig. 52). GRAPE bulk density is less well correlated between sites, apparently because of cracks in the sediment, although some systematic changes appear correlated between cores from ~150 mcd. The spliced records from this site were created by combining portions of the composite records from Holes 1058A, 1058B, and 1058C.

Site 1059

The magnetic susceptibility, lightness L*, and chromaticity parameters a* and b* appear well correlated between holes, and demonstrate a complete section for the total interval cored (117 mcd [99 mbsf]). The composite depth scale (mcd) is on average ~20% larger than drilled depths (mbsf) at this site (Fig. 53). This larger-than-average expansion could be caused by lateral variability in unit thicknesses, which can only be accommodated by shifting cores down. For example, a 13-m, low-susceptibility zone from ~25 to 38 mcd in Hole 1059A is only represented by 8 m in Holes 1059B and 1059C, necessitating a 5-m gap in the composite section in those cores. Also, a high-susceptibility zone in Hole 1059A centered at about 50 mcd is much shorter than similar zones in Holes 1059B and 1059C, again necessitating a large gap between cores. This high-susceptibility zone also has a somewhat different character in Holes 1059B and 1059C, most likely because of iron sulfides in Hole 1059B. The spliced records from this site were created by combining data from Holes 1059A and 1059C.

Correlations Among Sites 1056, 1057, 1058, and 1059

Spliced records from all sites are plotted in Figure 26 of the "Carolina Slope" chapter on the back-pocket foldout (back pocket,

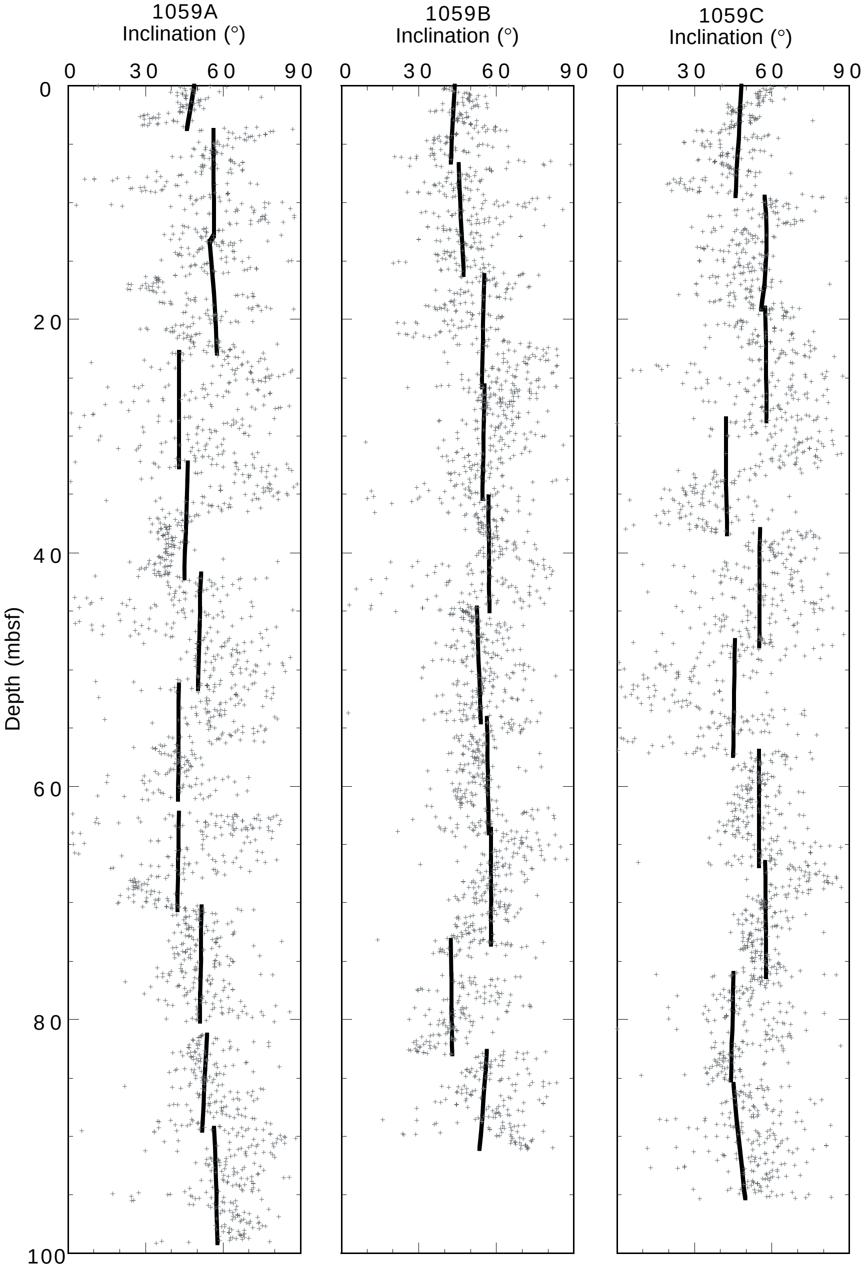

Figure 25. Comparisons between inclinations of long-core measurements (crosses) and calculated deflected inclinations (solid lines) at each core from Holes 1059A, 1059B, and 1059C.

this volume). Overall, the composited and spliced records for Sites 1056 through 1059 are very similar for magnetic susceptibility, lightness, and chromaticity, suggesting an overall similarity in sedimentation processes across this region. Exceptions to this occur at Sites 1056 and 1057 at depths where sediments have been disturbed by mass-transport deposits (see "Lithostratigraphy" section, this chapter). Correlation of individual peaks suggests that Site 1059 has the highest overall sedimentation accumulation rate, whereas Site 1057 has the lowest accumulation rate.

SEDIMENTATION AND MASS ACCUMULATION RATES

Site 1056

Average sedimentation rates are calculated between nannofossil datums in Hole 1056B (Fig. 54). The rates increase from the base of the section (~1.6 Ma) to ~1.0 Ma, and then decrease slightly between the reentrance of the medium-sized *Gephyrocapsa* and the top of the section. The average sedimentation rate (using the mbsf depth scale) in Hole 1056B is 9.6 cm/k.y.

For the last 900 k.y. the high-resolution sedimentation rates calculated using the magnetic susceptibility record (see "Explanatory Notes" chapter, this volume) vary from 5 to 27 cm/k.y., with an average value of 12 cm/k.y. (Table 22; Fig. 55). The maximum value is reached during marine isotope stages (MISs) 17 and 18. The sedimentation rates in interglacial MISs 5, 7, 9, and 11 never exceed 10 cm/k.y. and have an average value of 6 cm/k.y. The composite-depth scale increases the apparent length of the cored interval at this site by 10% to 20%, and thus the sedimentation rates calculated using the mcd scale are increased by the same factor. The top of the *P. lacunosa* range was observed at 82 mcd (see "Biostratigraphy" section, this chapter), which has a calculated age of 444 ka and is within MIS 12. This result is consistent with the published age (460 ka) for the top of the *P. lacunosa* range. The 16-k.y. difference between the calculated and published ages is likely caused by the technique used for the age/depth model (see "Explanatory Notes" chapter, this volume). The Brunhes/Matuyama boundary is found at 102 mcd (see "Paleomag-

Table 20. Composite depths and offsets for Sites 1056–1059.

Core, section	Depth (mbsf)	Offset (m)	Depth (mcd)
172-1056A-			
1H-1	0.00	0.60	0.60
172-1056B-			
1H-1	0.00	0.00	0.00
2H-1	3.60	0.30	3.90
3H-1	13.10	0.95	14.05
4H-1	22.60	2.15	24.75
5H-1	32.10	2.80	34.90
6H-1	41.60	5.95	47.55
7H-1	51.10	7.00	58.10
8H-1	60.60	8.75	69.35
9H-1	70.10	8.44	78.54
10H-1	79.60	12.14	91.74
11H-1	89.10	14.04	103.14
12H-1	98.60	16.09	114.69
13H-1	108.10	18.23	126.33
14H-1	117.60	19.37	136.97
15H-1	127.10	20.31	147.41
16H-1	136.60	20.31	156.91
17H-1	146.10	19.64	165.74
172-1056C-			
1H-1	0.00	0.16	0.16
2H-1	5.30	0.85	6.15
3H-1	14.80	1.45	16.25
4H-1	24.30	2.08	26.38
5H-1	33.80	3.91	37.71
6H-1	43.30	7.30	50.60
7H-1	52.80	7.40	60.20
8H-1	62.30	9.84	72.14
9H-1	71.80	11.21	83.01
10H-1	81.30	14.01	95.31
11H-1	90.80	16.54	107.34
12H-1	100.30	17.01	117.31
13H-1	109.80	18.47	128.27
14H-1	119.30	19.68	138.98
15H-1	126.30	20.39	146.69
16H-1	135.80	20.39	156.19
17H-1	145.30	20.39	165.69
172-1056D-			
1H-1	0.00	0.00	0.00
2H-1	7.80	0.25	8.05
3H-1	17.30	0.55	17.85
4H-1	26.80	1.45	28.25
5H-1	36.30	3.55	39.85
6H-1	45.80	6.20	52.00
7H-1	55.30	7.60	62.90
8H-1	64.80	7.75	72.55
9H-1	74.30	10.22	84.52
10H-1	83.80	13.12	96.92
11H-1	93.30	16.53	109.83
12H-1	102.80	16.99	119.79
13H-1	112.30	19.23	131.53
172-1057A-			
1H-1	0.00	0.00	0.00
2H-1	7.50	0.03	7.53
3H-1	17.00	0.76	17.76
4H-1	26.50	1.41	27.91
5H-1	36.00	2.81	38.81
6H-1	45.50	3.46	48.96
7H-1	55.00	4.71	59.71
8H-1	64.50	5.11	69.61
9H-1	74.00	7.11	81.11
10H-1	83.50	7.21	90.71
11H-1	93.00	8.72	101.72
12H-1	102.50	12.38	114.88
13H-1	112.00	13.95	125.95
14H-1	121.50	16.51	138.01
172-1057B-			
1H-1	0.00	0.04	0.04
2H-1	3.70	1.72	5.42
3H-1	13.20	2.16	15.36
4H-1	22.70	1.96	24.66
5H-1	32.20	2.76	34.96
6H-1	41.70	4.31	46.01
7H-1	51.20	5.56	56.76
8H-1	60.70	6.11	66.81
9H-1	70.20	6.89	77.09
10H-1	79.70	8.01	87.71
11H-1	89.20	9.56	98.76
12H-1	98.70	12.56	111.26
13H-1	108.20	13.76	121.96
14H-1	117.70	15.91	133.61
15H-1	127.20	17.56	144.76
172-1057C-			
1H-1	0.00	0.05	0.05
2H-1	7.00	-0.68	6.32
3H-1	16.50	0.47	16.97
4H-1	26.00	1.88	27.88
5H-1	35.50	2.61	38.11
6H-1	45.00	3.66	48.66
7H-1	54.50	4.44	58.94
8H-1	64.00	5.07	69.07
172-1058A-			
1H-1	0.00	1.39	1.39
2H-1	9.50	2.45	11.95
3H-1	19.00	2.85	21.85
4H-1	28.50	2.75	31.25
5H-1	38.00	4.20	42.20
6H-1	47.50	5.50	53.00
7H-1	57.00	6.19	63.19
8H-1	66.50	6.69	73.19
9H-1	76.00	7.67	83.67
10H-1	85.50	9.38	94.88
11H-1	95.00	9.78	104.78
12H-1	104.50	12.09	116.59
13H-1	114.00	13.37	127.37
14H-1	123.50	13.99	137.49
15H-1	133.00	16.27	149.27
16H-1	142.50	18.48	160.98
172-1058B-			
1H-1	0.00	0.00	0.00
2H-1	6.00	1.20	7.20
3H-1	15.50	1.50	17.00
4H-1	25.00	2.15	27.15
5H-1	34.50	2.90	37.40
6H-1	44.00	3.65	47.65
7H-1	53.50	4.75	58.25
8H-1	63.00	5.64	68.64
9H-1	72.50	6.43	78.93
10H-1	82.00	7.13	89.13
11H-1	91.50	7.90	99.40
12H-1	101.00	11.19	112.19
13H-1	110.50	13.04	123.54
14H-1	120.00	14.99	134.99
15H-1	129.50	15.59	145.09
16H-1	139.00	16.07	155.07
17H-1	148.50	15.39	163.89
172-1058C-			
1H-1	0.00	0.00	0.00
2H-1	2.50	1.89	4.39
3H-1	12.00	0.90	12.90
4H-1	21.50	1.40	22.90
5H-1	31.00	1.85	32.85
6H-1	40.50	2.85	43.35
7H-1	50.00	4.80	54.80
8H-1	59.50	5.85	65.35
9H-1	69.00	6.36	75.36
10H-1	78.50	7.07	85.57
11H-1	88.00	8.80	96.80
12H-1	97.50	11.09	108.59
13H-1	107.00	13.04	120.04
14H-1	116.50	13.39	129.89
15H-1	126.00	14.14	140.14
16H-1	135.50	15.63	151.13
17H-1	145.00	15.99	160.99
18H-1	154.50	15.99	170.49
172-1059A-			
1H-1	0.00	0.00	0.00
2H-1	3.80	2.07	5.87
3H-1	13.30	2.55	15.85
4H-1	22.80	3.03	25.83
5H-1	32.30	3.56	35.86
6H-1	41.80	10.00	51.80
7H-1	51.30	11.64	62.94
8H-1	60.80	13.48	74.28
9H-1	70.30	14.86	85.16
10H-1	79.80	17.02	96.82
11H-1	89.30	18.16	107.46
172-1059B-			
1H-1	0.00	0.32	0.32
2H-1	6.70	3.25	9.95
3H-1	16.20	3.89	20.09
4H-1	25.70	7.54	33.24
5H-1	35.20	7.90	43.10
6H-1	44.70	9.58	54.28
7H-1	54.20	12.50	66.70
8H-1	63.70	13.92	77.62
9H-1	73.20	15.46	88.66
10H-1	82.70	18.42	101.12
172-1059C-			
1H-1	0.00	1.34	1.34
2H-1	9.50	1.58	11.08
3H-1	19.00	2.35	21.35
4H-1	28.50	6.12	34.62
5H-1	38.00	6.76	44.76
6H-1	47.50	8.54	56.04
7H-1	57.00	10.26	67.26
8H-1	66.50	11.90	78.40
9H-1	76.00	14.60	90.60
10H-1	85.50	16.02	101.52

Table 21. Splice tie points for Sites 1056–1059.

Hole, section, interval (cm)	Depth (mbsf)	Depth (mcd)		Hole, section, interval (cm)	Depth (mbsf)	Depth (mcd)
Site 1056						
1056D-1H-5, 79.0	6.79	6.79	Tie	1056C-2H1, 64.0	5.94	6.79
1056C-2H-6, 20.0	13.00	13.85	Tie	1056D-2H-4, 128.0	13.60	13.85
1056D-2H6,134.0	16.64	16.89	Tie	1056B-3H-2,129.0	15.89	16.84
1056B-3H-6, 134.0	21.94	22.89	Tie	1056D-3H-4, 54.0	22.34	22.89
1056D-3H-7, 9.0	26.39	26.94	Tie	1056B-4H-2, 69.0	24.79	26.94
1056B-4H-7, 59.0	32.19	34.34	Tie	1056D-4H-5, 9.0	32.89	34.34
1056D-4H-7, 9.0	35.89	37.34	Tie	1056B-5H-3, 74.0	34.54	37.34
1056B-5H-8, 34.0	41.64	44.44	Tie	1056D-5H-4, 9.0	40.89	44.44
1056D-5H-7, 74.0	46.04	49.59	Tie	1056B-6H-2, 49.0	43.64	49.59
1056B-6H-7, 24.0	50.94	56.89	Tie	1056D-6H-4, 39.0	50.69	56.89
1056D-6H-6, 49.0	53.79	59.99	Tie	1056B-7H-2, 39.0	52.99	59.99
1056B-7H-7, 59.0	60.79	67.79	Tie	1056D-7H-4, 39.0	60.19	67.79
1056D-7H-7, 14.0	64.44	72.04	Tie	1056B-8H-2, 119.0	63.29	72.04
1056B-8H-6, 124.0	69.34	78.09	Tie	1056D-8H-5, 68.0	70.34	78.09
1056D-8H-8, 9.0	74.23	81.98	Tie	1056B-9H-3, 44.0	73.54	81.98
1056B-9H-7, 54.0	79.64	88.08	Tie	1056D-9H-3, 144.0	77.86	88.08
1056D-9H-7, 144.0	83.86	94.08	Tie	1056B-10H-3, 44.0	81.94	94.08
1056B-10H-7, 94.0	88.44	100.58	Tie	1056D-10H-3, 99.0	87.46	100.58
1056D-10H-7, 144.0	93.86	106.98	Tie	1056B-11H-3, 149.0	92.94	106.98
1056B-11H-7, 44.0	97.89	111.93	Tie	1056D-11H-3, 4.0	95.40	111.93
1056D-11H-7, 79.0	102.15	118.68	Tie	1056B-12H-4, 62.5	102.59	118.68
1056B-12H-7, 59.0	107.05	123.14	Tie	1056C-12H-4, 132.5	106.13	123.14
1056C-12H-6, 114.0	108.94	125.95	Tie	1056D-12H-5, 118.0	108.96	125.95
1056D-12H-8, 4.0	112.30	129.29	Tie	1056C-13H-1, 101.0	110.82	129.29
1056C-13H-6, 69.0	117.99	136.46	Tie	1056D-13H-4, 44.5	117.23	136.46
1056D-13H-7, 59.0	121.86	141.09	Tie	1056B-14H-3, 111.0	121.72	141.09
1056B-14H-7, 84.0	127.44	146.81	Tie	1056C-15H-1, 12.0	126.42	146.81
1056C-15H-7, 80.0	136.10	156.49	Tie	1056C-16H-1, 29.0	136.10	156.49
1056C-16H-7, 60.0	145.40	165.79	Tie	1056C-17H-1, 9.0	145.40	165.79
1056C-17H-7, 80.0	155.10	175.49				
Site 1057						
1057C-1H-5, 11.0	6.16	6.21	Tie	1057B-2H-1, 79.0	4.49	6.21
1057B-2H-6, 82.0	12.02	13.74	Tie	1057A-2H-5, 19.5	13.71	13.74
1057A-2H-7, 39.0	16.89	16.92	Tie	1057B-3H-2. 4.5	14.76	16.92
1057B-3H-7, 49.0	22.69	24.85	Tie	1057A-3H-5, 109.0	24.09	24.85
1057A-3H-6, 104.0	25.54	26.30	Tie	1057B-4H-2, 14.0	24.34	26.30
1057B-4H-7, 24.0	31.94	33.90	Tie	1057C-4H-5, 1.0	32.02	33.90
1057C-4H-7, 29.0	35.29	37.17	Tie	1057B-5H-2, 69.5	34.41	37.17
1057B-5H-6, 94.0	40.64	43.40	Tie	1057C-5H-4, 79.0	40.79	43.40
1057C-5H-6, 114.0	44.14	46.75	Tie	1057B-6H-1, 74.0	42.44	46.75
1057B-6H-7, 24.0	50.94	55.25	Tie	1057C-6H-5, 59.0	51.59	55.25
1057C-6H-6, 129.0	53.79	57.45	Tie	1057B-7H-1, 69.0	51.89	57.45
1057B-7H-6, 124.0	59.94	65.50	Tie	1057A-7H-4, 129.0	60.79	65.50
1057A-7H-7, 59.0	64.59	69.30	Tie	1057C-8H-1, 22.5	64.23	69.30
1057C-8H-8, 74.0	73.08	78.15	Tie	1057B-9H-2, 54.0	71.26	78.15
1057B-9H-7, 79.0	79.01	85.90	Tie	1057A-9H-4, 29.0	78.79	85.90
1057A-9H-7, 14.0	83.14	90.25	Tie	1057B-10H-2, 104.0	82.24	90.25
1057B-10H-7, 19.0	88.89	96.90	Tie	1057A-10H-5, 19.0	89.69	96.90
1057A-10H-6, 134.0	92.34	99.55	Tie	1057B-11H-1, 79.0	89.99	99.55
1057B-11H-6, 29.0	96.99	106.55	Tie	1057A-11H-4, 109.0	97.83	106.55
1057A-11H-8, 34.0	103.08	111.80	Tie	1057B-12H-1, 54.0	99.24	111.80
1057B-12H-7, 44.0	108.14	120.70	Tie	1057A-12H-5, 54.0	108.32	120.70
1057A-12H-8, 54.0	112.82	125.20	Tie	1057B-13H-3, 24.0	111.44	125.20
1057B-13H-5, 149.0	115.69	129.45	Tie	1057A-13H-3, 144.0	115.50	129.45
1057A-13H-8, 34.0	121.90	135.85	Tie	1057B-14H-2, 74.0	119.94	135.85
1057B-14H-7, 24.0	126.94	142.85	Tie	1057A-14H-5, 9.0	126.34	142.85
1057A-14H-8, 49.0	131.24	147.75	Tie	1057B-15H-2, 149.0	130.19	147.75
1057B-15H-7, 84.0	137.04	154.60				
Site 1058						
1058B-1H4, 19.0	4.69	4.69	Tie	1058A-1H-3, 29.0	3.30	4.69
1058A-1H-4, 112.0	5.62	7.01	Tie	1058C-2H-2, 111.0	5.12	7.01
1058C-2H-6, 134.0	11.34	13.23	Tie	1058B-2H-5, 2.5	12.30	13.23
1058B-2H-5, 134.0	13.34	14.54	Tie	1058A-2H-2, 109.0	12.09	14.54
1058A-2H-6, 124.0	18.24	20.69	Tie	1058B-3H-3, 69.0	19.19	20.69
1058B-3H-6, 49.0	23.49	24.99	Tie	1058C-4H-2, 59.0	23.59	24.99
1058C-4H-7, 29.0	30.79	32.19	Tie	1058A-4H-1, 94.0	29.44	32.19
1058A-4H-7, 24.0	37.74	40.49	Tie	1058B-5H-3, 9.0	37.59	40.49
1058B-5H-5, 69.0	41.19	44.09	Tie	1058A-5H-2, 39.0	39.89	44.09
1058A-5H-7, 44.0	47.44	51.64	Tie	1058B-6H-3, 99.0	47.99	51.64
1058B-6H-6, 4.0	51.54	55.19	Tie	1058C-7H-1, 39.0	50.39	55.19
1058C-7H-5, 134.0	57.34	62.14	Tie	1058B-7H-3, 89.0	57.39	62.14
1058B-7H-6, 24.0	61.24	65.99	Tie	1058C-8H-1, 64.0	60.14	65.99
1058C-8H-4, 79.0	64.79	70.64	Tie	1058B-8H-2, 48.0	65.00	70.64
1058B-8H-5, 84.0	69.84	75.48	Tie	1058A-8H-2, 79.0	68.79	75.48
1058A-8H-5, 94.0	73.44	80.13	Tie	1058B-9H-1, 118.0	73.70	80.13
1058B-9H-6, 119.0	81.19	87.62	Tie	1058C-10H-3, 11.0	80.55	87.62
1058C-10H-7, 89.0	86.35	93.42	Tie	1058B-10H-3, 129.0	86.29	93.42
1058B-10H-6, 94.0	90.44	97.57	Tie	1058C-11H-1, 76.0	88.77	97.57
1058C-11H-6, 84.0	96.34	105.14	Tie	1058A-11H-1, 34.5	95.36	105.14
1058A-11H-7, 9.0	103.30	113.08	Tie	1058C-12H-4, 87.5	101.99	113.08
1058C-12H-6, 99.0	105.10	116.19	Tie	1058B-12H-3, 108.0	105.00	116.19
1058B-12H-6, 99.0	109.39	120.58	Tie	1058A-12H-4, 59.0	108.49	120.58
1058A-12H-7, 99.0	113.39	125.48	Tie	1058B-13H-2, 44.0	112.44	125.48
1058B-13H-6, 109.0	119.09	132.13	Tie	1058A-13H-4, 119.0	118.76	132.13
1058A-13H-7, 29.0	122.36	135.73	Tie	1058B-14H-1, 74.0	120.74	135.73
1058B-14H-6, 144.0	128.94	143.93	Tie	1058A-14H-6, 4.0	129.94	143.93
1058A-14H-8, 79.0	133.69	147.68	Tie	1058B-15H-2, 109.0	132.09	147.68
1058B-15H-6, 119.0	138.19	153.78	Tie	1058C-16H-3, 89.0	138.15	153.78
1058C-16H-7, 4.0	143.30	158.93	Tie	1058B-16H-3, 89.0	142.86	158.93

Table 21 (continued).

Hole, section, interval (cm)	Depth (mbsf)	Depth (mcd)		Hole, section, interval (cm)	Depth (mbsf)	Depth (mcd)
1058B-16H-6, 74.0	147.21	163.28	Tie	1058A-16H-3, 54.0	144.80	163.28
1058A-16H-6, 84.0	149.60	168.08	Tie	1058B-17H-3, 119.0	152.69	168.08
1058B-17H-6, 104.0	157.04	172.43	Tie	1058C-18H-2, 44.0	156.44	172.43
1058C-18H-7, 74.0	164.24	180.23				
Site 1059						
1059A-1H-3, 14.0	3.14	3.14	Tie	1059C-1H-2, 29.0	1.80	3.14
1059C-1H-4, 68.0	5.18	6.52	Tie	1059A-2H-1, 64.5	4.45	6.52
1059A-2H-6, 68.0	11.98	14.05	Tie	1059C-2H-2, 147.0	12.47	14.05
1059C-2H-5, 132.0	16.82	18.40	Tie	1059A-3H-2, 104.5	15.85	18.40
1059A-3H-6, 86.0	21.66	24.21	Tie	1059C-3H-2, 136.0	21.86	24.21
1059C-3H-5, 36.0	25.36	27.71	Tie	1059A-4H-2, 38.0	24.68	27.71
1059A-4H-7, 128.0	31.80	34.83	Tie	1059C-4H-1, 60.0	29.10	35.22
1059C-4H-6, 128.0	37.28	43.40	Tie	1059B-5H-1, 29.0	35.50	43.40
1059B-5H-3, 132.0	39.52	47.42	Tie	1059C-5H-2, 143.0	40.88	47.64
1059C-5H-6, 28.0	45.78	52.54	Tie	1059A-6H-1, 73.0	42.54	52.54
1059A-6H-6, 36.0	49.66	59.66	Tie	1059C-6H-3, 61.0	51.12	59.66
1059C-6H-6, 72.0	55.72	64.26	Tie	1059A-7H-1, 130.0	52.60	64.24
1059A-7H-6, 68.0	59.48	71.12	Tie	1059C-7H-3, 85.0	60.86	71.12
1059C-7H-6, 84.0	65.34	75.60	Tie	1059A-8H-1, 132.0	62.12	75.60
1059A-8H-7, 46.0	69.96	83.44	Tie	1059C-8H-4, 84.0	71.84	83.74
1059C-8H-6, 40.0	74.40	86.30	Tie	1059A-9H-1, 117.0	71.48	86.34
1059A-9H-6, 108.0	78.88	93.74	Tie	1059C-9H-3, 13.0	79.10	93.70
1059C-9H-7, 104.0	84.77	99.37	Tie	1059A-10H-2, 103.5	82.35	99.37
1059A-10H-4, 84.0	85.14	102.16	Tie	1059C-10H-1, 64.0	86.14	102.16
1059C-10H-6, 16.0	93.16	109.18	Tie	1059A-11H-2, 19.5	91.02	109.18
1059A-11H-CC, 23.0	99.39	117.55				

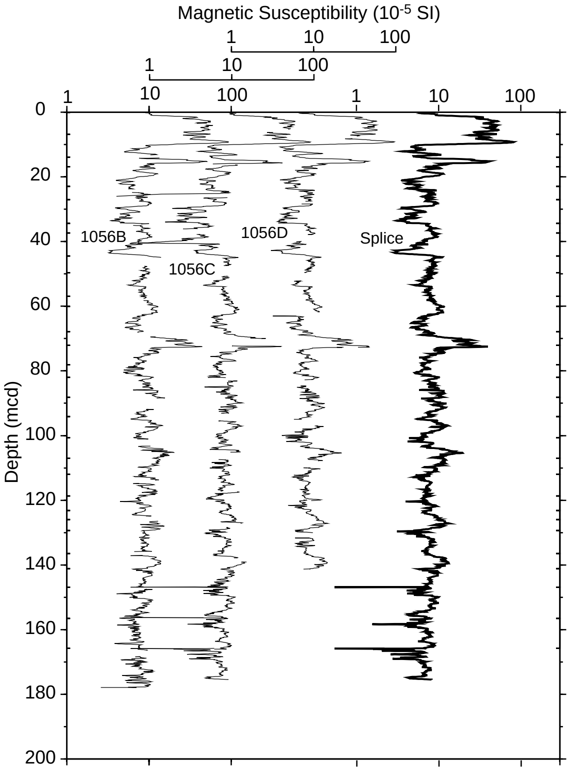

Figure 26. Smoothed magnetic susceptibility data (31-cm Gaussian window; logarithmic scale) for Site 1056 on the mcd scale for Holes 1056B through 1056D and the spliced record.

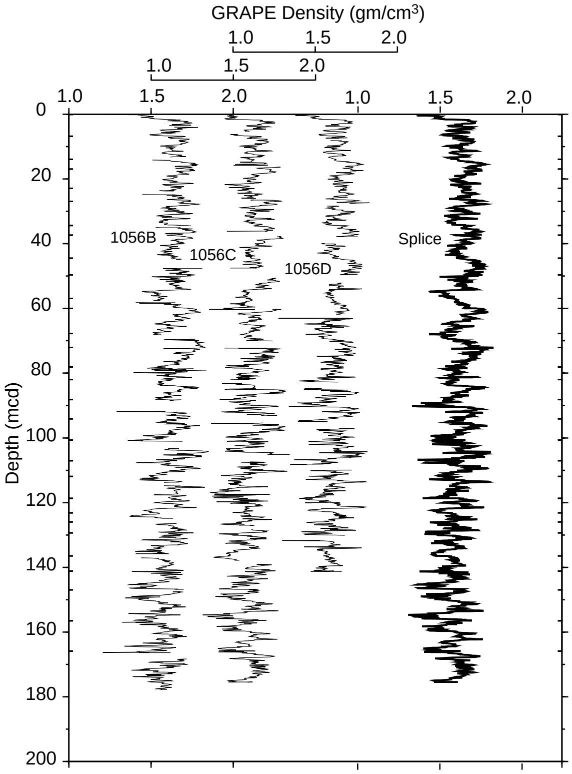

Figure 27. Smoothed GRAPE data (31-cm Gaussian window) for Site 1056 on the mcd scale for Holes 1056B through 1056D and the spliced record.

netism" section, this chapter), which corresponds to its published age of 780 ka, and apparently is in the transition between MISs 20 and 19 (Fig. 55).

Carbonate accumulation rates vary from 0.3 to 15 g/cm^2/k.y., with an average value of about 5 g/cm^2/k.y. (Tables 23, 24; Fig. 56). Organic carbon fluxes range from 0.01 to 0.21 g/cm^2/k.y., averaging 0.09 g/cm^2/k.y. Calcium carbonate and organic carbon accumulation rates show significant variations from MIS 16 to MIS 2, with values fluctuating from 5 to 0.1 g/cm^2/k.y., respectively. From MIS 20 to MIS 17, carbonate and organic carbon fluxes increase greatly, ranging from 15 to 0.21 g/cm^2/k.y., respectively. This pattern is associated with a general increase in sedimentation rates at that time. No consistent glacial–interglacial trends in organic carbon and calcium carbonate fluxes are observed in the present data. From ~1.6 to ~0.8

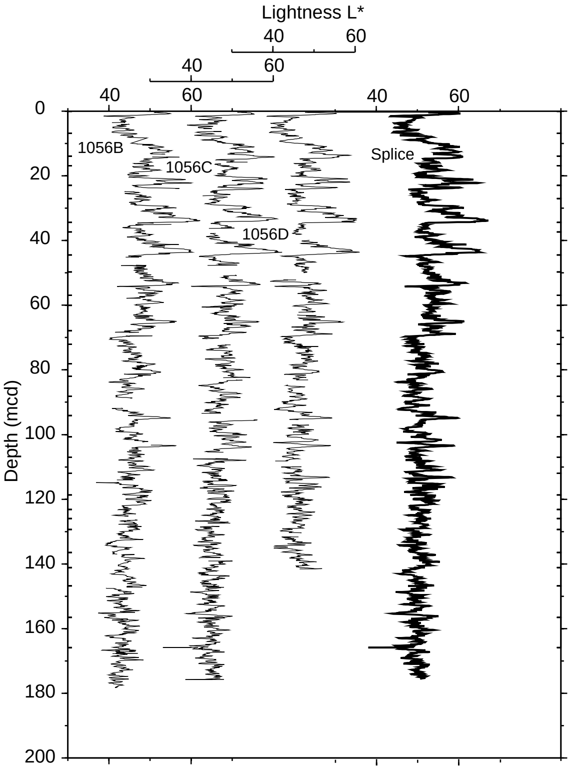

Figure 28. Smoothed lightness (L*) data (31-cm Gaussian window) from Site 1056 on the mcd scale for Holes 1056B through 1056D and the spliced record.

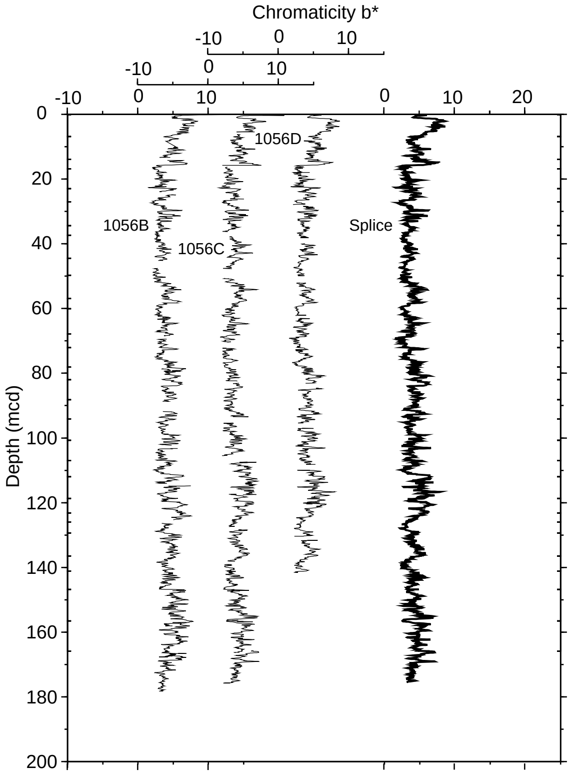

Figure 30. Smoothed chromaticity (b*) data (31 cm-Gaussian window) from Site 1056 on the mcd scale for Holes 1056B through 1056D and the spliced record.

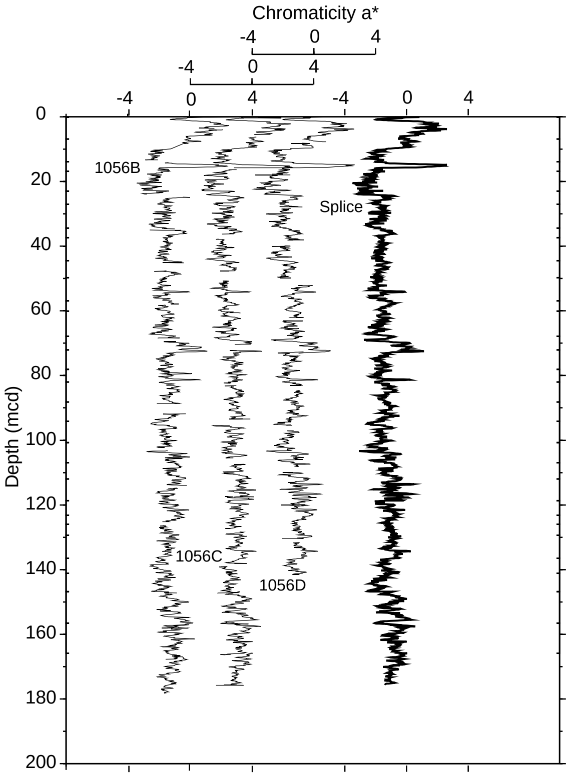

Figure 29. Smoothed chromaticity (a*) data (31-cm Gaussian window) from Site 1056 on the mcd scale for Holes 1056B through 1056D and the spliced record.

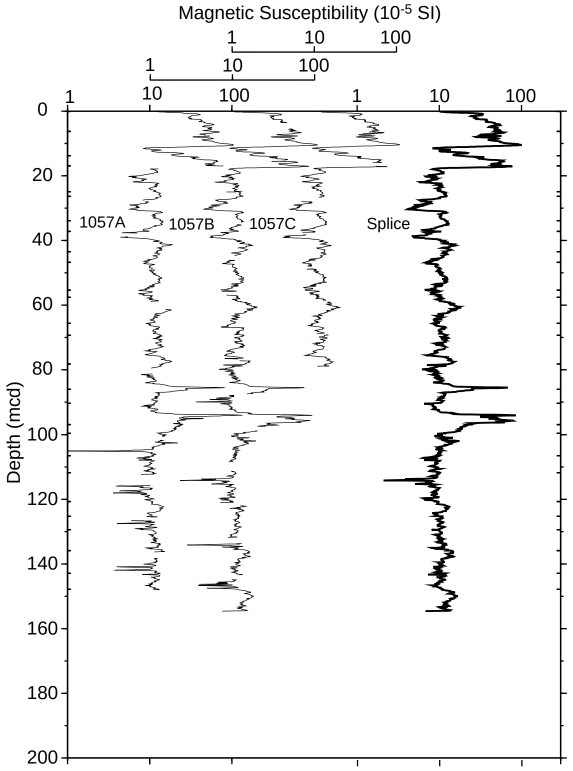

Figure 31. Smoothed magnetic susceptibility data (31-cm Gaussian window, logarithmic scale) from Site 1057 on the mcd scale for Holes 1057A through 1057C and the spliced record.

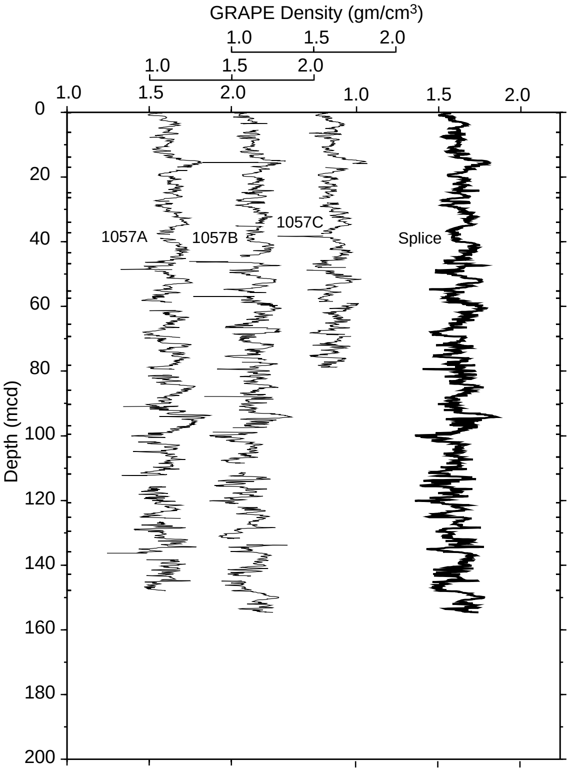

Figure 32. Smoothed GRAPE data (31-cm Gaussian window) from Site 1057 on the mcd scale for Holes 1057A through 1057C and the spliced record.

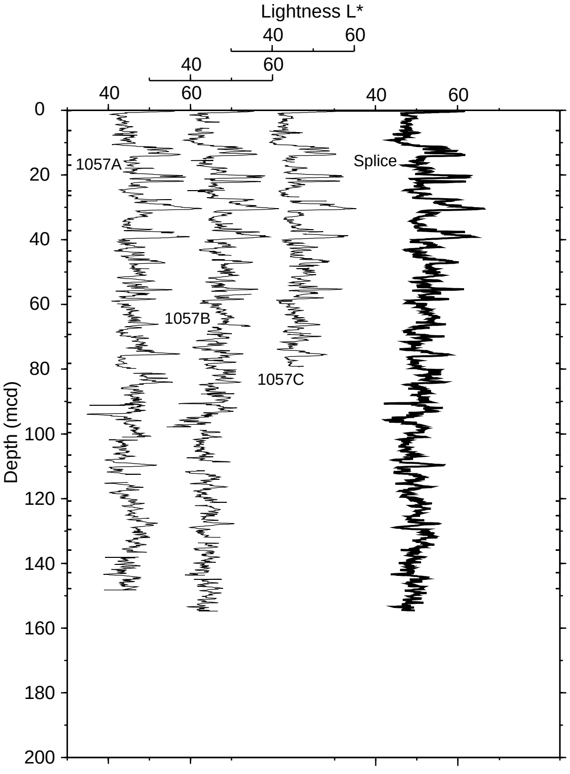

Figure 33. Smoothed lightness (L*) data (31-cm Gaussian window) from Site 1057 on the mcd scale for Holes 1057A through 1057C and the spliced record.

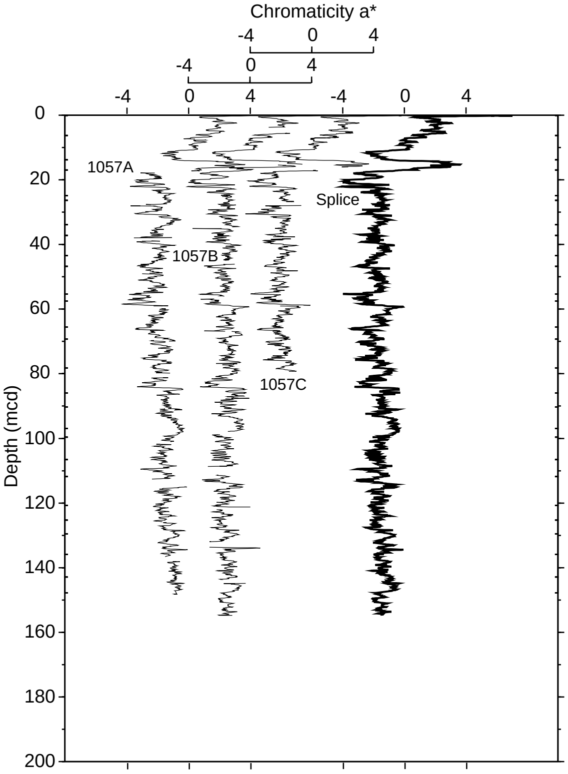

Figure 34. Smoothed chromaticity (a*) data (31-cm Gaussian window) from Site 1057 on the mcd scale for Holes 1057A through 1057C and the spliced record.

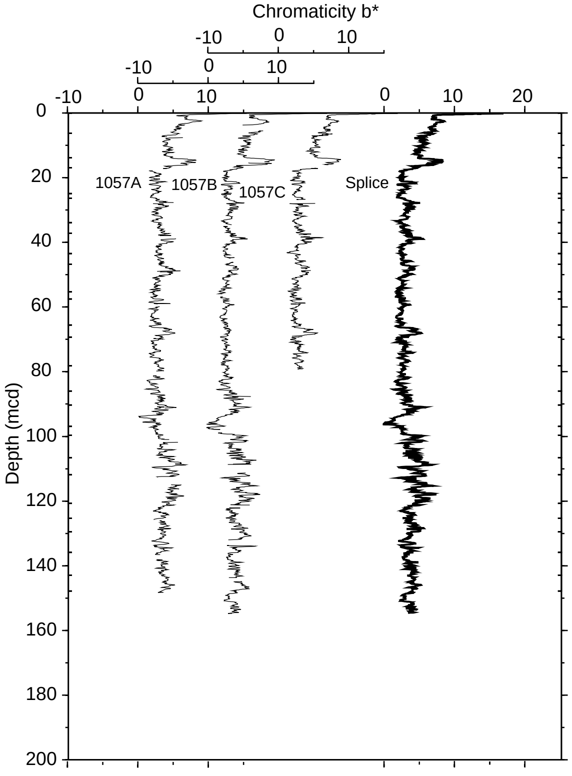

Figure 35. Smoothed chromaticity (b*) data (31-cm Gaussian window) from Site 1057 on the mcd scale for Holes 1057A through 1057C and the spliced record.

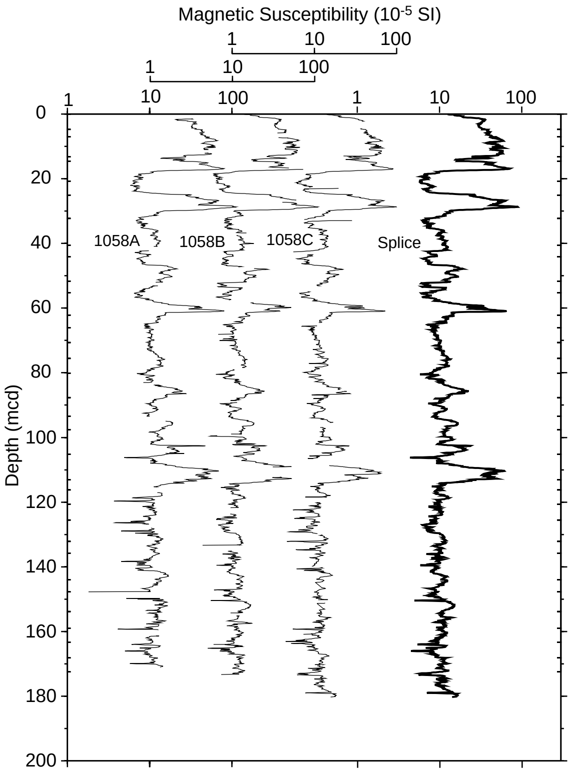

Figure 36. Smoothed magnetic susceptibility data (31-cm Gaussian window, logarithmic scale) from Site 1058 on the mcd scale for Holes 1058A through 1058C and the spliced record.

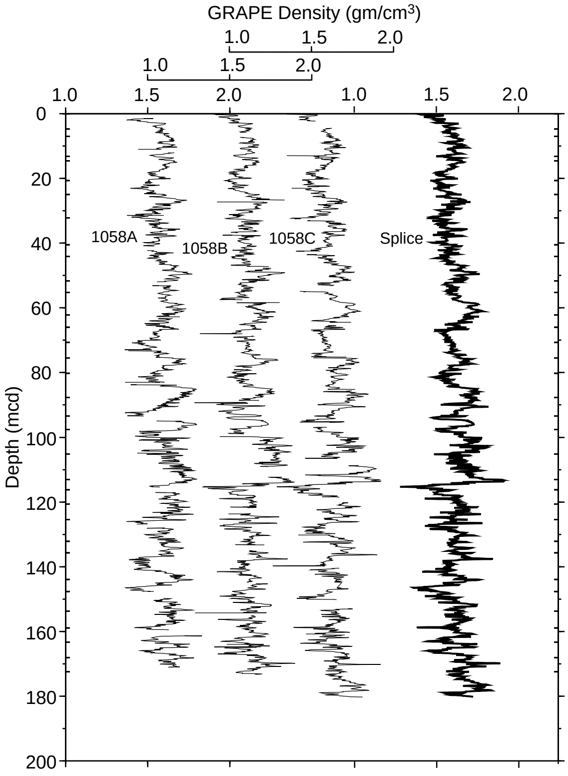

Figure 37. Smoothed GRAPE data (31-cm Gaussian window) from Site 1058 on the mcd scale for Holes 1058A through 1058C and the spliced record.

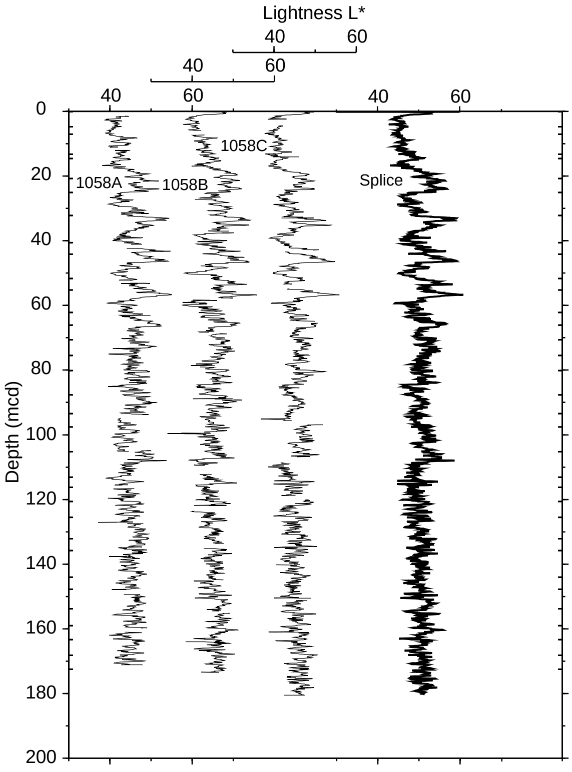

Figure 38. Smoothed lightness (L*) data (31-cm Gaussian window) from Site 1058 on the mcd scale for Holes 1058A through 1058C and the spliced record.

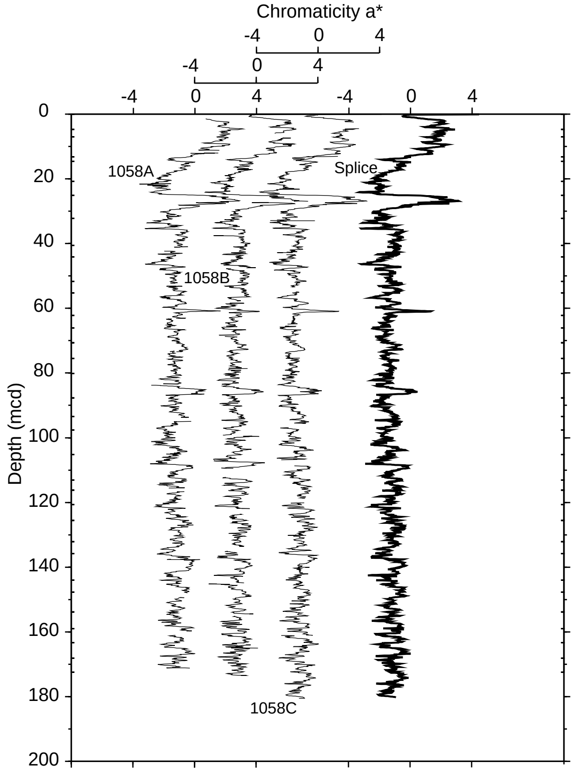

Figure 39. Smoothed chromaticity (a*) data (31-cm Gaussian window) from Site 1058 on the mcd scale for Holes 1058A through 1058C and the spliced record.

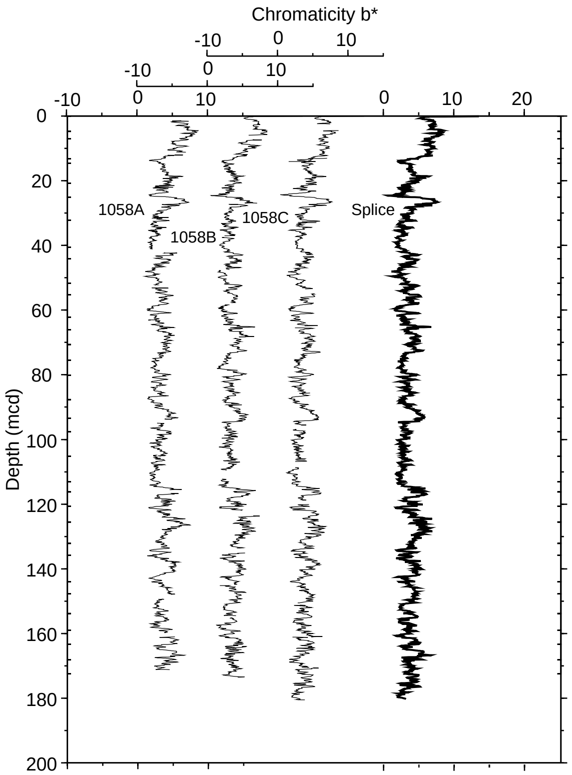

Figure 40. Smoothed chromaticity (b*) data (31-cm Gaussian window) from Site 1058 on the mcd scale for Holes 1058A through 1058C and the spliced record.

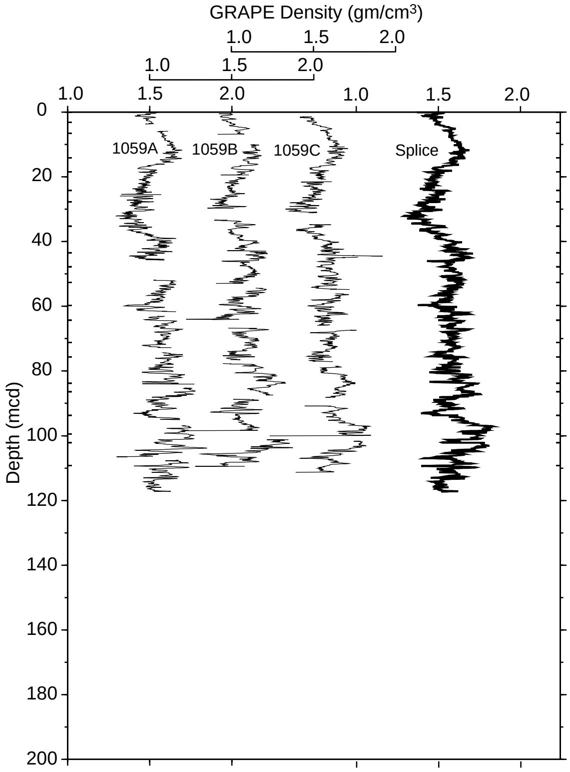

Figure 42. Smoothed GRAPE data (31-cm Gaussian window) from Site 1059 on the mcd scale for Holes 1059A through 1059C and the spliced record.

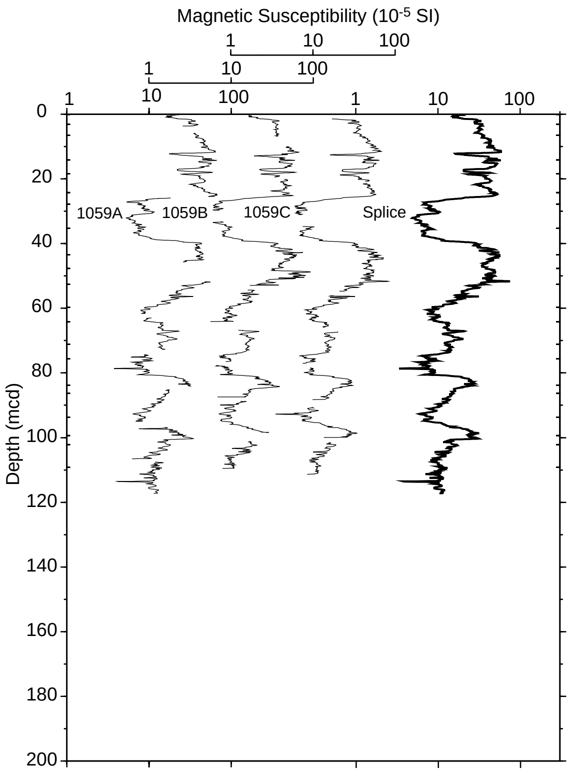

Figure 41. Smoothed magnetic susceptibility data (31-cm Gaussian window, logarithmic scale) from Site 1059 on the mcd scale for Holes 1059A through 1059C and the spliced record.

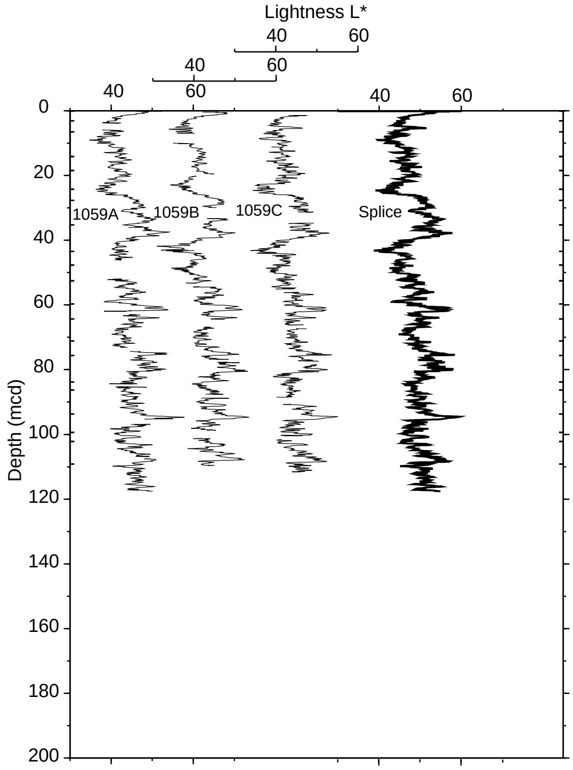

Figure 43. Smoothed lightness (L*) data (31-cm Gaussian window) from Site 1059 on the mcd scale for Holes 1059A through 1059C and the spliced record.

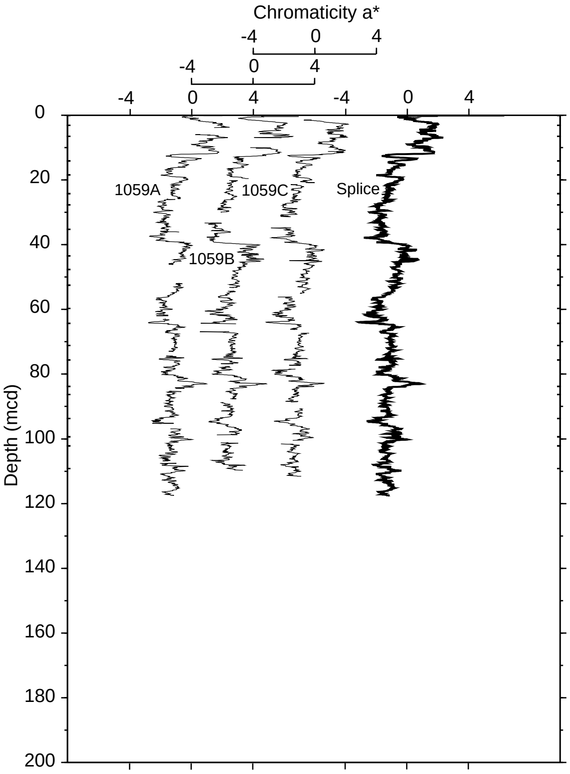

Figure 44. Smoothed chromaticity (a*) data (31-cm Gaussian window) from Site 1059 on the mcd scale for Holes 1059A through 1059C and the spliced record.

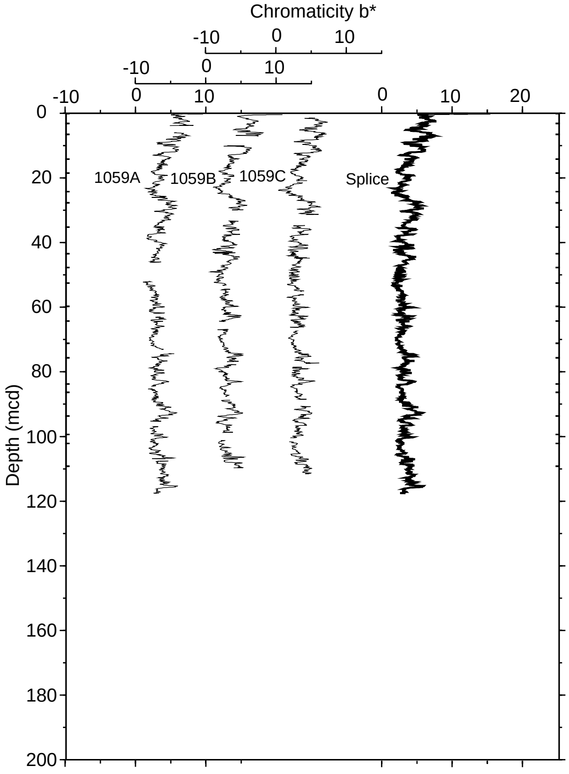

Figure 45. Smoothed chromaticity (b*) data (31-cm Gaussian window) from Site 1059 on the mcd scale for Holes 1059A through 1059C and the spliced record.

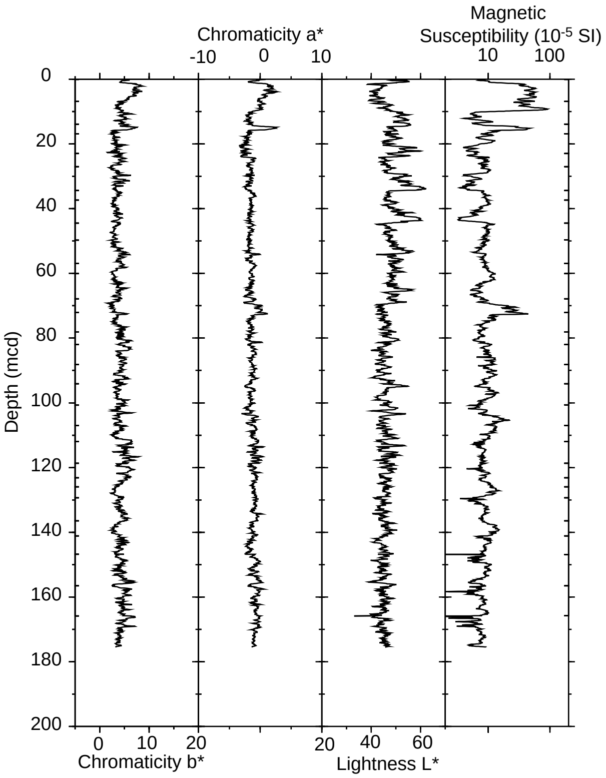

Figure 46. Summary of spliced records for Site 1056.

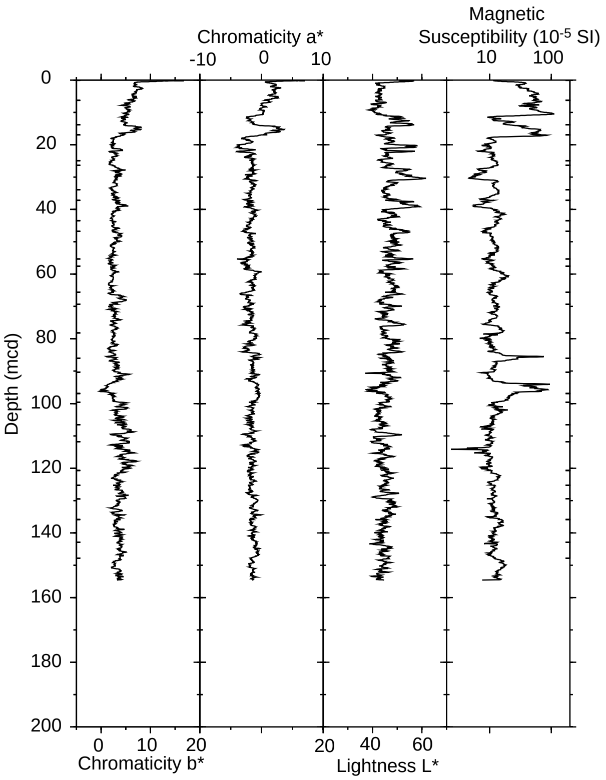

Figure 47. Summary of spliced records for Site 1057.

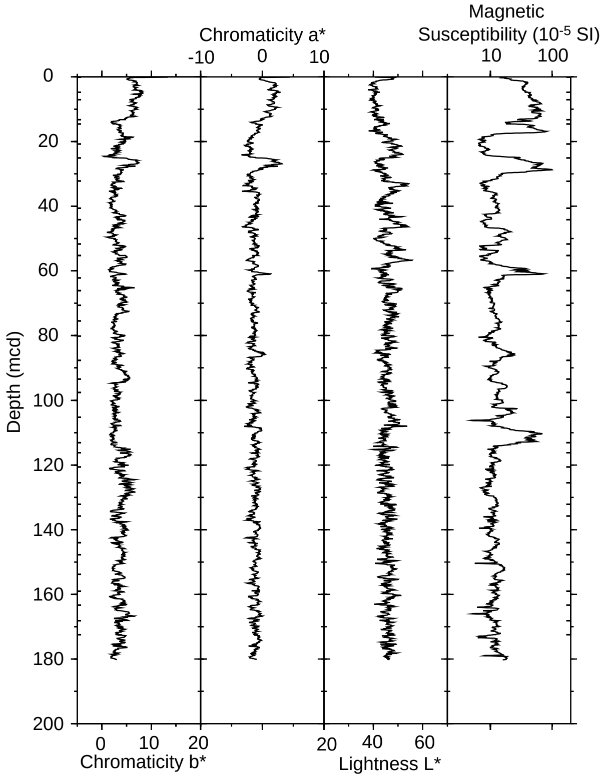

Figure 48. Summary of spliced records for Site 1058.

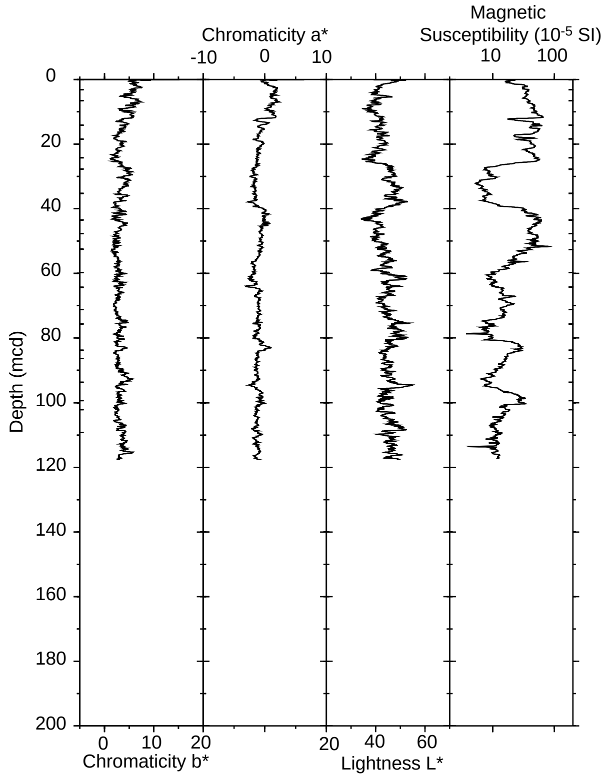

Figure 49. Summary of spliced records for Site 1059.

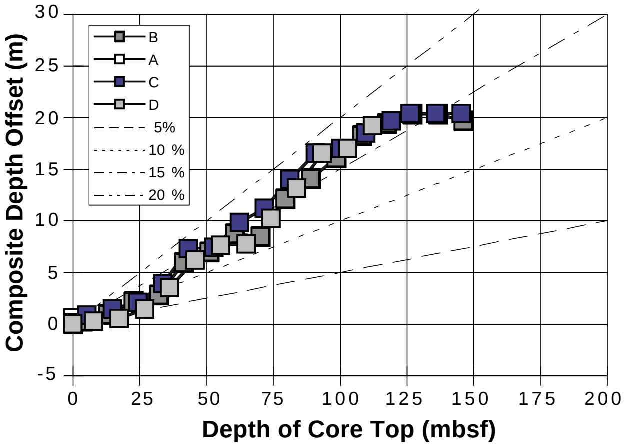

Figure 50. Composite depth offsets vs. core-top depth (mbsf) for Site 1056.

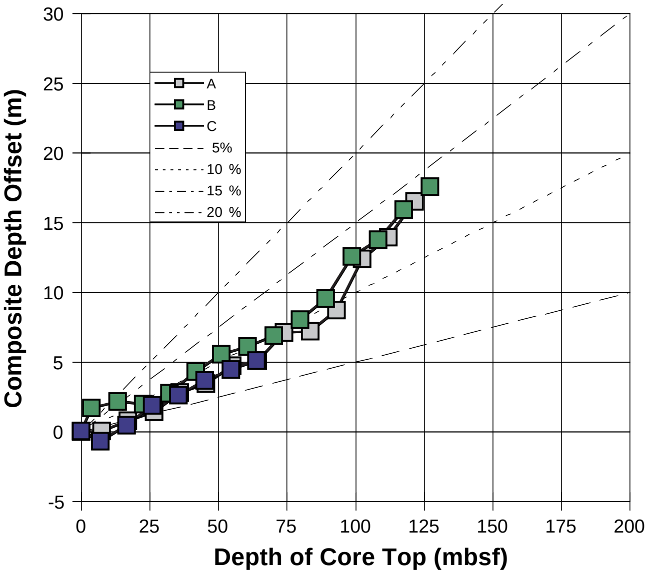

Figure 51. Composite depth offsets vs. core-top depth (mbsf) for Site 1057.

Ma, calcium carbonate and organic carbon fluxes show little variation.

Site 1057

Average sedimentation rates were calculated between two nannofossil datums and the top of the section in Hole 1057A (Fig. 57). The bottom of the cored section is difficult to date precisely, but appears to be ~1.3 Ma. The base and the top of the Jaramillo Subchron (1.07 and 0.99 Ma, respectively) are not identified with enough accuracy to be used as chronological tie points. The average sedimentation rate determined by using the biostratigraphic markers is 10.1 cm/k.y. in this hole (using the mbsf depth scale).

During the last 900 k.y., high-resolution sedimentation rates determined using the magnetic susceptibility record varied from 5 to 19 cm/k.y., with an average of 12 cm/k.y., comparable to the average calculated at Site 1056. The maximum value of 19 cm/k.y. is reached during glacial MIS 10. As in Site 1056, interglacial MISs 5, 7, 9, and 11 have an average sedimentation-rate value of 6 cm/k.y., lower by 2 to 6 cm/k.y. than the adjacent glacial MISs. The top of the *P. lacunosa* range is calculated to be at 441 ka and within MIS 12. As at Site

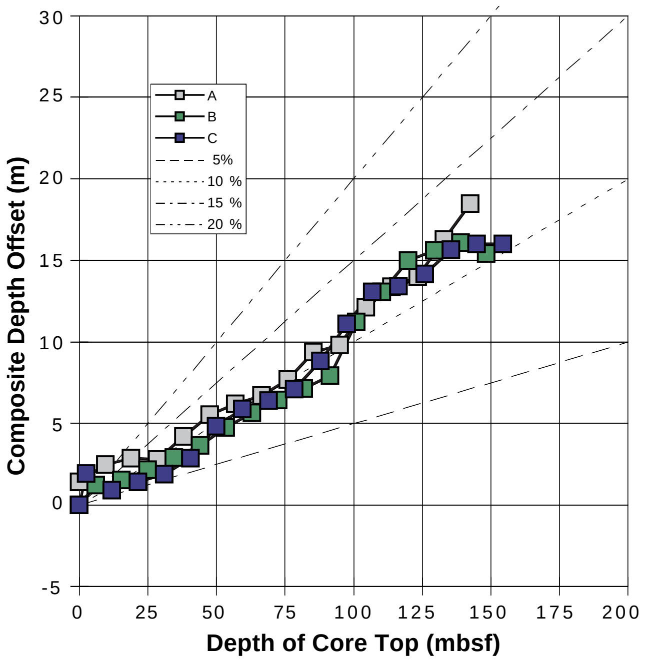

Figure 52. Composite depth offsets vs. core-top depth (mbsf) for Site 1058.

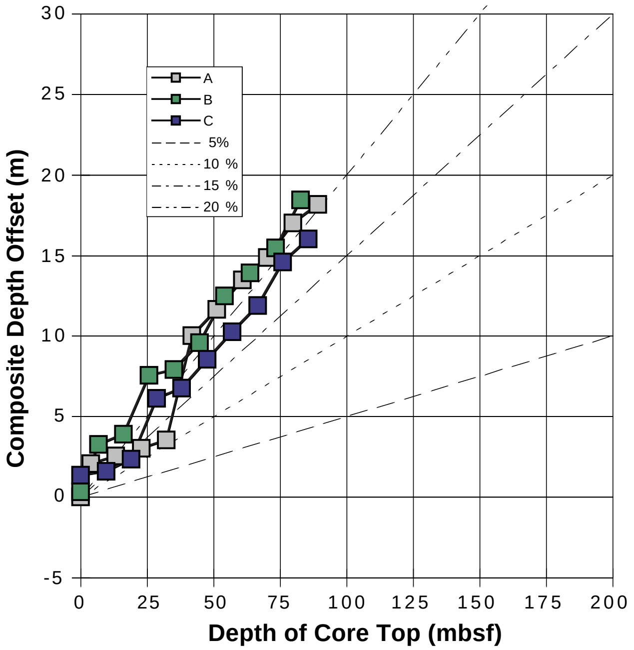

Figure 53. Composite depth offsets vs. core-top depth (mbsf) for Site 1059.

1056, the slight discrepancy between the published and calculated ages is likely caused by the technique used to calculate the ages. The age of the Brunhes/Matuyama boundary is calculated to be 807 ka (86 mcd) and, within MIS 20, almost 30 k.y. older than expected (Tables 25, 26; Fig. 58). This age difference may be caused by the overprint, which was not completely removed from the magnetic signal and thus increased difficulty in precise identification of the Brunhes/Matuyama boundary. However, the placement of the Brunhes/Matuyama boundary agrees well with the biostratigraphic age model when only the nannoplankton datums (top of the range of *P. lacunosa* and the reentrance of medium-sized *Gephyrocapsa*; see "Biostratigraphy" section, this chapter) are considered but not when the FO of the foraminifer marker *Truncorotalia crassaformis hessi*, (750 ka) is also considered. The inflation of the sedimentation rates at this site, caused by using the mcd scale, averages between 8% and 15%.

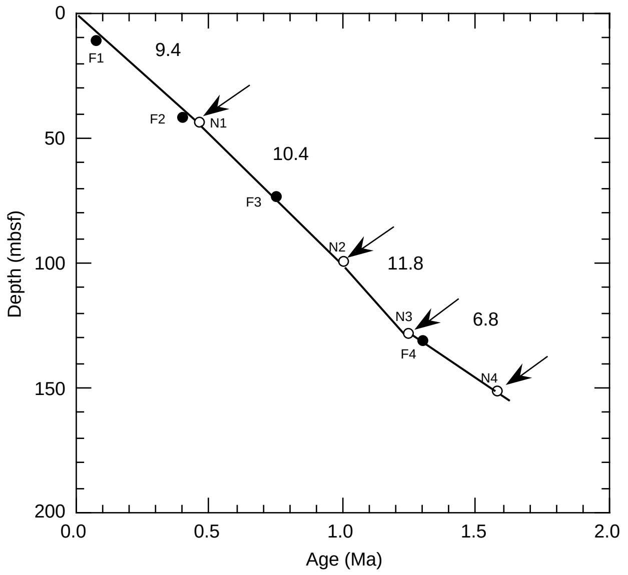

Figure 54. Age/depth plots for Hole 1056B based on biostratigraphic tie points (arrows). Solid circles = planktonic foraminifer markers, open circles = nannoplankton markers. See Table 3 in the "Biostratigraphy" section (this chapter) to associate species names with the labels used in this figure. Sedimentation rates are expressed in centimeters per thousand years.

Table 22. Age-depth relationship at Site 1056.

Depth (mcd)	Age (ka)	Average sedimentation rate (cm/k.y.)
0.14	10	15.83
9.64	70	15.83
14.59	128	8.53
20.79	188	10.33
24.04	244	5.80
31.19	302	12.33
34.39	338	8.89
40.14	364	22.12
44.29	426	6.69
50.04	476	11.50
69.34	620	13.40
75.29	672	11.44
99.43	762	26.82
103.78	788	16.73
111.28	864	9.87
113.03	900	4.86

Calcium carbonate and organic carbon accumulation rates are presented in Tables 27 and 28 and Figure 59. Carbonate accumulation rates vary from 1.9 to 8.7 g/cm^2/k.y. at this site, with an average value of about 3.5 g/cm^2/k.y., significantly lower than at the previous site. Organic carbon fluxes range from 0.02 to 0.15 g/cm^2/k.y., averaging 0.08 g/cm^2/k.y. Although the two sites have comparable organic carbon fluxes, calcium carbonate accumulation appears to be significantly lower at Site 1057 than at Site 1056.

The highest carbonate fluxes are observed during interglacials: the Holocene (~8 g/cm^2/k.y.), MIS 11 (~5 g/cm^2/k.y.), MIS 15 (~5.5 g/cm^2/k.y.), and early MIS 19 (~8 g/cm^2/k.y.). Organic carbon accumulation rates may be higher in glacial periods, such as MISs 10, 18, and 20, but the time resolution is not sufficient to confirm the existence of this trend. From ~0.84 to ~1.6 Ma, organic carbon fluxes were significantly higher, averaging 0.12 g/cm^2/k.y.

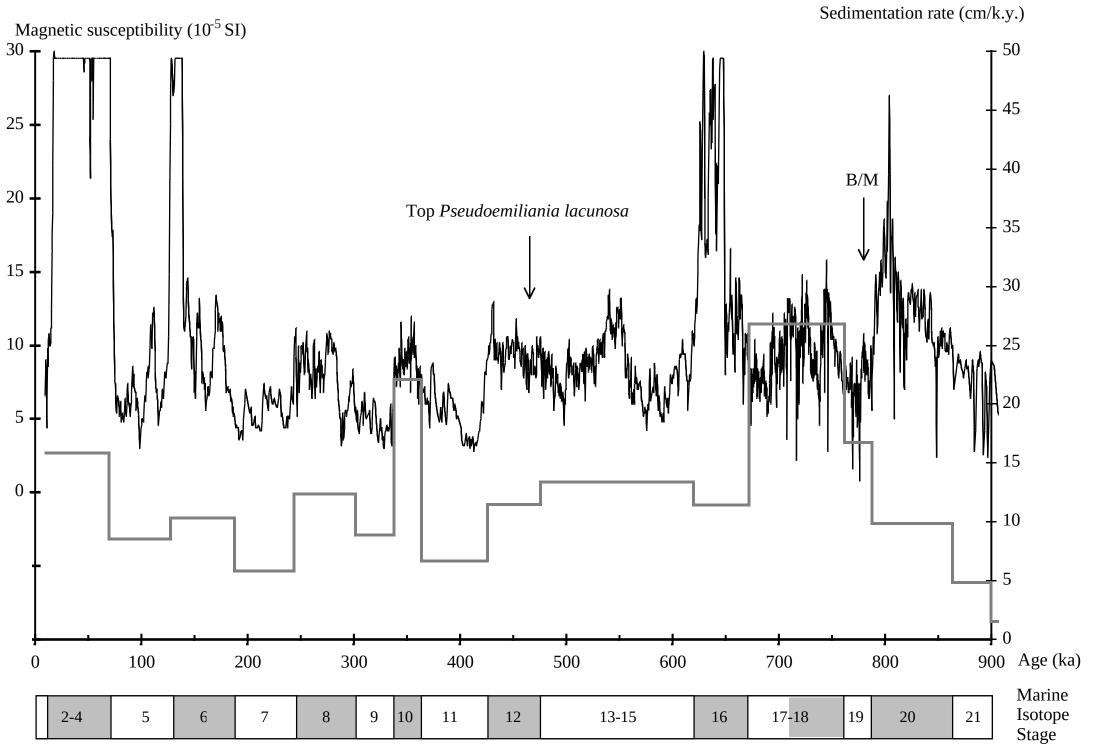

Figure 55. Magnetic susceptibility record (left scale, thin curve) and sedimentation rate (right scale, thick stepwise curve; composite record) of Site 1056 (32°29′N, 76°19′W, 2160 m). MISs are labeled, with glacial ones shaded. B/M = Brunhes/Matuyama boundary.

Site 1058

A nearly constant sedimentation rate is calculated between two nannofossil datums and the top of the section in Hole 1058A (Fig. 60). The base of the Brunhes/Matuyama boundary and the top and base of the Jaramillo Subchron fall directly on the age/depth line drawn between the biostratigraphic markers. The average sedimentation rate in this hole is 11.4 cm/k.y.

During the last 900 k.y., high-resolution sedimentation rates calculated from the magnetic susceptibility record from this site vary from 4 to 28 cm/k.y., with an average value of 13 cm/k.y. These values are comparable to those obtained at Sites 1056 and 1057, although the general trend of the sedimentation rates at the previous sites is different (Tables 29, 30; Fig. 61). Between 600 and 70 ka, glacial and interglacial MISs have comparable values of ~12 cm/k.y. The maximum value of 28 cm/k.y. is calculated in MIS 4 through MIS 2 during the past 70 k.y. This interval corresponds to the uppermost part of sedimentary Unit I, which consists largely of clay minerals, as described in the "Lithostratigraphy" section (this chapter). The age of the top of the range of *P. lacunosa* is calculated to be 442 ka within MIS 12, and the Brunhes/Matuyama boundary is calculated to be 781 ka. The inflation of the sedimentation-rate values at this site, caused by the use of the mcd scale, is between 6% and 12%.

Calcium carbonate and organic carbon accumulation rates are presented in Tables 31 and 32 and Figure 62. Carbonate accumulation rates vary from 0.9 to 7.7 g/cm^2/k.y., and average 4.5 g/cm^2/k.y. Organic carbon fluxes range from 0.03 to 0.17 g/cm^2/k.y., averaging 0.08 g/cm^2/k.y. Organic carbon and inorganic carbon fluxes are thus comparable to those calculated at Site 1057, and also show the same temporal variability. Carbonate fluxes are generally higher during interglacials, especially in MIS 11 and MIS 19, where they reach their maximum value of ~7.7 g/cm^2/k.y. Organic carbon accumulation rates do not seem to have such a cyclical feature, but the time resolution is not sufficient to see any pattern.

A general shift in organic carbon and calcium carbonate fluxes seems to occur below MIS 22. Carbonate fluxes in this interval are lower on average and do not show any cyclical fluctuations. Organic carbon fluxes show a marked increase, comparable to the one observed at Site 1057 during the same time interval. This increase cannot be related to higher sedimentation rates, because biostratigraphic data indicate they remain constant during this period (see also "Biostratigraphy" section, this chapter). This increase in organic carbon flux may be indicative of higher organic matter supply from terrigenous or marine sources, as suggested by the increased organic carbon concentrations.

Site 1059

An average sedimentation rate for Hole 1059A was calculated between the extinction of *P. lacunosa* (0.46 Ma) and the top of the section (Fig. 63). The estimated age of the bottom of the cored interval at this site is around 600 ka. Sedimentation rates calculated using the magnetic susceptibility record of this site vary from 8 to 41 cm/k.y., with an average value of 21 cm/k.y. (using the mbsf depth scale). The maximum value of 41 cm/k.y. was reached during the last glacial period (between 70 and 10 ka). The only independent marker available at this site is the top of the *P. lacunosa* range, which is calculated to be at 471 ka within MIS 12 (Tables 33, 34; Fig. 64). The inflation of the sedimentation rates at this site, caused by the use of mcd, is between 6% and 20%.

Calcium carbonate and organic carbon accumulation rates are presented in Tables 35 and 36 and Figure 65. The carbonate accumulation rates vary from 0.9 to 7.8 g/cm^2/k.y., averaging 3.2 g/cm^2/k.y. The organic carbon fluxes range from 0.04 to 0.31 g/cm^2/k.y., averaging 0.13 g/cm^2/k.y. The calcium carbonate accumulation rate is generally higher during interglacial periods. The lowest value is observed during MIS 8. The organic carbon accumulation rates do not mimic the downhole variation shown by the calcium carbonate data.

Table 23. Estimated ages, concentrations, and accumulation rates of calcium carbonate at Site 1056.

Age (ka)	$CaCO_3$ content (wt%)	$CaCO_3$ MAR ($g/cm^2/k.y.$)
14.70	53.16	5.65
21.63	38.63	4.83
28.86	26.36	3.30
34.88	35.87	6.03
53.86	48.72	6.03
61.75	37.60	6.10
143.97	26.15	2.54
178.71	26.96	2.55
196.27	66.61	3.44
256.98	45.90	5.16
289.83	39.41	4.42
327.65	43.54	3.77
344.96	24.82	6.49
353.33	23.69	5.89
366.99	27.76	1.73
462.52	29.89	4.16
485.14	32.10	5.14
513.44	35.25	4.49
532.16	27.39	4.03
551.33	30.01	4.37
567.43	46.69	4.94
625.77	18.90	2.82
649.36	33.43	5.01
672.98	41.26	13.45
686.73	39.04	11.41
696.88	30.87	8.30
707.04	28.34	8.64
727.93	45.13	14.92
736.29	45.85	15.08
767.08	39.28	8.10
786.80	55.17	9.68
809.79	18.03	1.90
940.65	17.48	0.33
1097.77	13.64	2.03
1119.89	15.62	2.42
1141.86	21.73	2.94
1171.13	12.73	1.66
1180.50	14.16	2.23
1201.73	25.63	3.78
1249.36	31.94	2.32
1289.72	24.59	1.63
1332.28	25.52	1.78
1397.94	32.91	2.38
1461.84	24.00	1.64
1527.94	32.40	1.94
1548.12	30.55	1.80

Notes: MAR = mass accumulation rate. Estimations based on geochemical measurements for Hole 1056B.

Table 24. Estimated ages, concentrations, and accumulation rates of organic carbon at Site 1056.

Age (ka)	C_{org} content (wt%)	C_{org} MAR ($g/cm^2/k.y.$)
21.63	0.74	0.09
34.88	0.44	0.07
61.75	0.59	0.10
143.97	0.51	0.05
178.71	1.12	0.11
344.96	0.30	0.08
353.33	0.25	0.06
485.14	0.44	0.07
532.16	0.58	0.09
625.77	0.59	0.09
707.04	0.52	0.16
736.29	0.63	0.21
809.79	0.12	0.01
1097.77	0.31	0.05
1171.13	0.63	0.08
1289.72	0.74	0.05
1461.84	1.41	0.10
1590.82	0.89	0.07

Notes: MAR = mass accumulation rate. Estimations based on geochemical measurements at Hole 1056B.

The highest values calculated are during MIS 11 (0.22 $g/cm^2/k.y.$), early MIS 4 (0.31 $g/cm^2/k.y.$), and MIS 2 (0.25 $g/cm^2/k.y.$).

ORGANIC GEOCHEMISTRY

Routine monitoring of headspace and vacutainer gases was done for drilling safety in at least every core of Holes 1056B, 1057A, 1058A, and 1059A located on the Blake Outer Ridge, using the standard ODP sampling techniques (see "Explanatory Notes" chapter, this volume). Calcium carbonate and organic carbon concentrations were also measured on selected samples obtained from all holes. Organic matter, atomic C/N values, and Rock-Eval pyrolysis analyses were employed to determine the type of organic matter contained within the sediments.

Volatile Hydrocarbons

Description

Headspace methane concentrations are below 25 ppm in the uppermost sections at each site (Table 37; Fig. 66). At Holes 1056B and 1057A, a rapid increase in methane concentrations to about 50,000 ppm occurred ~40 mbsf. At Hole 1058A, the same increase is recorded at approximately the same depth, but methane concentrations are slightly higher (~64,000 ppm). Hole 1059A displays a double peak in methane concentration at 14.80 and 30.52 mbsf, reaching a maximum of 49,492 ppm. Thus, the zone of increasing headspace methane concentrations in this hole is shallower than at the other sites. Sharply decreasing amounts of methane are observed for Holes 1056B, 1057A, and 1058A between 40 and 80 mbsf, where concentrations stabilize around 10,000 ppm. The same general pattern occurs in sediment from Hole 1059A; however, the sharp methane decrease is shallower, and concentration values hardly reach levels higher than 4000 ppm below 39.90 mbsf.

Headspace C_2–C_5 hydrocarbons are present in extremely low amounts in Holes 1056B, 1057A, 1058A, and 1059A. For example, ethane never reaches higher concentrations than ~5 ppm, and higher molecular-weight hydrocarbons are present in only trace amounts (Table 37).

The first obvious gas voids are found at 39.1 and 42.5 mbsf in sediment from Holes 1056B and 1059A, respectively, but are found deeper in Holes 1057A and 1058A at ~66 mbsf (Table 38). The gas voids contain methane, ethane, propane, and extremely low amounts of *iso*-butane, except for Hole 1059A where *iso*-butane is absent. *Iso*-pentane is only detected in deep sections from Hole 1056B. Methane concentrations of the gas voids are significantly higher (up to 90 vol%) than those obtained by the headspace technique, but both sampling methods display similar gas ratios for equivalent depth intervals, generally always higher than 4000 (Tables 37, 38). The difference between headspace and vacutainer data might be explained by the different sampling methods, causing a loss of the more labile methane before sealing the headspace sediment in glass vials (Stein et al., 1995).

Discussion

The C_1/C_2 values, as well as the low contribution of higher molecular-weight hydrocarbons, indicate that the methane is largely of microbial origin (Schoell, 1980). Methane is probably formed through microbial CO_2 reduction (Claypool and Kaplan, 1974). A similar origin of methane has been inferred in the Pliocene–Pleistocene sediments on the Walvis Ridge (Meyers and Brassell, 1985), in the middle Miocene sediments from Site 767 (Rangin, Silver, von Breymann, et al., 1990), in the Pliocene–Pleistocene sediments of the Alboran Sea (Comas, Zahn, Klaus, et al., 1996), and in sediments from Sites 994, 995, and 997 of the North American continental margin (Paull, Matsumoto, Wallace, et al., 1996).

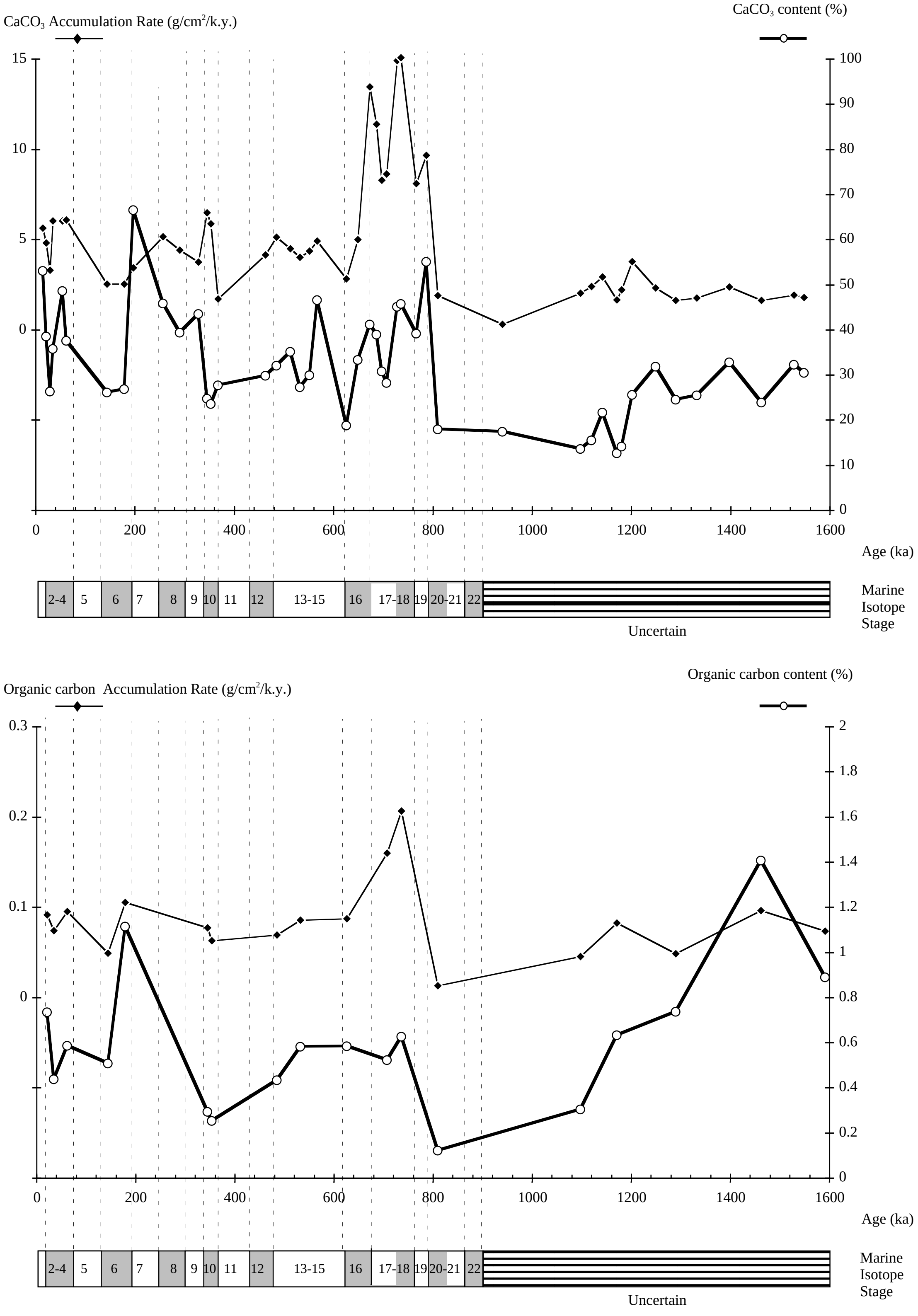

Figure 56. Downhole profiles of organic carbon and calcium carbonate accumulation rates at Site 1056 (composite). MISs are labeled, with the glacial ones shaded; striped section of MIS scale = stage assignment uncertain. Dashed lines = magnetic susceptibility-based boundaries.

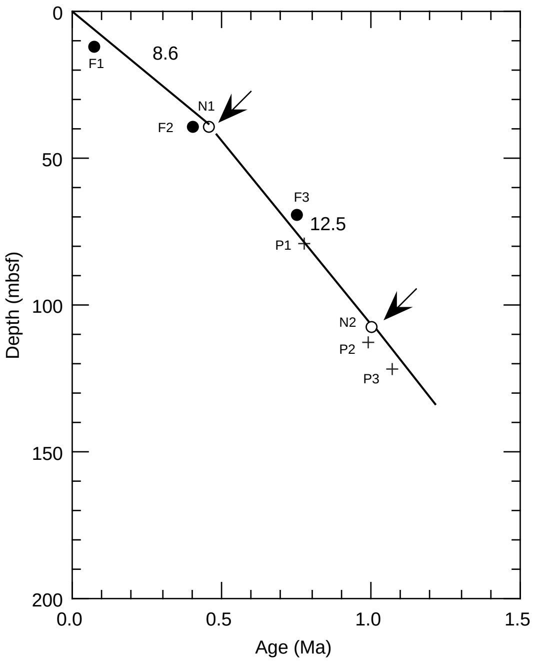

Figure 57. Age/depth plots for Hole 1057A based on biostratigraphic tie points (arrows). Solid circles = planktonic foraminifer markers, open circles = nannoplankton markers, and crosses = magnetostratigraphic markers. See Table 3 in the "Biostratigraphy" section (this chapter) to associate species names with the labels used in this figure. Sedimentation rates are expressed in centimeters per thousand years.

Methane concentrations measured by headspace gas procedures are heavily influenced by coring techniques, time exposure of cores to atmospheric pressure, stage of sediment diagenesis (lithification and water content), and analytical procedures (e.g., desorption conditions). Therefore, the measured gas amounts do not represent in situ concentrations (Dickens et al., 1996). However, methane concentrations can be divided into three general depth zones at Sites 1056, 1057, 1058 and 1059. In the first zone, methane concentrations within the sulfate reduction zone are very low, because the presence of interstitial sulfate inhibits bacterial methanogenesis in sediments (Claypool and Kvenvolden, 1983). Furthermore, predominant amounts of methane are consumed through the process of anaerobic methane oxidation at the sulfate/methane boundary (Reeburgh, 1976), leaving the sediments above depleted in methane. The second zone occurs below the top of the methanogenesis zone, and is characterized by higher methane concentrations. The highest amounts of methane occur at Site 1058. The depth of the top of the methanogenesis zone is shallowest at Sites 1058 and 1059 (~12 mbsf), and is found at ~17 mbsf at Sites 1056 and 1057. The third zone occurs in sediments below these intermediate depths, which exhibit decreasing C_1 concentrations, presumably because of sediment outgassing caused by sediment cracking and the formation of gas voids within the core liners. Similar methane concentration profiles have been observed at other ODP sites associated with gas hydrate (e.g., Peruvian outer continental margin; Kvenvolden and Kastner, 1990).

Inorganic and Organic Carbon

Description

The results of calcium carbonate and organic carbon analyses are presented in Table 39 and Figures 67 through 70. Variations of calcium carbonate values are comparable for Holes 1056B and 1057A, and range from ~11 to 66 wt%, assuming that all of the carbonate present is pure calcite. The calcium carbonate content is somewhat lower in Hole 1058A, ranging from 6.6 to 53.0 wt%. In these three holes, the distribution of $CaCO_3$ is markedly different above and below the depth of reentrance of medium *Gephyrocapsa spp.* (99.55, 107.5, and 114.62 mbsf, respectively, corresponding to an age of ~1.0 Ma; see "Biostratigraphy" section, this chapter). Above this boundary, calcium carbonate amounts seem to exhibit cyclic variations. A preliminary stratigraphy established on the three holes using magne-

Table 25. Depth-to-depth correlation (mcd) between Sites 1057 and 1056.

Site 1057 depth (mcd)	Site 1056 depth (mcd)	Age (ka)
1.11	0.09	9.70
2.61	1.64	19.04
4.09	2.84	26.27
4.35	3.09	27.77
4.85	3.44	29.88
5.19	3.99	33.19
5.67	4.29	35.00
5.93	4.64	37.11
6.57	5.44	41.93
7.26	6.14	46.14
7.68	6.79	50.06
7.98	7.19	52.47
8.52	7.73	55.48
8.94	8.17	58.19
10.44	9.23	66.25
11.37	10.23	76.44
11.97	11.49	91.68
13.05	13.27	112.18
14.22	14.64	128.48
15.27	15.19	133.81
15.62	15.44	136.23
16.17	15.59	137.68
16.62	16.74	148.81
17.05	17.39	155.10
18	18.04	161.39
18.95	19.09	171.55
19.95	21.39	198.34
20.5	22.39	215.57
22.35	24.14	244.81
26.95	28.94	283.75
28.4	30.89	299.57
31.1	34.49	338.45
35.08	38.59	356.99
37.25	40.79	373.71
39.1	43.54	414.80
41.55	44.94	431.65
42.25	45.79	439.04
45.85	51.99	488.46
47.2	53.49	498.04
51.45	60.24	541.17
55.45	65.19	575.96
59.15	70.04	626.12
61.5	72.54	647.97
65.65	80.33	689.06
67.35	82.28	695.66
71.66	88.53	716.82
75.55	94.93	738.49
77.5	96.88	745.09
85.5	105.38	804.21

Note: Correlations based on depth-to-depth relationship between magnetic susceptibility records, using Site 1056 as a reference.

Table 26. Age-depth relationship for Site 1057.

Age (ka)	Depth (mcd)	Average sedimentation rate (cm/k.y.)
10	1.16	16.04
70	10.78	16.04
128	14.19	5.87
188	19.56	8.96
244	22.30	4.88
302	28.57	10.81
338	31.07	6.94
364	35.99	18.93
426	40.73	7.64
476	44.94	8.43
620	58.70	9.55
672	63.93	10.05
762	79.79	17.62
788	83.31	13.53
864	96.07	16.80
900	102.44	17.68

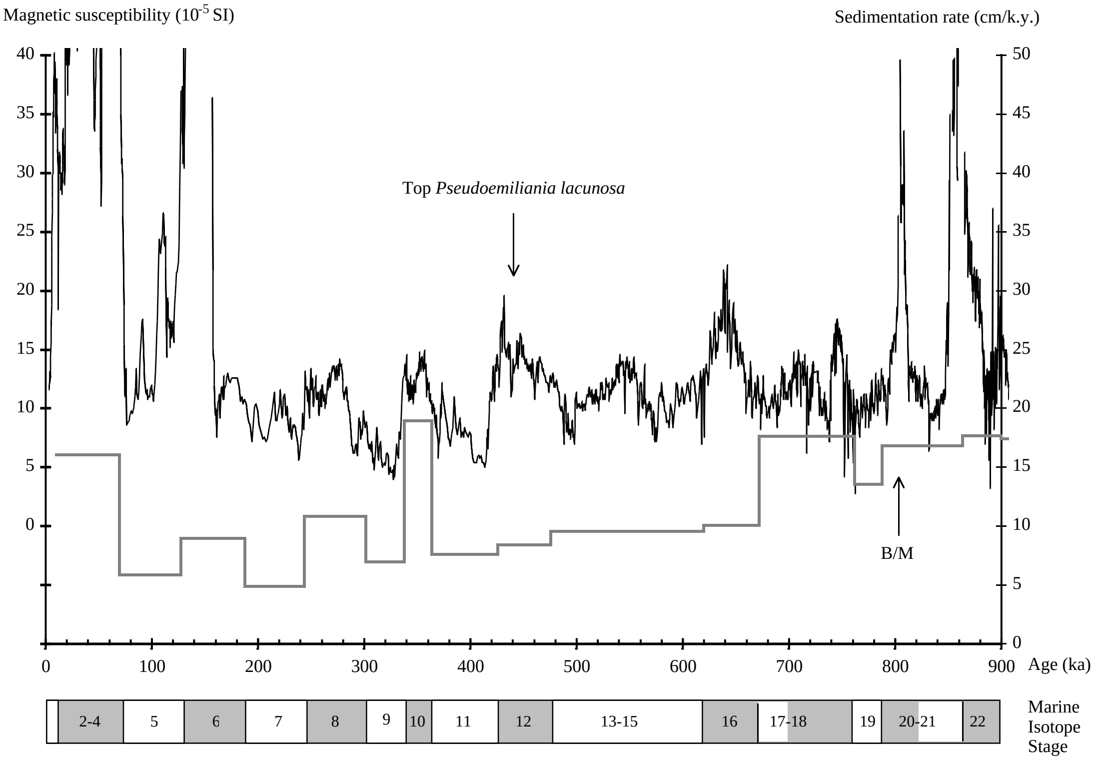

Figure 58. Magnetic susceptibility record (left scale, thin curve) and sedimentation rate (right scale, thick stepwise curve; composite record) of Site 1057 (32°01′N, 76°04′W, 2585 m). MISs are indicated, with glacial ones shaded. B/M = Brunhes/Matuyama boundary.

Table 27. Estimated ages, concentrations, and accumulation rates of calcium carbonate at Site 1057.

Age (ka)	$CaCO_3$ content (wt%)	$CaCO_3$ MAR (g/cm^2/k.y.)
5.47	42.32	7.91
19.92	17.33	2.36
22.46	22.77	3.31
99.46	47.76	2.14
130.97	28.46	2.34
133.88	28.20	2.83
161.06	37.46	3.27
262.16	23.24	2.48
276.81	19.40	1.88
300.72	30.67	2.92
339.99	15.75	2.34
353.17	15.33	3.20
415.14	64.37	4.87
439.31	40.41	3.80
483.11	23.52	2.42
522.19	31.11	3.17
548.48	19.78	2.15
575.96	55.56	5.52
710.83	26.65	4.67
726.57	23.85	4.99
741.40	21.57	4.88
792.90	51.20	8.71
804.14	10.77	2.16
816.26	25.24	4.45
849.85	17.30	3.71
858.33	19.44	4.01
870.55	13.88	3.08
897.13	13.02	2.17
909.91	20.46	4.27
940.22	30.38	5.44
1077.17	24.65	2.40
1112.60	17.60	1.98
1144.03	20.38	2.11
1199.17	25.89	2.78
1227.85	21.92	2.32
1265.30	23.54	2.52

Notes: MAR = mass accumulation rate. Estimations based on geochemical data collected at Hole 1057A.

Table 28. Estimated ages, concentrations, and accumulation rates of organic carbon at Site 1057.

Age (ka)	C_{org} content (wt%)	C_{org} MAR (g/cm^2/k.y.)
19.92	0.56	0.08
130.97	0.47	0.04
262.16	0.43	0.05
276.81	0.21	0.02
339.99	0.35	0.05
353.17	0.68	0.14
483.11	0.34	0.03
548.48	0.19	0.02
726.57	0.50	0.10
804.14	0.50	0.10
816.26	0.77	0.14
870.55	0.32	0.07
897.13	0.90	0.15
1077.17	1.37	0.13
1112.60	0.47	0.05
1199.17	0.89	0.10
1265.30	1.10	0.12

Notes: MAR = mass accumulation rate. Estimations based on geochemical data collected for Hole 1057A.

tic susceptibility and biostratigraphy data (see “Paleomagnetism” and “Lithostratigraphy” sections, this chapter) indicates that high carbonate deposition patterns occur during interglacial periods, whereas low values are recorded in glacial periods. Conversely, generally low $CaCO_3$ values occur below the reentrance of medium *Gephyrocapsa* spp.

Sediments from Holes 1056B, 1057B, and 1058A average 0.6 wt% TOC, about two times higher than the average of 0.3 wt% compiled by McIver (1975) from DSDP Legs 1 through 33. TOC concentrations globally range from 0.1 to 1.4 wt%. A general increase of TOC content with depth seems to be the main feature of Holes 1056B, 1057A, and 1058A, especially in the lower part older than 1.0 Ma, where the highest values are reached.

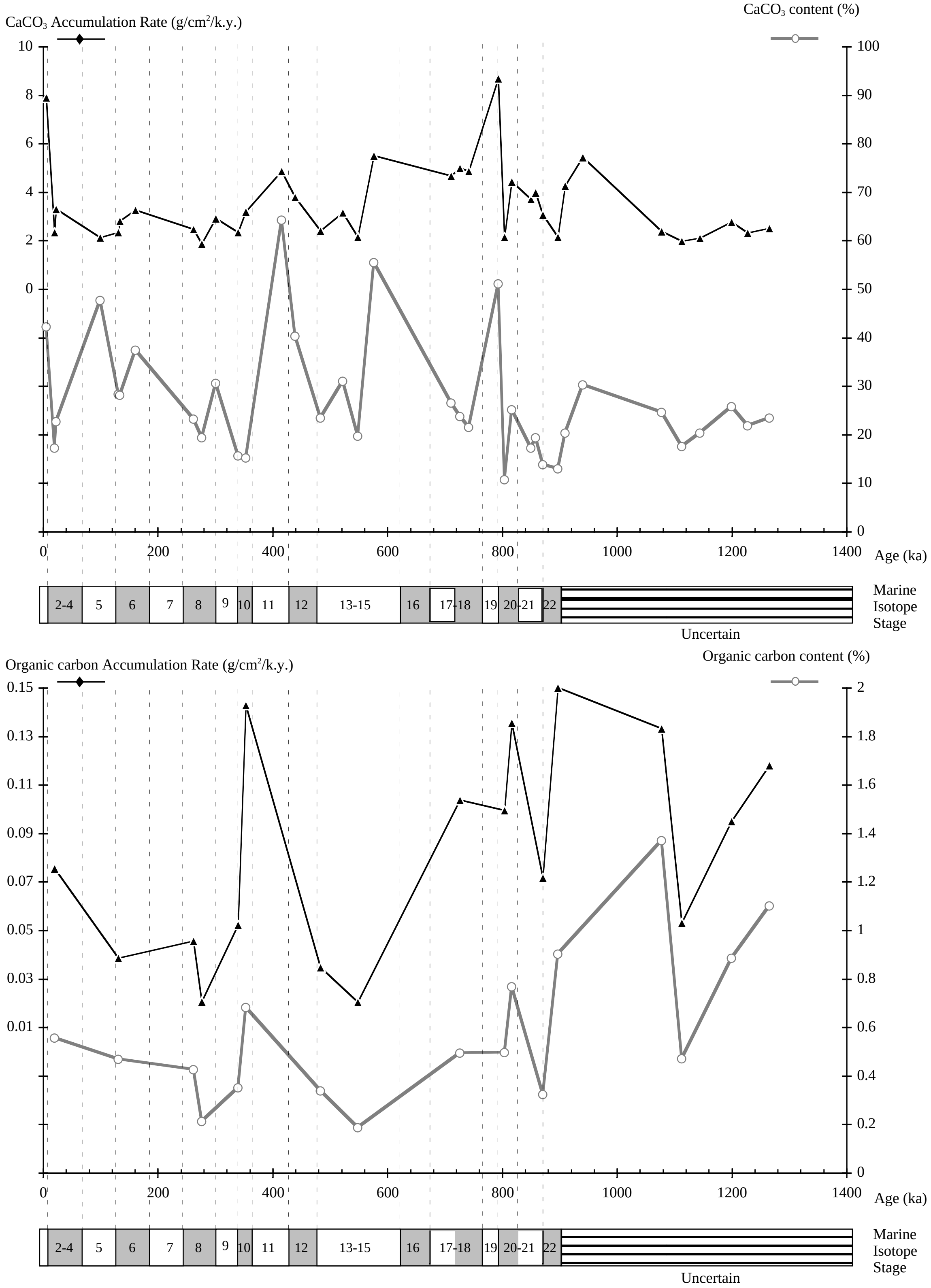

Figure 59. Downhole profiles of organic carbon and calcium carbonate accumulation rates at Site 1057 (composite). MISs are labeled, with glacial ones shaded. Dashed lines = magnetic susceptibility-based boundaries.

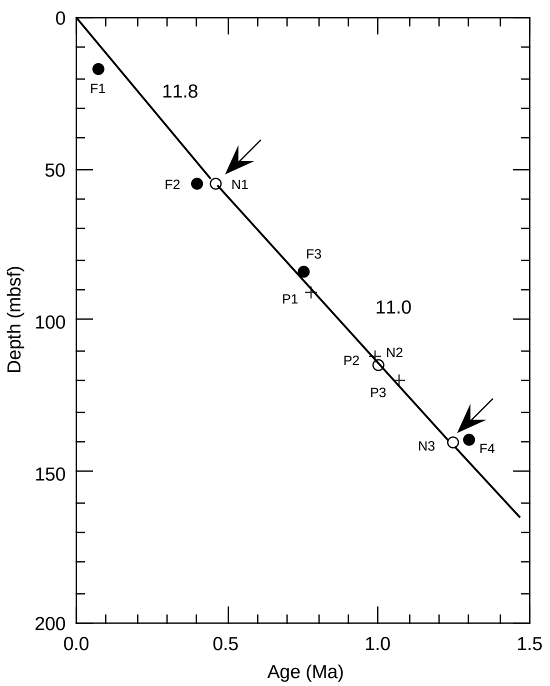

Figure 60. Age/depth plots for Hole 1058A, based on biostratigraphic tie points (arrows). Solid circles = planktonic foraminifer markers, open circles = nannoplankton markers, crosses = magnetostratigraphic markers. See Table 3 in the "Biostratigraphy" section (this chapter) to associate species names with the labels used in this figure. Sedimentation rates are expressed in centimeters per thousand years.

Table 29. Depth-to-depth correlation (mcd) between Sites 1058 and 1061.

Site 1058 depth (mcd)	Site 1061 depth (mcd)	Age (ka)
0.14	0.1	10.00
8.28	9.7	30.37
10.73	12.12	35.51
14.14	19.8	51.81
16.94	27.93	69.07
24.99	38.79	129.47
31.84	55.11	189.15
35.64	71.85	246.28
41.99	84.11	300.07
46.94	95.97	337.50
50.29	100.31	361.73
51.84	103.59	375.29
56.69	114.91	419.65
58.94	117.21	430.49
61.44	121.67	459.91
65.19	124.93	480.80
82.97	146.68	608.17
84.87	148.26	617.42
86.07	152.12	662.55
95.07	163.3	737.55
96.57	166.22	759.56
97.79	169.28	770.53
99.69	171.46	777.12
102.09	173.28	782.62
103.49	177.04	802.17
106.28	180.08	823.92
108.93	185.72	864.15
113.89	194.23	895.50

Note: Correlation based on depth-to-depth relationship between magnetic susceptibility records, using Site 1058 as a reference.

Table 30. Age-depth relationship for Site 1058.

Age (ka)	Depth (mcd)	Average sedimentation rate (cm/k.y.)
10	0.14	28.21
70	17.06	28.21
128	24.79	13.33
188	31.71	11.52
244	35.49	6.75
302	42.25	11.65
338	47.01	13.23
364	50.55	13.62
426	58.01	12.03
476	64.33	12.64
620	84.94	14.31
672	87.20	4.36
762	96.84	10.71
788	102.48	21.67
864	108.92	8.48
900	114.83	16.42

Hole 1059A displays different downhole carbonate patterns (Table 39; Fig. 70). First, calcium carbonate values are lower than in the previous three holes, ranging from ~9 to 49 wt%. Second, the interpretation of magnetic susceptibility and biostratigraphy data (see "Sedimentation and Mass Accumulation Rates" and "Lithostratigraphy" sections, this chapter) allows the recognition of only the upper 13 MISs. The Hole 1059A downhole record ends at MIS 13, just below the disappearance of *P. lacunosa.* Sediments average 0.58 wt% TOC, ranging from 0.20 (48.78 mbsf) to 1.14 wt% (77.38 mbsf). Once again, TOC values do not mimic the downhole variation in calcium carbonate.

Discussion

In the three sites with long temporal records (1056, 1057, and 1058), the reentrance of medium *Gephyrocapsa* spp. (1.0 Ma) seems to separate two distinct modes of carbonate and organic carbon deposition. Below this event, relatively low but uniform values of calcium carbonate are observed. Above the event, cyclic, highly variable carbonate values occur, which appear to be correlative with magnetic susceptibility cycles (see "Sedimentation and Mass Accumulation Rates" section, this chapter). These cycles may be indicative of the transition between obliquity and eccentricity forcings associated with the enhancement of ice sheets in the Northern Hemisphere. Dissolution of $CaCO_3$ could explain the cyclicity in the uppermost sections, if there were higher organic carbon rain rates during glacials and oxidation/dissolution processes of carbonate with shallow burial (Emerson and Bender, 1981). Low $CaCO_3$ levels may also be the result of a decrease in calcium carbonate production or an increase in terrigenous fluxes. This latter explanation would be consistent with higher magnetic susceptibility during glacial stages (see "Paleomagnetism" section, this chapter).

Organic Matter Source Characterization

Description

C/N values range from 1 to 18 in the four holes (Table 39). The C/N values below 4 are generally associated with low organic carbon values (<0.5%). This may be an artifact associated with low carbon values and the tendency of clay minerals to absorb ammonium ions during diagenesis (Müller, 1977). The C/N values for these samples are consequently inaccurate indicators of organic matter sources. The high C/N value of 13.5 occurring at 48.8 mbsf in Hole 1057A may be explained by the low nitrogen concentration (about 0.1 wt%), close to the detection limit of the CNS device. Average C/N values of marine zooplankton and phytoplankton lie between 5 and 8, whereas land plants have ratios between 20 and 200 (Emerson and Hedges, 1988). Except for a high value of 18.0 measured at 32.9 mbsf in sediment from Hole 1057A, perhaps reflecting some admixture of terrigenous inputs, the C/N values of samples containing more than 0.5

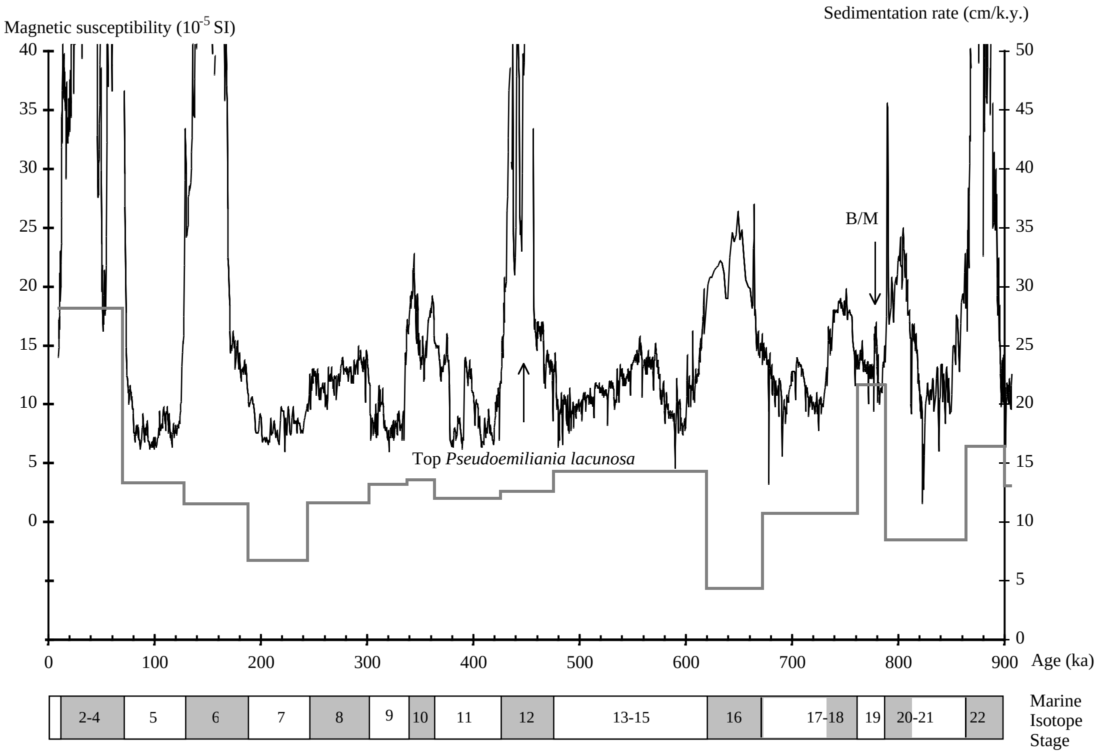

Figure 61. Magnetic susceptibility record (left scale, thin curve) and sedimentation rate (right scale, thick stepwise curve; composite record) of Site 1058 (31°41′N, 75°25′W, 2975 m). The MISs are indicated, with the glacial ones shaded. B/M = Brunhes/Matuyama boundary.

wt% TOC average 5.5, 9.0, 6.5, and 7.0 for Holes 1056B, 1057A, 1058A, and 1059A, respectively (Table 39). Although C/N values may change during diagenesis and maturation, such C/N values reflect a predominant contribution of marine algal material (Meyers, 1994).

Some sediment samples having elevated TOC concentrations (>0.5 wt%) were selected for Rock-Eval characterization of the type and thermal maturity of their organic matter content (Table 40). Van Krevelen-type plots of the hydrogen index (HI) and oxygen index (OI) values suggest that the sedimentary organic matter of the four holes mostly contains type III land-derived organic matter (Figs. 71A, 72A, 73A, 74A). This source assignment conflicts with the relatively low C/N values for these samples, indicating a predominance of marine organic material. The contradiction between the Rock-Eval and elemental source characterizations is evidence of heavy oxidation of the marine organic matter, probably by microbial reworking (Espitalié et al., 1986). Well-preserved type II organic matter has high HI values (Espitalié et al., 1986). This is consistent with results from the SEEP experiment conducted on the continental slope between Cape Hatteras and Martha’s Vineyard, which showed that the C_{org} on slope was essentially refractory (Biscaye and Anderson, 1994).

In Holes 1056B, 1057A, and 1058A, sediments having higher organic carbon Rock-Eval values also have higher HI values (Figs. 71B, 72B, 73B). This relationship is consistent with preservation being more important in elevating the organic matter content of sediments older than 1.0 Ma. Such a trend is not observed for Hole 1059A (Fig. 74B), which does not show organic carbon accumulation layers. Rock-Eval T_{max} values are relatively low at all depths for Holes 1056B, 1057A, 1058A and 1059A (Table 40), indicating that organic matter is thermally immature with respect to petroleum generation.

Discussion

Elemental and Rock-Eval analyses attempted to answer the following question: what is the reason for higher accumulations of organic carbon below the reentrance of medium *Gephyrocapsa* spp.? Is it due to higher primary production, better preservation, or both? Generally, high organic productivity leads to low oxygen content in bottom waters in an environment like Blake Ridge. This may explain the better preservation of samples older than 1.0 Ma, as indicated by high organic values and high HI-index values. Alternatively, deposition rates may decrease after 1 Ma, but for now they are poorly constrained.

Summary

Methane concentration data and methane/ethane ratios indicate that gases are produced microbially at all four sites of the Blake Outer Ridge. The methanogenesis zone occurs at intermediate depths within the holes, below the sulfate reduction zone.

Carbonate and organic carbon concentrations are highly variable, showing reciprocal trends below the reentrance of medium *Gephyrocapsa* spp. at ~1.0 Ma. Low carbonate values and high organic carbon contents are generally observed below that horizon. It is known that calcium carbonate producers (coccolithophorids for instance) prefer oligotrophic conditions. TOC and calcium carbonate data are thus not contradictory, but may indicate some increase in primary productivity at that time.

Cyclical variations in calcium carbonate and low TOC values are recorded above this boundary, emphasizing the importance of glacial–interglacial cycles younger than ~1.0 Ma. If carbonate accumulation rates reflect the glacial–interglacial cycles, TOC does not seem to obey the same cyclicity. Finally, organic matter at these four sites is characteristic of heavily oxidized, immature marine organic matter.

INORGANIC GEOCHEMISTRY

Interstitial waters were extracted and analyzed from 69 whole-round sections of core from Sites 1056, 1057, 1058, and 1059, which

Table 31. Estimated ages, concentrations, and accumulation rates of calcium carbonate at Site 1058.

Age (ka)	$CaCO_3$ content (wt%)	$CaCO_3$ MAR (g/cm^2/k.y.)
16.18	16.24	4.83
22.99	7.29	2.04
29.22	15.27	3.78
47.08	13.07	2.81
62.66	11.94	3.04
84.90	41.66	4.26
115.81	40.19	4.58
137.57	15.59	1.79
166.15	12.26	1.48
197.12	25.53	1.39
227.34	34.72	2.24
261.87	34.78	3.64
304.91	26.67	3.39
326.08	41.73	5.29
348.93	26.80	4.01
390.02	33.26	3.72
402.00	49.61	5.98
418.00	53.01	7.64
479.91	38.02	5.49
501.00	26.00	3.44
522.64	24.03	2.79
541.12	22.12	3.07
562.68	15.28	2.67
582.95	34.96	4.87
620.43	22.38	1.21
675.38	15.85	2.25
703.72	20.61	2.24
741.81	13.73	1.63
771.26	16.82	3.63
781.47	33.51	7.79
822.59	40.30	3.74
849.27	42.08	3.88
876.10	6.64	1.32
912.48	7.21	0.96
934.23	23.17	3.17
945.14	26.31	3.67
1004.38	25.09	2.91
1042.06	14.42	1.64
1067.77	15.96	2.08
1091.05	16.85	2.55
1114.49	13.38	1.49
1139.61	16.02	1.96
1188.26	8.59	1.20
1211.71	23.41	3.08
1283.22	19.26	3.02
1326.76	23.48	3.65
1343.34	18.51	2.44

Notes: MAR = mass accumulation rate. Estimations based on geochemical measurements at Hole 1058A.

Table 32. Estimated ages, concentrations, and accumulation rates of organic carbon at Site 1058.

Age (ka)	C_{org} content (wt%)	C_{org} MAR (g/cm^2/k.y.)
16.18	0.30	0.09
22.99	0.39	0.11
62.66	0.41	0.11
137.57	0.37	0.04
166.15	0.39	0.05
348.93	0.40	0.06
479.91	0.56	0.08
522.64	0.59	0.07
562.68	0.20	0.03
620.43	0.59	0.03
703.72	0.79	0.09
741.81	0.36	0.04
876.10	0.40	0.08
912.48	0.31	0.04
945.14	0.31	0.04
1042.06	0.66	0.08
1091.05	0.95	0.14
1139.61	0.94	0.12
1188.26	0.65	0.09
1283.22	0.94	0.15
1343.34	1.32	0.17

Notes: MAR = mass accumulation rate. Estimations based on geochemical measurements at Hole 1058A.

are located on the Blake Outer Ridge. Samples were collected from every core of Holes 1056B, 1057A, and 1058A. In Hole 1059A, samples were taken at a frequency of one sample per section to a depth of 23 mbsf, and at one sample per core thereafter. The main objectives were to document the early diagenetic changes and to locate possible gas hydrate zones. Interstitial water data for the four sites are given in Table 41, and are presented as downhole concentration profiles in Figures 75 through 83.

Early Diagenesis Associated with Organic Matter Decomposition

Interstitial sulfate, alkalinity, ammonium, and phosphate concentrations are related to the microbial decomposition of sedimentary organic matter. The sulfate reduction zone is characteristically thin at these sites, with the sulfate/methane interface located between 10 and 20 mbsf (Figs. 75−78). In addition, the depth of the oxic/sulfate reduction interface is very close to the seafloor.

Alkalinity generally increases with depth (Figs. 75−78), indicating the decomposition of sedimentary organic matter by microorganisms. At Site 1059, however, it rises to a peak of 32.54 mM at 20.75 mbsf and then slightly decreases to the 28 to 31-mM range below this depth. The alkalinity gradient is steeper in the sulfate reduction zone than in the zone of methanogenesis. In the former zone, the lowest and highest alkalinity values occur at Sites 1056 and 1059, respectively, suggesting that alkalinity tends to rise with increasing water depth along the crest of the Blake Outer Ridge.

Interstitial ammonium and phosphate concentrations commonly represent the different rates of organic matter decomposition in the zones of sulfate reduction and methanogenesis. Ammonium values tend to increase with depth, with the ammonium concentrations at a given depth being highest at Site 1057 and lowest at Site 1059. At the latter site, ammonium concentrations form a local peak in the methanogenesis zone, and then increase gradually with depth.

Phosphate profiles tend to be more irregular than the ammonium profiles. Although phosphate concentrations display a general increase with depth, a reversal in the trend of downhole increasing values occurs at 100 mbsf at Sites 1057 and 1058. The phosphate profiles at Sites 1057 and 1059 show their highest values within the zone of methanogenesis (92.4 mbsf) and sulfate reduction (9.75 mbsf), respectively. Site 1059 exhibits the highest phosphate concentration of the intermediate water depth sites along the Blake Outer Ridge, reaching 244 µM (9.75 mbsf); the lowest phosphate concentrations (14−43 µM) occur at Site 1056.

Discussion

Sites 1056, 1057, 1058, and 1059 are located in progressively increasing water depths on the Blake Outer Ridge. Downhole, interstitial sulfate, alkalinity, ammonia, and phosphate concentrations are determined by early diagenesis involving microbially mediated organic matter decomposition. The sulfate/methane interface is consistently found at depths between 10 and 20 mbsf, with the depth of the oxic/sulfate reduction interface very close to the seafloor. Thus, the onset of sulfate reduction at these Blake Outer Ridge sites occurs at shallower depths than those observed at the Carolina Slope (Sites 1054 and 1055) (see “Inorganic Geochemistry” section, “Carolina Slope” chapter, this volume). Alkalinity increases with depth, with a steeper gradient in the sulfate reduction zone than in the zone of methanogenesis. This is related to the greater production of bicarbonate ions (HCO_3^-) in the former diagenetic zone and to carbonate precipitation in the latter zone. The slight reduction in alkalinity in the zone of methanogenesis at Site 1059 may be due to a reduced rate of organic matter degradation and to carbonate precipitation.

At Sites 1056, 1057, and 1058, there are only a few data points in the sulfate reduction zone, making the shape of the sulfate profiles uncertain. The sulfate profile at Site 1059, however, is roughly linear. This, together with linear sulfate profiles elsewhere on the Blake

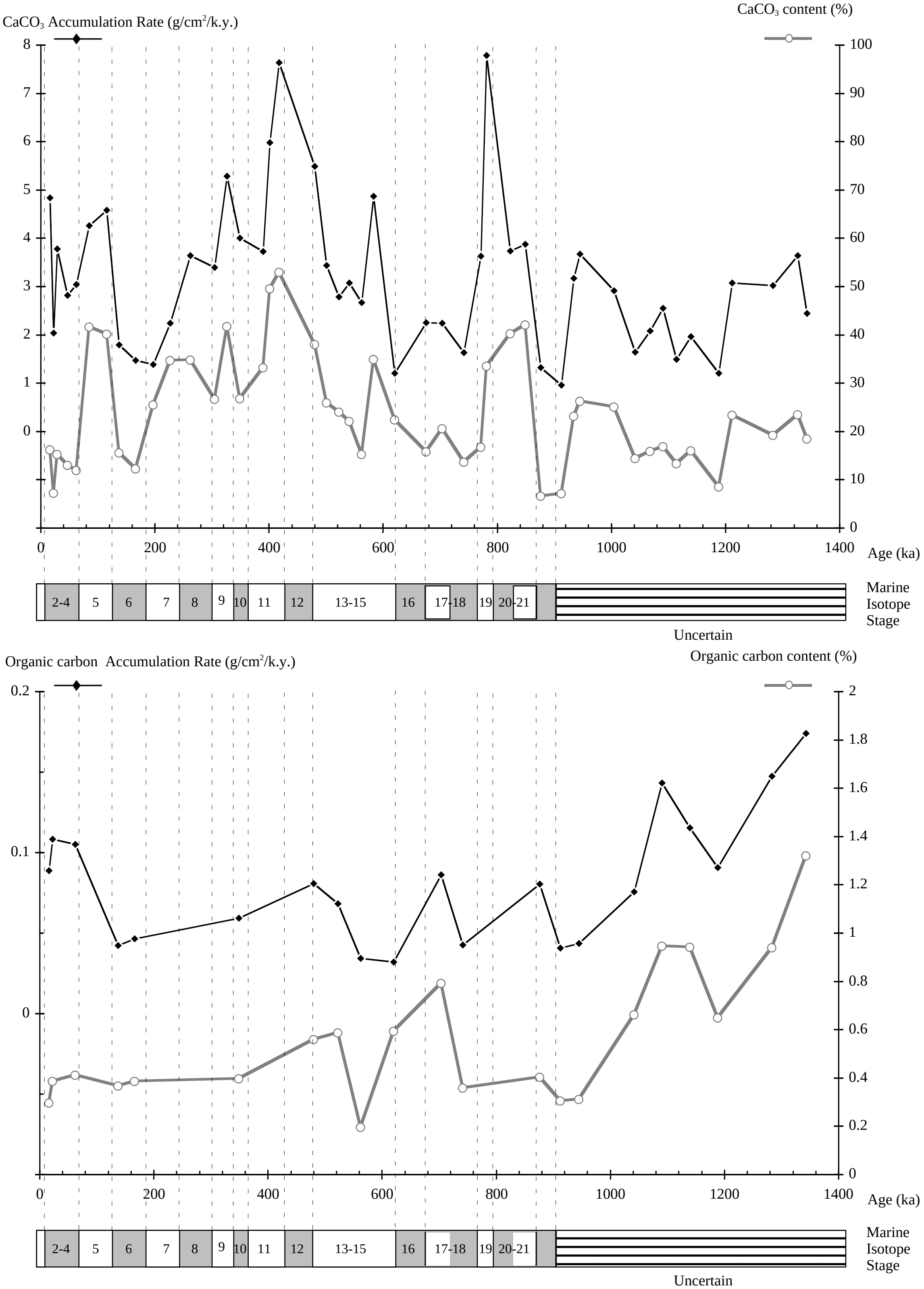

Figure 62. Downhole profiles of organic carbon and calcium carbonate accumulation rates at Site 1058 (composite). MISs are labeled, with glacial ones shaded. Striped section of MIS scale = stage assignment uncertain. Dashed lines = magnetic susceptibility-based boundaries.

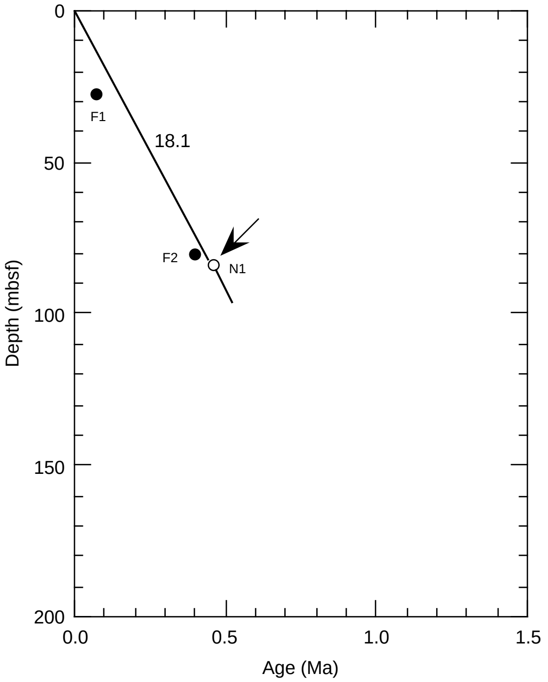

Figure 63. Age/depth plots for Hole 1059A based on biostratigraphic tie points (arrows). Solid circles = planktonic foraminifer markers; open circles = nannoplankton markers. See Table 3 in the "Biostratigraphy" section (this chapter) to associate species names with the labels used in this figure. Sedimentation rates are expressed in centimeters per thousand years.

Table 33. Depth-to-depth correlation between Sites 1059 and 1061.

Site 1059 depth (mcd)	Site 1061 depth (mcd)	Age (ka)
0.06	0.08	9.96
24.91	27.97	69.15
27.17	29.63	77.29
40.2	38.79	129.47
42.72	44.03	148.66
46.74	50.37	171.88
56.36	56.15	192.67
56.96	57.37	196.79
67.12	71.73	245.75
69.56	75.39	261.81
73.58	83.99	299.54
82.22	97.15	343.79
83.28	99.13	355.03
83.86	100.31	361.73
97.03	116.53	426.00
98.65	118.59	439.59
99.13	121.07	455.95
100.18	123.21	470.06
117.07	139.58	566.59

Note: Correlations based on depth-to-depth relationship between magnetic susceptibility records, using Site 1061 as a reference.

Table 34. Age-depth relationship for Site 1059.

Age (ka)	Depth (mcd)	Average sedimentation rate (cm/k.y.)
10	0.08	41.78
70	25.15	41.78
128	39.83	25.32
188	54.20	23.94
244	66.76	22.42
302	74.06	12.59
338	81.09	19.53
364	84.33	12.45
426	97.03	20.49
476	101.22	8.38

Outer Ridge (Borowski et al., 1996; Paull, Matsumuto, Wallace, et al., 1996), suggests that sulfate gradients at Sites 1056, 1057, and 1058 are also linear.

The pervasive existence of linear sulfate profiles and relatively thin sulfate reduction zones on the Carolina Slope and Blake Outer Ridge suggest a relationship between sulfate and methane (Borowski et al., 1996; Paull, Matsumoto, Wallace, et al., 1996). Linear sulfate profiles imply diffusion of sulfate from overlying seawater through the sediments to the methane/sulfate interface, where sulfate and methane are co-consumed by the process of anaerobic methane oxidation ($CH_4 + SO_4^{2-} \rightarrow HCO_3^- + HS^- + H_2O$; Reeburgh, 1976; Hoehler et al., 1994). This process links the sulfate and methane pools so that the flux of methane diffusing from below may influence the magnitude of sulfate gradients and the depth to the sulfate/methane interface (Borowski et al., 1996). As methane flux increases, sulfate gradients should steepen, and the sulfate/methane interface shoals toward the seafloor. Preliminary results from other sites on the Blake Outer Ridge (Leg 164; see Paull, Matsumoto, Wallace, et al., 1996) demonstrate that anaerobic methane oxidation is common, readily affecting early diagenetic processes.

Authigenic Mineral Precipitation and Dissolution

Calcium and magnesium concentrations of interstitial waters decrease sharply with depth in the sulfate reduction zone (Figs. 79−82). Calcium concentrations display a gradient change near the sulfate/methane boundary (between 10 and 20 mbsf). In the zone of methanogenesis, calcium concentrations uniformly range between ~2 mM (Site 1058) and 3 mM (Site 1056), a variation of ~10% with respect to the seawater calcium value. Downhole magnesium profiles usually display less distinct inflection points than the calcium profiles close to the sulfate/methane boundary. The ranges of magnesium values in the methanogenesis zone are 34–35.5, 19.6–35.7, 24.2–41.9, and 33.7–44.7 mM at Sites 1056, 1057, 1058, and 1059, respectively (Table 41). These ranges suggest that the rate of dolomite precipitation in the zone of methanogenesis is much less at Site 1056 than at the other three sites.

Potassium profiles at Sites 1056 and 1058 increase downhole (Figs. 79, 81). At Site 1057, potassium concentrations increase downhole until ~75 mbsf, with a zone of relatively low values (~11.5 mM) between 85 and 110 mbsf (Fig. 80). At Site 1059, potassium contents are relatively high in the sulfate reduction zone and show a slight downhole decrease after a low interval between ~7 and 19 mbsf (Fig. 82). Silica concentrations increase with depth at all four sites (Figs. 79–82), with the values varying between 733 µM (Site 1057) and 912 µM (Site 1056) in the deepest samples.

Discussion

Depth profiles of calcium and magnesium at Sites 1056, 1057, 1058, and 1059 suggest that there is an influx of these ions from the overlying seawater into the sedimentary column (Figs. 79–82). Their rapid downhole decrease in the zones of sulfate reduction and methanogenesis suggests active carbonate precipitation in the zone of methanogenesis. This is supported by the common presence of dolomite in the sediment column (see "Lithostratigraphy" section, this chapter). In the zone of methanogenesis, the downhole decreasing magnesium gradient is much steeper at Sites 1057, 1058, and 1059 than that at Site 1056, suggesting a higher rate of dolomite formation in the former sites.

Increasing potassium concentrations downhole are mainly due to an ion exchange process involving the replacement of potassium ions by ammonium ions at the clay exchange sites as the concentration of ammonium builds up in the lower part of the sediment column (e.g., Rosenfeld, 1979; Mackin and Aller, 1984). Increasing dissolved silica concentrations with depth probably reflect the effect of increasing

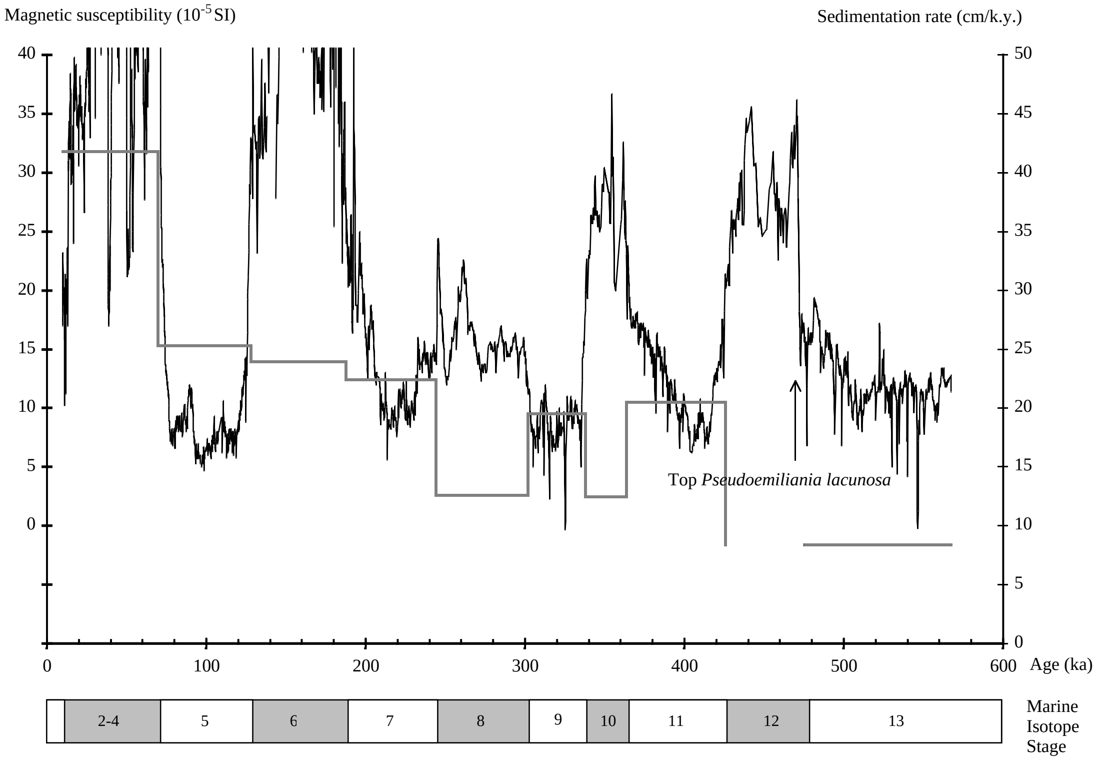

Figure 64. Magnetic susceptibility record (left scale, thin curve) and sedimentation rate (right scale, thick stepwise curve; composite record) of Site 1059 (31°40′N, 75°25′W, 2995 m). MISs are labeled, with the glacial ones shaded.

Table 35. Estimated ages, concentrations, and accumulation rates of calcium carbonate at Site 1059.

Age (ka)	$CaCO_3$ content (wt%)	$CaCO_3$ MAR ($g/cm^2/k.y.$)
12.63	24.23	5.50
16.20	13.31	3.60
26.77	11.57	3.99
33.18	13.89	5.29
39.14	19.06	6.62
50.24	15.83	5.06
60.96	15.62	5.68
68.34	8.77	3.31
76.93	36.76	7.37
88.90	35.44	7.40
106.92	35.98	7.71
123.34	29.94	7.03
139.21	19.53	4.88
160.50	19.77	5.44
187.07	14.12	3.61
205.56	13.76	2.78
219.20	49.45	10.81
234.91	22.82	5.30
255.03	10.90	1.37
280.21	11.68	1.55
309.12	30.71	5.78
320.18	31.69	6.51
337.95	21.46	5.17
373.54	8.90	2.13
385.01	10.04	1.97
402.62	37.78	7.29
426.17	21.07	1.95
478.58	10.98	1.13
500.18	20.70	2.01
514.24	28.94	2.59
531.62	27.80	2.36
545.22	22.20	2.11

Notes: MAR = mass accumulation rate. Estimations based on geochemical measurements at Hole 1059A.

Table 36. Estimated ages, concentrations, and accumulation rates of organic carbon at Site 1059.

Age (ka)	C_{org} content (wt%)	C_{org} MAR ($g/cm^2/k.y.$)
12.63	0.46	0.10
16.20	0.61	0.17
33.18	0.65	0.25
39.14	0.60	0.21
60.96	0.52	0.19
68.34	0.82	0.31
123.34	0.47	0.11
187.07	0.43	0.11
205.56	0.20	0.04
255.03	0.53	0.07
280.21	0.54	0.07
337.95	0.38	0.09
373.54	0.61	0.15
402.62	1.14	0.22
478.58	0.60	0.06
514.24	0.70	0.06
545.22	0.63	0.06

Notes: MAR = mass accumulation rate. Estimations based on geochemical measurements at Hole 1059A.

alkalinity on silica solubility. Toward the bottom of the holes at all four sites, silica concentrations approach the solubility limit of opal-A (Kastner, 1979).

Gas Hydrate

As gas hydrate dissociates during core recovery, it releases freshwater into the pore space, diluting interstitial chloride concentrations and salinity (Hesse and Harrison, 1981; Hesse et al., 1985; Kastner et al., 1990). Thus, the presence of gas hydrate is recognized by the freshening of interstitial waters as indicated by relatively low, interstitial chloride concentrations.

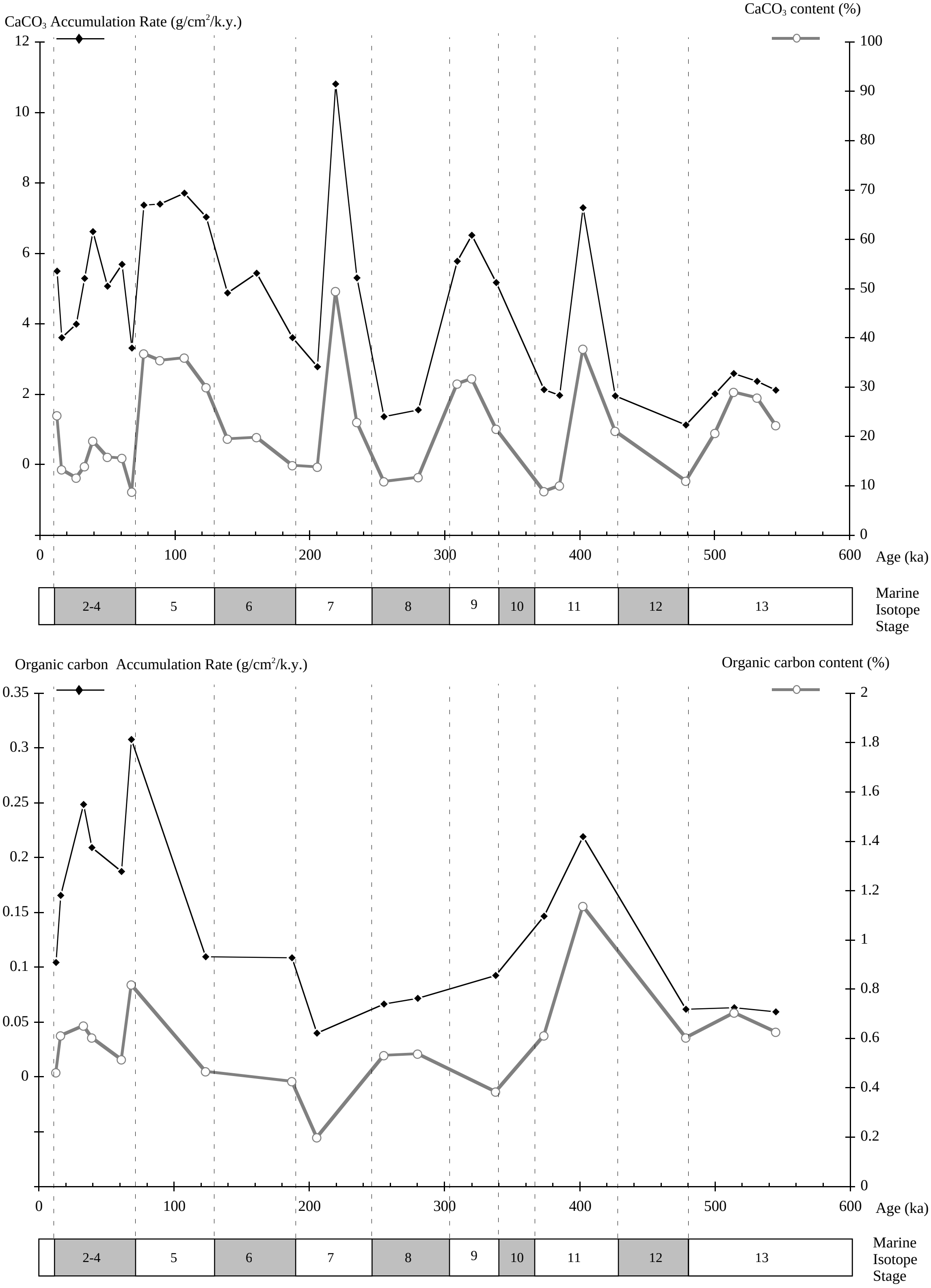

Figure 65. Downhole profiles of organic carbon and calcium carbonate accumulation rates at Site 1059 (composite). MISs are labeled, with glacial ones shaded. Striped section of MIS scale = stage assignment uncertain. Dashed lines = magnetic susceptibility-based boundaries.

Table 37. Results of headspace gas analyses of sediments from Sites 1056, 1057, 1058, and 1059.

Core, section, interval (cm)	Depth (mbsf)	C_1 (ppm)	C_2 (ppm)	C_3 (ppm)	C_1/C_2
172-1056B-					
1H-3, 0-5	3.0	15	ND	ND	—
2H-2, 0-5	5.1	3	ND	ND	—
2H-6, 0-5	11.1	3	ND	ND	—
3H-3, 0-5	16.1	253	1.0	ND	253
3H-6, 0-5	20.6	13,624	1.0	ND	13,624
4H-3, 0-5	25.6	20,332	2.0	ND	10,166
4H-6, 0-5	30.1	15,613	1.0	ND	15,613
5H-2, 0-5	33.6	30,381	3.0	0.6	10,127
5H-6, 0-5	38.3	53,316	5.0	ND	10,663
6H-6, 0-5	49.2	47,856	4.0	ND	11,964
7H-6, 0-5	58.7	27,372	3.0	ND	9,124
8H-6, 0-5	68.1	18,569	2.0	ND	9,285
9H-6, 0-5	77.6	28,837	3.0	ND	9,612
10H-7, 0-5	87.5	9,884	1.0	ND	9,884
11H-7, 0-5	97.5	18,918	3.5	ND	5,483
12H-7, 0-5	106.5	5,577	1.2	ND	4,648
13H-6, 0-5	114.7	4,640	1.5	ND	3,093
14H-5, 0-5	123.6	4,822	1.0	ND	4,822
15H-6, 0-5	133.8	4,163	1.0	ND	4,163
16H-7, 0-5	144.6	6,277	1.5	ND	4,185
17H-7, 0-5	154.0	4,179	0.7	ND	5,970
172-1057A-					
1H-4, 0-5	4.5	4	ND	ND	—
2H-5, 0-5	13.5	5	ND	ND	—
3H-6, 0-5	24.5	21,175	0.5	ND	42,350
4H-7, 0-5	35.5	36,815	0.6	ND	61,358
5H-7, 0-5	45.0	50,772	1.0	1.0	50,772
6H-7, 0-5	54.5	38,393	1.0	1.0	38,393
7H-7, 0-5	64.0	20,364	1.0	ND	20,364
8H-7, 0-5	73.5	9,321	1.0	ND	9,321
9H-7, 0-5	83.0	18,823	0.5	0.5	37,646
10H-7, 0-5	92.5	6,303	0.5	ND	12,606
11H-7, 0-5	101.2	20,274	0.6	0.8	34,363
12H-6, 0-5	109.3	7,567	0.4	ND	19,913
13H-6, 0-5	118.6	14,063	0.5	ND	26,043
14H-3, 0-5	123.3	7,547	0.5	ND	16,057
172-1058A-					
1H-6, 0-5	7.5	23	ND	ND	—
2H-6, 0-5	17.0	7,031	ND	ND	—
3H-6, 0-5	26.5	36,505	1.0	ND	36,505
4H-6, 0-5	36.0	59,028	2.0	0.5	29,514
5H-6, 0-5	45.5	64,344	2.0	0.5	32,172
6H-6, 0-5	55.0	46,839	1.0	0.4	46,839
7H-6, 0-5	64.5	37,143	2.0	0.5	18,572
8H-6, 0-5	74.0	26,695	1.0	0.3	26,695
9H7, 0-5	85.0	15,779	1.0	ND	15,779
10H-6, 0-5	93.0	14,747	1.0	ND	14,747
11H-8, 0-5	104.7	12,513	0.7	ND	17,141
12H-6, 0-5	110.9	16,301	1.2	ND	13,584
13H-6, 0-5	120.8	8,973	0.6	ND	14,955
14H-8, 0-5	132.9	5,993	0.5	ND	11,098
15H-6, 0-5	139.4	10,827	1.1	ND	10,025
16H-6, 0-5	148.8	6,311	0.5	ND	13,428
172-1059A-					
1H-2, 0-5	1.5	2	ND	ND	—
2H-2, 0-5	5.3	3	ND	ND	—
2H-3, 0-5	6.8	3	ND	ND	—
2H-4, 0-5	8.3	5	ND	ND	—
2H-5, 0-5	9.8	195	ND	ND	—
2H-6, 0-5	11.3	4,835	ND	ND	—
3H-2, 0-5	14.8	15,731	0.3	ND	52,437
3H-3, 0-5	16.3	11,581	0.2	ND	57,905
3H4, 0-5	17.8	6,958	ND	ND	—
3H-5, 0-5	19.3	5,344	ND	ND	—
3H-6, 0-5	20.8	5,394	ND	ND	—
4H-7, 0-5	30.5	49,482	1.0	0.2	49,482
5H-6, 0-5	39.9	9,755	0.3	ND	32,517
6H-7, 0-5	50.8	2,992	ND	ND	—
7H-7, 0-5	60.3	4,047	ND	ND	—
8H-7, 0-5	69.5	1,706	ND	ND	—
9H-6, 0-5	77.8	1,881	ND	ND	—
10H-5, 0-5	85.8	1,223	ND	ND	—
11H-6, 0-5	96.3	949	ND	ND	—

Notes: ND = not detected; — = not applicable.

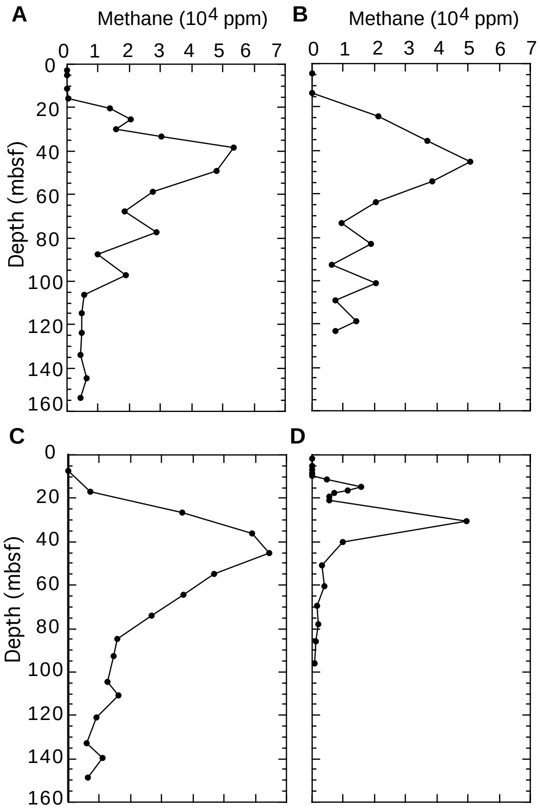

Figure 66. Downhole profile of headspace methane concentrations for (**A**) Hole 1056B, (**B**) Hole 1057A, (**C**) Hole 1058A, and (**D**) Hole 1059A.

At Site 1056, chloride values range from 495 to 572 mM (Fig. 83). Chloride concentrations first slightly freshen with depth, and then form a gradient (~0.24 mM/m) of increasing chloride concentrations downhole. Superimposed upon this general trend, individual samples form anomalous excursions toward fresher chloride values. At 58.6, 77.5, and 106.4 mbsf, the respective chloride values are 11%, 7.5%, and 10% lower than the baseline trend. These chloride excursions represent the occurrence of gas hydrate that, assuming a sediment porosity of 50%, comprise approximately 5.5%, 3%, and 5% of the sediment volume, respectively.

Gas hydrate underlies Sites 1057, 1058, and 1059, based on downhole freshening of interstitial chloride concentrations. At Site 1057, the chloride profile remains close to the seawater value down to ~83 mbsf, and then shows a trend toward lower values, reaching a minimum value of 510 mM at 101 mbsf (Fig. 83). Dependent on various chloride baselines, chloride excursions deviate a maximum of 8.4% to 6.5% from a chloride baseline, so that, if present, gas hydrate may occupy a maximum of 4.2% to 3.2% of the sediment volume.

At Site 1058, chloride concentrations are near seawater values to a depth of ~40 mbsf, but freshen gradually downhole (Fig. 83). The total variation in chloride values is only slightly above 3%, so that the case for recovery of gas hydrate here is equivocal. A baseline seems to form at ~551 mM, with several excursions toward fresher values. The lowest chloride value of 532 mM occurs at 94 and 139 mbsf. These excursions deviate about 3.4% from the baseline chloride value, suggesting a gas-hydrate volume of ~1.5%, and assuming a sediment porosity of ~50%.

The chloride profile at Site 1059 is erratic in the upper 20 mbsf, varying between 547 and 561 mM. It shows some slight freshening downhole (Fig. 83), without any significantly anomalous chloride excursions. This profile does not suggest the presence of gas hydrate in the recovered sediments, but its downhole decreasing trend suggest the possible presence of gas hydrate at depth.

Discussion

Although gas hydrate was not directly observed, based on the interstitial chloride data they may underlie all of the intermediate was depth sites of the Blake Outer Ridge sites. Also, gas hydrate was cer-

Table 38. Results of vacutainer gas analyses of sediments from Sites 1056, 1057, 1058, and 1059.

Core, section, interval (cm)	Depth (mbsf)	C_1 (ppm)	C_2 (ppm)	C_3 (ppm)	i-C_4 (ppm)	i-C_5 (ppm)	C_1/C_2
172-1056B-							
5H-6, 75-76	39.1	54,584	ND	ND	ND	ND	—
8H-1, 22-23	60.8	832,452	201	17.0	ND	ND	4,142
9H-1, 88-89	71.0	921,710	224	20.0	ND	ND	4,115
10H-2, 5-6	80.1	935,827	290	21.0	1.0	ND	3,227
11H-4, 14-15	93.1	930,288	237	24.0	ND	ND	3,925
12H-3, 125-126	101.7	885,680	230	ND	ND	ND	3,851
13H-3, 100-101	111.7	802,785	185	23.5	ND	ND	4,339
14H-3, 100-101	121.6	920,239	223	35.0	2.3	ND	4,127
15H6, 100-101	134.8	853,208	200	32.5	2.0	1.4	4,266
16H-3, 100-101	139.6	1,182,064	280	49.0	5.0	3.0	4,222
17H-8, 100-101	156.5	689,510	155	29.0	4.6	2.3	4,448
172-1057A-							
8H-1,98-99	65.5	934,893	193	26.0	ND	ND	4,844
10H-1, 69-70	84.2	941,585	40	18.0	0.8	ND	23,540
11H-4, 40-41	97.1	940,945	206	20.0	5.0	ND	4,568
12H-3, 40-41	105.2	1,131,237	367	26.0	7.7	ND	3,082
13H-2, 40-41	113.0	790,007	121	17.6	6.2	ND	6,529
14H-6, 40-41	128.2	874,715	136	21.4	ND	ND	6,432
172-1058A-							
8H-1, 110-11	67.6	918,542	176	7.8	ND	ND	5,219
9H-1, 129-130	76.4	891,561	359	8.5	ND	ND	2,485
11H-2, 129-130	97.0	930,489	158	1.9	ND	ND	5,889
12H-3, 118-119	107.6	774,485	163	8.1	ND	ND	4,746
13H-3, 131-132	117.6	937,985	175	12.9	1.0	ND	5,363
14H-2, 17-18	124.1	1,210	1	12.9	1.0	ND	864
15H-3, 123-124	136.2	725,045	126	8.6	1.0	ND	5,754
16H-4, 1-2	145.8	1,264,794	219	20.2	5.0	ND	5,775
172-1059A-							
6H-1, 67-68	42.5	891,327	227	3.4	ND	ND	3,927
8H-2, 4-5	62.3	944,429	221	6.1	ND	ND	4,273
9H-3, 46-47	73.8	933,416	175	5.5	ND	ND	5,334
10H-4, 12-13	84.4	733,871	250	4.9	ND	ND	2,935
11H-2, 120-121	92.0	808,821	181	7.0	ND	ND	4,469

Note: ND = not detected; — = not applicable.

tainly cored at Site 1056, and possibly at Sites 1057 and 1058. No gas hydrate was cored at Site 1059, but its presence at depth is suggested by a downcore freshening trend in the chloride concentrations.

Most DSDP/ODP sites on the Blake Outer Ridge display strong, downhole freshening profiles indicative of gas hydrate below (Leg 11, Sites 102, 103, and 104; Sayles et al., 1972; Leg 76, Site 533, Jenden and Gieskes, 1983; Leg 164, Sites 994, 995, and 997, Paull, Matsumoto, Wallace, et al., 1996). Sites 1057, 1058, and 1059 also show chloride freshening with depth, but chloride concentrations at Site 1056 increase downhole.

The positive chloride gradient observed at Site 1056 is anomalous with respect to most other Blake Outer Ridge sites. Site 1056 is located approximately 6.6 nmi west of the most southerly diapir (the Blake Ridge Diapir; Paull, Matsumoto, Wallace, et al., 1996) emanating from the Carolina Trough, a north-northeast–south-southwest-trending basin subparallel to the continental margin (Dillon et al., 1982). Salt apparently forms the core of the diapir (Paull, Matsumoto, Wallace, et al., 1996), so that the positive chloride gradient observed at Site 1056 may reflect the presence of salt near the floor of the Carolina Trough. This conclusion is supported by an increase in salinity values toward the bottom of Hole 1056A (Table 41). Positive chloride gradients have been observed in other gas hydrate terrains (e.g., Kvenvolden and Kastner, 1990).

PHYSICAL PROPERTIES

Higher resolution sampling of the intermediate-depth sites along the Blake Outer Ridge combined with their higher sedimentation rates provide an opportunity to determine whether millennial-scale variations in physical properties have been recorded in these sediments. When time allowed, the MST was run at higher sampling rates to capture smaller scale variations, especially in the upper two to three cores where compressional wave velocities could be reliably recorded by the *P*-wave logger (PWL). The sampling interval for index properties and discrete compressional wave velocity measurements was increased to two per section of core with an emphasis on capturing variations driven by lithologic changes. Vane-shear measurements were supplemented at greater depths by pocket penetrometer measurements and measurement intervals were also increased to up to two per section of core when time allowed.

MST Measurements

GRAPE, bulk densities, and magnetic susceptibilities were measured on all unsplit sections. Because of gas expansion voids, PWL data could generally be collected only to a depth of 10 to 20 mbsf. The data collection depth for reliable PWL measurements decreased from >20 mbsf to ~16 mbsf between Sites 1058 and 1059, reflecting the shallower interface between sulfate reduction and methanogenesis zones (see “Organic Geochemistry” section, this chapter). The sampling interval for the three sensors’ measurements varied between 2 and 5 cm. To resolve the decimeter-scale variability, the upper cores of at least one hole at each site, starting with Site 1057, were measured at intervals of 2 to 3 cm, to as deep as the PWL sensor could collect reliable data. Natural gamma-ray (NGR) measurements were taken at 50-cm intervals from one hole at each site. The data from all four sensors (on CD-ROM, back pocket, this volume) are graphically presented in Figures 84 through 87.

At Sites 1056 to 1059 MST measurements show variations that are attributed to glacial–interglacial changes in sediment composition. Maxima in velocity, bulk density, magnetic susceptibility, and natural gamma ray are observed for glacial periods and are most probably caused by higher contents of clays and heavy minerals during these periods (see “Lithostratigraphy” section, this chapter). On the other hand, more carbonate-rich intervals are characterized by lower values. Changes from low to higher frequency variations in GRAPE, magnetic susceptibility, and NGR records are visible at Sites 1056 (64 mbsf), 1057 (94 mbsf), and 1058 (107 mbsf). These transitions are close to the Brunhes/Matuyama boundary (see “Mag-

Table 39. Results of coulometrics and elemental analyses from Sites 1056, 1057, 1058, and 1059.

Core, section, interval (cm)	Depth (mbsf)	IC (wt%)	$CaCO_3$ (wt%)	TC (wt%)	TOC (wt%)	TN (wt%)	TS (wt%)	C/N
172-1056B-								
1H-1, 92-93	0.9	6.38	53.16					
1H-2, 57-58	2.1	4.64	38.63	5.37	0.74	0.12	0.15	6.39
1H-3, 27-28	3.3	3.17	26.36					
2H-1, 37-38	4.0	4.31	35.87	4.30	0.44	0.10	0.16	4.54
2H-3, 52-53	7.1	5.85	48.72					
2H-4, 25-26	8.4	4.51	37.60	5.10	0.59	0.12	0.14	4.94
3H-2, 69-70	15.3	3.14	26.15	3.65	0.51	0.13	0.28	3.97
3H-4, 128-129	18.9	3.24	26.96	4.35	1.12	0.11	0.13	10.05
3H-5, 122-123	20.3	8.00	66.61					
4H-1, 89-90	23.5	5.51	45.90					
4H-4, 44-45	27.5	4.73	39.41					
4H-6, 122-123	31.3	5.23	43.54					
5H-1, 103-104	33.1	2.98	24.82	3.28	0.30	0.04	0.33	7.14
5H-3, 118-119	35.0	2.84	23.69	3.10	0.25	0.03	0.40	7.35
5H-5, 74-75	37.5	3.33	27.76					
6H-1, 94-95	42.5	3.59	29.89					
6H-3, 92-93	45.5	3.85	32.10	4.29	0.44	0.10	0.10	4.44
6H-5, 75-76	50.0	4.23	35.25					
7H-1, 73-74	51.8	3.29	27.39	3.87	0.58	0.12	0.55	4.94
7H-3, 73-74	54.8	3.60	30.01					
7H-5, 25-26	57.4	5.61	46.69					
8H-1, 65-66	61.3	2.27	18.90	2.85	0.59	0.14	0.57	4.06
8H-3, 35-36	64.0	4.01	33.43					
8H-5, 23-24	66.8	4.95	41.26					
9H-1, 110-111	71.2	4.69	39.04					
9H-3, 110-111	74.2	3.71	30.87					
9H-5, 110-111	77.2	3.40	28.34	3.93	0.52	0.14	0.00	3.82
10H1, 63-64	79.7	5.42	45.13					
10H-3, 63-64	82.1	5.50	45.85	6.13	0.63	0.08	0.26	8.40
10H-7, 64-65	88.1	4.72	39.28					
11H-1, 44-45	89.5	6.62	55.17					
11H-3, 44-45	91.9	2.17	18.03	2.29	0.12	0.12	0.07	1.04
11H-8, 67-68	99.6	2.10	17.48					
12H-2, 92-93	109.6	1.64	13.64	1.94	0.31	0.16	0.75	1.97
13H-4, 92-93	112.6	1.88	15.62					
13H-6, 90-91	115.6	2.61	21.73					
14H-1, 82-83	118.4	1.53	12.73	2.16	0.63	0.15	0.83	4.14
14H-2, 59-60	119.7	1.70	14.16					
14H-4, 47-48	122.6	3.08	25.63					
15H-1, 37-38	127.5	3.83	31.94					
15H-3,94-95	130.2	2.95	24.59	3.69	0.74	0.15	1.99	4.93
15H-5, 85-86	133.1	3.06	25.52					
16H-2, 48-49	137.6	3.95	32.91					
16H-5, 35-36	142.0	2.88	24.00	4.29	1.41	0.22	1.37	6.29
16H-8, 37-38	146.5	3.89	32.40					
17H-3, 57-58	148.6	3.67	30.55					
17H-5, 49-50	151.5	3.57	29.74	4.46	0.89	0.12	0.76	7.42
17H-6, 38-39	152.9	3.37	28.09	3.98	0.61	0.16	0.96	3.81
172-1057A-								
1H-1, 43-44	0.4	5.08	42.32					
1H-2, 129-130	2.8	2.08	17.33	2.64	0.56	0.07	0.05	7.96
1H-3, 31-32	3.3	2.73	22.77					
2H-4, 35-36	12.4	5.73	47.76					
2H-5, 118-119	14.7	3.42	28.46	3.89	0.47	0.05	0.00	9.40
2H-6, 25-26	15.3	3.39	28.20					
3H-1, 19-20	17.2	4.50	37.46					
3H-5, 64-65	23.6	2.79	23.24	3.22	0.43	0.05	0.25	8.56
3H-6, 87-88	25.4	2.33	19.40	2.54	0.21	0.04	0.28	5.35
4H-1, 57-58	27.1	3.68	30.67					
4H-3, 52-53	30.0	1.89	15.75	2.24	0.35	0.05	0.56	7.20
4H-5, 35-36	32.9	1.84	15.33	2.52	0.68	0.04	0.58	18.00
5H-1, 34-35	36.3	7.73	64.37					
5H-3, 46-47	39.5	4.85	40.41					
5H-5, 65-66	42.7	2.82	23.52	3.16	0.34	0.05	0.20	7.06
6H-1, 62-63	46.1	3.74	31.11					
6H-3, 33-34	48.8	2.37	19.78	2.56	0.19	0.01	0.16	13.50
6H-5, 49-50	52.0	6.67	55.56					
8H-1, 83-84	65.3	3.20	26.65					
8H-3, 80-81	68.3	2.86	23.85	3.36	0.50	0.07	0.41	7.09
8H-5, 80-81	71.3	2.59	21.57					
9H-2, 136-137	76.9	6.15	51.20					
9H-3, 138-139	78.4	1.29	10.77	1.79	0.50	0.07	0.97	7.10
9H-5, 52-53	80.5	3.03	25.24	3.80	0.77	0.10	0.43	7.70
10H-2, 136-137	86.4	2.08	17.30					
10H-3, 136-137	87.9	2.33	19.44					
10H-5, 52-53	90.0	1.67	13.88	1.99	0.32	0.05	0.00	6.48
11H1, 21-22	93.2	1.56	13.02	2.47	0.90	0.10	0.12	9.03
10H-3, 23-24	95.5	2.46	20.46					
11H-6, 109-110	100.8	3.65	30.38					
13H-2, 46-47	113.0	2.96	24.65	4.33	1.37	0.16	0.46	8.57
13H-4, 73-74	116.3	2.11	17.60	2.59	0.47	0.07	0.67	6.76
13H-6, 63-64	119.2	2.45	20.38					
14H-2, 48-49	122.2	3.11	25.89	4.00	0.89	0.13	0.97	6.82
14H-4, 101-102	125.8	2.63	21.92					
14H-7, 112-113	130.4	2.83	23.54	3.93	1.10	0.13	0.70	8.29
1H-1, 122-123	1.2	1.95	16.24	2.25	0.30	0.06	0.05	4.63

Table 39 (continued).

Core, section, interval (cm)	Depth (mbsf)	IC (wt%)	$CaCO_3$ (wt%)	TC (wt%)	TOC (wt%)	TN (wt%)	TS (wt%)	C/N
172-1058A-								
1H-3, 94-95	3.9	0.88	7.29	1.26	0.39	0.06	0.06	6.79
1H-5, 43-44	6.4	1.83	15.27					
2H-1, 120-121	10.7	1.57	13.07					
2H-3, 95-96	13.5	1.43	11.94	1.85	0.41	0.06	0.13	7.00
2H-5, 110-111	16.6	5.00	41.66					
3H-1, 132-133	20.3	4.83	40.19					
3H-3, 107-108	23.1	1.87	15.59	2.24	0.37	0.05	0.00	7.31
3H-5, 135-137	26.4	1.47	12.26	1.86	0.39	0.06	0.18	6.84
4H-1, 112-113	29.6	3.07	25.53					
4H-3, 13-14	31.6	4.17	34.72					
4H-5, 23-24	34.7	4.18	34.78					
5H-1, 43-44	38.4	3.20	26.67					
5H-3, 23-24	41.2	5.01	41.73					
5H-5, 32-33	44.3	3.22	26.80	3.61	0.40	0.05	0.31	7.54
6H-1, 45-46	48.0	3.99	33.26					
6H-3, 56-57	51.1	5.96	49.61					
6H-5, 45-46	54.0	6.36	53.01					
7H-2, 33-34	58.8	4.56	38.02	5.12	0.56	0.08	0.15	7.23
7H-4, 32-33	61.8	3.12	26.00					
7H-6, 34-35	64.8	2.89	24.03	3.47	0.59	0.07	0.95	8.27
8H-1, 42-43	66.9	2.66	22.12					
8H-3, 43-44	69.9	1.83	15.28	2.03	0.20	0.02	0.32	8.54
8H-5, 25-26	72.8	4.20	34.96					
9H-1, 128-129	77.3	2.69	22.38	3.28	0.59	0.06	0.06	10.40
9H-3, 98-99	79.9	1.90	15.85					
9H-5, 138-139	83.3	2.47	20.61	3.27	0.79	0.10	0.55	7.96
10H1, 48-49	86.0	1.65	13.73	2.01	0.36	0.05	0.72	7.44
10H-3, 15-16	88.6	2.02	16.82					
10H-5, 74-75	92.2	4.02	33.51					
11H-2, 62-63	96.3	4.84	40.30					
11H-3, 96-97	98.2	5.05	42.08					
11H-5, 83-84	101.0	0.80	6.64	1.20	0.40	0.07	0.05	6.05
12H-2, 45-46	105.4	0.87	7.21	1.17	0.31	0.04	1.26	7.68
12H-4, 32-33	108.2	2.78	23.17					
12H-5, 7-8	109.5	3.16	26.31	3.47	0.31	0.08	0.71	3.72
13H-2, 42-43	115.0	3.01	25.09					
13H-5, 42-43	119.5	1.73	14.42	2.39	0.66	0.09	1.10	7.11
13H-7, 49-50	122.6	1.92	15.96					
14H-2, 82-83	124.7	2.02	16.85	2.97	0.95	0.12	1.25	8.12
14H-4, 62-63	127.5	1.61	13.38					
14H-6, 62-63	130.5	1.92	16.02	2.87	0.94	0.13	0.31	7.54
15H-2, 63-64	134.1	1.03	8.59	1.68	0.65	0.09	0.81	7.41
15H-4, 43-44	136.9	2.81	23.41					
16H-2, 42-43	143.2	2.31	19.26	3.25	0.94	0.12	1.16	7.92
16H-5, 112-113	148.4	2.82	23.48					
16H-7, 10-11	150.4	2.22	18.51	3.54	1.32	0.14	0.95	9.38
172-1059A-								
1H-1, 118-119	1.18	2.91	24.23	3.37	0.46	0.09	0.09	5.18
1H-2, 118-119	2.68	1.60	13.31	2.21	0.61	0.10	0.13	6.18
2H-1, 125-126	5.05	1.39	11.57					
2H-3, 94-95	7.74	1.67	13.89	2.32	0.65	0.09	0.00	7.33
2H-5, 44-45	10.24	2.29	19.06	2.89	0.60	0.10	0.10	6.02
3H-1, 112-113	14.42	1.90	15.83					
3H-4, 112-113	18.92	1.88	15.62	2.39	0.52	0.08	0.18	6.44
3H-6, 122-123	22.02	1.05	8.77	1.87	0.82	0.11	0.43	7.43
4H-1, 124-125	24.04	4.41	36.76					
4H-3, 124-125	27.04	4.26	35.44					
4H-7, 102-103	31.54	4.32	35.98					
5H-2, 131-132	35.11	3.59	29.94	4.06	0.47	0.10	0.18	4.91
5H-4, 112-113	37.92	2.35	19.53					
5H-6, 131-132	41.21	2.37	19.77					
6H-2, 47-48	43.77	1.70	14.12	2.12	0.43	0.07	0.10	5.74
6H-5, 98-99	48.78	1.65	13.76	1.85	0.20	0.09	0.09	2.25
6H-7, 81-82	51.61	5.94	49.45					
7H-2, 43-44	53.23	2.74	22.82					
7H-4, 109-110	56.89	1.31	10.90	1.84	0.53	0.10	1.16	5.32
7H-6, 108-109	59.88	1.40	11.68	1.94	0.54	0.07	0.26	7.27
8H-1, 117-118	61.97	3.69	30.71					
8H-3, 33-34	64.13	3.80	31.69					
8H-5, 110-111	67.6	2.58	21.46	2.96	0.38	0.06	0.00	6.86
9H-1, 112-113	71.42	1.07	8.90	1.68	0.61	0.06	0.30	9.87
9H-3, 47-48	73.77	1.21	10.04					
9H-5, 108-109	77.38	4.54	37.78	5.67	1.14	0.13	0.33	8.73
10H-1, 23-24	80.03	2.53	21.07					
10H4, 35-36	84.65	1.32	10.98	1.92	0.60	0.08	0.31	7.82
10H-6, 113-114	88.43	2.49	20.70					
11H-1, 45-46	89.75	3.47	28.94	4.18	0.70	0.12	0.77	5.86
11H-3, 49-50	92.79	3.34	27.80					
11H-5, 42-43	95.17	2.67	22.20	3.29	0.63	0.10	0.23	6.25

Note: IC = inorganic carbon, TC = total carbon, TOC = total organic carbon, TN = total nitrogen, TS = total sulfur.

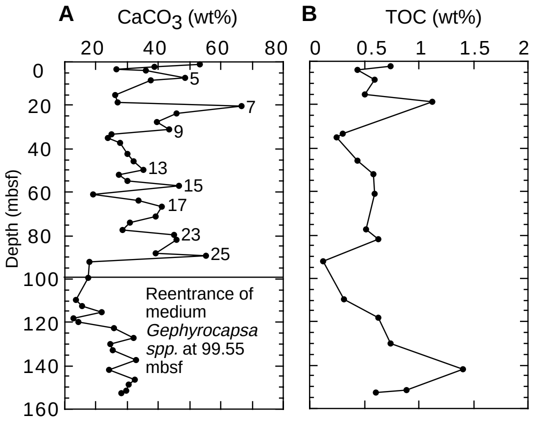

Figure 67. Downhole profile of (**A**) calcium carbonate content and (**B**) total organic carbon for Hole 1056B. Numbers along the curve in (A) denote MIS.

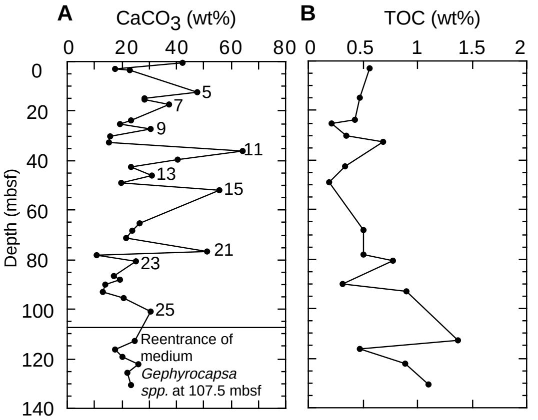

Figure 68. Downhole profile of (**A**) calcium carbonate content and (**B**) total organic carbon for Hole 1057A. Numbers along the curve in (A) denote MIS.

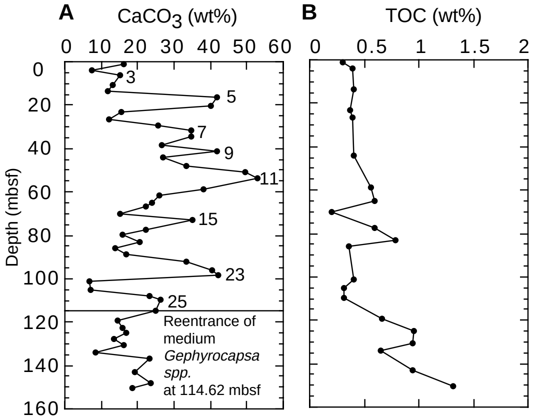

Figure 69. Downhole profile of (**A**) calcium carbonate content and (**B**) total organic carbon for Hole 1058A. Numbers along the curve in (A) denote MIS.

netostratigraphy” section, this chapter), suggesting that the variability above and below the transition is driven by 100- and 40-k.y. climatic cycles, respectively. At Sites 1057 and 1058 the transitions correlate with the boundary between lithostratigraphic Units I and II (see “Lithostratigraphy” section, this chapter).

Bulk density records measured with the GRAPE show an increasing noisiness of the data with depth, most probably caused by an increasing amount of microscopic gas bubbles. Gas bubbles and voids

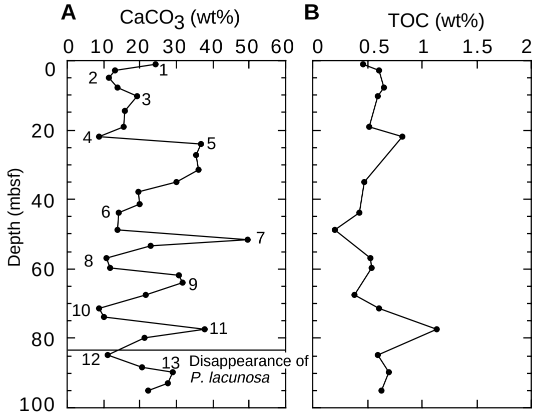

Figure 70. Downhole profile of (**A**) calcium carbonate content and (**B**) total organic carbon for Hole 1059A. Numbers along the curve in (A) denote MIS.

are characterized by low density spikes. However, discrete gravimetric and whole-core measurements of bulk density generally agree in trend (see “Index Properties” section below) and display a decrease in density below the observed transition zones.

The magnetic susceptibility pattern is very similar for all the sites when the different sedimentation rates are considered. Over long intervals a weak susceptibility signal ($<20 \times 10^{-5}$ SI units) with interglacial values of $5–8 \times 10^{-5}$ SI units and glacial values of $10–12 \times 10^{-5}$ SI units is observed. On the other hand, certain glacial intervals are characterized by much higher susceptibilities of $>100 \times 10^{-5}$ SI units.

NGR counts and magnetic susceptibility show similar cyclicity. This indicates that the long-term covariation is related to a variable clay input (Hoppie et al., 1994), except for the high susceptibility intervals where the relatively weak paramagnetic susceptibility of the clay minerals is considerably enhanced by the presence of a ferromagnetic component, possibly of diagenetic origin.

Index Properties

Index properties samples were taken at a spacing of approximately two per section from Sites 1056 through 1059 (Tables 42–45).

Bulk density, which shows a similar trend at all sites (Figs. 88–91), increases from 1.5–1.6 g/cm^3 at the surface to 1.8–1.9 g/cm^3 at 80–110 mbsf. Superimposed on the general trend are cyclical fluctuations caused by varying grain density and water content with a 100-k.y. periodicity (based on the biostratigraphic age model; see “Biostratigraphy” section, this chapter). At Holes 1056A, 1057A, and 1058A, bulk density decreases below 90, 90, and 110 mbsf, respectively. At Hole 1056A, the transition appears relatively progressive. At Hole 1057A, the transition occurs below a 5-m-thick disturbed layer with a high bulk density (1.9 g/cm^3) at 80 mbsf. At Site 1058, although no disturbed layer was noted, the transition is similarly sharp and occurs at 110 mbsf. Site 1059 did not intersect a zone of low bulk density. The cyclicity observed in index measurements of bulk density matches that observed in the GRAPE data.

Grain density shows cyclical variations with low values typically around 2.70 g/cm^3 and high values around 2.78 g/cm^3 (Figs. 88–91). Of note is a low-density event (2.60–2.62 g/cm^3) recorded in Hole 1058A at 19 mbsf (Fig. 90) and Hole 1059A at 25 mbsf (Fig. 91). Mean grain density increases downslope from 2.710 g/cm^3 at Site 1056 to 2.729 g/cm^3 at Site 1059 (Table 46).

Porosity and water content at these sites vary inversely with bulk density (Figs. 88–91). All sites have maximum porosity values in the first two meters below the seafloor of 72%–80%. Porosity decreases with depth to minimum values of 44%–51% at 80–100 mbsf. Porosity then abruptly increases again to ~60% below 100 mbsf (at Sites 1057 and 1058) and remains at this level to the base of the holes. In

Table 40. Results of Rock-Eval analyses from Sites 1056, 1057, 1058, and 1059.

Core, section, interval (cm)	Depth (mbsf)	TOC (%)	T_{max} (°C)	S_1	S_2	S_3	S_2/S_3	PC	HI	OI	PI
172-1056B-											
7H-1, 73-74	51.8	0.58	400	0.08	0.40	1.51	0.26	0.04	68	260	0.17
8H-1, 65-66	61.3	0.59	506	0.02	0.35	1.00	0.35	0.03	59	169	0.06
10H-3, 63-64	82.1	0.63	399	0.12	0.49	2.03	0.24	0.05	77	322	0.20
15H-3, 94-95	130.2	0.74	413	0.09	1.05	1.56	0.67	0.09	141	210	0.08
16H-5, 35-36	133.1	1.41	412	0.41	3.68	2.22	1.65	0.34	260	157	0.10
17H-5, 49-50	151.5	0.89	414	0.25	1.81	2.02	0.89	0.17	203	226	0.12
17H-6, 38-39	152.9	0.89	390	0.14	0.79	1.39	0.56	0.07	88	156	0.15
172-1057A-											
1H-2, 129-130	2.8	0.56	433	0.04	0.35	1.87	0.18	0.03	62	333	0.11
4H-5, 35-36	32.9	0.68	522	0.03	0.31	1.01	0.30	0.02	45	148	0.09
8H-3, 80-81	68.3	0.58	390	0.10	0.48	1.57	0.30	0.04	82	270	0.17
9H3, 138-139	78.4	0.50	488	0.04	0.34	1.28	0.26	0.03	68	256	0.11
9H-5, 52-53	80.5	0.77	398	0.22	1.04	1.86	0.55	0.10	135	241	0.17
11H-1, 21-22	93.2	0.90	414	0.15	1.39	1.64	0.84	0.12	154	182	0.10
13H-2, 46-47	113	1.37	418	0.30	2.23	2.58	0.86	0.21	162	188	0.12
14H-2, 48-49	122.2	0.89	418	0.17	1.60	2.26	0.70	0.14	179	253	0.10
14H-7, 112-113	130.4	1.10	416	0.22	1.84	2.29	0.80	0.17	167	208	0.11
172-1058A-											
7H-2, 34-35	58.8	0.56	396	0.13	0.76	2.19	0.34	0.07	135	391	0.15
7H-6, 34-35	64.8	0.59	407	0.13	0.91	1.76	0.51	0.08	154	298	0.12
9H-1, 128-129	77.3	0.59	425	0.04	0.46	1.31	0.35	0.04	77	222	0.08
9H-5, 138-139	83.3	0.79	411	0.15	1.19	1.65	0.72	0.11	150	208	0.11
13H-5, 42-43	119.5	0.66	409	0.08	0.68	1.69	0.40	0.06	103	256	0.11
14H-2, 82-83	124.7	0.95	415	0.20	1.61	1.78	0.90	0.15	169	187	0.11
14H-6, 62-63	130.5	0.94	424	0.32	1.81	2.22	0.81	0.17	192	236	0.15
15H-2, 63-64	134.1	0.65	410	0.10	0.86	1.55	0.55	0.08	132	238	0.10
16H-2, 42-43	143.2	0.94	413	0.25	1.64	2.12	0.77	0.15	174	225	0.13
16H-7, 10-11	150.4	1.32	419	0.27	2.80	2.19	1.27	0.25	212	165	0.09
172-1059A-											
1H-2, 118-119	2.68	0.61	247	0.16	0.64	1.51	0.42	0.06	104	247	0.20
2H-3, 94-95	7.74	0.65	206	0.24	0.80	1.34	0.59	0.08	123	206	0.23
2H-5, 44-45	10.24	0.60	325	0.25	0.47	1.95	0.24	0.06	78	325	0.35
3H-4, 112-113	18.92	0.52	290	0.14	0.38	1.51	0.25	0.04	73	290	0.27
3H-6, 122-123	22.02	0.82	247	0.12	0.39	2.03	0.19	0.04	47	247	0.24
7H-6, 108-109	59.88	0.54	216	0.19	0.70	1.17	0.59	0.07	129	216	0.22
9H-1, 112-113	71.42	0.61	150	0.11	0.40	0.92	0.43	0.04	65	150	0.22
9H-5, 108-109	77.38	0.70	228	0.18	0.55	1.6	0.34	0.06	78	228	0.25
11H-1, 45-46	89.75	1.14	200	0.33	1.88	2.29	0.82	0.18	164	200	0.15
11H-5, 42-43	95.17	0.63	233	0.2	0.99	1.47	0.67	0.09	157	233	0.17

Note: TOC = total organic carbon, PC = petroleum potential, HI = hydrogen index, OI = oxygen index, and PI = production index.

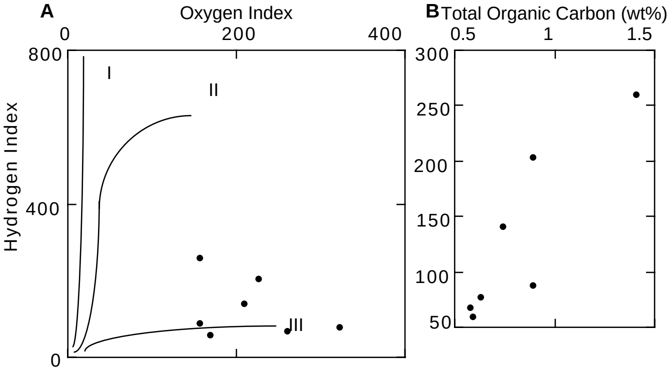

Figure 71. Organic matter properties for Hole 1056B. **A.** Rock-Eval van Krevelen-type diagram of sediments (Hydrogen Index = mg HC/g TOC, Oxygen Index = mg CO_2/g TOC). The curves I, II, and III refer to three types of organic matter: type I = algal, oil-prone organic matter; type II = marine, oil/gas-prone organic matter; and type III = terrestrial/gas-prone organic matter. **B.** Comparison of Rock-Eval Hydrogen Index values and total organic carbon concentrations of selected samples.

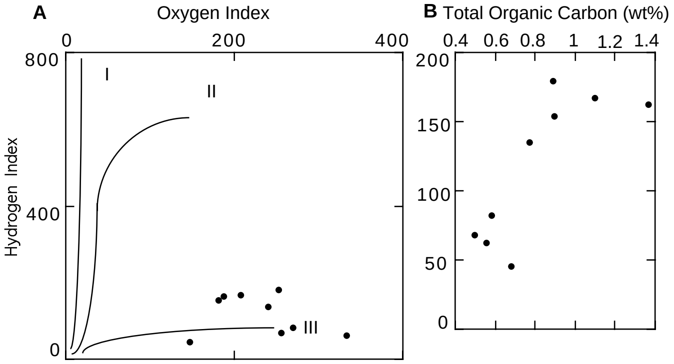

Figure 72. Organic matter properties for Hole 1057A. **A.** Rock-Eval van Krevelen-type diagram of sediments (Hydrogen Index = mg HC/g TOC, Oxygen Index = mg CO_2/g TOC). Curve types as in Figure 71. **B.** Comparison of Rock-Eval Hydrogen Index values and total organic carbon concentrations of selected samples.

Hole 1056A, porosity increases in a more gradual manner from 100 mbsf to the base of the hole.

Discrete Velocity Measurements

Compressional wave velocities were measured on split cores (Tables 47–50) in the longitudinal (z) and transverse (y) directions using the Digital Sonic Velocimeter (DSV). DSV-measurements are generally in reasonable agreement with the PWL data for whole-round samples obtained on the MST (Fig. 92). In some intervals, however, the discrete DSV values are significantly higher.

Sound waves propagate through a continuous medium at a constant speed. The presence of both micropores and macroscopic cracks caused by gas expansion are discontinuities that preclude accurate measurements of the sound velocity of the sediments below a certain depth level (Fig. 92). For DSV measurements, this level is at ~30 mbsf at the shallowest site (Site 1056) and becomes shallower with increasing water depth, probably reflecting shallowing of the methanogenesis zone. Another observation in correlation with water depth is the decreasing average velocity from 1525 m/s at Site 1056 to 1490 m/s at Sites 1058 and 1059. The average velocity value for Site 1057 is 1505 m/s. There is no significant trend visible in the velocity records, except at Site 1059, where increasing velocity from about 1480 to 1520 m/s is observed in the upper 20 mbsf.

Shear Strength

At Sites 1056 through 1059 one or two measurements of undrained shear strength (Tables 51–54) were taken per section using the vane-shear device and the pocket penetrometer (see “Explanatory Notes” chapter, this volume). In general, shear strength increases from about 2 kPa at the seafloor to 120 kPa at 160 mbsf (Fig. 93). At Site 1056, a lower gradient of 0.38 kPa/m is observed, compared with 0.5 kPa/m at the deeper sites. Superimposed on the general trend is a curvature that shows similarities with the water content record (Figs. 88–91). Normalized shear strength expressed by the ratio of undrained to the effective overburden stress (S_u/P_o') shows only minor variations (Fig. 94). The average S_u/P_o' ratio of 0.12 is similar to that of the Carolina Slope sites (see “Physical Properties” section, “Carolina Slope” chapter, this volume), indicating that sediments are underconsolidated.

Thermal Conductivity

Thermal conductivity for Sites 1056 through 1059 was generally measured three times per core when time was available (Tables 55–58). The range of measurements (0.6–1.2 W/[m·K]) and their average values (0.96–0.99 W/[m·K]) are remarkably constant for all four sites (Fig. 95). There is no distinctive depth trend for the thermal conductivity data in any of the sites.

Resistivity Calibrations and Measurements

Resistivity at Sites 1056 through 1059 was measured using the Wayne-Kerr Precision Component Analyzer with a four-electrode probe (see “Physical Properties” section, “Explanatory Notes” chapter, this volume). In general, two measurements per section were made (Tables 59–62). Resistivity at these sites is largely controlled by porosity (Fig. 96) indicating that variations in tortuosity and conductive mineral phases are low at these sites.

Evaluation of Millennial-Scale Variability at Site 1059

A primary goal of Leg 172 was to examine millennial-scale variations in climate and paleoceanography. Cursory examination of MST data from Holes 1059A and 1059C suggests that millennial-scale variations of physical properties exist within the uppermost sediments at this site and that these variations are correlatable between holes.

A 2-cm sampling interval for GRAPE-density and *P*-wave velocity within the top two cores for Holes 1059A and 1059C allowed us to examine fine-scale variability of physical properties in a depth range where the formation of voids by gas expansion had not yet degraded the quality of these data. Acceptable quality *P*-wave data extended to only 13.22 mbsf from Hole 1059A and 15.45 mbsf from Hole 1059C and, thus, limited this study.

Conversion of the bulk densities and compressional wave velocities measured with the MST to acoustic impedance (= bulk density × the compressional wave velocity) enabled us to examine the seabed acoustic properties within the upper 15 m at these two holes (Fig. 97). The overall trend at both holes is very similar. An initial drop in acoustic impedance in the uppermost core section is followed by a gradual, sometimes stepwise, increase in values to peak values at 10.4 mbsf (Hole 1059A) and 10.6 mbsf (Hole 1059C).

The pattern of variability at both holes is similar, suggesting variation of acoustic impedance on a scale of 0.2 to 0.5 m. Given that the average sedimentation rate at this site is about 40 cm/k.y., 0.2- to 0.5-m variations in acoustic impedance translate to temporal variations on a 500- to 1000-yr scale.

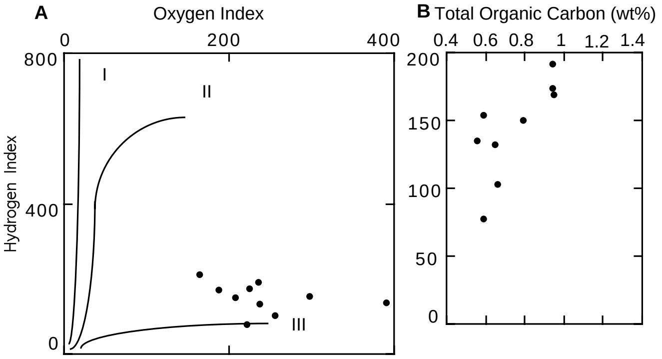

Figure 73. Organic matter properties for Hole 1058A. **A.** Rock-Eval van Krevelen-type diagram of sediments (Hydrogen Index = mg HC/g TOC, Oxygen Index = mg CO_2/g TOC). Curve types as in Figure 71. **B.** Comparison of Rock-Eval Hydrogen Index values and total organic carbon concentrations of selected samples.

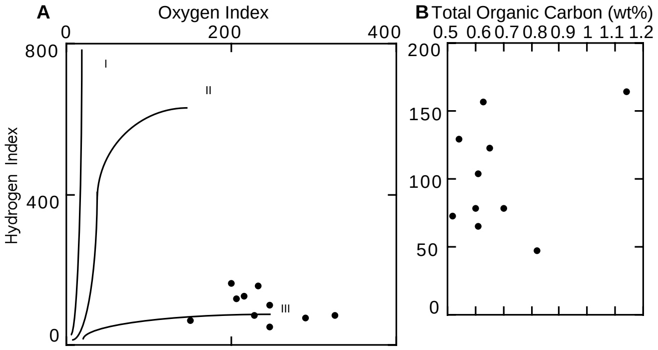

Figure 74. Organic matter properties for Hole 1059A. **A.** Rock-Eval van Krevelen-type diagram of sediments (Hydrogen Index = mg HC/g TOC, Oxygen Index = mg CO_2/g TOC). Curve types as in Figure 71. **B.** Comparison of Rock-Eval Hydrogen Index values and total organic carbon concentrations of selected samples.

The prominent spike in acoustic impedance seen at 10.4 and 10.6 mbsf at Holes 1059A and 1059C, respectively, was examined in more detail (Fig. 98) because of its magnitude and the likelihood that it could form an acoustic reflector in the 3.5-kHz record. The two spikes are similar in width, magnitude, and details. Both fall within a single core section, away from section boundaries, and are unlikely to be caused by measurement artifacts induced by splitting the core into sections before running them through the MST. On closer examination, both acoustic impedance spikes are the result of covariation in both bulk density and compressional wave velocity (Fig. 99). Within this interval, the sediments recovered from both holes become denser and exhibit higher compressional wave velocities.

Preliminary examination of the lithology of this interval reveals no obvious reason for the observed increases in bulk density and compressional wave velocity. The interval falls within a zone of homogeneous clay, separate from either the zones of higher carbonate or black, pyrite-rich banding, and represents millennial-scale variation in sediment properties that are unrelated to some artifact of sample collection or measurement technique. By analogy, many of the other submeter-scale variations in physical properties seen in these cores may also be due to processes operating on a similar time scale.

Table 41. Interstitial water analyses for Holes 1056B, 1057A, 1058A, and 1059A.

Core, section, interval (cm)	Depth (mbsf)	pH	Alkalinity (mM)	Salinity	Cl (mM)	SO_4 (mM)	PO_4 (µM)	NH_4 (µM)	Na (mM)	Mg (mM)	Ca (mM)	K (mM)	SiO_2 (µM)
172-1056B-													
1H-2, 145-150	2.95	7.43	6.529	34.5	558	22.85	14	540	479	51.14	8.33	12.01	522
2H-5, 145-150	11.05	7.62	12.359	33.5	542	8.96	32	1000	465	43.68	3.94	11.90	628
3H-5, 145-150	20.50	7.48	14.602	32.0	547	0.15	34	1000	472	36.06	2.84	12.00	552
4H-5, 145-150	30.00	7.62	15.650	32.0	551	0.00	27	1630	480	33.94	3.21	12.33	604
5H-5, 145-150	38.20	7.62	16.591	32.0	550	0.19	32	2380	481	33.55	3.11	12.44	622
6H-5, 140-150	49.10	7.49	17.937	32.5	559	0.35	32	3030	492	33.36	2.93	12.77	652
7H-5, 140-150	58.60	7.46	20.828	32.5	495	0.14	32	2060	429	34.09	2.92	12.61	591
8H-6, 140-150	69.50	7.69	22.089	33.0	561	0.54	30	4640	498	34.14	2.47	13.30	633
9H-5, 140-150	77.50	7.16	24.196	33.0	515	0.75	30	5280	453	35.03	2.80	12.49	761
10H-6, 140-150	87.40	7.56	25.514	33.5	563	0.01	36	5500	502	34.20	2.55	13.15	735
11H-6, 140-150	97.35	7.41	28.810	34.0	552	0.17	41	5500	493	34.38	2.93	13.53	778
12H-6, 140-150	106.36	7.52	28.936	33.5	508	0.18	32		449	34.54	2.68	13.66	834
13H-5, 140-150	114.59	7.62	31.196	34.0	564	0.15	34	5500	505	35.16	3.04	13.74	771
14H-4, 140-150	123.50	7.55	33.557	34.5	559	0.15	41	5500	502	34.93	3.27	13.95	756
15H-5, 140-150	133.60	7.38	32.860	34.5	572	0.14	36	6350	514	34.91	3.07	14.96	832
16H-6, 140-150	144.54	7.27	35.598	35.0	565	0.00	38	7210	511	34.33	3.16	14.48	834
17H-6, 140-150	153.89	7.31	36.260	35.0	560	0.00	43	7640	504	35.41	3.28	14.52	912
172-1057A-													
1H-3, 145-150	4.45	7.38	9.884	34.0	558	18.84	38	710	481	48.86	7.32	11.79	541
2H-4, 145-150	13.40	7.46	15.719	32.5	560	4.24	47	1550	485	41.27	2.85	11.32	455
3H-3, 145-150	24.40	7.60	19.046	32.0	560	0.16	71	2430	492	35.71	2.25	11.49	546
4H-6, 145-150	35.40	7.44	18.948	32.0	561	0.00	67	3070	495	34.04	2.32	11.88	566
5H-6, 145-150	44.90	7.49	20.772	32.0	558	0.00	65	3930	499	31.98	2.28	11.69	561
6H-6, 140-150	54.40	7.73	22.441	32.0	560	0.36	52	4740	506	30.21	1.90	12.83	453
7H-6, 140-150	63.90	7.63	24.396	32.0	561	0.03	80	5140	511	29.07	1.92	12.32	685
8H-6, 140-150	73.40	7.80	26.187	32.0	558	0.00	71	5750	513	27.19	1.85	12.78	574
9H-6, 140-150	82.90	7.65	28.013	32.0	558	0.00	85	6410	517	26.36	2.23	12.28	691
10H-6, 140-150	92.40	7.67	30.098	32.0	552	0.00	133	7010	517	24.78	2.16	11.35	720
11H-6, 140-150	101.14	7.75	31.644	32.0	510	0.00	131	7320	477	23.98	2.39	11.51	793
12H-6, 140-150	109.18	7.75	33.356	32.0	541	0.48	118	8030	514	22.75	1.98	11.43	773
13H-6, 140-150	118.46	7.95	33.221	32.0	538	0.00	107	8740	510	22.30	2.38	11.94	784
14H-6, 140-150	127.65	7.75	35.642	32.0	544	0.40	85	8530	525	19.63	1.68	12.58	733
172-1058A-													
1H-5, 145-150	7.45	7.38	20.587	33.5	562	9.24	126	1650	488	45.84	5.22	11.43	661
2H5, 140-150	16.90	7.34	28.238	33.0	564	0.21	139	2430	492	41.94	2.54	11.23	723
3H-5, 140-150	26.40	7.46	27.856	33.0	562	0.20	131	2810	496	39.03	2.05	12.20	582
4H-5, 140-150	35.90	7.66	28.161	32.5	562	0.17	137	3400	499	37.49	2.14	12.42	736
5H-5, 140-150	45.40	7.63	29.997	33.0	557	0.08	137	3770	498	35.95	1.99	12.82	672
6H-5, 140-150	54.90	7.58	31.043	33.0	551	0.12	131	4130	496	35.04	1.96	12.29	639
7H-5, 140-150	64.40	7.60	31.151	33.0	551	0.11	129	4790	500	33.43	1.89	12.22	827
8H-5, 140-150	73.90	7.50	31.703	32.5	547	0.11	137	4890	498	32.28	1.82	12.62	729
9H-6, 140-150	84.90	7.44	32.237	32.5	544	0.00	135	5700	499	30.60	1.89	12.25	840
10H-5, 140-150	92.87	7.54	33.238	32.5	532	0.00	148		492	28.86	1.90	11.92	736
11H-7, 140-150	104.61	7.58	35.421	32.5	544	0.46	153	6260	509	27.58	1.96	12.51	758
12H-5, 140-150	110.80	7.52	36.982	32.5	551	0.31	140	6710	519	26.60	1.80	12.63	846
13H-5, 140-150	120.65	7.76	36.407	33.0	544	0.18	128	7220	513	25.82	1.68	13.11	809
14H-7, 140-150	132.80	7.60	40.929	33.0	541	0.00	128	7370	515	25.18	1.71	12.86	924
15H-5, 140-150	139.32	7.71	42.135	33.0	532	0.35	113	6910	509	24.69	1.68	13.13	793
16H-5, 140-150	148.66	7.69	44.634	33.0	551	0.00	120	7270	531	24.15	1.79	12.79	851
172-1059A-													
1H, 1, 145-150	1.45	7.47	6.13	35.0	559	24.45	27	250	479	51.34	9.81	12.47	577
1H, 2, 145-150	2.95	7.39	9.85	34.5	559	21.07	82	650	480	50.81	8.70	11.97	655
2H, 1, 145-150	5.25	7.64	19.38	34.0	560	9.56	90	1560	481	46.41	6.16	12.62	490
2H, 2, 145-150	6.75	7.58	20.52	34.0	560	6.68	178	2010	481	45.31	5.44	11.49	585
2H, 3, 145-150	8.25	7.74	25.55	33.5	557	3.15	201	2240	479	45.05	4.10	11.59	505
2H, 4, 145-150	9.75	7.82	29.59	33.5	560	1.04	244	2500	486	43.77	3.11	11.46	659
2H, 5, 145-150	11.25	7.75	28.56	33.0	552	0.53	168	2660	477	43.65	2.75	11.45	722
2H, 6, 145-150	12.75	7.75	29.80	33.0	561	0.21	80	2920	485	44.42	2.93	11.29	633
3H, 1, 145-150	14.75	8.28	31.53	33.0	547	0.24	125	3250	473	44.54	2.76	11.34	688
3H, 2, 145-150	16.25	8.18	31.46	33.5	557	0.95	94	3340	483	44.65	3.13	11.49	618
3H, 3, 145-150	17.75	8.13	31.77	34.0	556	0.50	121	3230	484	43.91	2.86	11.31	629
3H, 4, 145-150	19.25	7.75	31.65	33.5	553	0.81	103	3160	479	44.45	3.40	11.44	609
3H, 5, 145-150	20.75	7.40	32.54	33.0	558	0.46	160	2870	487	43.47	2.52	12.00	670
3H, 6, 145-150	22.25	7.74	31.40	33.5	551	0.39	195	3090	481	42.72	2.37	11.82	609
4H, 6, 62-72	30.42	7.74	30.56	33.0	563	0.00	205	3270	493	42.06	2.26	11.84	766
5H, 5, 150-160	39.80	8.08	29.61	32.5	552	0.46	191	4070	488	39.31	2.36	11.52	692
6H, 6, 140-150	50.70	7.25	29.41	33.0	558	0.00	166	4400	493	39.13	2.15	11.89	722
7H, 6, 140-150	60.20	7.82	30.61	33.0	555	0.00	203	4870	492	38.76	2.22	11.93	753
8H, 6, 140-150	69.40	7.64	30.34	33.0	557	0.09	185	4910	497	37.47	2.07	11.66	668
9H, 5, 140-150	77.70	7.69	30.57	33.0	552	0.00	156	5010	494	36.20	2.05	11.96	742
10H, 4, 140-150	85.70	7.75	28.35	33.0	554	0.26	168	5010	497	34.71	2.26	11.63	736
11H, 7, 140-150	96.15	7.75	31.17	33.0	553	0.08	135	5200	501	33.65	2.02	12.34	814

Note: Blank values in the table indicate that measurements were not made.

SITE GEOPHYSICS

The Survey

At 1300 hr (local time) on 23 February 1997, we deployed the seismic gear for a survey of Sites 1056 and 1057 (Line 2). A north–south survey line was collected over Site 1056 at 6 kt followed by a west-to-east crossing line (Fig. 100). The survey gear was left in as the ship followed a southeast course toward Site 1057 at 8 kt. The *JOIDES Resolution* again slowed to 6 kt as it crossed over Site 1057 on a northwest-to-southeast course and made an east-to-west crossing line slightly south of Site 1057 (Fig. 101). This was the second survey of Leg 172. The total survey length was 85 km. The multichannel streamer failed again during this survey, but was later fixed by changing the polarity of its pin configuration.

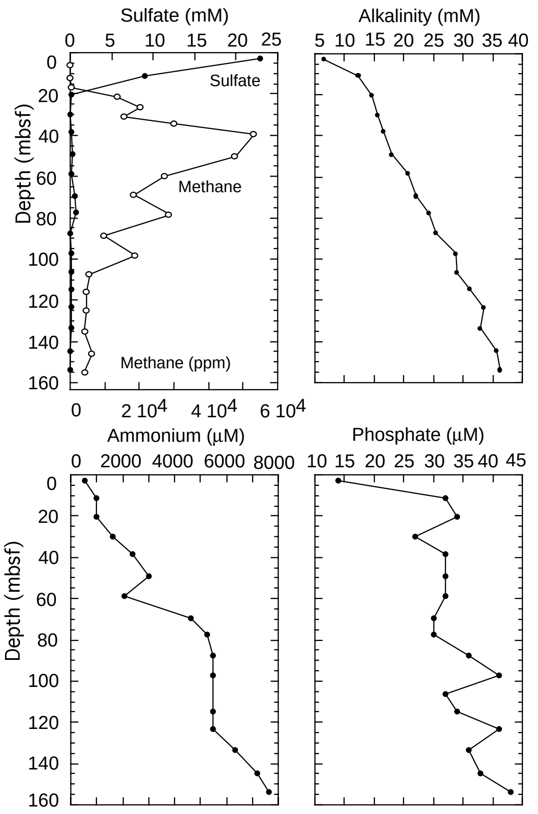

Figure 75. Concentration vs. depth profiles for interstitial waters, Hole 1056B.

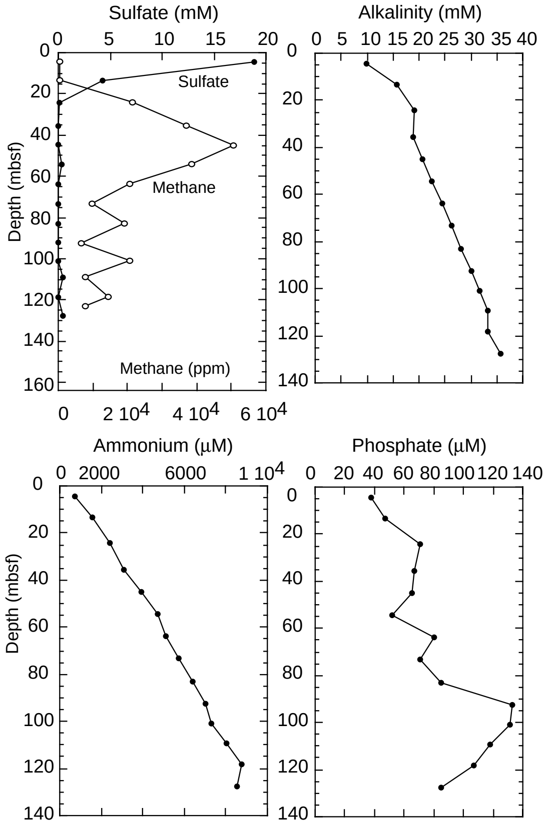

Figure 76. Concentration vs. depth profiles for interstitial waters, Hole 1057A.

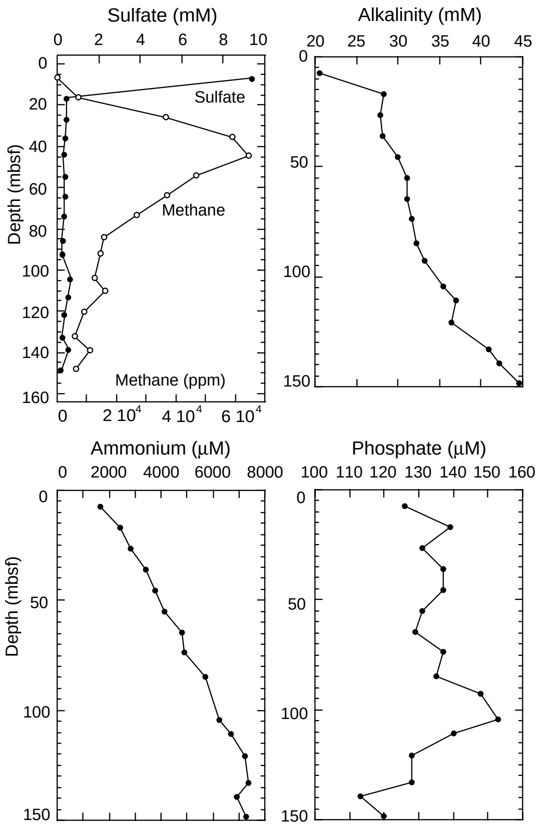

Figure 77. Concentration vs. depth profiles for interstitial waters, Hole 1058A.

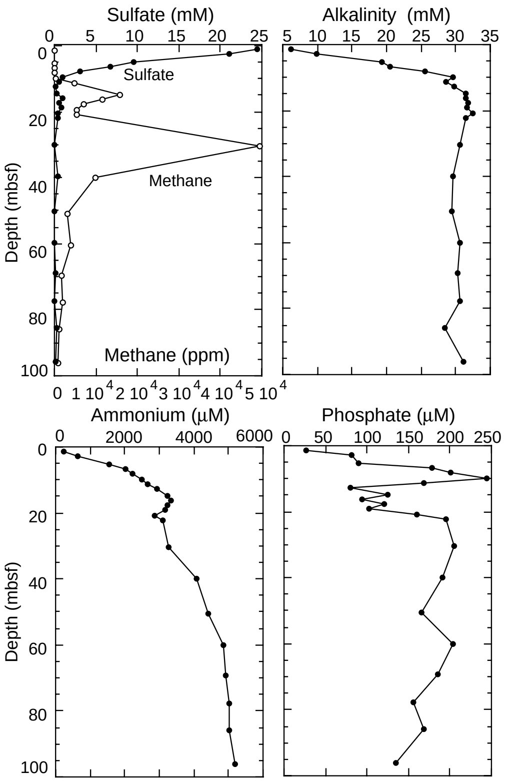

Figure 78. Concentration vs. depth profiles for interstitial waters, Hole 1059A.

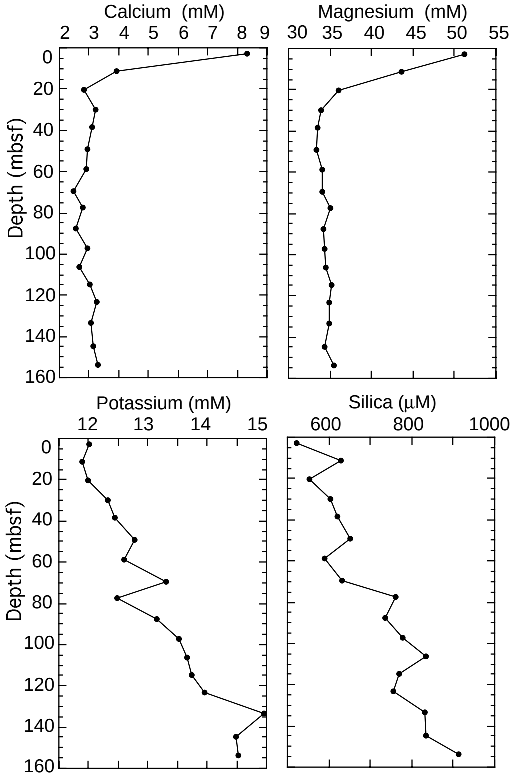

Figure 79. Concentration vs. depth profiles for interstitial waters, Hole 1056B.

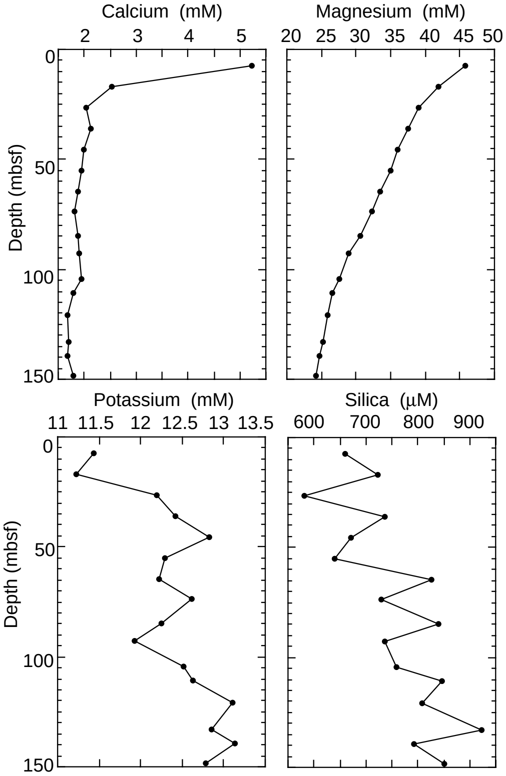

Figure 81. Concentration vs. depth profiles for interstitial waters, Hole 1058A.

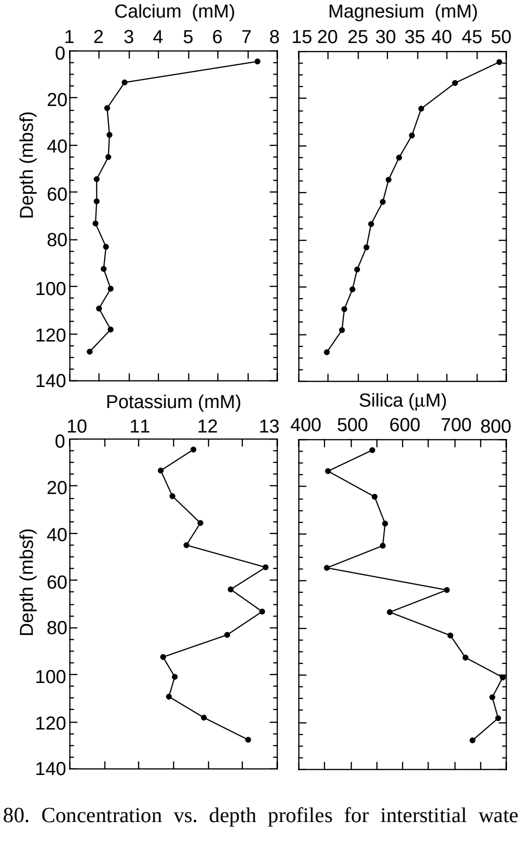

Figure 80. Concentration vs. depth profiles for interstitial waters, Hole 1057A.

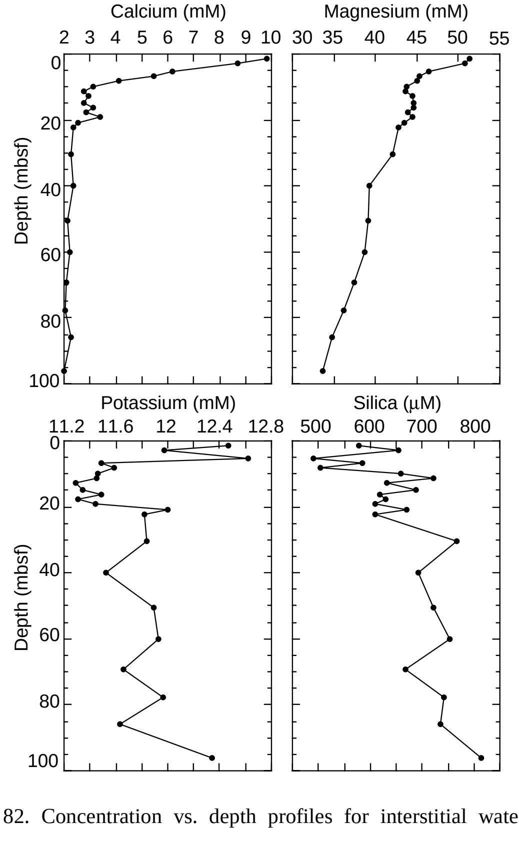

Figure 82. Concentration vs. depth profiles for interstitial waters, Hole 1059A.

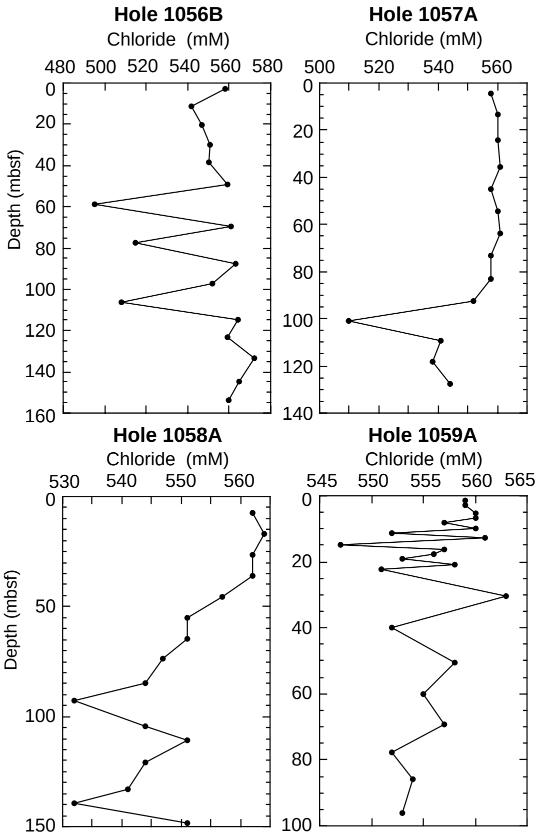

Figure 83. Downhole chloride profiles for holes 1056B, 1057A, 1058A, and 1059A.

Following coring operations at Site 1057, we had a 30-nmi transit to Site 1058, and then began the third seismic survey of Leg 172 (Line 3). At 1745 hr, the vessel slowed as the seismic gear was deployed about 8 nmi before Site 1058. The survey proceeded over both sites along a southeasterly course (Fig. 102). The vessel came about and performed a northeast-to-southwest crossing over Site 1059 and then a southwest-to-northeast crossing over Site 1058. During the 24-km-long survey, data were collected simultaneously with a single-channel and a six-channel streamer. Accurate survey and drilling positions were obtained owing to the availability of differential GPS.

PDR (3.5-kHz) Data

The 3.5-kHz record at Sites 1056 and 1057 shows a clear seafloor reflection and few very shallow reflections below. The chart recorder record for neither Sites 1056 and 1057 nor for Sites 1058 and 1059 is exceptional, partly because at the depth of these sites (2100−3000 m), the chart recorder prints part of the record at the top and part at the bottom of the paper copy. Regardless, the deepest reflectors imaged by the echo sounder are not nearly as deep at the intermediate-water-depth sites (particularly Sites 1056 and 1057) as at the shallower or deeper sites in the Leg 172 depth transect. For example, at Site 1056 the deepest reflector is only 0.015 s two-way traveltime (TWT) below the seafloor (about 11 mbsf; for the depth estimates we use a velocity of 1500 m/s). Similarly, at Site 1057, the deepest reflector is at about 0.022 s TWT (16 mbsf).

A high-quality 3.5-kHz record was collected on the same track as Line 3 during the precruise survey (*Knorr*, Cruise 140, Leg 2; Fig. 103). The 3.5-kHz profile shows that sediment layers thicken toward the southwest. Halfway between Sites 1058 and 1059, the thickening becomes pronounced and the character of the sediment surface changes. The hummocky seafloor at Site 1059 is likely the result of small furrows which create a rougher sea bed. Hyperbolic seafloor reflections, caused by larger furrows, are present at the southeast end of

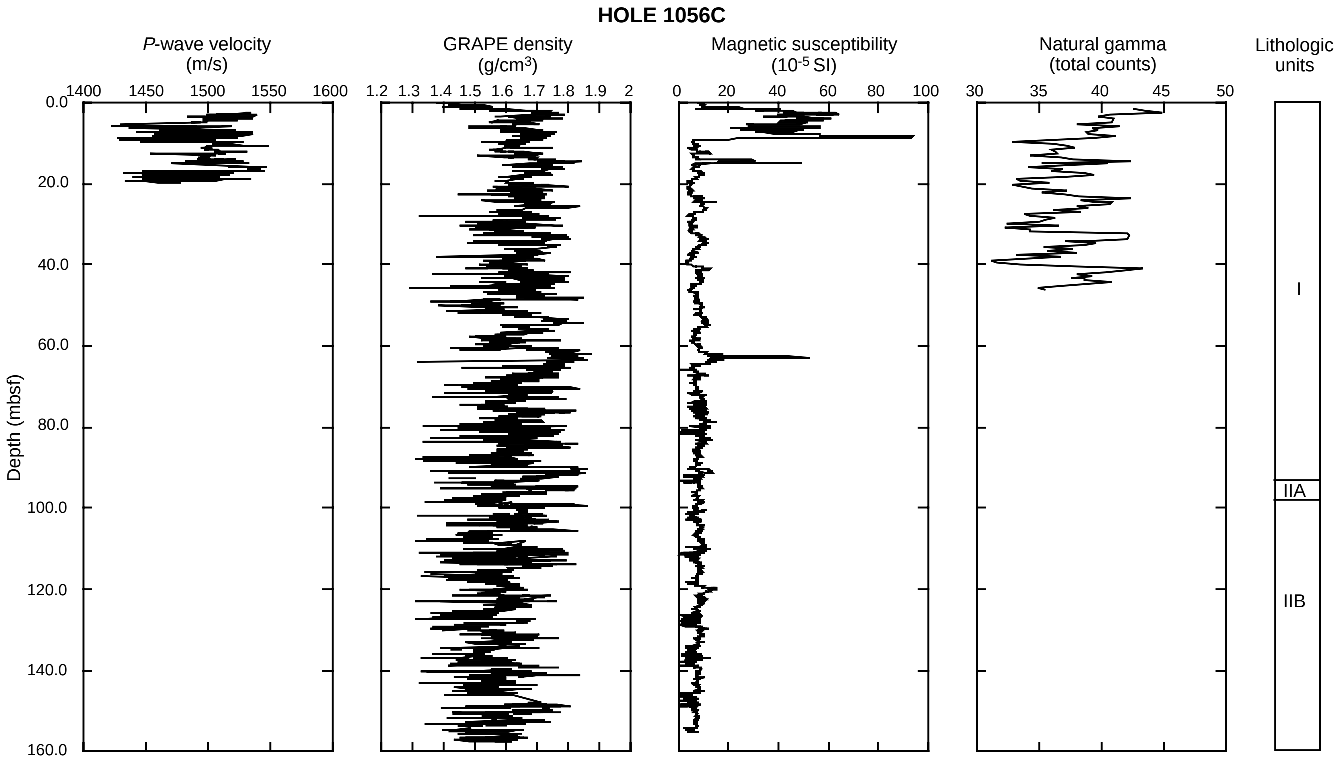

Figure 84. Vertical profiles of MST data for Hole 1056C.

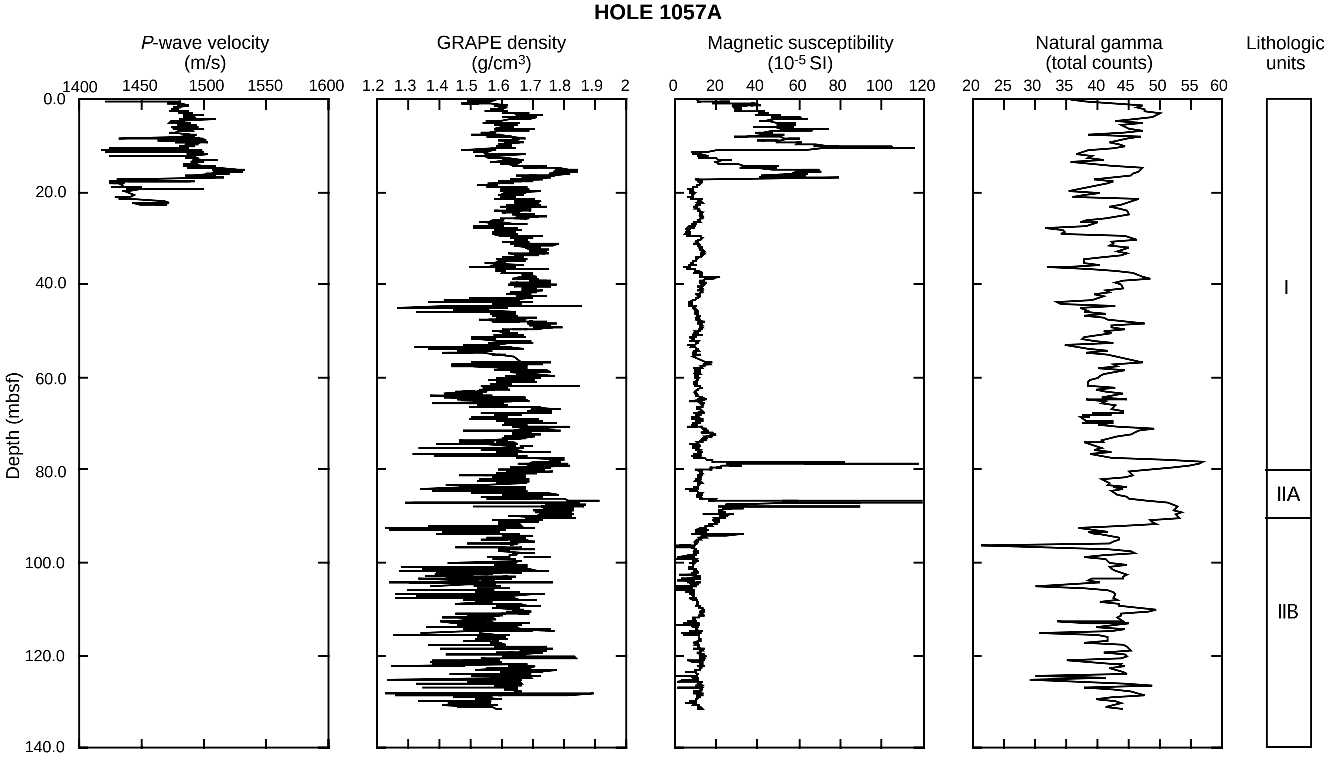

Figure 85. Vertical profiles of MST data for Hole 1057A.

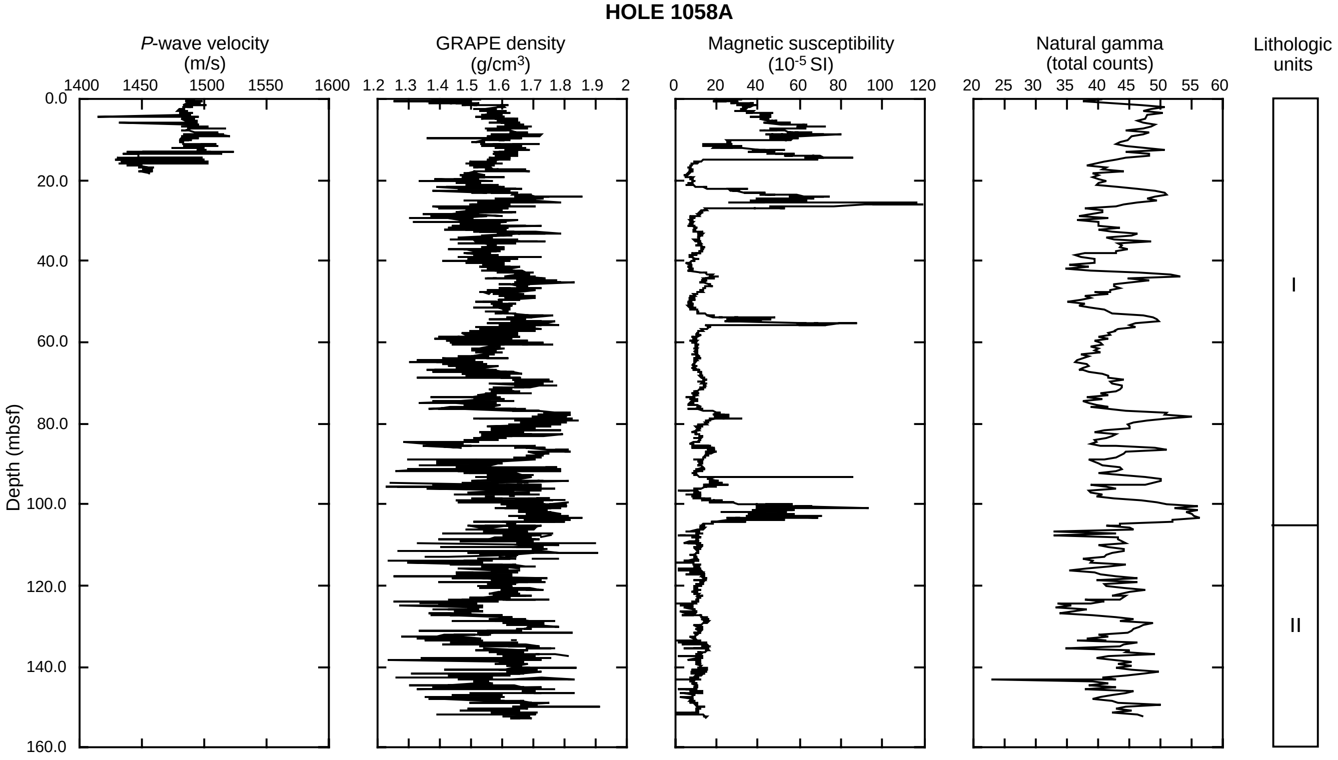

Figure 86. Vertical profiles of MST data for Hole 1058A.

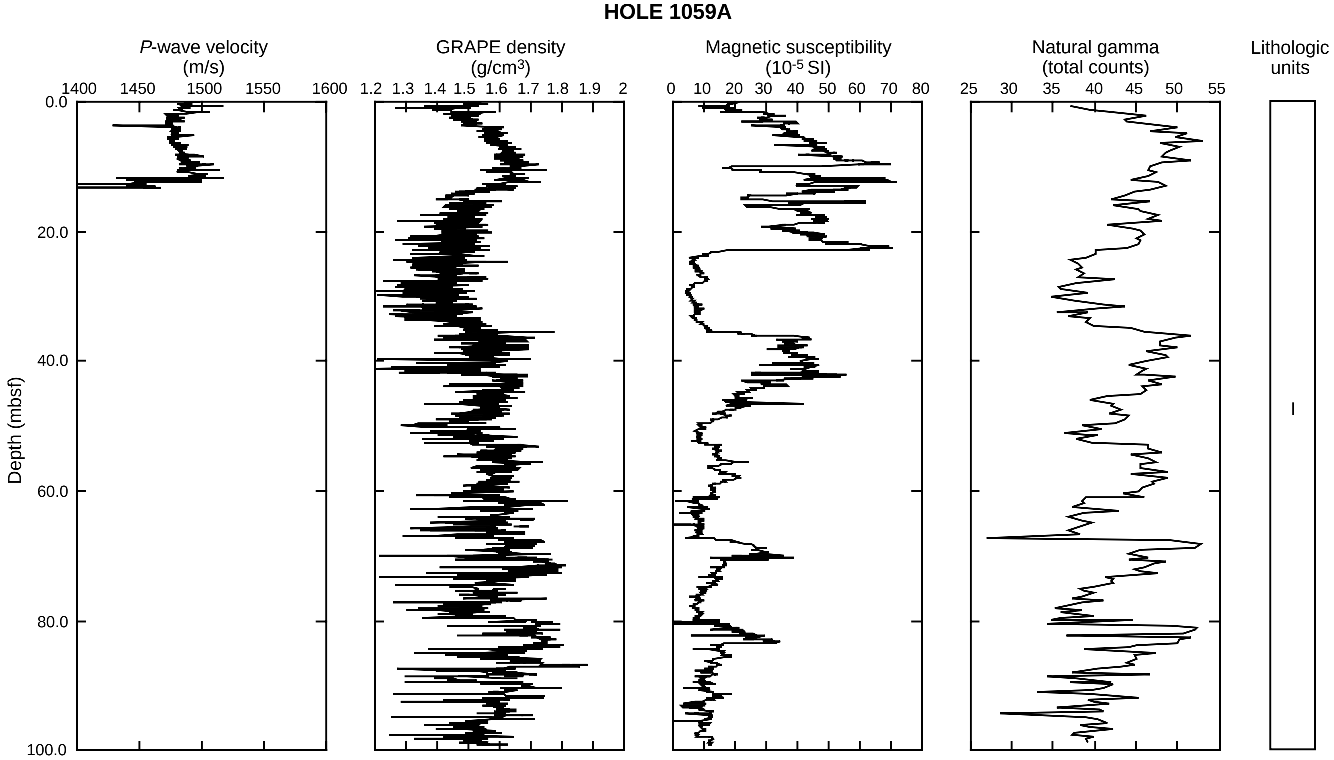

Figure 87. Vertical profiles of MST data for Hole 1059A.

Table 42. Index properties of samples from Site 1056.

Leg	Site	Hole	Core	Type	Section	Top	Bottom	Depth (mbsf)	Water content wet (%)	Water content dry (%)	Wet bulk density (g/cm^3)	Dry density (g/cm^3)	Grain density (g/cm^3)	Porosity (%)	Void ratio
172	1056	A	1	H	5	134	136	7.34	40.10	67.00	1.63	0.98	2.70	63.80	1.77
172	1056	B	1	H	1	74	76	0.74	47.80	91.70	1.52	0.79	2.70	70.70	2.42
172	1056	B	1	H	1	89	91	0.89	53.60	115.70	1.44	0.67	2.72	75.50	3.08
172	1056	B	1	H	2	54	56	2.04	48.30	93.50	1.51	0.78	2.71	71.20	2.47
172	1056	B	1	H	2	129	131	2.79	38.10	61.50	1.67	1.03	2.73	62.10	1.64
172	1056	B	1	H	3	25	27	3.25	48.10	92.50	1.51	0.79	2.70	71.00	2.44
172	1056	B	2	H	1	35	37	3.95	36.70	57.90	1.69	1.07	2.70	60.40	1.53
172	1056	B	2	H	1	118	120	4.78	47.10	89.00	1.52	0.81	2.69	70.10	2.34
172	1056	B	2	H	2	35	37	5.45	43.80	78.00	1.58	0.89	2.72	67.50	2.07
172	1056	B	2	H	2	135	137	6.45	32.00	47.00	1.78	1.21	2.74	55.70	1.26

This is a sample of the table that appears on the volume CD-ROM.

Table 43. Index properties of samples from Site 1057.

Leg	Site	Hole	Core	Type	Section	Top	Bottom	Depth (mbsf)	Water content wet (%)	Water content dry (%)	Wet bulk density (g/cm^3)	Grain density (g/cm^3)	Dry density (g/cm^3)	Porosity (%)	Void ratio
172	1057	A	1	H	1	41	43	0.41	48.72	95.02	1.50	2.70	0.77	71.51	2.51
172	1057	A	1	H	1	130	132	1.3	45.73	84.27	1.57	2.85	0.85	70.12	2.35
172	1057	A	1	H	2	39	41	1.89	45.15	82.32	1.56	2.76	0.86	68.97	2.22
172	1057	A	1	H	2	127	129	2.77	45.66	84.02	1.56	2.76	0.85	69.34	2.26
172	1057	A	1	H	3	29	31	3.29	43.13	75.84	1.59	2.76	0.91	67.12	2.04
172	1057	A	1	H	3	116	118	4.16	42.84	74.95	1.60	2.74	0.91	66.73	2.01
172	1057	A	1	H	4	35	37	4.85	49.03	96.19	1.50	2.71	0.77	71.83	2.55
172	1057	A	1	H	4	122	124	5.72	45.46	83.35	1.55	2.70	0.85	68.76	2.20
172	1057	A	1	H	5	33	35	6.33	45.77	84.41	1.55	2.73	0.84	69.26	2.25
172	1057	A	1	H	5	110	112	7.1	49.26	97.07	1.50	2.73	0.76	72.12	2.59

This is a sample of the table that appears on the volume CD-ROM.

Table 44. Index properties of samples from Site 1058.

Leg	Site	Hole	Core	Type	Section	Top	Bottom	Depth (mbsf)	Water content wet (%)	Water content dry (%)	Grain density (g/cm^3)	Wet bulk density (g/cm^3)	Dry density (g/cm^3)	Porosity (%)	Void ratio
172	1058	A	1	H	1	18	20	0.18	51.40	105.80	1.47	0.72	2.74	73.90	2.83
172	1058	A	1	H	2	30	32	1.8	45.40	83.00	1.57	0.86	2.80	69.40	2.27
172	1058	A	1	H	2	125	127	2.75	47.70	91.10	1.53	0.80	2.77	71.10	2.46
172	1058	A	1	H	3	30	32	3.3	48.90	95.60	1.51	0.77	2.76	72.10	2.58
172	1058	A	1	H	3	96	98	3.96	38.90	63.70	1.64	1.00	2.64	62.10	1.64
172	1058	A	1	H	4	18	20	4.68	45.30	82.90	1.56	0.85	2.73	68.80	2.21
172	1058	A	1	H	5	46	48	6.46	44.20	79.10	1.57	0.88	2.72	67.70	2.10
172	1058	A	1	H	5	114	116	7.14	40.90	69.30	1.61	0.95	2.68	64.40	1.81
172	1058	A	1	H	6	36	38	7.86	46.30	86.20	1.55	0.83	2.79	70.10	2.35
172	1058	A	1	H	6	120	122	8.7	46.90	88.20	1.55	0.82	2.81	70.70	2.42

This is a sample of the table that appears on the volume CD-ROM.

Table 45. Index properties of samples from Site 1059.

Leg	Site	Hole	Core	Type	Section	Top	Bottom	Depth (mbsf)	Water content wet (%)	Water content dry (%)	Wet bulk density (g/cm^3)	Grain density (g/cm^3)	Dry density (g/cm^3)	Porosity (%)	Void ratio
172	1059	A	1	H	1	36	38	0.36	47.91	91.97	1.52	2.71	0.79	70.89	2.44
172	1059	A	1	H	1	119	121	1.19	60.18	151.12	1.35	2.66	0.54	79.70	3.92
172	1059	A	1	H	2	41	43	1.91	58.79	142.67	1.37	2.67	0.56	78.86	3.73
172	1059	A	1	H	2	116	118	2.66	54.82	121.33	1.42	2.73	0.64	76.38	3.23
172	1059	A	1	H	3	30	32	3.3	50.46	101.84	1.49	2.81	0.74	73.67	2.79
172	1059	A	2	H	1	36	38	4.16	47.04	88.82	1.53	2.74	0.81	70.35	2.37
172	1059	A	2	H	1	118	120	4.98	46.98	88.61	1.53	2.74	0.81	70.31	2.37
172	1059	A	2	H	2	30	32	5.6	47.17	89.29	1.52	2.67	0.80	69.96	2.33
172	1059	A	2	H	2	87	89	6.17	47.58	90.75	1.52	2.69	0.80	70.45	2.38
172	1059	A	2	H	3	36	38	7.16	45.79	84.46	1.58	2.90	0.86	70.51	2.39

This is a sample of the table that appears on the volume CD-ROM.

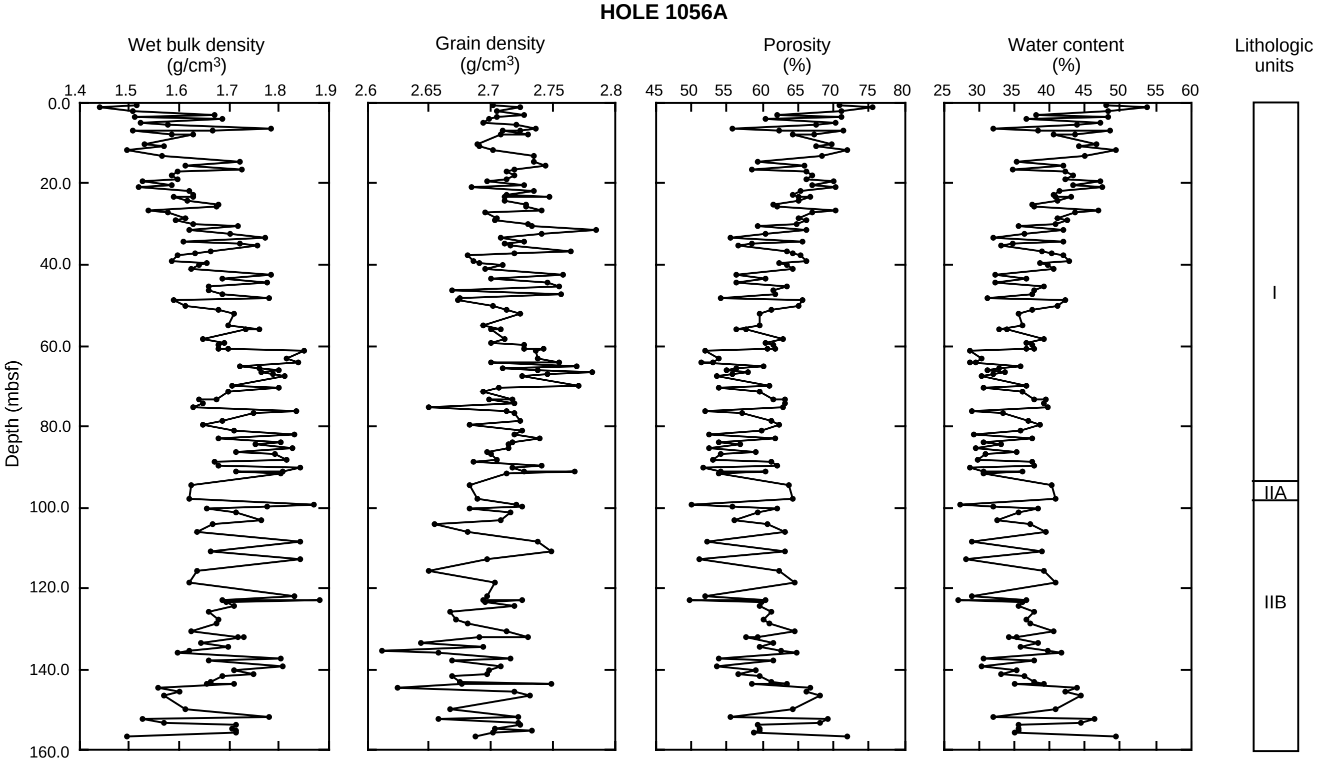

Figure 88. Index properties measurements of wet bulk density, grain density, porosity, and water content vs. depth for Hole 1056A.

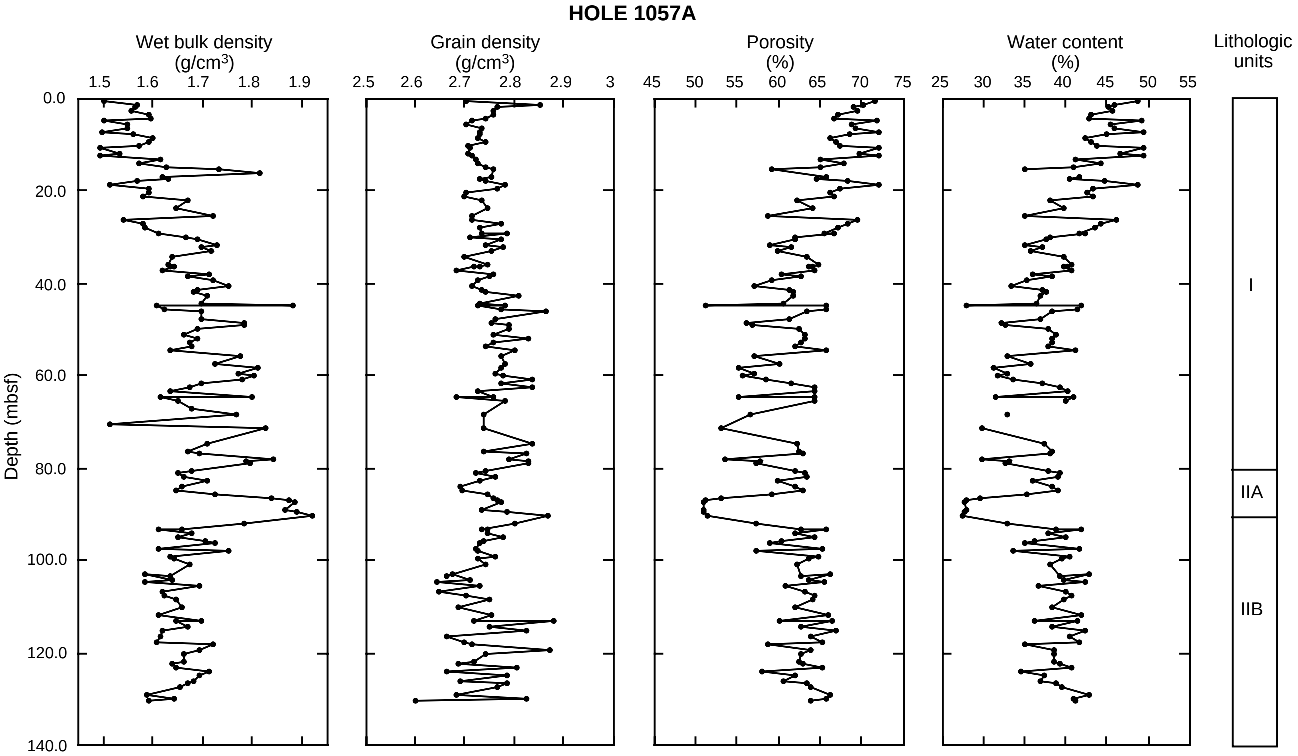

Figure 89. Index properties measurements of wet bulk density, grain density, porosity, and water content vs. depth for Hole 1057A.

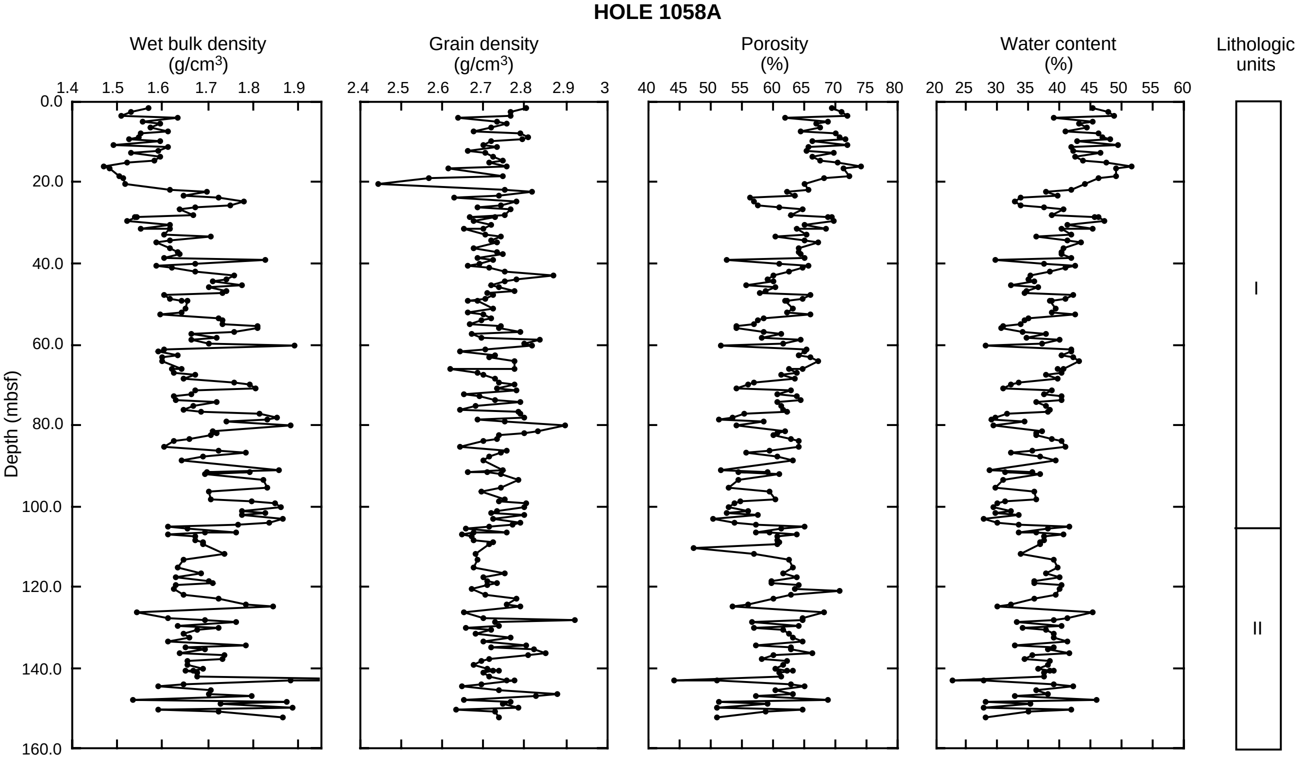

Figure 90. Index properties measurements of wet bulk density, grain density, porosity, and water content vs. depth for Hole 1058A.

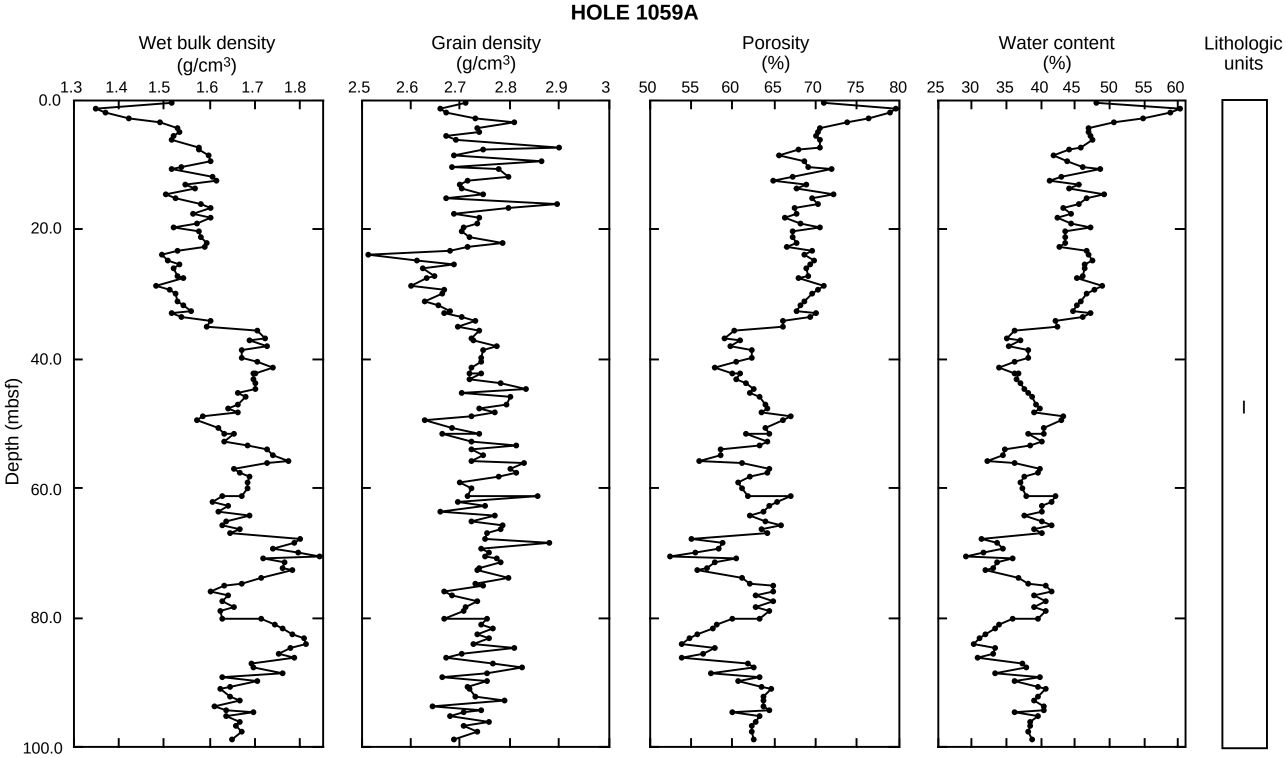

Figure 91. Index properties measurements of wet bulk density, grain density, porosity, and water content vs. depth for Hole 1059A.

Table 46. Average values and standard deviation of index properties measured at Sites 1056, 1057, 1058, and 1059.

Site	Water content dry (%)	SD	Bulk density (g/cm^3)	SD	Porosity (%)	SD	Grain density (g/cm^3)	SD
1056	37.59	5.32	1.68	0.09	61.17	5.30	2.710	0.03
1057	39.62	4.94	1.65	0.08	63.33	4.99	2.725	0.05
1058	37.87	5.42	1.67	0.10	61.57	5.27	2.726	0.08
1059	40.46	5.48	1.64	0.09	64.15	4.99	2.729	0.06

Note: SD = standard deviation.

Table 47. Compressional wave velocity measurements from Site 1056.

Leg	Site	Hole	Core	Type	Section	Interval (cm)	Depth (mbsf)	Temp. (°C)	Velocity 1 Z-direction (m/s)	Velocity 2 Y-direction (m/s)	Velocity 3 X-direction (m/s)
172	1056	A	1	H	1	50	0.5	20.1	1519	1530	
172	1056	A	1	H	1	125	1.25	20.1	1553	1582	
172	1056	A	1	H	2	28	1.78	20.6	1567	1570	
172	1056	A	1	H	2	129	2.79	20.6	1534	1549	
172	1056	A	1	H	3	32	3.32	21.1	1571	1577	
172	1056	A	1	H	3	132	4.32	21.1	1514	1515	
172	1056	A	1	H	4	55	5.05	20.5	1548	1553	
172	1056	A	1	H	4	130	5.8	20.5	1500	1506	
172	1056	A	1	H	5	10	6.1	21.5	1500	1491	
172	1056	A	1	H	5	135	7.35	21.5	1572	1604	

This is a sample of the table that appears on the volume CD-ROM.

the profile. Reflectors are present to about 0.080 s TWT (60 mbsf) at Sites 1058 and 1059. Fewer reflections are present below the hummocky reflections. The furrows are only present in the Site 1059 record, with parallel layering being typical in the surrounding areas.

Seismic Data and Lithologic Correlation

Very good seismic images were obtained using the GI gun and the Teledyne single-channel oil-filled streamer (Figs. 104–106). The seismic data were processed using the SIOSEIS seismic processing package. The processing consisted of a 15–200 Hz band-pass filter, deconvolution, and automatic gain control.

The seismic profile at Site 1056 (Fig. 104) shows numerous parallel reflections to 0.35 s TWT (278 m) where there is an unconformity to deeper, dipping reflections. A BSR is present on the northern half of the profile at 0.45 s TWT. There is a minor discontinuity within the region of parallel reflections at 0.13- to 0.15 s TWT (100 to 115 m). These diffuse reflections may mark a region of disturbed sedi-

Table 48. Compressional wave velocity measurements from Site 1057.

Leg	Site	Hole	Core	Type	Section	Interval (cm)	Depth (mbsf)	Temp. (°C)	Velocity 1 Z-direction (m/s)	Velocity 2 Y-direction (m/s)
172	1057	A	1	H	1	42	0.42	20.8	1524	1538
172	1057	A	1	H	1	131	1.31	20.8	1502	1499
172	1057	A	1	H	2	40	1.9	21.3	1496	1506
172	1057	A	1	H	2	130	2.8	21.3	1495	1491
172	1057	A	1	H	3	30	3.3	20.4	1502	1493
172	1057	A	1	H	3	124	4.24	20.4	1503	1515
172	1057	A	1	H	4	36	4.86	21.2	1493	1487
172	1057	A	1	H	4	124	5.74	21.2	1506	1492
172	1057	A	1	H	5	34	6.34	20.9	1497	1492
172	1057	A	1	H	5	113	7.13	20.9	1487	1486
172	1057	A	2	H	1	35	7.85	20.1	1507	1491
172	1057	A	2	H	1	100	8.5	20.1	1509	1502
172	1057	A	2	H	2	34	9.34	20.8	1515	1502
172	1057	A	2	H	2	123	10.23	20.8	1502	1488
172	1057	A	2	H	3	24	10.74	21.4	1491	1468
172	1057	A	2	H	3	34	10.84	21.4	1511	1504
172	1057	A	2	H	4	35	12.35	21.1	1517	1485
172	1057	A	2	H	4	115	13.15	21.1	1548	1541
172	1057	A	2	H	5	32	13.82	21.8	1506	1502
172	1057	A	2	H	5	121	14.71	21.8	1513	1514
172	1057	A	2	H	6	28	15.28	21.2	1544	1541
172	1057	A	2	H	6	123	16.23	21.2	1545	1552
172	1057	A	2	H	7	31	16.81	21.2	1510	1512
172	1057	A	3	H	1	18	17.18	21.1		1521
172	1057	A	3	H	1	92	17.92	21.4		1516
172	1057	A	3	H	2	10	18.6	21.6		1504
172	1057	A	3	H	2	99	19.49	21.7		1518
172	1057	A	3	H	2	134	19.84	21.6		1510
172	1057	A	3	H	3	40	20.4	21.6		1520
172	1057	A	3	H	3	124	21.24	21.6		1516
172	1057	A	3	H	4	69	22.19	21.3		1506
172	1057	A	3	H	5	63	23.63	21.4		1502
172	1057	A	3	H	7	41	26.41	21		1490
172	1057	A	4	H	1	59	27.09	21.3		1505
172	1057	A	4	H	1	130	27.8	21.5		1512
172	1057	A	4	H	2	96	28.96	21.6		1517
172	1057	A	4	H	2	112	29.12	21.5		1516
172	1057	A	4	H	3	50	30	21.8		1458

This table also appears on the volume CD-ROM.

Table 49. Compressional wave velocity measurements from Site 1058.

Leg	Site	Hole	Core	Type	Section	Interval (cm)	Depth (mbsf)	Temp (°C)	Velocity 1 Z-direction (m/s)	Velocity 2 Y-direction (m/s)
172	1058	A	1	H	1	19	0.19	21.3		1499.4
172	1058	A	1	H	1	118	1.18	22.5	1492.6	1497.1
172	1058	A	1	H	2	32	1.82	22.4	1499.7	1462
172	1058	A	1	H	2	127	2.77	22.4	1487.5	1490.3
172	1058	A	1	H	3	33	3.33	22.2	1489.4	1471.8
172	1058	A	1	H	3	97	3.97	22.2	1487.5	1483.1
172	1058	A	1	H	4	19	4.69	22.5	1501	1498.4
172	1058	A	1	H	4	113	5.63	22.5	1495.2	1484.4
172	1058	A	1	H	5	45	6.45	22.2	1501	1495
172	1058	A	1	H	5	113	7.13	22.2	1542.9	1522
172	1058	A	1	H	6	38	7.88	22	1492.6	1489.4
172	1058	A	1	H	6	122	8.72	22	1490.7	1488.2
172	1058	A	1	H	7	30	9.3	22.1	1497.4	1498.2
172	1058	A	2	H	1	30	9.8	22.9	1504.2	1465.5
172	1058	A	2	H	1	118	10.68	22.9	1493.3	1493.3
172	1058	A	2	H	2	32	11.32	22.7	1514	1499
172	1058	A	2	H	2	110	12.1	22.7	1504.5	1508.8
172	1058	A	2	H	3	44	12.94	22.9	1509.7	1503.6
172	1058	A	2	H	3	130	13.8	22.9		1440.6
172	1058	A	2	H	4	44	14.44	22.9		1510.9
172	1058	A	2	H	4	108	15.08	22.9		1485.9
172	1058	A	2	H	5	30	15.8	22.5		1510.1
172	1058	A	2	H	5	108	16.58	22.5		1502.9
172	1058	A	2	H	6	30	17.3	22.9		1521.4
172	1058	A	2	H	6	120	18.2	22.9		1502.6
172	1058	A	2	H	7	30	18.8	22.7		1510.2
172	1058	A	3	H	1	50	19.5	24		1468.3
172	1058	A	3	H	1	120	20.2	23.8		1443.9
172	1058	A	3	H	1	132	20.32			1476.7
172	1058	A	3	H	2	24	20.74	24		1506.2
172	1058	A	3	H	2	44	20.94			1489.3
172	1058	A	3	H	2	106	21.56	24		1475.1
172	1058	A	3	H	3	122	23.22	23.6		1505.8

This table also appears on the volume CD-ROM.

Table 50. Compressional wave velocity measurements from Site 1059.

Leg	Site	Hole	Core	Type	Section	Interval (cm)	Depth (mbsf)	Temp. (°C)	Velocity 1 Z-direction (m/s)	Velocity 2 Y-direction (m/s)
172	1059	A	1	H	1	37	0.37	20.9	1512.2	1516.5
172	1059	A	1	H	1	121	1.21	21.4	1498.5	1498.5
172	1059	A	1	H	2	42	1.92	21	1494	1494.4
172	1059	A	1	H	2	117	2.67	21.1	1487.6	1491.8
172	1059	A	1	H	3	31	3.31	21.8	1497.9	1498.3
172	1059	A	2	H	1	38	4.18	21.9	1490.8	1493.1
172	1059	A	2	H	1	120	5	21.4	1485.7	1480.4
172	1059	A	2	H	2	30	5.6	21.3	1486.3	1480.4
172	1059	A	2	H	2	80	6.1	21.3	1488.9	
172	1059	A	2	H	3	38	7.18	22.1	1495.3	1483
172	1059	A	2	H	3	92	7.72	22.1	1497.9	1504.7
172	1059	A	2	H	4	26	8.56	21.8	1509.5	1505.7
172	1059	A	2	H	4	110	9.4	21.8	1502.4	1515.2
172	1059	A	2	H	5	44	10.24	22.1	1492.6	1497
172	1059	A	2	H	5	90	10.7	22.1	1497.9	1499.5
172	1059	A	2	H	6	42	11.72	22		1476.7
172	1059	A	2	H	6	100	12.3	27		1513.9
172	1059	A	2	H	7	20	13	22.7		1450
172	1059	A	3	H	1	30	13.6	24.9		1464.1
172	1059	A	3	H	2	78	15.58	23.5		

This table also appears on the volume CD-ROM.

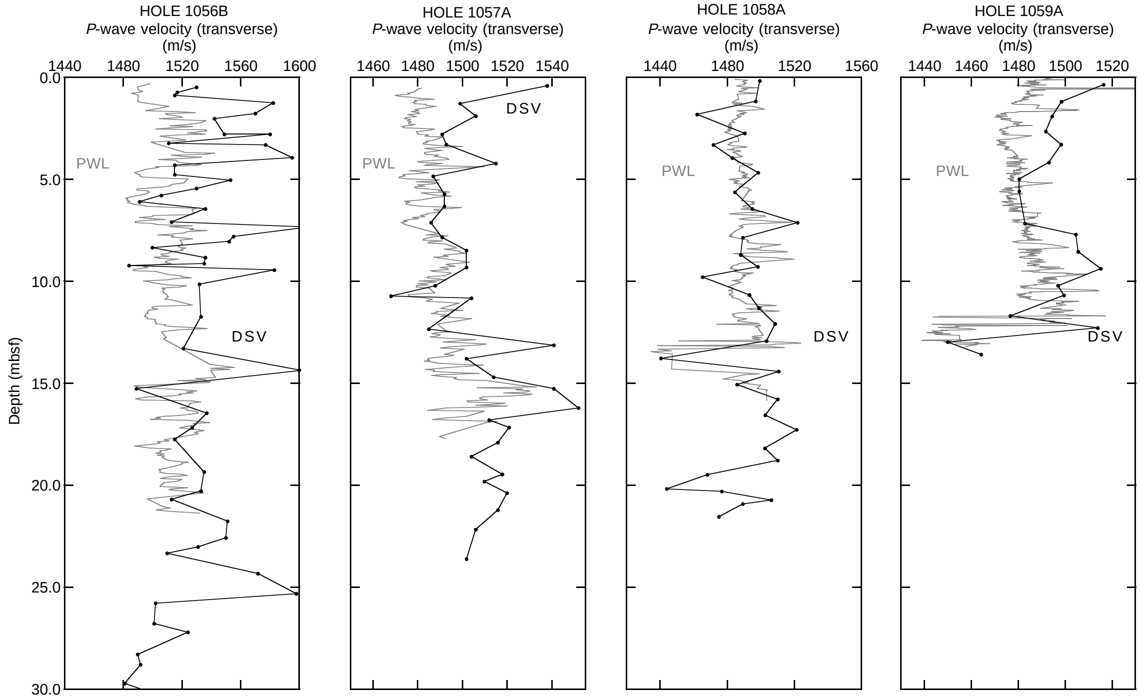

Figure 92. Comparison of compressional wave velocity measurements (PWL and DSV) for Holes 1056B, 1057A, 1058A, and 1059A.

Table 51. Undrained shear-strength measurements from Site 1056.

Leg	Site	Hole	Core	Type	Section	Interval (cm)	Depth (mbsf)	Method	Spring no.	Undrained shear strength (kPa)	Residual strength (kPa)
172	1056	A	1	H	1	75	0.75	Vane	B-4	10.5	4.5
172	1056	A	1	H	2	75	2.25	Vane	B-4	9.4	3.8
172	1056	A	1	H	3	81	3.812	Vane	B-4	5.9	3.9
172	1056	A	1	H	4	90	5.4	Vane	B-4	5.1	2.4
172	1056	A	1	H	5	63	6.63	Vane	B-4	9.6	3.9
172	1056	A	1	H	6	90	8.4	Vane	B-4	14.0	6.2
172	1056	A	1	H	7	65	9.647	Vane	B-4	13.0	6.3
172	1056	B	1	H	1	57	0.574	Vane	B-4	3.0	1.3
172	1056	B	1	H	2	88	2.381	Vane	B-4	8.3	4.0
172	1056	B	1	H	3	16	3.16	Vane	B-4	6.3	4.1

This is a sample of the table that appears on the volume CD-ROM.

Table 52. Undrained shear-strength measurements from Site 1057.

Leg	Site	Hole	Core	Type	Section	Interval (cm)	Depth (mbsf)	Method	Spring no.	Undrained shear strength (kPa)	Residual strength (kPa)
172	1057	B	1	H	1	92	0.92	Vane	B-1	3.6	1.7
172	1057	B	1	H	2	99		Vane	B-2	4.7	3.2
172	1057	B	2	H	1	101	4.71	Vane	B-2	7.6	4.2
172	1057	B	2	H	2	94	6.14	Vane	B-4	9.5	4.8
172	1057	B	2	H	3	110	7.8	Vane	B-4	12.1	5.8
172	1057	B	2	H	4	110	9.3	Vane	B-4	16.9	7.8
172	1057	B	2	H	5	110	10.8	Vane	B-4	12.7	7.3
172	1057	B	2	H	6	96	12.16	Vane	B-4	11.2	5.5
172	1057	B	3	H	1	70	13.9	Vane	B-4	17.9	9.9
172	1057	B	3	H	2	114	15.84	Vane	B-4	14.9	7.2

This is a sample of the table that appears on the volume CD-ROM.

Table 53. Undrained shear-strength measurements from Site 1058.

Leg	Site	Hole	Core	Type	Section	Interval (cm)	Depth (mbsf)	Method	Spring no.	Undrained shear strength (kPa)	Residual strength (kPa)
172	1058	B	1	H	1	114	1.14	Vane	B-1	2.5	1.2
172	1058	B	1	H	2	118	2.68	Vane	B-1	2.5	1.4
172	1058	B	1	H	2	63	2.13	Vane	B-1	2.7	1.2
172	1058	B	1	H	3	90	3.9	Vane	B-1	3.0	1.9
172	1058	B	1	H	4	71	5.21	Vane	B-2	4.3	2.7
172	1058	B	2	H	1	67	6.67	Vane	B-2	6.1	2.6
172	1058	B	2	H	2	55	8.05	Vane	B-4	7.7	4.1
172	1058	B	2	H	2	126	8.76	Vane	B-4	9.7	5.9
172	1058	B	2	H	3	56	9.56	Vane	B-4	10.1	4.9
172	1058	B	2	H	3	123	10.23	Vane	B-4	9.6	4.9

This is a sample of the table that appears on the volume CD-ROM.

Table 54. Undrained shear-strength measurements from Site 1059.

Leg	Site	Hole	Core	Type	Section	Interval (cm)	Depth (mbsf)	Method	Spring no.	Undrained shear strength (kPa)	Residual strength (kPa)
172	1059	A	1	H	1	79	0.79	Vane	B-1	3.8	2.2
172	1059	A	1	H	2	143	2.93	Vane	B-1	3.0	1.5
172	1059	A	1	H	3	40	3.4	Vane	B-1	3.0	1.7
172	1059	A	2	H	1	79	4.59	Vane	B-1	5.2	2.8
172	1059	A	2	H	2	59	5.89	Vane	B-1	7.8	4.1
172	1059	A	2	H	3	76	7.56	Vane	B-1	6.9	3.4
172	1059	A	2	H	4	72	9.02	Vane	B-1	8.3	9.1
172	1059	A	2	H	4	60	8.9	Penetrometer		24.5	
172	1059	A	2	H	5	66	10.46	Vane	B-1	12.2	6.2
172	1059	A	2	H	5	20	10	Penetrometer		44.1	

This is a sample of the table that appears on the volume CD-ROM.

ment that is about 2 to 3 km wide crossing the track, perhaps a mass-transport deposit. However, the geometry of this deposit suggests that little material was eroded from beneath it. An apparent mass-flow deposit 5 m thick was recovered at Site 1056 (lithologic Subunit IIA) from 95 to 99 mbsf which appears to correlate with the anomalous layering on the seismic record.

The seismic profile at Site 1057 (Fig. 105) shows numerous parallel reflections to 0.17 s TWT (131 m) where there is a contact to underlying irregular layering that extends to 0.27 s TWT. A clearly imaged BSR is present at 0.525 s TWT. There is a minor discontinuity within the region of parallel reflections at 0.105 s TWT (80 m). The apparent discontinuity appeared to be large at the original site. Therefore the site location was moved to the northwest to a location where the seismic profiles suggest less material missing at this discontinuity. The discontinuity may be related to a mass-flow deposit 10 m thick recovered at Site 1057 (lithologic Subunit IIA) from 80 to 90 mbsf.

The seismic profile at Sites 1058 and 1059 (Fig. 106) shows a region of increasing sediment thickness from northwest to southeast. This is similar to the record seen on the 3.5-kHz profile, but the seismic profile verifies that the same reflection pattern extends deeper into the sediment. The more pronounced thickening observed on the 3.5-kHz records between Sites 1058 and 1059 is also observed on the seismic profile, but that increased lateral change in sediment thickness appears to be restricted to the upper sediment layers because a prominent reflector continues undisturbed beneath Site 1058 at 0.075 s TWT (57 m), and Site 1059 at 0.11 s TWT (84 m). This prominent reflector may have been caused by a carbonate-rich layer marked by high lightness at about 52 mbsf at Site 1058 and a correlated layer at about 80 mbsf at Site 1059. This carbonate layers appears to have been deposited in MIS 11 (see “Sedimentation Rates” section, this chapter), suggesting that the increased preferential sedimentation at Site 1059 began after about 400 ka.

The region of parallel reflections at Sites 1058 and 1059 overlies a region of more disturbed reflections at 0.24 s TWT at Site 1058 and 0.32 s TWT at Site 1059. A prominent BSR is observed at 0.57 s TWT. The BSR appears to be enhanced because of gently folded layers at this depth.

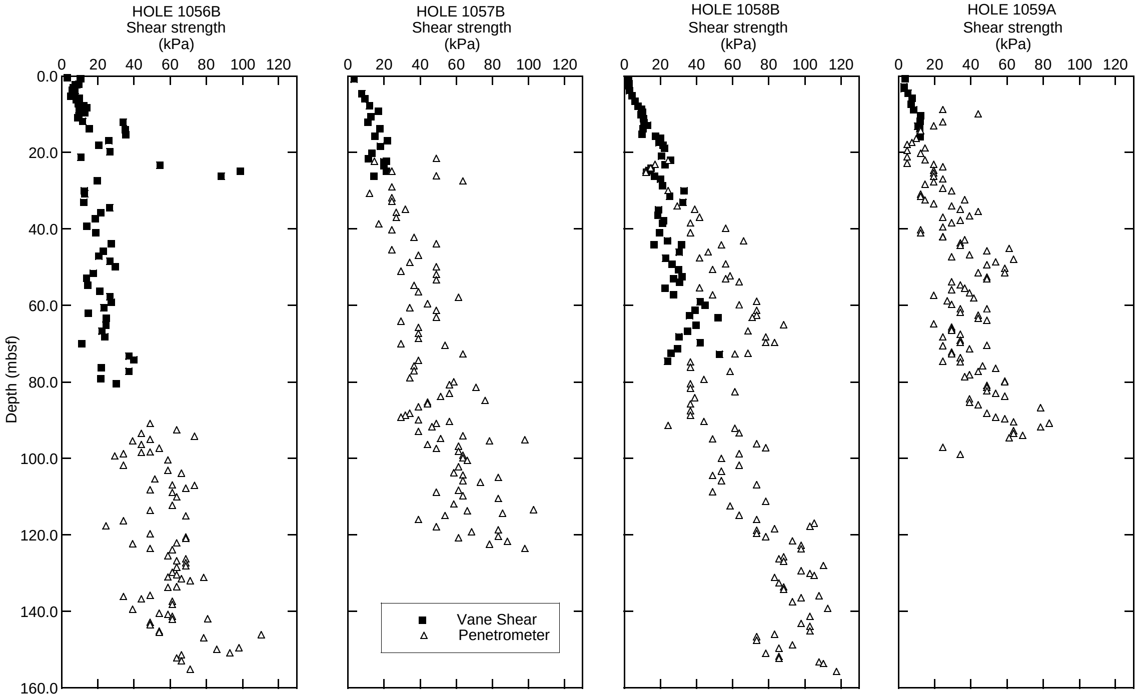

Figure 93. Comparison of vertical profiles of undrained shear strength for Holes 1056B, 1057B, 1058B, and 1059A.

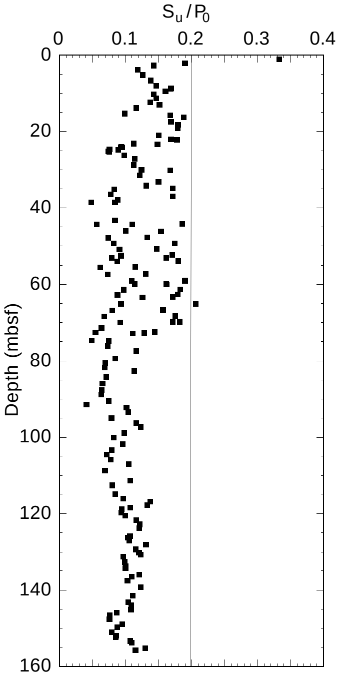

Figure 94. Normalized shear strength for Hole 1058B. The vertical line indicates normalized shear strength for normally consolidated sediments (Ladd et al., 1977).

REFERENCES

Baldauf, J.G., 1984. Cenozoic diatom biostratigraphy and paleoceanography of the Rockall Plateau region, North Atlantic, Deep Sea Drilling Project Leg 81. *In* Roberts, D.G., Schnitker, D., et al., *Init. Repts. DSDP,* 81: Washington (U.S. Govt. Printing Office), 439–478.

————, 1987. Diatom biostratigraphy of the middle- and high-latitude North Atlantic Ocean, Deep Sea Drilling Project Leg 94. *In* Ruddiman, W.F., Kidd, R.B., Thomas, E., et al., *Init. Repts. DSDP,* 94 (Pt. 2): Washington (U.S. Govt. Printing Office), 729–762.

Balsam, W.L., 1983. Carbonate and sedimentation on the Mid-Atlantic continental margin. *Science,* 217:929–931.

Barranco, F.T., Jr., Balsam, W.L., and Deaton, B.C., 1989. Quantitative reassessment of brick red lutites: evidence from reflectance spectrophotometry. *Mar. Geol.,* 89:299–314.

Barron, J.A., 1985. Late Eocene to Holocene diatom biostratigraphy of the equatorial Pacific Ocean, Deep Sea Drilling Project Leg 85. *In* Mayer, L., Theyer, F., Thomas, E., et al., *Init. Repts. DSDP,* 85: Washington (U.S. Govt. Printing Office), 413–456.

Berggren, W.A., Hilgen, F.J., Langereis, C.G., Kent, D.V., Obradovich, J.D., Raffi, I., Raymo, M.E., and Shackleton, N.J., 1995. Late Neogene chronology: new perspectives in high-resolution stratigraphy. *Geol. Soc. Am. Bull.,* 107:1272–1287.

Biscaye, P.E., and Anderson, R.F., 1994. Fluxes of particulate matter on the slope of the southern Middle Atlantic Bight: SEEP II. *Deep-Sea Res.,* 41:459–509.

Borowski, W.S., Paull, C.K., and Ussler, W., III, 1996. Marine pore-water sulfate profiles indicate in situ methane flux from underlying gas hydrate. *Geology,* 24:655–658.

Claypool, G.E., and Kaplan, I.R., 1974. The origin and distribution of methane in marine sediments. *In* Kaplan, I.R. (Ed.), *Natural Gases in Marine Sediments:* New York (Plenum), 99–139.

Claypool, G.E., and Kvenvolden, K.A., 1983. Methane and other hydrocarbon gases in marine sediment. *Annu. Rev. Earth Planet. Sci.,* 11:299–327.

Comas, M.C., Zahn, R., Klaus, A., et al., 1996. *Proc. ODP, Init. Repts.,* 161: College Station, TX (Ocean Drilling Program).

Dickens, G.R., Paull, C.K., Wallace, P., and the ODP Leg 164 Scientific Party, 1996. Direct measurement of in situ methane quantities in a large gas-hydrate reservoir. *Nature,* 385:426–428.

Dillon, W.P., Popenoe, P., Grow, J.A., Klitgord, K.D., Swift, B.A., Paull, C.K., and Cashman, K.V., 1982. Growth faulting and salt diapirism: their relationship and control in the Carolina Trough, Eastern North America. *In* Watkins, J.S., and Drake, C.L. (Eds.), *Studies of Continental Margin Geology.* AAPG Mem., 34:21–46.

Emerson, S., and Bender, M., 1981. Carbon fluxes at the sediment-water interface of the deep-sea: calcium carbonate preservation. *J. Mar. Res.,* 39:139–162.

Emerson, S., and Hedges, J.I., 1988. Processes controlling the organic carbon content of open ocean sediments. *Paleoceanography,* 3:621–634.

Espitalié, J., Deroo, G., and Marquis, F., 1986. La pyrolyse Rock-Eval et ses applications, Partie III. *Rev. Inst. Fr. Pet.,* 41:73–89.

Hajós, M., 1973. The Mediterranean diatoms, Deep Sea Drilling Project, Leg 13. *In* Ryan, W.B.F., Hsü, K.J., et al., *Init. Repts. DSDP,* 13: Washington (U.S. Govt. Printing Office), 944–970.

Haskell, B.J., and Johnson, T.C., 1993. Bottom circulation control of surface sediment characteristics on the Blake Outer Ridge, western North Atlantic: paleoceanographic implications. *Sediment. Geol.,* 82:133–144.

Haskell, B.J., Johnson, T.C., and Showers, W.J., 1991. Fluctuations in deep western North Atlantic circulation on the Blake Outer Ridge during the last deglaciation. *Paleoceanography,* 6:21–31.

Heezen, B.C., Hollister, C.D., and Ruddiman, W.F., 1966. Shaping of the continental rise by deep geostrophic contour currents. *Science,* 152:502–508.

Hesse, R., and Harrison, W.E., 1981. Gas hydrates (clathrates) causing pore-water freshening and oxygen isotope fractionation in deep-water sedimentary sections of terrigenous continental margins. *Earth Planet. Sci. Lett.,* 55:453–462.

Hesse, R., Lebel, J., and Gieskes, J.M., 1985. Interstitial water chemistry of gas-hydrate-bearing sections on the Middle America Trench slope, Deep-Sea Drilling Project Leg 84. *In* von Huene, R., Aubouin, J., et al., *Init. Repts. DSDP,* 84: Washington (U.S. Govt. Printing Office), 727–737.

Hoehler, T.M., Alperin, M.J., Albert, D.B., and Martens, C.S., 1994. Field and laboratory studies of methane oxidation in anoxic marine sediment: Evidence for a methanogen-sulfate reducer consortium. *Global Biogeochem. Cycles,* 8:451–463.

Hoppie, B.W., Blum, P., and the Shipboard Scientific Party, 1994. Natural gamma-ray measurements on ODP cores: introduction to procedures with examples from Leg 150. *In* Mountain, G.S., Miller, K.G., Blum, P., et al., *Proc. ODP, Init. Repts.,* 150: College Station, TX (Ocean Drilling Program), 51–59.

Hustedt, F., and Jensen, N.G., 1985. *The Pennate Diatoms:* Koenigstein (Koeltz Scientific Books).

Jenden, P.D., and Gieskes, J.M., 1983. Chemical and isotopic composition of interstitial water from Deep Sea Drilling Project Sites 533 and 534. *In* Sheridan, R.E., Gradstein, F.M., et al., *Init. Repts. DSDP,* 76: Washington (U.S. Govt. Printing Office), 453–461.

Johnson, T.C., Lynch, E.L., Showers, W.J.,and Palczuk, N.C., 1988. Pleistocene fluctuations in the western boundary undercurrent on the Blake Outer Ridge. *Paleoceanography,* 3:191–207.

Kastner, M., 1979. Silica polymorphs. *In* Burns, R.G. (Ed.), *Marine Minerals.* Mineral. Soc. Am., Rev. Mineral., 6:99–111.

Kastner, M., Elderfield, H., Martin, J.B., Suess, E., Kvenvolden, K.A., and Garrison, R.E., 1990. Diagenesis and interstitial-water chemistry at the Peruvian continental margin—major constituents and strontium isotopes. *In* Suess, E., von Huene, R., et al., *Proc. ODP, Sci. Results,* 112: College Station, TX (Ocean Drilling Program), 413–440.

Keigwin, L.D., and Jones, G.A., 1995. The marine record of deglaciation from the continental margin off Nova Scotia. *Paleoceanography,* 10:973–985.

Kvenvolden, K.A., and Kastner, M., 1990. Gas hydrates of the Peruvian outer continental margin. *In* Suess, E., von Huene, R., et al., *Proc. ODP, Sci. Results,* 112: College Station, TX (Ocean Drilling Program), 517–526.

Ladd, C.C., Foott, R., Ishihara, K., Schlosser, F., and Poulos, H.G., 1977. Stress-deformation and strength characteristics: state-of-the-art report. *Proc. 9th Int. Conf. Soil Mech. and Found. Eng.,* Tokyo, 2:421–482.

Mackin, J.E., and Aller, R.C., 1984. Ammonium adsorption in marine sediments. *Limnol. Oceanogr.,* 29:250–257.

McIver, R.D., 1975. Hydrocarbon occurrences from JOIDES Deep Sea Drilling Project. *Proc. Ninth Petrol. Congr.,* 269–280.

Meyers, P.A., 1994. Preservation of elemental and isotopic source identification of sedimentary organic matter. *Chem. Geol.,* 144:289–302.

Meyers, P.A., and Brassell, S.C., 1985. Biogenic gases in sediments deposited since Miocene times on the Walvis Ridge, South Atlantic Ocean. *In* Caldwell, D.E, Brierley, J.A., and Brierley, C.L. (Eds.), *Planetary Ecology:* New York (Van Nostrand Reinhold), 69–80.

Müller, P.J., 1977. C/N ratios in Pacific deep sea sediments: effect of inorganic ammonium and organic nitrogen compounds sorbed by clays. *Geochim. Cosmochim. Acta,* 41:765–776.

Paull, C.K., Matsumoto, R., Wallace, P.J., et al., 1996. *Proc. ODP, Init. Repts.,* 164: College Station, TX (Ocean Drilling Program).

Pickering, K.T., Hiscott, R., and Hein, F.J., 1989. *Deep-marine Environments: Clastic Sedimentation and Tectonics:* London (Unwin Hyman).

Rangin, C., Silver, E.A., von Breymann, M.T., et al., 1990. *Proc. ODP, Init. Repts.,* 124: College Station, TX (Ocean Drilling Program), 121–193.

Reeburgh, W.S., 1976. Methane consumption in Cariaco Trench waters and sediments. *Earth Planet. Sci. Lett.,* 28:337–344.

Roberts, A.P., Stoner, J.S., and Richter, C., 1996. Coring induced magnetic overprints and limitations of the long-core paleomagnetic measurements technique: some observations from Leg 160, eastern Mediterranean Sea. *In* Emeis, K.-C., Robertson, A.H.F., Richter, C., et al., *Proc. ODP, Init. Repts.,* 160: College Station, TX (Ocean Drilling Program), 497–505.

Rosenfeld, J.K., 1979. Ammonium absorption in nearshore anoxic sediments. *Limnol. Oceanogr.,* 24:356–364.

Sayles, F.L., Manheim, F.T., and Waterman, L.S., 1972. Interstitial water studies on small core samples, Leg 11. *In* Hollister, C.D., Ewing, J.I., et al., *Init. Repts. DSDP,* 11: Washington (U.S. Govt. Printing Office), 1197–1008.

Schoell, M., 1980. The hydrogen and carbon isotopic composition of methane from natural gases of various origins. *Geochim. Cosmochim. Acta,* 44:649–661.

Schrader, H.-J., 1973. Cenozoic diatoms from the Northeast Pacific, Leg 18. *In* Kulm, L.D., von Huene, R., et al., *Init. Repts. DSDP,* 18: Washington (U.S. Govt. Printing Office), 673–797.

Stein, R., Brass, G., Graham, D., Pimmel, A., and the Shipboard Scientific Party, 1995. Hydrocarbon measurements at Arctic Gateways sites (ODP Leg 151). *In* Myhre, A.M., Thiede, J., Firth, J.V., et al., *Proc. ODP, Init. Repts.,* 151: College Station, TX (Ocean Drilling Program), 385–395.

Ms 172IR-104

NOTE: Core-description forms (“barrel sheets”) and core photographs can be found in Section 4, beginning on page 325. Forms containing smear-slide data can be found on CD-ROM. See Table of Contents for material contained on CD-ROM.

Table 55. Thermal conductivity measurements from Site 1056.

Leg	Site	Hole	Core	Type	Section	Interval (cm)	Depth (mbsf)	Thermal conductivity (W/[m·K])
172	1056	C	1	H	1	50	0.5	0.780
172	1056	C	1	H	2	50	2	1.110
172	1056	C	1	H	3	50	3.5	0.990
172	1056	C	1	H	4	50	5	0.940
172	1056	C	2	H	1	50	5.8	0.980
172	1056	C	2	H	2	50	7.3	1.050
172	1056	C	2	H	3	50	8.8	1.010
172	1056	C	2	H	4	50	10.3	1.040
172	1056	C	2	H	5	50	11.8	1.050
172	1056	C	2	H	6	50	13.3	1.000
172	1056	C	3	H	1	50	15.3	1.020
172	1056	C	3	H	3	50	18.3	1.000
172	1056	C	3	H	5	50	21.3	1.010
172	1056	C	3	H	7	40	24.2	1.010
172	1056	C	4	H	1	50	24.8	1.230
172	1056	C	4	H	3	50	27.8	0.960
172	1056	C	4	H	5	50	30.8	0.940
172	1056	C	5	H	1	50	34.3	0.970
172	1056	C	5	H	3	50	37.3	0.910
172	1056	C	5	H	5	50	40.3	0.990
172	1056	C	6	H	1	50	43.8	1.050
172	1056	C	6	H	3	50	46.8	1.040
172	1056	C	6	H	5	50	49.8	0.820
172	1056	C	7	H	1	50	53.3	1.060
172	1056	C	7	H	3	60	56.4	1.020
172	1056	C	7	H	5	50	59.3	1.100
172	1056	C	8	H	3	50	64.8	0.960
172	1056	C	9	H	3	80	74.68	1.110
172	1056	C	10	H	3	50	84.8	1.060
172	1056	C	11	H	3	50	94.3	0.930
172	1056	C	12	H	3	50	103.8	0.920
172	1056	C	13	H	3	80	113.6	0.870
172	1056	C	14	H	3	50	122.8	0.950
172	1056	C	15	H	3	50	129.8	0.770
172	1056	C	16	H	3	50	139.3	0.850
172	1056	C	17	H	3	53	148.83	0.910
172	1056	D	6	H	1	50	46.3	0.980
172	1056	D	6	H	3	50	49.3	0.940
172	1056	D	6	H	5	50	52.3	1.010
172	1056	D	6	H	7	50	55.3	0.860
172	1056	D	7	H	1	50	55.8	1.090
172	1056	D	7	H	3	50	58.8	0.820
172	1056	D	7	H	5	50	61.8	0.820
172	1056	D	7	H	7	50	64.8	0.900
172	1056	D	8	H	2	50	65.64	0.590
172	1056	D	8	H	5	48	70.12	0.910
172	1056	D	8	H	7	50	73.14	0.850
172	1056	D	9	H	2	70	75.62	1.170
172	1056	D	9	H	5	50	79.92	0.940
172	1056	D	10	H	5	45	89.87	0.920
172	1056	D	10	H	7	80	93.22	1.030

This table also appears on the volume CD-ROM.

Table 56. Thermal conductivity measurements from Site 1057.

Leg	Site	Hole	Core	Type	Section	Interval (cm)	Depth (mbsf)	Thermal conductivity (W/[m·K])
172	1057	B	1	H	1	50	0.5	0.933
172	1057	B	1	H	3	50	3.5	1.037
172	1057	B	2	H	1	50	4.2	1.009
172	1057	B	2	H	3	50	7.2	1.033
172	1057	B	2	H	5	50	10.2	1.062
172	1057	B	3	H	1	50	13.7	1.152
172	1057	B	3	H	3	50	16.7	0.978
172	1057	B	3	H	5	50	19.7	0.989
172	1057	B	4	H	1	70	23.4	1.077
172	1057	B	4	H	3	50	26.2	1.032
172	1057	B	4	H	5	50	29.2	1.005
172	1057	B	5	H	1	50	32.7	0.971
172	1057	B	5	H	3	50	35.7	0.909
172	1057	B	6	H	3	50	45.2	0.879
172	1057	B	7	H	3	50	54.7	0.980
172	1057	B	8	H	3	50	64.2	0.803
172	1057	B	9	H	3	10	72.32	0.921
172	1057	B	10	H	3	50	83.2	0.956
172	1057	B	11	H	3	60	92.8	0.639
172	1057	B	12	H	3	50	102.2	0.777
172	1057	B	13	H	3	50	111.7	1.051
172	1057	B	14	H	3	50	121.2	1.067
172	1057	B	15	H	3	50	130.7	0.985
172	1057	C	1	H	3	50	3.5	1.120
172	1057	C	2	H	3	50	10.5	1.062
172	1057	C	3	H	3	50	20	1.024
172	1057	C	4	H	3	50	29.5	1.131
172	1057	C	5	H	3	50	39	1.077
172	1057	C	7	H	3	50	57.97	0.950
172	1057	C	6	H	3	50	48.5	1.027
172	1057	C	8	H	3	50	67.5	0.922

This table also appears on the volume CD-ROM.

Table 57. Thermal conductivity measurements from Site 1058.

Leg	Site	Hole	Core	Type	Section	Interval (cm)	Depth (mbsf)	Thermal conductivity (W/[m·K])
172	1058	C	1	H	1	50	0.5	0.955
172	1058	C	2	H	3	50	6	1.041
172	1058	C	2	H	5	50	9	0.985
172	1058	C	3	H	1	50	12.5	0.919
172	1058	C	4	H	3	50	25	1.113
172	1058	C	4	H	5	50	28	1.032
172	1058	C	3	H	1	50	12.5	0.993
172	1058	C	3	H	3	50	15.5	1.090
172	1058	C	3	H	5	50	18.5	0.898
172	1058	C	4	H	1	50	22	0.917
172	1058	C	5	H	1	50	31.5	1.008
172	1058	C	5	H	3	50	34.5	1.084
172	1058	C	5	H	5	50	37.5	0.958
172	1058	C	6	H	1	50	41	1.038
172	1058	C	6	H	3	50	44	1.101
172	1058	C	6	H	5	50	47	0.967
172	1058	C	7	H	1	50	50.5	0.971
172	1058	C	7	H	3	50	53.5	1.020
172	1058	C	7	H	5	50	56.5	1.077
172	1058	C	8	H	1	40	59.9	0.956
172	1058	C	8	H	3	50	63	0.821
172	1058	C	8	H	5	50	66	0.948
172	1058	C	9	H	1	50	69.5	1.039
172	1058	C	9	H	3	50	72.5	1.086
172	1058	C	9	H	5	50	75.5	0.987
172	1058	C	10	H	1	20	78.7	1.050
172	1058	C	10	H	3	60	81.03	1.090
172	1058	C	11	H	1	50	88.5	0.960
172	1058	C	11	H	3	50	91.5	1.220
172	1058	C	11	H	5	45	94.45	1.064
172	1058	C	12	H	1	50	98	1.054
172	1058	C	12	H	5	66	103.27	0.973
172	1058	C	12	H	7	50	106.11	0.768
172	1058	C	13	H	1	50	107.5	1.001
172	1058	C	13	H	3	50	110.5	0.994
172	1058	C	13	H	5	50	113.5	0.872
172	1058	C	14	H	2	50	117.2	0.926
172	1058	C	14	H	6	50	123.2	0.934
172	1058	C	15	H	2	50	126.75	0.983
172	1058	C	15	H	6	50	132.75	1.135
172	1058	C	16	H	3	50	137.76	0.963
172	1058	C	17	H	3	50	148.5	0.978
172	1058	C	18	H	3	50	158	0.985

This table also appears on the volume CD-ROM.

Table 58. Thermal conductivity measurements from Site 1059.

Leg	Site	Hole	Core	Type	Section	Interval (cm)	Depth (mbsf)	Thermal conductivity (W/[m·K])
172	1059	B	1	H	1	60	0.6	0.943
172	1059	B	1	H	3	50	3.5	0.969
172	1059	B	1	H	5	30	6.3	1.009
172	1059	B	2	H	1	50	7.2	1.098
172	1059	B	2	H	3	50	10.2	1.135
172	1059	B	2	H	5	50	13.2	1.016
172	1059	B	3	H	1	50	16.7	0.998
172	1059	B	3	H	3	50	19.7	0.935
172	1059	B	3	H	5	50	22.7	0.876
172	1059	B	4	H	1	50	26.2	0.949
172	1059	B	4	H	3	50	29.2	0.933
172	1059	B	4	H	5	50	32.2	1.045
172	1059	B	5	H	1	50	35.7	1.096
172	1059	B	5	H	3	50	38.7	0.843
172	1059	B	5	H	5	50	41.7	0.842
172	1059	B	6	H	1	50	45.2	1.006
172	1059	B	6	H	3	50	48.2	1.003
172	1059	B	6	H	5	50	51.2	1.135
172	1059	B	7	H	1	50	54.7	1.111
172	1059	B	7	H	3	50	57.7	0.969
172	1059	B	7	H	5	50	60.7	1.022
172	1059	B	8	H	1	50	64.2	0.962
172	1059	B	8	H	3	50	67.2	1.069
172	1059	B	9	H	1	50	73.7	1.034
172	1059	B	9	H	5	50	79.5	0.729
172	1059	B	10	H	1	50	83.2	1.057
172	1059	B	10	H	5	55	88.92	0.845
172	1059	C	7	H	1	50	57.5	0.844
172	1059	C	7	H	3	55	60.55	0.858
172	1059	C	7	H	5	50	63.5	0.912
172	1059	C	8	H	1	50	67	0.953
172	1059	C	8	H	3	50	70	0.978
172	1059	C	8	H	5	50	73	1.032
172	1059	C	9	H	1	50	76.5	0.935
172	1059	C	9	H	3	50	79.5	0.973
172	1059	C	10	H	1	60	86.1	1.067
172	1059	C	10	H	3	60	89.1	0.953
172	1059	C	10	H	5	60	92.1	0.942

This table also appears on the volume CD-ROM.

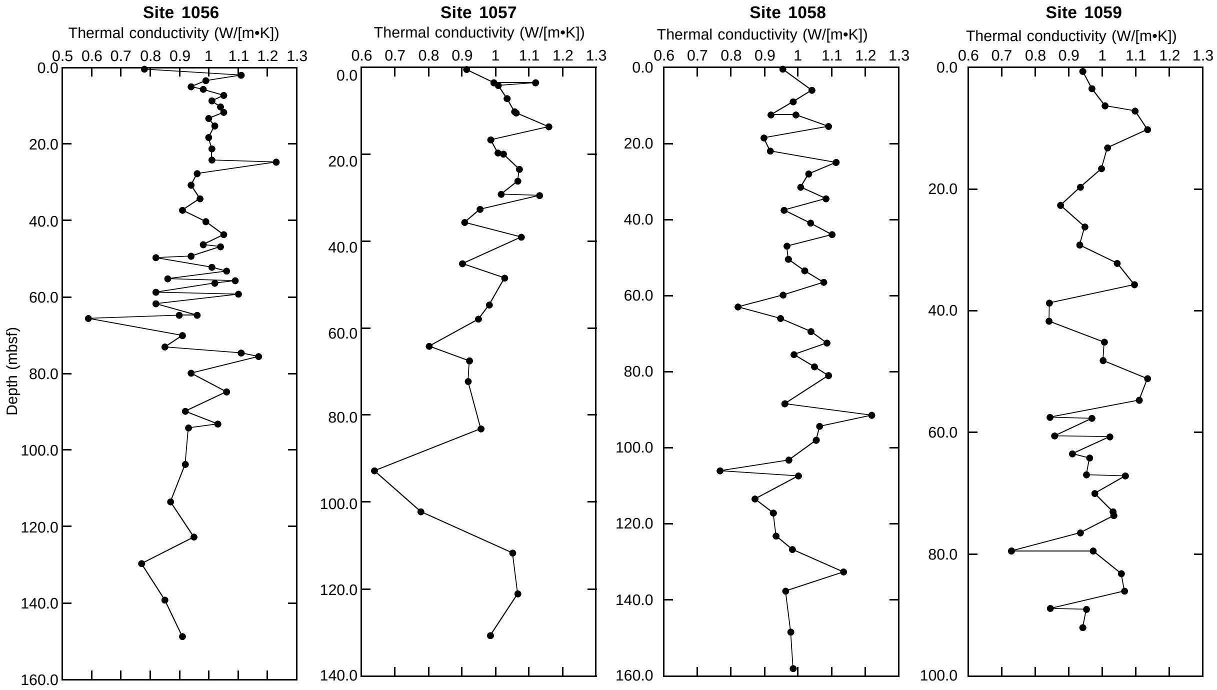

Figure 95. Thermal conductivity vs. depth at Sites 1056, 1057, 1058, and 1059.

Table 59. Resistivity measurements from Site 1056.

Leg	Site	Hole	Core	Type	Section	Top (cm)	Depth (mbsf)	Sediment temperature (°C)	Resistivity Z-direction (Ωm)	Resistivity Y-direction (Ωm)
172	1056	B	1	H	1	90	0.9		0.518	0.548
172	1056	B	1	H	1	75	0.75		0.594	0.633
172	1056	B	1	H	2	56	2.06		0.484	0.578
172	1056	B	1	H	2	130	2.8		0.739	0.632
172	1056	B	1	H	3	10	3.1	20.1	0.584	0.652
172	1056	B	1	H	1	36	0.36	20.6	0.665	0.743
172	1056	B	1	H	1	119	1.19	20.6	0.567	0.627
172	1056	C	1	H	1	50	0.5	20	0.486	0.483
172	1056	C	1	H	1	140	1.4	20	0.491	0.5
172	1056	C	1	H	2	50	2	19.2	0.617	0.653

This is a sample of the table that appears on the volume CD-ROM.

Table 60. Resistivity measurements from Site 1057.

Leg	Site	Hole	Core	Type	Section	Interval (cm)	Depth (mbsf)	Temp. (°C)	Resistivity Z-direction (Ωm)	Resistivity Y-direction (Ωm)
172	1057	B	1	H	1	130	1.3	23.4	0.522	0.534
172	1057	B	1	H	1	40	0.4	23.4	0.510	0.529
172	1057	B	1	H	2	134	2.84	23.1	0.529	0.568
172	1057	B	1	H	2	70	2.2	23.1	0.514	0.534
172	1057	B	1	H	3	23	3.23	23.2	0.565	0.587
172	1057	B	2	H	1	134	5.04	23	0.548	0.581
172	1057	B	2	H	1	70	4.4	23	0.516	0.548
172	1057	B	2	H	2	130	6.5	23.2	0.564	0.600
172	1057	B	2	H	2	50	5.7	23.2	0.488	0.510
172	1057	B	2	H	3	140	8.1	23.5	0.551	0.560

This is a sample of the table that appears on the volume CD-ROM.

Table 61. Resistivity measurements from Site 1058.

Leg	Site	Hole	Core	Type	Section	Interval (cm)	Depth (mbsf)	Temp. (°C)	Resistivity Z-direction (Ωm)	Resistivity Y-direction (Ωm)
172	1058	B	1	H	1	124	1.24	20.9	0.359	0.346
172	1058	B	1	H	2	143	2.93	21	0.452	0.452
172	1058	B	1	H	3	120	4.2	21	0.423	0.398
172	1058	B	1	H	4	125	5.75	20.7	0.421	0.406
172	1058	B	1	H	4	60	5.1	20.7	0.454	0.430
172	1058	B	2	H	1	104	7.04	20.1	0.521	0.486
172	1058	B	2	H	1	63	6.63	20.7	0.468	0.449
172	1058	B	2	H	2	52	8.02	20.7	0.425	0.433
172	1058	B	2	H	2	134	8.84	20.7	0.507	0.488
172	1058	B	2	H	3	120	10.2	20.9	0.440	0.439

This is a sample of the table that appears on the volume CD-ROM.

Table 62. Resistivity measurements from Site 1059.

Leg	Site	Hole	Core	Type	Section	Interval (cm)	Depth (mbsf)	Temp. (°C)	Resistivity Z-direction (Ωm)	Resistivity Y-direction (Ωm)
172	1059	A	1	H	1	40	0.4	21		0.553
172	1059	A	1	H	1	108	1.08	21.5		0.456
172	1059	A	1	H	2	44	1.94	20.9	0.473	0.465
172	1059	A	1	H	2	119	2.69	21.3		0.468
172	1059	A	1	H	3	29	3.29	21.6		0.479
172	1059	A	2	H	1	120	5	21.9		0.591
172	1059	A	2	H	1	66	4.46	21.9		0.713
172	1059	A	2	H	2	103	6.33	21.3		0.542
172	1059	A	2	H	2	20	5.5	21.3		0.577
172	1059	A	2	H	3	20	7	22.1		0.545

This is a sample of the table that appears on the volume CD-ROM.

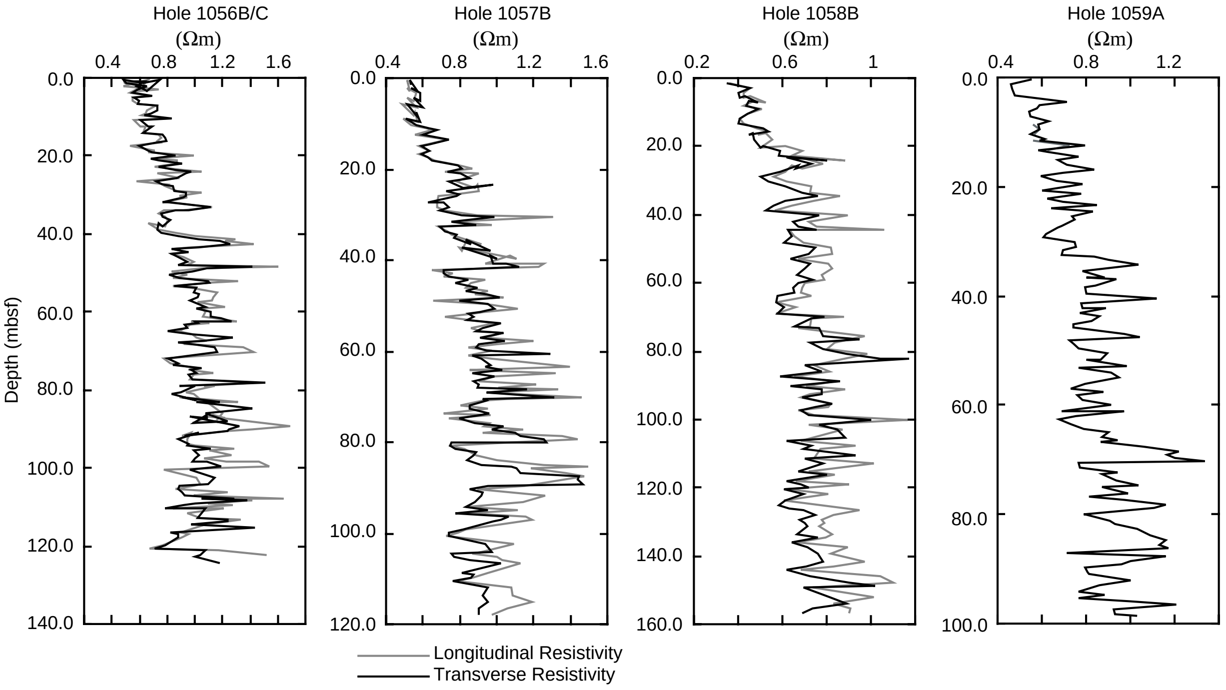

Figure 96. Longitudinal and transverse resistivity vs. depth at Sites 1056–1059.

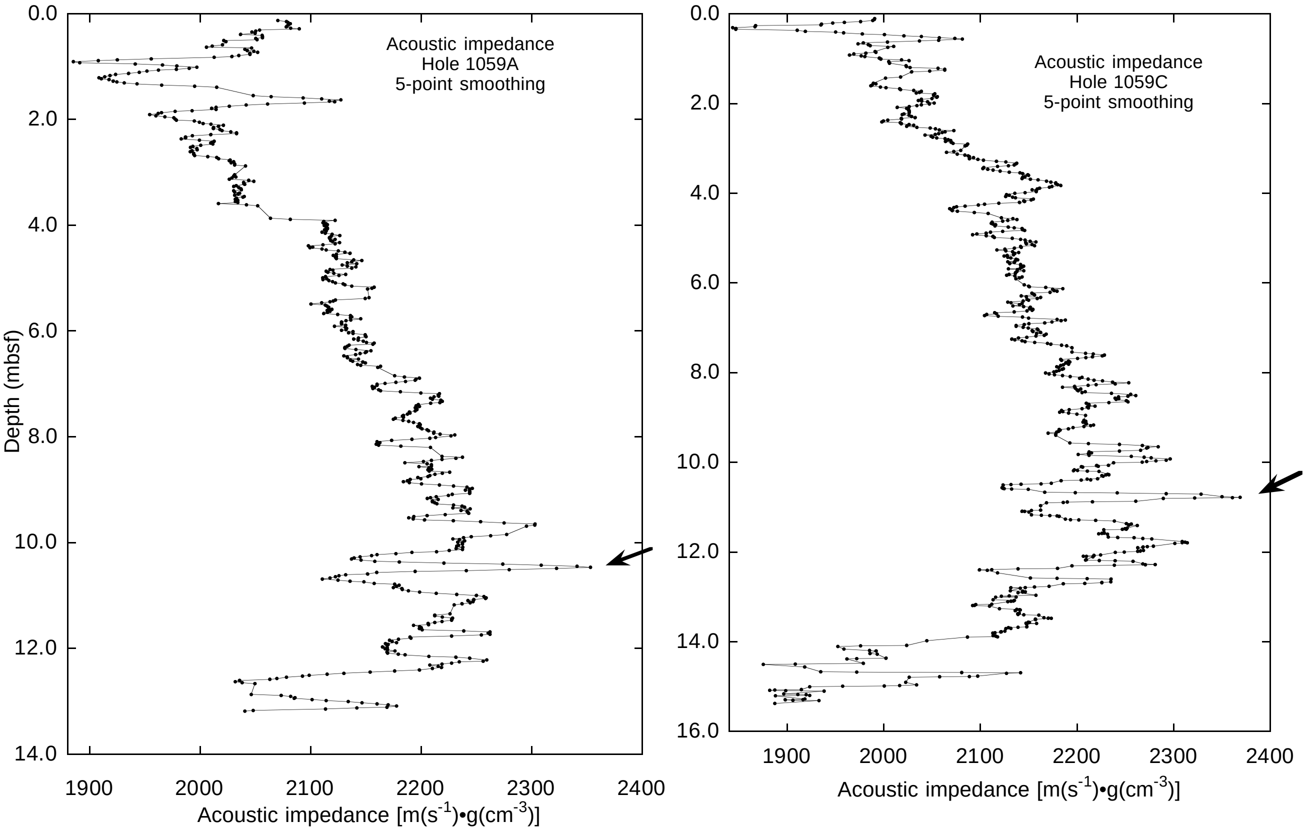

Figure 97. Acoustic impedance profiles from the upper 13 m of Hole 1059A and the upper 15 m of Hole 1059C. The arrows point to the peaks in acoustic impedance discussed in the text.

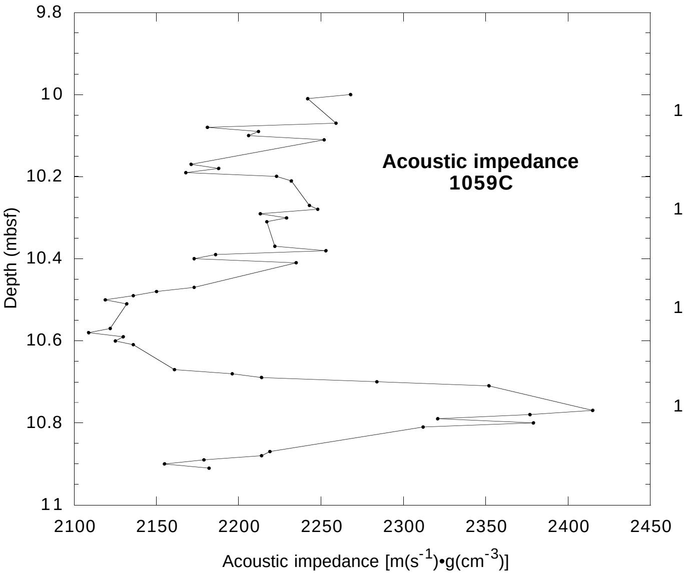

Figure 98. Acoustic impedance profiles between 10 and 11 mbsf for Holes 1059C and 1059A.

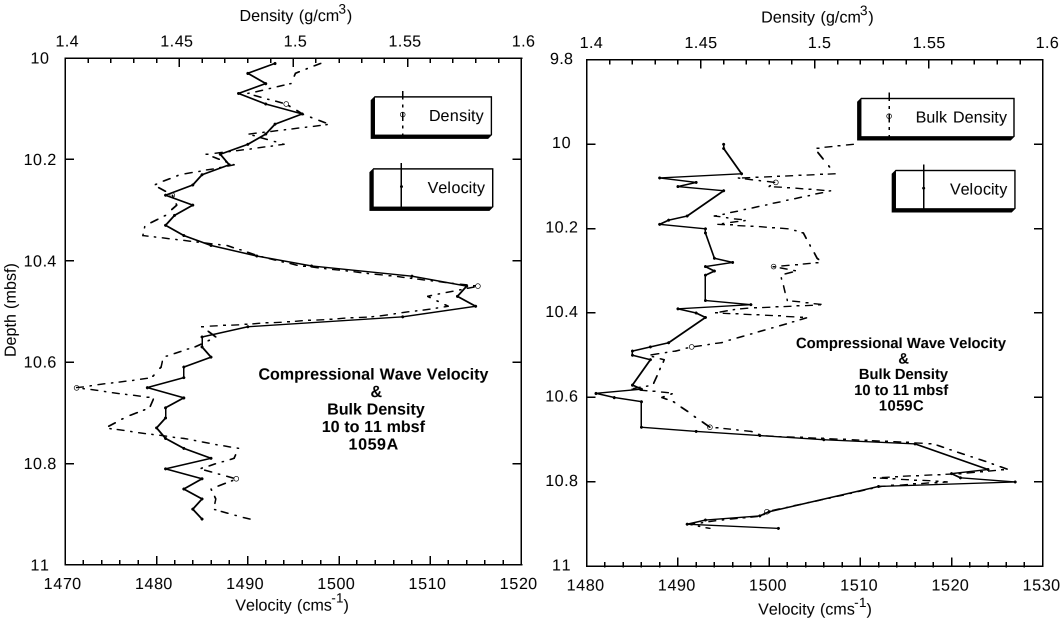

Figure 99. Bulk density and compressional wave velocity between 10 and 11 mbsf for Holes 1059A and 1059C.

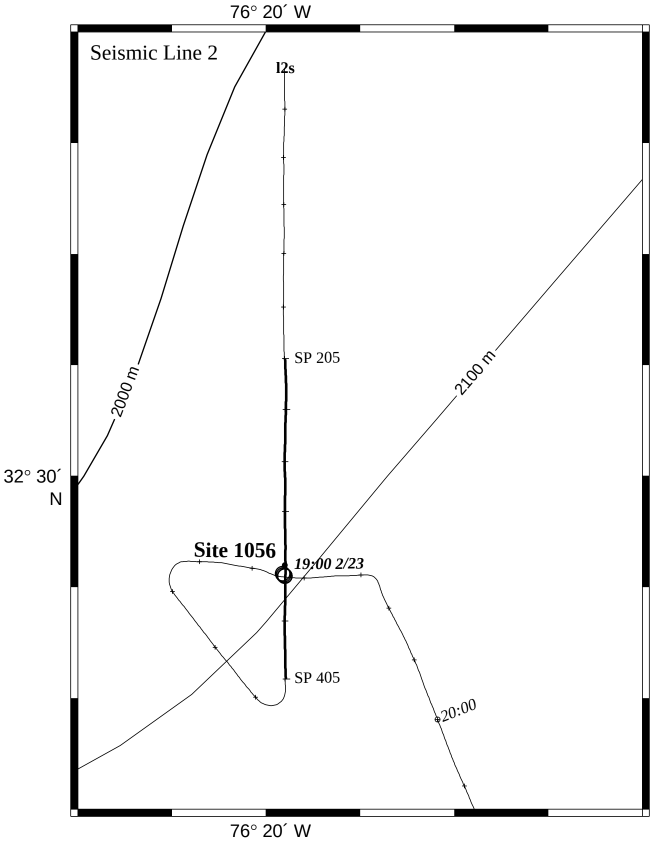

Figure 100. Survey track over Site 1056, with dates, times (Universal Time Coordinated [UTC]), and selected shotpoints (SP) given by the numbers along the survey line. Track for seismic profile in Figure 103 is thicker.

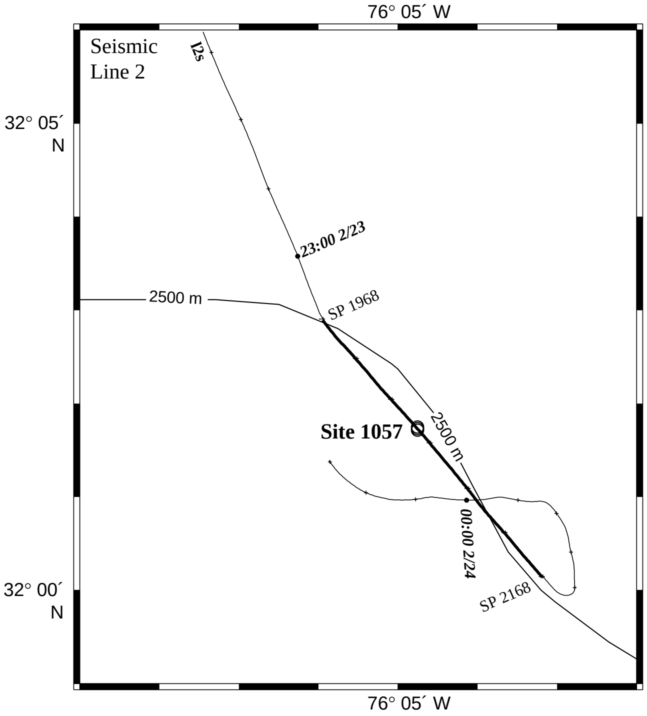

Figure 101. Survey track over Site 1057, with dates, times (UTC), and selected shot points (SP) given by the numbers along the survey line. Track for seismic profile in Figure 104 is thicker.

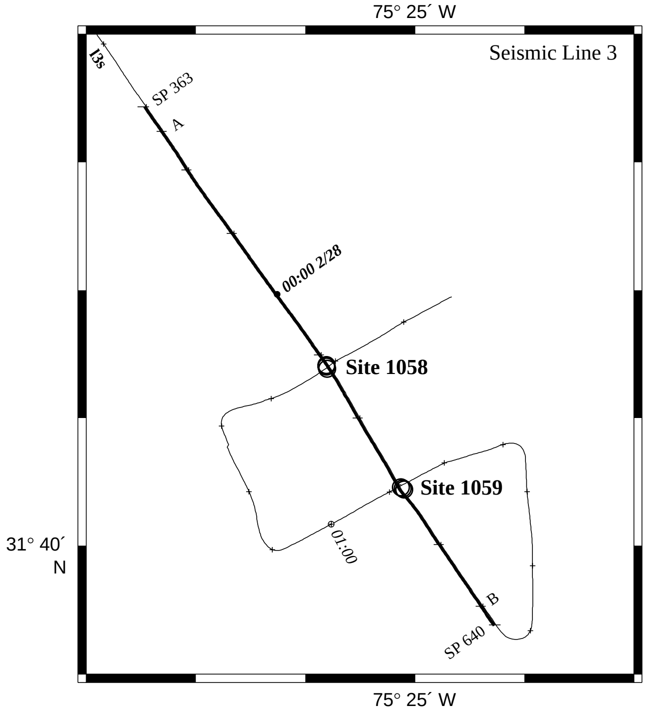

Figure 102. Survey track over Sites 1058 and 1059, with dates, times (UTC), and selected shot points (SP) given by the numbers along the survey line. Track for seismic profile in Figure 105 is thicker. A and B mark the ends of the 3.5-kHz profile in Figure 106.

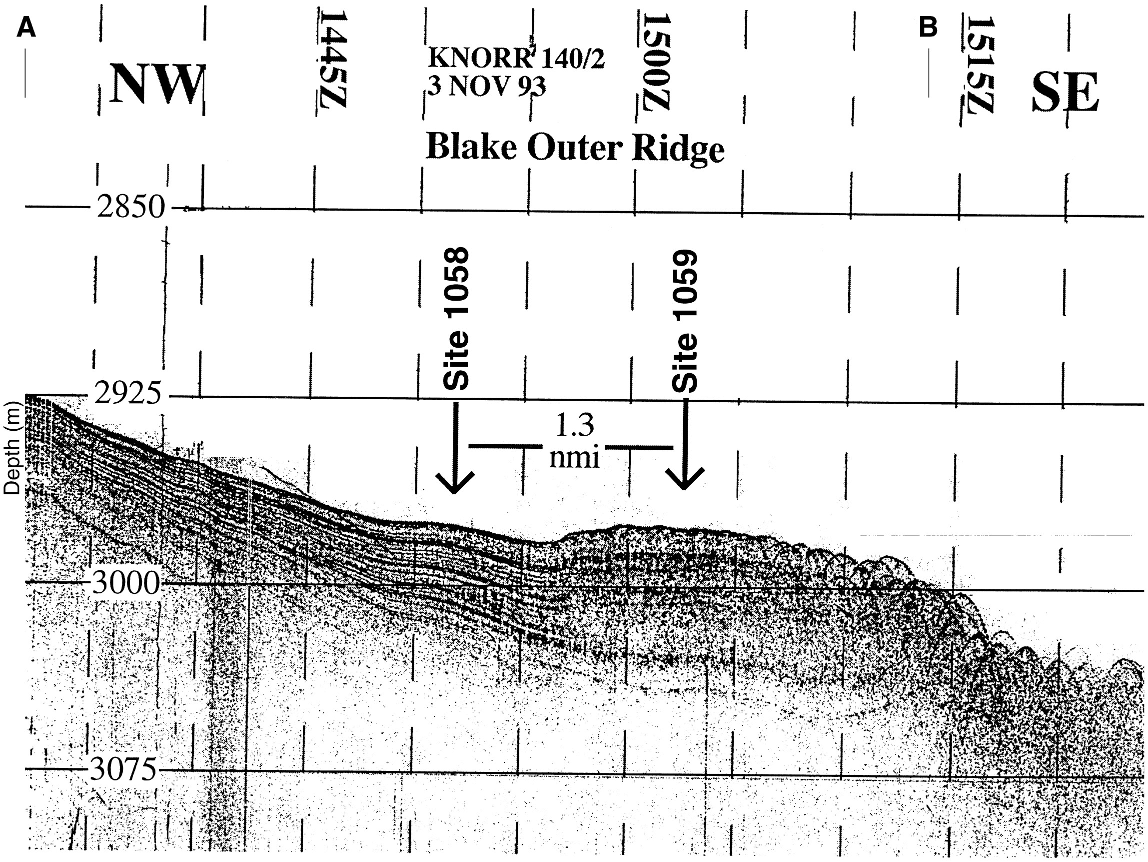

Figure 103. Locations of Sites 1058 and 1059 on a 3.5-kHz profile obtained during the November 1993 *Knorr* site-survey cruise.

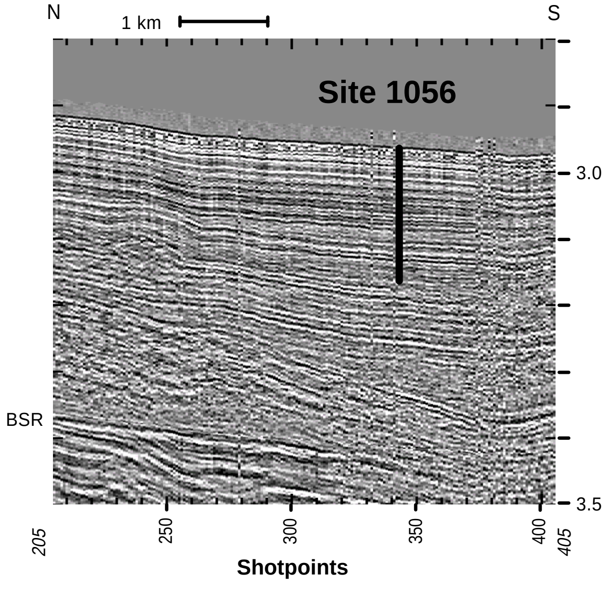

Figure 104. Seismic profile along the track shown in Figure 100 showing the location of Site 1056. BSR = bottom-simulating reflector.

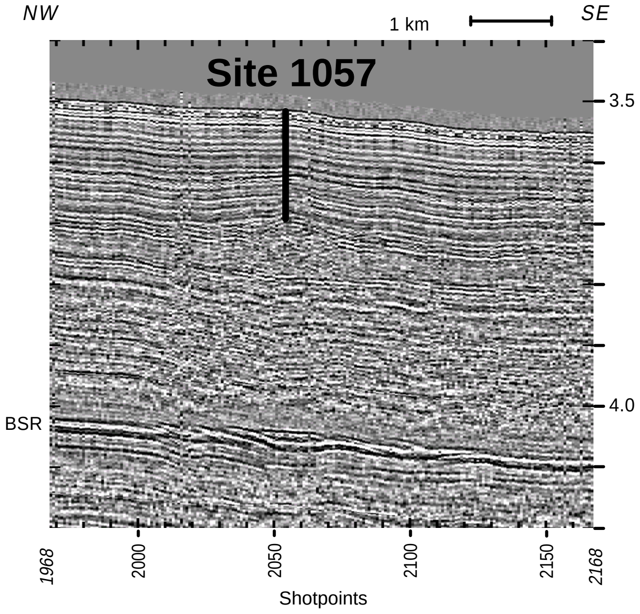

Figure 105. Seismic profile along the track shown in Figure 101 showing the location of Site 1057. BSR = bottom-simulating reflector.

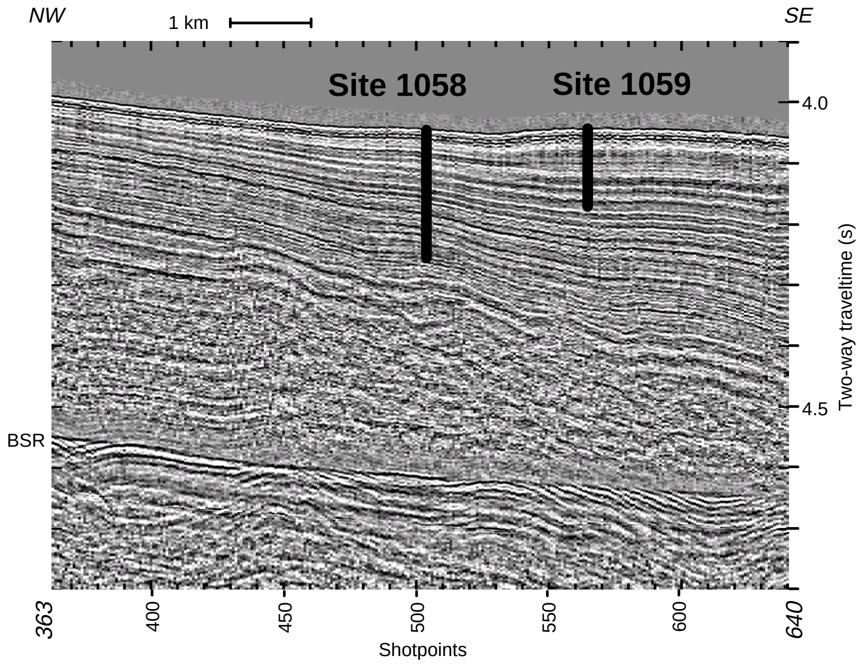

Figure 106. Seismic profile along the track shown in Figure 102 showing the locations of Sites 1058 and 1059. BSR = bottom-simulating reflector.